Mechanisms and functions of molecular interactions during plasmid rolling circle replication

Thesis submitted in accordance with the requirements of the

University College London, UCL

Claudia Arbore

Student No. 949843

Degree of Doctor of Philosophy

Division of Physical Biochemistry

National Institute for Medical Research

Mill Hill

London

NW7 1AA

I, Claudia Arbore, confirm that the work presented in this thesis is my own. Where information has been derived from other sources, I confirm that this has been indicated in the thesis.

_____

Acknowledgements

Foremost, I would like to thank my primary supervisor, Dr. Martin Webb, for his exceptional advice and support throughout my PhD. Also, I wish to thank Dr. Justin Molloy, for his support during my PhD and for teaching me how to use the AFM.
I would like to thank the members of my thesis committee, Dr. Justin Molloy, Dr. John Offer and Dr. Ian Taylor, for their valuable advice and shared knowledge at different stages of my PhD. I would also like to thank the Webb lab group for their encouragement, and for making various reagents/biosensors that I have used in several experiments.
I wish to thank my boyfriend, Emilio Pagliarulo, for his care, love and patience. Finally, I wish to thank my family for being very supportive and encouraging throughout the course of my studies.

I dedicate this thesis to my beloved parents.

The work presented in Chapter 3 has been published in:

Claudia Arbore, Lori M. Lewis, Martin R. Webb. *Kinetic Mechanism of initiation by RepD as a Part of Asymmetric, Rolling Circle Plasmid Unwinding.* Biochemistry. 2012; 51(17): 3684-3693.

This work has also been presented at:

2011: Poster presentation, Helicases and NTP-driven Nucleic Acid Motors: Structure, Function, Mechanism and Roles in Human Disease. FASEB Summer Research Conference, Colorado, USA.
2012: Oral presentation, UCL-NIMR day, UCL, London, UK.

Abstract

The system under investigation in this project is the replication of plasmid DNA belonging to the pT181 family from the Gram-positive *Staphylococcus aureus.* This plasmid replicates through an asymmetric rolling circle mechanism, initiated by a plasmid-encoded protein that nicks the supercoiled plasmid allowing unidirectional unwinding by the helicase and elongation by a polymerase. The proteins involved in this process are the replication initiator protein, *Staphylococcus aureus* RepD, the ATP-driven 3' to 5' helicase, *Bacillus Stearothermophilus* PcrA, and the *S. aureus* DNA polymerase III.

The project is mainly focused on three different aspects of plasmid replication including the formation of the initiation complex, the involvement of DNA polymerase III during plasmid elongation and the analysis of plasmid replication dynamics using AFM imaging.

The kinetic mechanism of RepD initiation is examined here. Plasmid nicking occurs at a rate > 25 s^{-1} (30 °C). Without RepD, PcrA is a poor helicase as it is unable to unwind as short as 20 bp DNA junctions. The function of nicking is also investigated as requirement of PcrA processivity and Rep-PcrA translocation complex.

The inclusion of DNA polymerase in these *in vitro* experiments generates a full *in vitro* plasmid replication system. The kinetics of PcrA-mediated unwinding has been studied previously, but the involvement of polymerase is little understood. PcrA is able to unwind plasmid DNA at a rate of ~30 bp s^{-1} (30 °C), however the inclusion of polymerase increased the unwinding rate to ~71 bp s^{-1} (30 °C).

Using a fluorescence-based kinetic approach combined with rapid-mix techniques and AFM imaging, a variety of processes are investigated during RepD, PcrA and PolC mediated DNA replication. These *in vitro* data would provide an understanding of kinetics and dynamics of several complex processes during plasmid replication.

Abbreviations

ADP	Adenosine diphosphate
AFM	Atomic force microscopy
ATP	Adenosine triphosphate
Cy3B-SSB	SSB (see below) W88C, labelled with Cy3B
DCC-SSB	SSB G26C, labelled with IDCC (see below)
DETA	(3-(2-(2-aminoethylamino)ethylamino)propyl trimethoxysilane
DMSO	Dimethyl sulfoxide
DNA	Deoxyribonucleic acid
ddH_2O	Distilled water
dATP	Deoxyadenosine triphosphate
dCTP	Deoxycytidine triphosphate
dGTP	Deoxyguanosine triphosphate
dTTP	Deoxythymidine triphosphate
dNTP	Deoxyribonucleotide triphosphate
dsDNA	Double stranded DNA
DSO	Double stranded origin
DTT	Dithiothreitol
EDTA	Ethylenediaminetetraacetic acid
FRET	Förster resonance energy transfer
HPLC	High Performance Liquid Chromatography
ICR	Inverted complementary repeat
IDCC	*N*-[2-(iodoacetamido)ethyl]-7-diethylaminocoumarin-3-carboxamide
IPTG	Isopropyl-beta-D-thiogalactopyranoside
Mant	N-methylanthraniloyl
MDCC	*N*-[2-(1-maleimidyl)ethyl]-7-diethylaminocoumarin-3-carboxamide
MDCC-PBP	PBP (see below) A197C labelled with MDCC
PBP	Phosphate binding protein
PCR	Polymerase chain reaction
PcrA	Plasmid copy number reduction A
P_i	Inorganic phosphate
PPase	Inorganic pyrophosphatase
PP_i	Pyrophosphate
PMSF	Phenylmethanesulphonylfluoride
RNA	Ribonucleic acid
SDS-PAGE	Sodium Dodecasulphate-Polyacrylamide gel electrophoresis
SF	Superfamily
SSB	Single stranded DNA binding protein
ssDNA	Single stranded DNA
SSO	Single stranded origin
TIRFM	Total internal reflection fluorescence microscopy
wt	Wild type

Table of contents

List of Figures

List of Tables

1. Introduction

1.1. DNA replication mechanisms

Genetic information of any organism ranging from single cells such as bacteria to higher eukaryotes is contained in DNA. The survival and proliferation of all organisms depends on the ability to duplicate the DNA molecule in an accurate and efficient way.

DNA replication is a biological process in which a single parental DNA molecule is duplicated to form two daughter molecules. The DNA molecule is formed by two complementary strands of opposite polarity arranged in the form of a double helix through hydrogen bonding [1]. During replication one strand of the parent DNA is passed to each of the daughter molecules and is used for the synthesis of the newly generated strand.

The process of replication is accomplished through the exquisite coordination of multiple proteins that collectively form the replisome. Despite the common replicative function in all organisms, the number, and the interactions of such macromolecules differ between species [2-5]. Generally, the formation of the replisome requires the coordinated assembly of motor proteins such as helicases and polymerases that guarantee a faithful transmission of the genetic information in living systems.

1.1.1. Bacterial DNA replication

The genetic material of bacteria is contained in nucleoids and located in the cytoplasm. During bacterial replication, the DNA is duplicated and equally distributed to the daughter cells. Generally, DNA replication begins on the bacterial chromosome at a specific sequence of nucleotides called the origin [6]. The latter contains peculiar DNA sequences that are recognized by initiator proteins, which recruit other replicative proteins. Initiation of replication is accomplished by the loading of the helicase on the origin. In order to generate the replication fork, such enzymes perform unwinding by breaking the hydrogen bonds that hold the DNA strands together using the energy of ATP hydrolysis. Reannealing of the DNA is prevented by the binding of the single-stranded binding protein (SSB) along the separated strands. The activity of a primase

generates the free 3'-OH to promote polymerase catalysis. At this stage, the free nucleoside triphosphates in the cytoplasm are paired up with their complementary base and joined to the growing strand by the DNA polymerase [2].

In the Gram-negative *E. coli* organism, the replisome contains the replicative polymerase (Pol III holoenzyme), the hexameric DnaB helicase, DnaG primase, and SSB (Figure 1.1) [7]. Due to the antiparallel orientation of the DNA strands and the unidirectional synthesis of the DNA pol III, the leading strand and the lagging strand synthesis requires the coordinated use of two pol III molecules within the replisome. The synthesis of the lagging strand is discontinuous requires and occurs as synthesis of short RNA primed fragments, the Okazaki fragments.

Gram-positive and Gram-negative bacteria share many of the replisome components (Table 1.1) [7, 8]. In the Gram-positive *Bacillus subtilis* organism, PolC is the replicative polymerase analogous to the *E. coli* DNA pol III α subunit. However, a second, less processive polymerase, DnaE has been shown to be involved in lagging strand synthesis [9].

In this thesis, the replication of the pC221 plasmid from the Gram-positive *Staphylococcus aureus* was investigated. For many characterized plasmids, replication occurs in a bi-directional manner. However, some plasmids, including pC221, replicate with an alternative mechanism, termed asymmetric, rolling-circle replication [10, 11]. The sequential synthesis of the two DNA strands is the main feature of such replicating process. In view of this, the process of replicating an organism's genomic material is complex and understanding how DNA replication is accomplished provides important information about potential control elements.

Several biochemical mechanisms during plasmid replication have been studied in terms of DNA-protein and protein-protein interactions. Particularly, the initiation and elongation of replication were explored by measuring the activity of the replicative proteins.

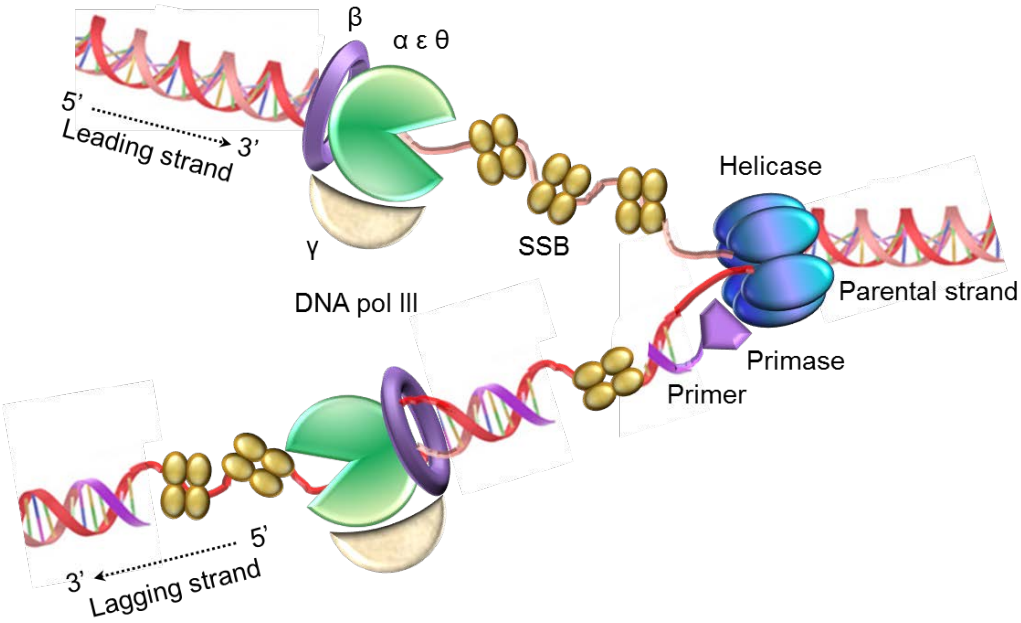

Figure 1.1. General features of the *E. coli* replication fork. The DNA duplex unwinding is performed by a DNA helicase. SSB proteins bind the ssDNA generated by the helicase hereby preventing reannealing. A primase periodically synthetizes short RNA primers on the lagging strand to allow bidirectional DNA synthesis by the DNA polymerase III. The DNA polymerase III catalyzes leading and lagging strands synthesis in the 3' to 5' direction.

Function	*Gram-negative (E. coli) protein*	*Gram-positive (B. subtilis) protein*
Leading strand synthesis	*DNA pol III*	*DNA pol III*
Lagging strand synthesis	*DNA pol III*	*DnaE*
Primase	*DnaG*	*DnaB*
Hexameric helicase	*DnaB*	*DnaC*
Single stranded DNA binding	*SSB*	*SSB*

Table 1.1. Proteins forming the *E. coli* and *B. subtilis* replisomes.

1.1.2. Asymmetric rolling circle replication

Plasmids are circular genetic elements, made of either single or double stranded DNA, which are capable of replicating independently from the chromosomal DNA in a controlled way within the host. Therefore, they are good models to explore the mechanisms involved in DNA replication and control. Plasmids often carry genes that offer the host a selective advantage, such as antibiotic resistance, and so it is important to control their replication and spread [12].

Plasmid replication can be conveniently divided into three stages: initiation, elongation, and termination. The first basic problem of any process of DNA replication is that of priming, since none of the replicative polymerases can start DNA synthesis without a primed DNA. Priming is achieved during initiation. Although, the replicative DNA polymerase is unable to initiate *de novo* replication of a circular plasmid, the latter is generally substrate of an initiator protein that cleaves one DNA strand to generate a free 3′-OH end. Therefore, initiation plays an additional role, as it forms a point of control for replication [13].

Staphylococcal plasmid replication has been well studied as many of the plasmids encode antibiotic resistance genes [12]. As mentioned above, staphylococcal plasmids, belonging to the pT181 family, replicate by an asymmetrical rolling circle mechanism (Figure 1.2) [14]. In this process, the synthesis of the two DNA strands is not concurrent. According to the terminology being used to describe this process, the two DNA strands are named as (+)- and (-)-strand, and the (+)-strand is the first to be synthesized by the polymerase. The plasmids belonging to the pT181 family contain a *Rep* gene encoding an initiator protein, a double stranded origin (DSO or *ori*) containing a series of inverted complementary repeats (the ICR sequences), at least one single stranded origin (SSO) and other regulatory elements [14-16].

The asymmetric rolling circle replication starts with the interaction between the initiator protein, Rep, and the DSO sequence on the plasmid [15]. Origin sequences differ in the recognition site for a specific Rep protein. RepD is the replication initiator from the staphylococci plasmid pC221, member of the pT181 plasmid family [17]. RepD binds as a dimer to the high affinity ICRIII site contained in the DSO, whilst allowing the cruciform structure containing ICRII into close proximity (Figure 1.2, step 1) [15, 18]. The protein nicks the DNA on the (+)-strand of the ICRII sequence resulting in a covalent phosphotyrosine bond between the tyrosine 188 within the active site of RepD and the 5′ end of the nicked DNA (Figure 1.2, step 2) [17]. It then remains part of the replication complex during the complete replication of the plasmid DNA.

Strand elongation is initiated by recruitment of PcrA helicase and DNA polymerase III (Figure 1.2, step 3). PcrA binds to the exposed single stranded DNA and unwinds the duplex in the 3′ to 5′ direction. The DNA polymerase III is then able to extend the free 3′ OH of the (+)-strand around the plasmid (Figure 1.2, step 4). RepD protein remains associated with PcrA during extension, resulting in displacement of a single stranded DNA loop. Reannealing of the ssDNA is prevented through (+)-strand synthesis by the polymerase and SSB binding on the displaced ssDNA. DNA synthesis continues around the plasmid until the complex reaches the DSO again where termination starts.

At this point, RepD performs a series of transesterfication (strand exchange) events in order to resolve the complex (Figure 1.2, step 5) [19, 20]. During strand exchange, the Rep protein is thought to use catalytic nicking sites on each subunit of the dimer to sequentially nick the newly synthesized strand and the single stranded loop. The details of this process remain to be elucidated.

The complete double stranded plasmid is released, along with a circular single stranded plasmid and RepD as an inactive form (Figure 1.2, step 6) [20]. The displaced single stranded plasmid is able to initiate replication from a region of secondary structure, the single stranded origin (SSO) [21]. Finally, the new plasmid is substrate for a DNA gyrase, whose activity generates a supercoiled plasmid (Figure 1.2, step 7). The latter can then be substrate for a fresh RepD protein to start a new replication event.

The wealth of genetic information carried by plasmids and its impact on the environment and human health, have stimulated research into plasmid maintenance and antibiotic resistance.

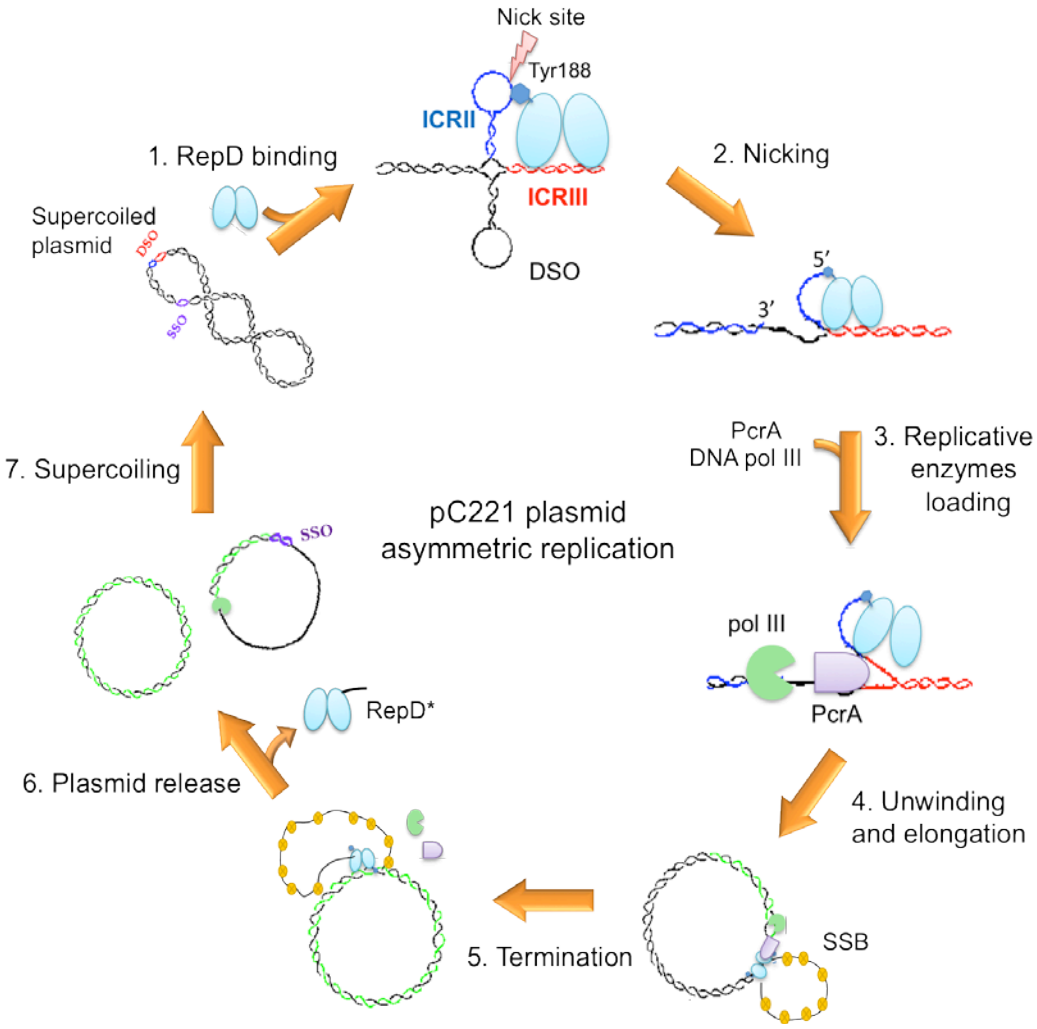

Figure 1.2. Schematic representation of asymmetric rolling-circle plasmid replication. RepD interacts with the *oriD* (step 1) and nicks the ICRII sequence (step 2). The replicative enzymes, DNA polymerase III and PcrA helicase, are loaded on the ssDNA formed by RepD activity (step 3). PcrA performs unwinding and the polymerase synthesizes the new (+)-strand (step 4). The SSB protein binds the displaced (+)-strand. Replication continues until termination occurs on the DSO (step 5). The newly synthesized plasmid is released (step 6). This is substrate for a DNA gyrase (step 7).

1.1.3. Replication initiator proteins of the pT181-like plasmids

As mentioned, staphylococcal plasmids, which replicate by a rolling circle mechanism, encode a replication initiator protein (Rep). The first Rep protein to be identified, RepC, is a 38-kDa protein encoded by the tetracycline resistance pT181 plasmid [22, 23]. A number of Rep proteins homologous to RepC have since been identified. The *Rep* gene sequences of six pT181-like plasmids are currently known and they encode proteins sharing 62% amino acid sequence identity [24]. Such plasmids also contain the origin of replication (*ori*), which include specific inverted repeated sequences (ICR) that finely regulate replication being the substrate for the initiator proteins [17]. The ICRII sequences involved in nicking are highly conserved among the different plasmid groups, whereas an adjacent less conserved binding sequence (ICRIII) is found in different origins. A comparison between two different origins is shown in Figure 1.3A.

The initiator proteins have origin-specific, nicking-closing activities that are responsible for their biological functions of initiation and termination of replication [25, 26]. Replication is started through Rep binding to the ICRIII sequence and nicking at a unique position within the (+)-strand of the ICRII sequence. Since the ICRII sequence is highly conserved, it is the interaction between Rep and ICRIII sequence, which confers specificity in plasmid replication [27]. Structure-function analyses have shown that the initiator proteins belonging to a particular family have highly conserved nicking domains but rather divergent DNA binding domains [28]. Hence, the DNA interaction site confers specificity and each Rep protein is active, *in vivo,* only at the cognate origin of replication of the encoding plasmid [17]. Mutational analysis of the Rep proteins showed that switching six specific amino acids between Rep proteins could switch their replication specificity.

This study deals with the RepD initiator protein specified by the plasmid pC221. RepD binds as dimer on the *oriD* sequence. Such DNA-protein interaction can induce a cruciform structure in the origin (Figure 1.3B) [15, 19].

Previous studies showed that incubation of the pC221 plasmid with RepD caused a double-strand break. The precise location of the nicking on the (+)-strand of the ICRII (shown with a red arrow in Figure 1.3B) was previously determined through sequencing electrophoresis [25].

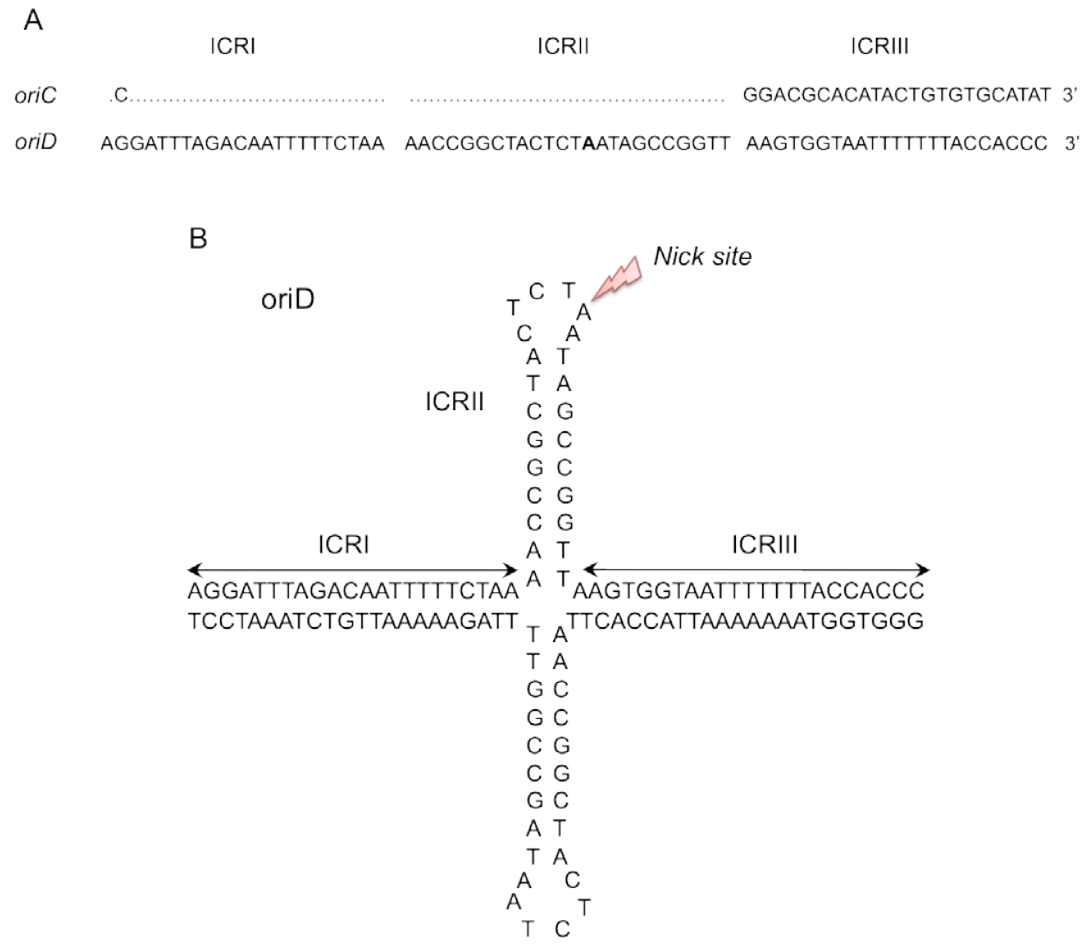

Figure 1.3. The origin of replication. (A) Sequence alignment of the origins, oriC and oriD, of the pT181 and pC221 plasmids. The nick site is shown in bold. The sequence identity is indicated with dots. (B) The sequence and predicted secondary structure of the *oriD*. RepD binds the supercoiled plasmid on ICRIII sequence at the *oriD*. RepD binding bends the DNA and promotes the ICRII extrusion. The nick site, indicated by the arrow, is located within a loop of the ICRII sequence.

1.1.3.1. Initiator protein activities and functions

One of the main biological activities of the initiator proteins is the removal of supercoiling in the DNA plasmid [25]. The formation of a 'relaxation complex' is achieved through the nicking activity. As the final result is a change in the plasmid topology and loss of supercoiling, such proteins are closely related to relaxases like the topoisomerase enzymes. For this reason, RepD activity is also termed "topoisomerase I-like" [17, 22]. DNA relaxation promotes the loading of the replicative proteins and their activities.

The chemistry of the nicking reaction is a transesterification, whose final product is a nicked double-stranded DNA with a sequestered 3'-OH and the covalently bound Rep protein to the 5'-end via a phosphotyrosine linkage [25]. The mechanism for a transesterification reaction catalysed by a relaxase is shown in Figure 1.4 [29]. A base catalyst acts abstracting a proton to the tyrosine residue that performs a nucleophilic attack to the phosphorus in the DNA backbone. Upon attack, a pentavalent phosphorane transition state is formed, accompanied by the buildup of negative charge on the non-bridging oxygens. A general acid resolves the transition state promoting the expulsion of the 3' hydroxyl group. This results in DNA strand cleavage and opening of the helix. The overall reaction is isoenergetic and reversible as a second transesterification can religate the DNA. The reversibility is important for RepD biological function in termination.

Cofactors are often required for full catalytic activity. Divalent metal ions are essential cofactors as they can perform both structural and catalytic functions [30]. In the transesterification reaction, Mg^{2+} would stabilize the negative transition state by neutralizing its charge, and/or assist the negative leaving group at the 3'-end [30]. However, there are still many open questions regarding the atomic mechanism of the catalysis. Such a mechanism of cleavage and religation might involve several basic or acidic amino acid residues within the protein. The manner in which the free 3′-end interacts with the protein during the reaction and the atomic mechanism of strand passage, as well as the function

of magnesium during several catalysis steps are some of the questions that remain to be answered. Structural information would be essential to address these questions.

The Rep proteins support just one round of plasmid replication [31]. Once nicking is performed, RepD recruits PcrA helicase and assists unwinding up to the termination stage. At the end of one replication event, RepD is released as an inactive form having a short oligonucleotide (11 nucleotides) attached to its active site [20, 31]. RepD inactivation would be a potential mechanism to control replication, as the released inactive protein is unable to act on a new plasmid substrate [32]. Little is currently known about the molecular events of termination except that the initiator protein needs part of the ICRII including the nick site for strand exchange. The binding site, ICRIII, is dispensable in order to terminate replication [28]. There is also a lack of structural information for the pT181 family of initiator proteins. The acquisition of such information would elucidate the molecular mechanisms of the protein-DNA interactions, the position of the amino acids involved on a three-dimensional level and clarify previous mutational and functional studies.

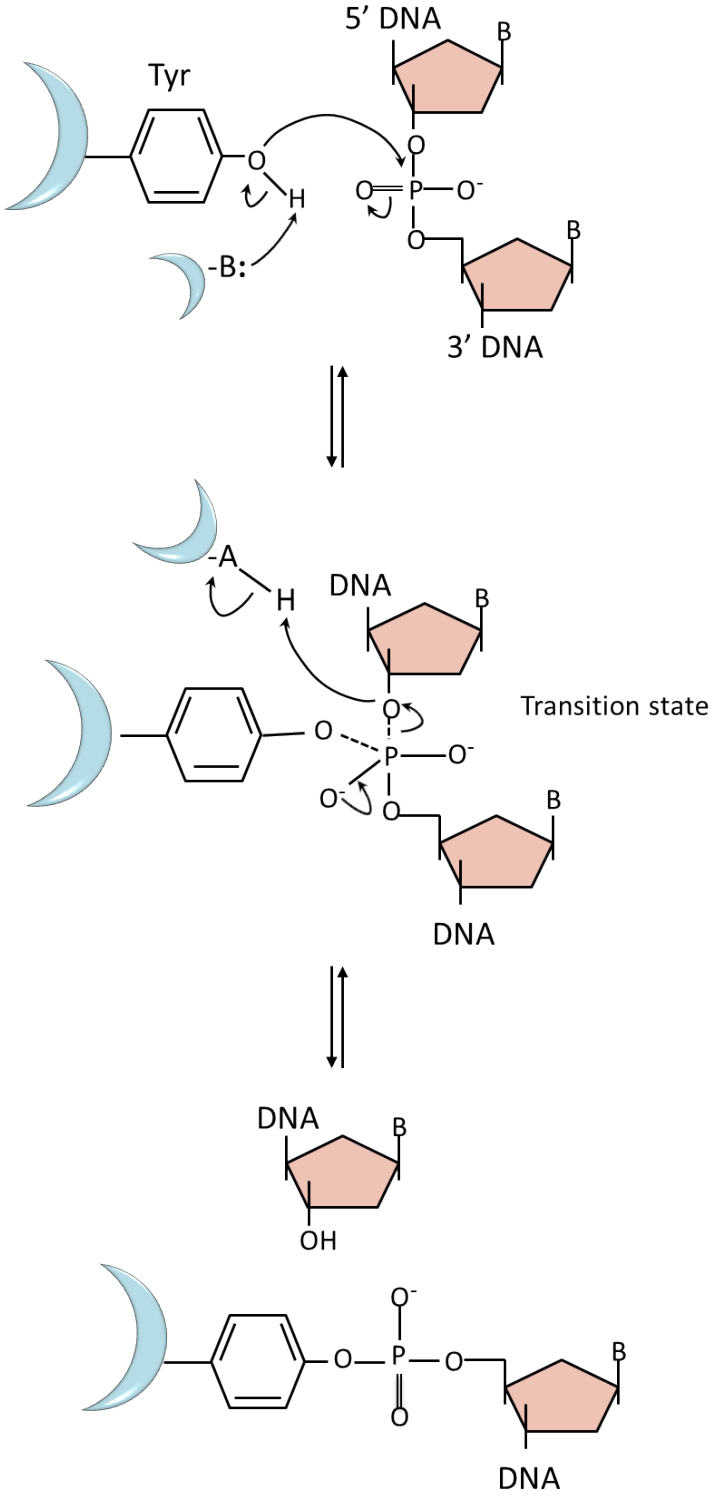

Figure 1.4. Steps of a transesterification reaction catalysed by a relaxase. "A" and "B" are general acid or base catalysts. See text for details.

1.1.4. Helicases

Helicases are a ubiquitous class of motor proteins that use the energy of nucleoside triphosphate hydrolysis to translocate along nucleic acids and separate the complementary strands of the duplex [33]. As consequence, helicases are a subgroup of translocases. They play essential roles in many cellular processes including DNA replication, repair, recombination, transcription and chromatin remodeling, and thus are involved in most aspects of DNA and RNA metabolism.

The translocation rates of these enzymes can vary from a few to several thousand base pairs per second [34]. Most helicases are processive and some can catalyze several thousand base pair separations before dissociation. However, their activity can be modulated by the interaction with particular protein partners and accessory factors [35].

Different helicases can function as monomers, dimers or higher-order oligomers and they can either use DNA, RNA or DNA/RNA hybrids as substrates [34]. DNA helicases became prominent with the discovery that mutations in their genes are associated with numerous human syndromes including chromosomal instability and age-related diseases along with cancer [36, 37].

1.1.4.1. Classification of helicases

Helicases were originally classified into families, in 1993 by Gorbalenya and Koonin. In their work helicases were divided in 6 superfamilies (SF) on the basis of primary structure similarity and structure-function analysis. However, subsequent studies revealed that many helicases use the energy of NTP hydrolysis to move along nucleic acids rather than unwinding the duplex. With the discovery of new mechanistic functions became apparent that there were some deficiencies in the original classification.

Consequently, Singleton et al., made a new classification used to date, including new motifs and dividing the proteins into A and B type, according to their direction of movement (Figure 1.5) [34]. For the largest two groups, SF1 and SF2, the seven motifs originally described were expanded to include new motifs, TxGx [38], TRG [39], Q-motif [40], motif 4a [41]. The six superfamilies and their motifs are shown in Figure 1.5A. Despite the diversity between the SF, there are a few common features. All enzymes retain the “core domains” formed by neighboring RecA-like folds. This domain couples NTP binding and hydrolysis to protein conformational changes as mechanism for energy transduction [42].

The helicases belonging to the SF1 and 2 contain two RecA-like folds on a single polypeptide chain, the other superfamilies contain from 6 to 12 individual RecA folds. They are generally considered to act as monomers or dimers [34]. However, the oligomeric state of these two helicases groups is still disputed.

Helicases belonging to SF3 to SF6 are ring-shaped hexamers or double-hexamers [34, 43]. The nucleotide binding pockets are located between the subunits. Several models of ATP hydrolysis exist from alternate subunit to sequential ATP binding and hydrolysis, to stochastic and concerted models.

Helicases can also be subdivided on the basis of the direction of translocation (Figure 1.5B) [34]. Of all the enzymes characterized to date, SF1, 2 and 6 contain helicases with both type of directions of translocation, 3′ > 5′ (type A) and 5′ > 3′ (type B). SF3 retain 3′ > 5′ translocation directionality, whereas SF 4 and 5 contain 5′ > 3′ helicases. According to the nature of the nucleic acid substrate, we can distinguish type α or β helicase whether they translocate on ssDNA or dsDNA (Figure 1.5B). To date, all SF1 enzymes appear to be type α whereas SF 2 contains both types of enzymes.

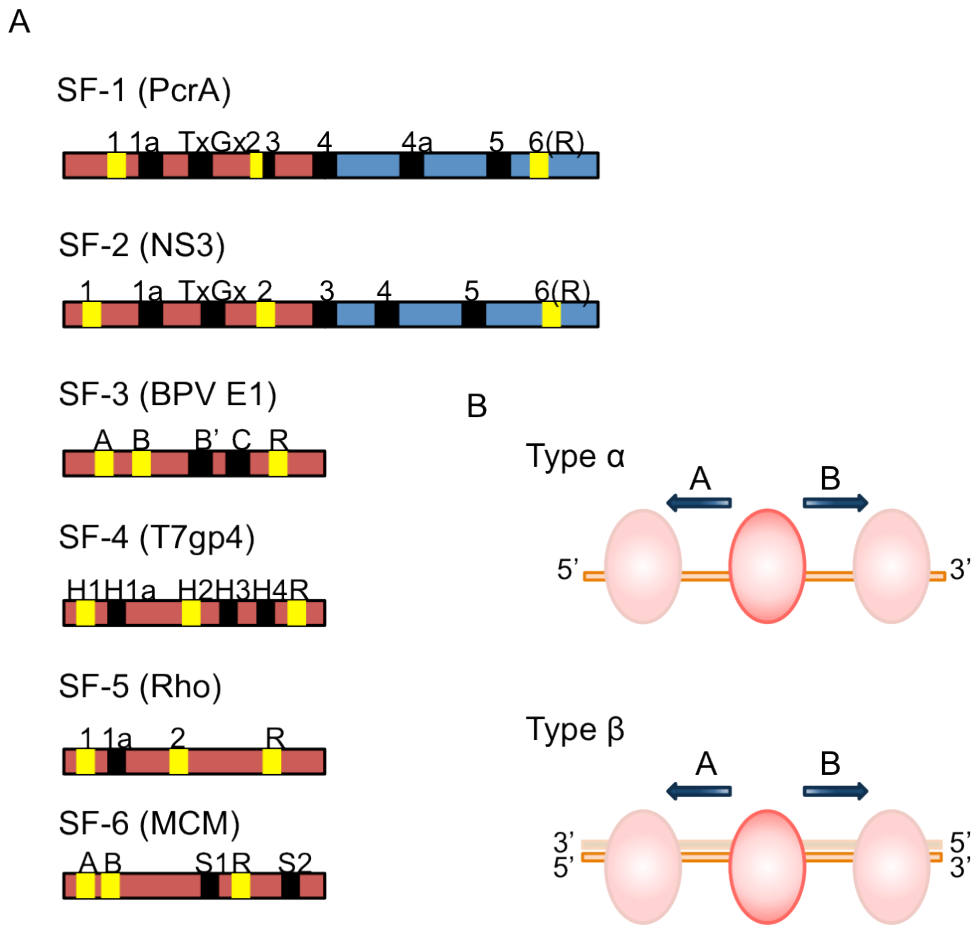

Figure 1.5. Helicase classification. (A) The six superfamilies of helicases sharing the universal motifs. Examples of helicase members of each family are also indicated. The core helicase domains are shown in red and blue. These regions are assigned to the SF based on conserved sequences/domains. Universal domains are shown in yellow, while the domains specific to each SF are shown in black. The location of these domains is arbitrary in these examples. (B) Helicase classification by direction of translocation and nucleic acid substrates (shown in schematic form). Helicases can bind to ssDNA or dsDNA and translocate 3´ > 5´ or 5´ > 3´ directions.

1.1.4.2. PcrA helicase

PcrA is an ATP-driven 3′ > 5′ helicase, member of the SF1, and an essential enzyme in many Gram-positive bacteria. It is involved in several processes, such as rolling circle replication and DNA repair. This enzyme was first discovered in *Staphylococcus aureus* as conditional mutants of *PcrA* causing

reduced plasmid copy number, giving rise to the name of ‘plasmid copy number reduction A’ [44].

The crystal structure of the *Bacillus Stearothermophilus* PcrA has been solved at high resolution revealing two domains (1 and 2) that are further divided into two subdomains, A and B (Figure 1.6A) [45]. The ATP-binding site is situated in a cleft between domains 1A and 2A. Subsequent crystal structures of PcrA in complex with a 3' tailed DNA duplex and a nonhydrolyzable ATP analogue revealed the main conformational changes and the mechanism of PcrA-mediated DNA unwinding (Figure 1.6A). Conformational changes start with the interaction between the ssDNA and the helicase through the 2B domain. This causes the 2B subdomain to fold over the 1B domain. At this stage, another conformational change occurs upon nucleotide binding. This allows the 1A and 2A subdomains to close around the ATP (Figure 1.6B). The cleft closure has two main consequences: it destabilizes the double strand by moving the duplex onto a negatively charged surface and it promotes the movement of the single-stranded region towards the core motor domain (1A, 2A). These movements coupled with ATP hydrolysis and release result in translocation along the DNA and duplex destabilisation, leading to strand separation (Figure 1.6B).

The amino acid residues of PcrA involved in ssDNA interaction during translocation are shown in Figure 1.6C. The DNA binding site is composed of a series of aromatic amino acids. Two phenylalanine residues, F64 and F626 make alternating contacts with individual bases. Initially, F64 in domain 1A is tightly bound with the ssDNA. Upon ATP binding, the ssDNA interacts with 2A domain through F626, while it is released from F64. At the same time the two domains move closer together. ATP hydrolysis causes the ssDNA binding to the pockets in 1A and release from the pockets in 2A. The domains move apart, causing the ssDNA to be pulled along the DNA binding channel relative to domain 2A, translocating along the DNA. In this conformation a new cycle can start [45]. Thus, two independent processes occur, each dependent upon ATP:

translocation along the ssDNA and destabilisation of duplex DNA leading to DNA unwinding [46].

In this model of translocation, it is assumed that the translocation step-size is one nucleotide and the ATP cost per base pair unwound is also one. It further presumes that dsDNA binding is an independent process from ssDNA translocation. These assumptions are supported by previous work measuring ATP hydrolysis during PcrA ssDNA translocation [47].

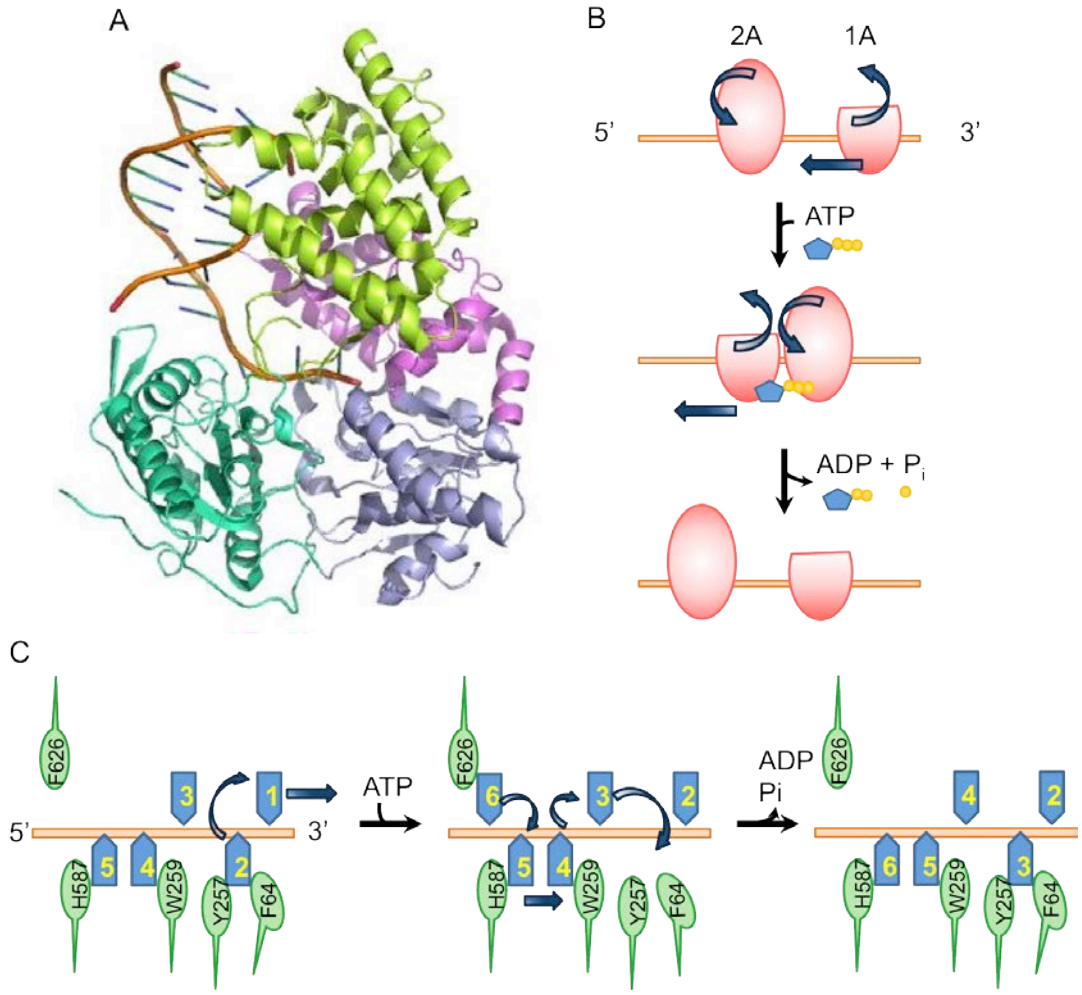

Figure 1.6. PcrA structure and function. (A) High resolution crystal structure of PcrA in complex with DNA and the ATP analogue (AMPPNP). PcrA 1A, 2A, 1B, 2B domains shown respectively in violet, green, pink and lime (B) Model of PcrA translocation on ssDNA. The diagram shows the action of these domains (by the curve arrows) in response to ATP binding and hydrolysis. The linear arrow shows the direction of movement along the DNA. (C) Amino acid residues involved in translocation. The aromatic residues involved in binding ssDNA are shown in green and the ssDNA bases in blue. The mechanism is described in the text.

1.1.4.3. *In vitro* studies of PcrA activity

The *B. stearothermophilus* PcrA activity has been well characterised *in vitro*. The main features of this motor enzyme are translocation on ssDNA and dsDNA unwinding through the energy generated from ATP hydrolysis [47]. The helicase is able to translocate along short stretches of ssDNA at a rate of ~80 bases s^{-1} at 20°C [48]. PcrA binding affinities for different length oligonucleotides were determined in previous *in vitro* studies as K_d ~160 nM for dT_{16}, and its ATPase activity during translocation was one ATP per base [47].

The kinetics mechanism of the ATPase cycle of PcrA has been analysed previously [49]. The study showed that the chemical cleavage is the rate-limiting step in the cycle and is greatly accelerated by bound DNA. The cleavage step, rather than Pi release, was proposed to be associated with a major transition in the helicase structure and possibly movement along DNA.

PcrA is required for rolling circle replication of the *S. aureus* plasmid *in vivo* [50]. Previous studies performed *in vitro* have shown that PcrA requires Rep initiator protein for its recruitment on the origin [51, 52]. Although PcrA can efficiently translocate on ssDNA, it is not able to unwind short lenghts of DNA duplex on its own [52]. The helicase is unable to unwind DNA substrates as short as 30 bp on its own, but in the presence of RepD a single PcrA molecule can unwind a plasmid of over 6 kb at a rate of 30 bp s^{-1} (at 30° C) with a coupling ratio of one ATP per base pair *in vitro* [52]. It was suggested that PcrA and RepD interact to form a functional and processive translocation complex. However, the location of this interaction is not known yet.

More recent single-molecule studies have shown that PcrA and RepD unwind plasmid lengths of DNA in a single run, and that PcrA is active as a monomer [53].

Generally, a passive helicase relies on the transient fraying of the base pairs at the ssDNA–dsDNA fork for unwinding, whereas an active helicase directly interacts with the fork destabilizing it. A direct comparison between helicase

activities when either moving along dsDNA or ssDNA can be made to determine whether unwinding occurs through an active or a passive mechanism. Hence, helicases that have similar rates of movement on dsDNA and ssDNA are considered active. Dda is an example of active helicase [54].

From recent studies it was shown that PcrA unwinding rate was several-fold slower than the translocation rate on single-stranded DNA, and so a partially passive mechanism of DNA unwinding was proposed for PcrA [53].

The function of PcrA in DNA metabolism has been extended with previous studies showing that the helicase can displace proteins effectively from DNA [55]. This is the case of RecA protein that is typically found to trap ssDNA during recombination in order to facilitate repairs. RecA binds to ssDNA in the presence of ATP to form helical nucleoprotein filaments serving as scaffolds upon which homologous recombination occurs. A proposed mechanism for this activity is that PcrA can dismantle RecA filaments by reeling-in DNA [55]. Using single-molecule fluorescence approaches, another study showed that such a displacement by PcrA requires the RecA ATPase activity [56]. This would indicate a possible role of PcrA in DNA repair and recombination. In support of this hypothesis is the finding that deletion of PcrA is lethal to an organism, and that the PcrA homologue, *E. coli* UvrD helicase, was shown to perform RecA filament removal [57].

1.1.5. DNA polymerases

DNA polymerases are involved in many DNA metabolic pathways such as DNA repair and replication. During DNA synthesis, such enzymes "read" an intact DNA strand and use it as a template to synthesize the new strand. The final product is a newly polymerized molecule complementary to the template strand and identical to the template's original partner strand. Despite the continuous substrate changes during subsequent incorporation events, DNA polymerases retain a remarkable degree of specificity and selectivity. They recognize and select the correct base pairing partners from four distinct bases [5, 58].

Most replicative DNA polymerases also have an exonuclease activity in the opposite direction of DNA synthesis. This exonuclease activity provides the proofreading function and enables the enzyme to “erase” misinsertions and prevent mutation events. Structural resolution of DNA polymerases complexed with a DNA substrate has given insights about the principles that govern the transference of the 3′ terminus between both active sites [59-61]. Briefly, the exonuclease domain does not participate in the polymerization reaction itself. When an incorrect base is incorporated in the template strand, a greater structural fluctuation, permitted by the weaker hydrogen bonding of the non-complementary base, frequently brings the newly synthesized strand to the exonuclease site, followed by excision of the incorrect base. This process further enhances the fidelity of replication of the replicative enzymes [59].

Based on sequence homology as well as crystal structure studies, DNA polymerases can be divided into seven different families: A, B, C, D, X, Y, and RT [4]. Family A contains both replicative enzymes such as T7 DNA polymerase as well as repair members like *E. coli* DNA pol I and *B. stearothermophilus* pol I. Family B includes replicative polymerases encoded by some bacteria, bacteriophages and eukaryotic organisms. An example of polymerase belonging to this family is the *E. coli* pol II.

The primary bacterial replicative polymerases are included in family C. This comprises the α subunit of the DNA pol III in Gram-negative bacteria and the PolC in Gram-positive bacteria. C family polymerases are large multidomain proteins and have only recently been studied [62].

Polymerases belonging to the D family are still not well characterized and are thought to be replicative polymerases. Family X contains eukaryotic polymerases such as pol β, pol σ, and pol λ. These are mostly involved in DNA replication and repair. Members of the Y family are translesion synthesis (TLS) polymerases, which perform DNA synthesis across template lesions. Pol IV and Pol V also belong to this family. The reverse transcriptase (RT) family contains polymerases that use an RNA template for DNA synthesis. Members of this

family are the eukaryotic telomerases and polymerases encoded by retroviruses.

The existence of different replicative DNA polymerases performing the same function suggests that DNA replication process experienced a complex evolution.

1.1.5.1. C family of replicative polymerases

The DNA polymerases involved in duplication of bacterial chromosomes are the DNA polymerase III in Gram-negative bacteria and the PolC in Gram-positive pathogens [63, 64]. Such polymerases are also termed replicative enzymes as they catalyse the incorporation of mononucleotides into a growing primer using a DNA template to direct each incorporation event. They perform the repetitive cycle of nucleotide binding, base-pairing, phosphodiester bond formation, product release and movement to the next templating position.

The chemistry required to elongate the DNA is a simple phosphoryl transfer reaction in which the α-phosphate of the incoming dNTP undergoes nucleophilic attack by the 3'-OH of the primer strand of the nucleic acid. The reaction is catalyzed with the participation of carboxylate residues that coordinate two metal ions (Mg^{2+}) within the active site of the DNA polymerase. Typically, an aspartate residue serves as base to abstract the proton from the 3'-OH on the deoxyribose of the dNTP to form a more reactive nucleophile. The latter can now attack the α-phosphate, creating a transition state that is stabilized through metal ion coordination with the β-γ phosphate groups. This step results in the inversion of the α-phosphate stereochemistry and the release of the pyrophosphate group coordinated to another divalent metal ion (Figure 1.7).

In vitro studies of several replicative polymerases revealed that the speed of synthesis (up to 1000 bp s^{-1}), the fidelity (1 error every 10^6 incorporation events) and processivity (>50 kb) are remarkable features of these enzymes [58, 65]. However, the high speed of synthesis and the processivity of the replicative

subunit can be reduced in the absence of the accessory subunits, such as the β subunit (Table 1.2).

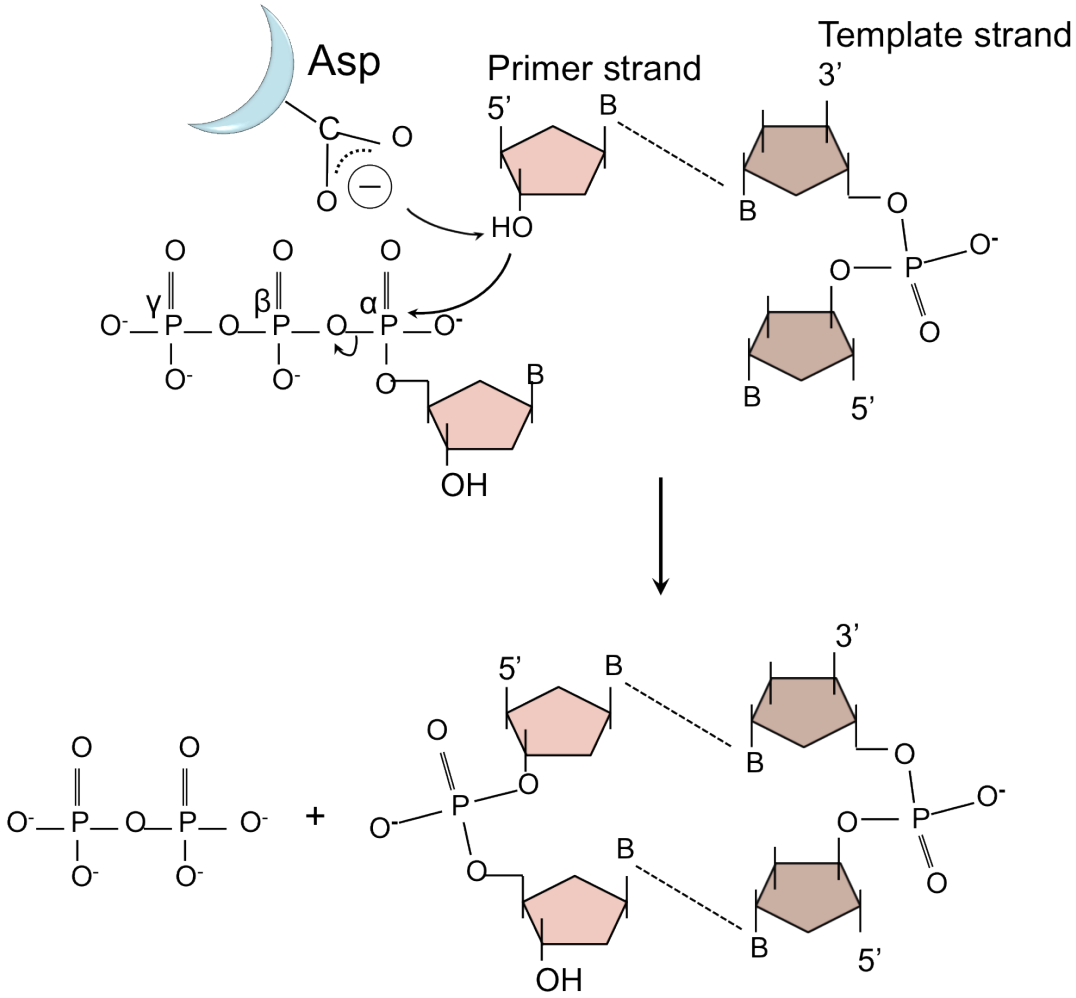

Figure 1.7. Simplified scheme of the phosphoryl transfer reaction catalysed by a DNA polymerase. The arrows illustrate the movement of electrons. See text for details.

The most studied polymerase belonging to the C family is the DNA polymerase III holoenzyme from *E. coli*. It is a multicomponent protein consisting of three assemblies: the pol III core, the clamp loader complex and the β sliding clamp [63]. The β clamp encircles the DNA duplex and binds the polymerase, tethering it to DNA for rapid and processive chain extension. The clamp loader uses energy derived from ATP hydrolysis to load the β clamp on the primer. The holoenzyme is made of 10 different subunits, which finely cooperate in order to load the enzyme on the DNA template, drive the

replication and make contacts with the whole replisome. Details of the holoenzyme subunits and their functions are listed in Table 1.2.

Gene	Subunit	Mass (kDa)	Protein function
dnaE	α	130	Replicative polymerase
dnaQ	ε	27.5	3'>5' exonuclease activity
holE	θ	8.6	Stimulates exonuclease
dnaX	τ	71	Forms trimers
dnaX	γ	47.5	ATP dependent clamp loader
holA	δ	38.7	Interacts with β
holB	δ'	3 6.9	Stimulates γ
holC	χ	16.6	Binds SSB
holD	ψ	15.2	High affinity for γ
dnaN	β	40.6	Sliding clamp protein

Table 1.2. Components of the *E.coli* DNA polymerase III holoenzyme. The subunits forming the PolC core, clamp loader complex and the sliding clamp assemblies are highlighted in red, blue and green, respectively. The gamma subunit (highlighted in white) would not be required to form the initiation complex at the replication fork but it may play a role in forming clamp loader complexes that unload sliding clamps from the DNA after replication fork passage. However, such a mechanism is still unclear.

PolIIIC is the polymerase responsible for the genomic replication in many Gram-positive bacteria and is the analog of the *E. coli* DNA pol III core. This thesis deals specifically with the replicative subsunit, PolC, of the PolIII-C type enzyme from the Gram-positive organism *Staphylococcus aureus*. The enzyme holds both synthesis and proofreading activities. It consists in a 162 kDa protein with unknown crystal structure, sharing around 54% of amino acid identity with the *Geobacillus kaustophilus* PolC protein [64].

A high-resolution crystal structure of the PolC from the *G. kaustophilus,* has been solved in a ternary complex with DNA and dGTP [62]. This is shown in

Figure 1.8 and it is the first structure of a replicative polymerase from a Gram-positive bacterium.

The overall shape of the enzyme can be compared with a right hand containing “thumb,” “palm,” and “fingers” domains. Such features are conserved in the replicative polymerases. The function of the palm domain appears to be catalysis of the phosphoryl transfer reaction whereas that of the fingers domain includes important interactions with the incoming nucleoside triphosphate as well as the template base to which it is paired. The thumb domain contacts the DNA minor groove and may play a role in positioning the DNA duplex in the correct position for the incoming nucleotide and in translocation along the template.

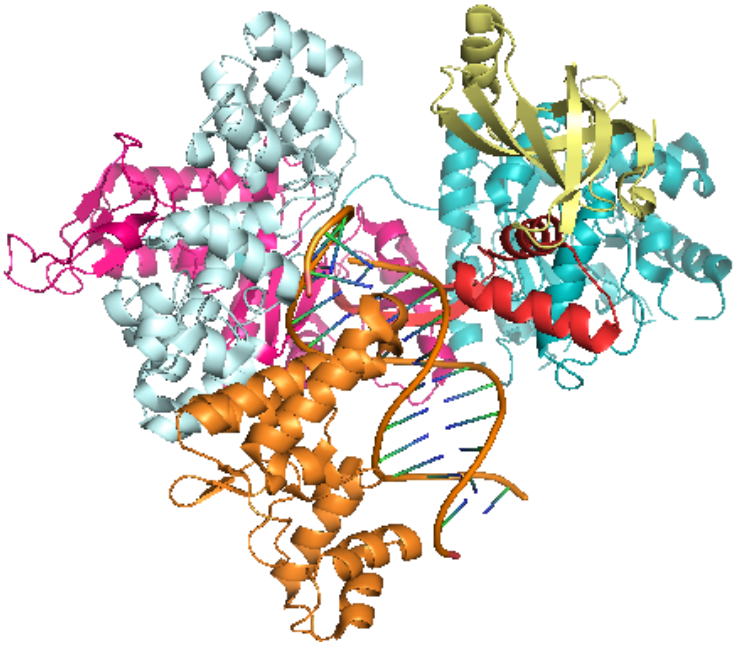

Figure 1.8. Crystal structure of the replicative DNA polymerase. PolC from *G. kaustophilus* in complex with DNA and dGTP. Ribbon representation of the hand-shaped PolC, showing the palm (pink), the fingers (in aquamarine) and the thumb (in red) domains. The exonuclease domain (ExoΔ) was deleted from the protein. See text for details.

1.1.6. Dynamic coupling between the motors of DNA replication

During replication, the replicative helicase works closely with the other enzymes within the replisome. Generally, physical and functional couplings of the helicase with the primase as well as with the DNA polymerase can occur during their coordinated activity [35]. Such interactions might have different effects on the helicase enzymatic activities.

In vitro studies have revealed that DNA polymerases can modulate helicases with a direct effect on the helicase unwinding speed and processivity [66-69]. The interdependence of the helicase and the polymerase was observed from studies of T7, T4, *E. coli,* and human mithocondrial replication proteins [67, 70, 71].

The coupling between the helicase and DNA polymerase can either increase or decrease the speed of unwinding. It is commonly believed that the helicase is the leading motor and that the DNA polymerase either increases the helicase's forward movement on DNA (push) or decreases its backward slips (brake). However, it is also possible that the polymerase or even both motors together lead the replication. The effects on the enzymatic rates that result from such interactions in different replication complexes are listed in Table 1.3.

While we understand the function of the individual enzymes at the cellular and molecular levels, studies on the detailed mechanisms of interactions with other partners within the replisome to coordinate DNA replication still need to be extended in the future.

Activity	E. coli	T4	T7
Helicase translocation (nt s^{-1})	-	500 (37 °C)	130 (18 °C)
Helicase unwinding (bp s^{-1})	35 (30 °C)	30 (37 °C)	50-10 (18 °C)
Polymerase synthesis (nt s^{-1})	500 (30 °C)	160 (30 °C)	228 (18 °C)
Coupled strand synthesis (bp s^{-1})	730 (30 °C)	250 (37 °C)	90 (18 °C)

Table 1.3. DNA unwinding and synthesis kinetics of the replicative proteins. The rates (bulk assays) of the motor proteins functioning as individual protein or in a complex [35].

1.2. Experimental Approach

1.2.1. Fluorescence and fluorophores

Fluorescence has been widely used in analytical chemistry and biochemistry to study a variety of processes in biological systems. With the recent development of fluorescent dyes and fluorescent imaging systems, fluorescence methodologies have extensively been used in place of radioactivity. The speed, the comparable sensitivity, the time resolution and the possibility to monitor reactions in real time are winning benefits of these approaches over methods that use hazardous radioisotopes.

Fluorescence is a simple physical process and occurs when a molecule relaxes to its ground state (S_0) by emitting a photon of light after being excited to a higher quantum state (S_1). This is schematically shown in a simple way with the Jablonsky diagram in Figure 1.9A. The electronic transition due to light absorption is almost instantaneous (10^{-15} s), whereas the excited state lasts for 10^{-9} sec and is known as the fluorescence lifetime [72]. After excitation from S_0 to S_1, the molecule rapidly relaxes by means of internal conversion to the lowest energy level of the excited state S_1.

According to the quantum theory, the amount of energy transported by the light through a quantum is expressed by the Planck's law, which is given by:

$$E = hv \quad (1)$$

Where h is the Planck's constant and *v* is the frequency. As frequency is related to the wavelength (λ) and the velocity (c), the equation (1) can also be written as:

$$E = h\, c/\lambda \quad (2)$$

Since *h* and *c* are constants, the E value varies inversely to λ. As mentioned above, some of the light energy initially absorbed is usually lost in transitions between vibrational energy levels therefore, from equation 2, the wavelength of the emitted fluorescence is longer than that of the absorbed light. This means that molecules that exhibit fluorescence, termed fluorophores, own a characteristic fluorescence or emission spectrum as well as a characteristic absorbance spectrum [72]. An example of excitation and emission spectral profiles is given in Figure 1.9B, the difference in wavelength between the peaks of these bands is referred to as the Stokes shift [73].

Fluorophore compounds are usually aromatic or contain conjugated double bonds (i.e., alternating single and double bonds between atoms).
The most important intrinsic fluorophores in proteins are tryptophan, tyrosine and phenylalanine residues, with tryptophan giving the strongest spectra. Many proteins may have only one or two of such residues being an advantage in order to carry out biochemical studies. The bases of DNA nucleotides and of some enzyme cofactors are also intrinsic fluorophores although they display very weak fluorescence spectra. In such cases, a protein or a macromolecule can be labelled with organic dyes and quantum dots in order to perform structural and functional studies.

The fluorescence intensity of a compound can be affected by several factors, such as concentration, temperature, pH and solvent. Due to these factors, fluorescence is only ever quoted in arbitrary values [74]. Lastly, there are photochemical reactions that cause the fluorescence of a dye to decrease with time, an effect called photobleaching. This is an irreversible reaction between an excited molecule and oxygen, and it is often a problem when using a high intensity light source.

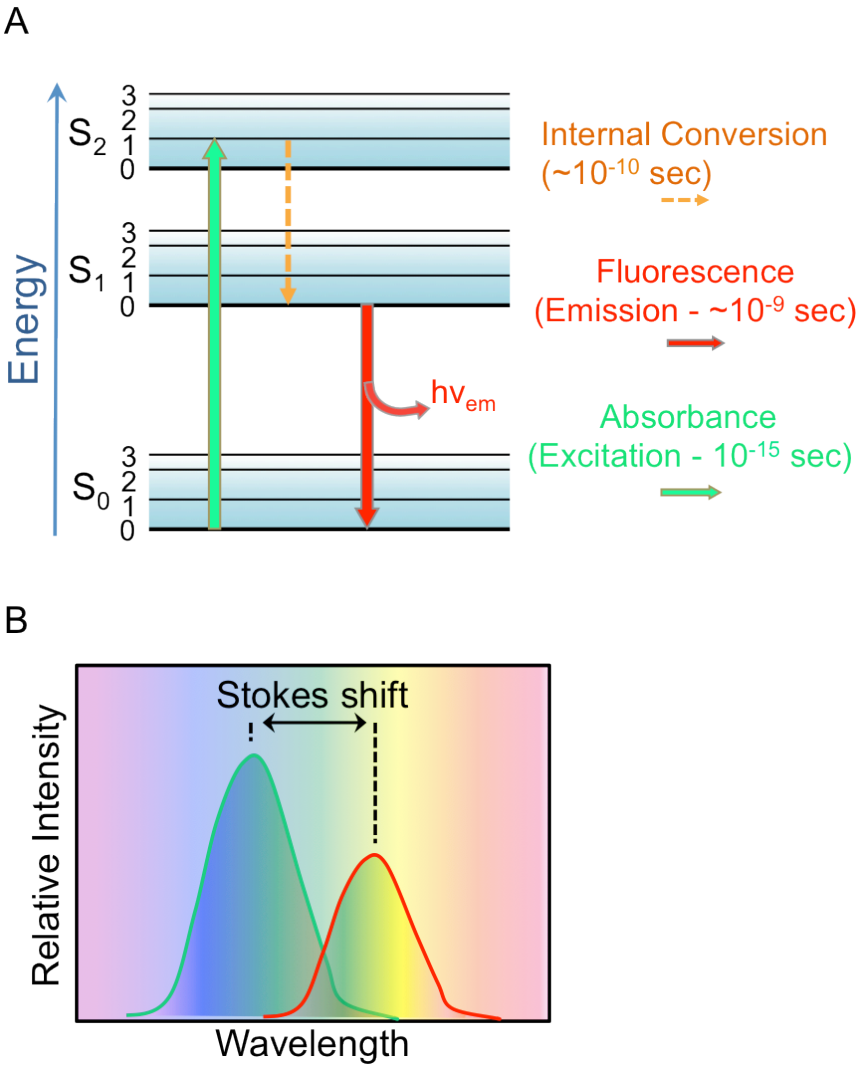

Figure 1.9. Physical basis of fluorescence. (A) Jablonsky diagram. the energy levels are represented by horizontal lines and the directions of energy transitions by arrows. Different vibrational levels (for example 0-3) exist in each energy level. See text for details. (B) Examples of excitation (green profile) and emission (red profile) spectra for a fluorescent probe. Because of their electronic configurations, fluorophores have unique and characteristic spectra. See text for details.

1.2.1.1. Fluorescence anisotropy

Fluorescence emission is characterized by several parameters such as intensity, lifetime and polarization that are correlated to a multitude of factors including conformation, orientation, as well as environmental conditions like temperature and pH. The fluorescence anisotropy can give information about the molecular orientation, aggregation and rotational diffusion. A fluorescently labelled molecule will have a high fluorescence anisotropy (and polarisation) when bound to a macromolecule complex than when alone. For this reason polarization assays are widely used to study binding of proteins and macromolecules.

The physical process behind this phenomenon is based on the use of the polarized light in a process termed photoselection (Figure 1.10) [72]. When light is transmitted through a polarizer it emerges with half of the intensity and with vibrations in a single plane having been plane polarized. If plane polarized light encounters a solution of absorbers, only those molecules whose excitation dipole is oriented in a direction parallel with the incident light path will be preferentially excited (Figure 1.10A). The excited molecules, which will be a small subset of the total population, may be able to rotate their axes before the fluorescence is emitted and the polarization of the emitted light can be determined based on their new positions (Figure 1.10B).

Quantitatively, anisotropy (r) is defined as:

$$r = \frac{I_{\parallel} - I_{\perp}}{I_{\parallel} + 2I_{\perp}} \qquad (3)$$

Where $I_{//}$ represents the intensity of the emitted light in the parallel plane, and $I_{\perp}$ represents light emitted in the perpendicular plane. In practical terms, for a fully depolarized solution r = 0, as light is emitted equally in both planes [72].

As mentioned above, fluorescence anisotropy is a useful tool to monitor macromolecule interactions. The main advantage of this approach is that it represents a real-time solution-based equilibrium technique. Since fluorescence anisotropy works particularly well for binding interactions that lead to a significant change in size of the fluorophore reporter, binding assay experiments use labelled substrate, usually DNA or a small molecule [75, 76]. Generally, such measurements are performed varying the ligand concentration in the molecular system. Additional information can also be gained if the system involves a substrate cleavage event with subsequent reduction of the molecular weight, as it occurs upon DNA nicking and release. The use of anisotropy to study the binding and nicking functions of RepD has been previously described [52]. In other studies, the technique was employed to monitor the unwinding activity of a helicase [77]. Here, fluorescence anisotropy is mainly used to investigate the activities of wild-type and an active mutant RepD during initiation.

Fluorescence anisotropy can be influenced by the inherent properties of the sample. Fluorophores are frequently attached to molecules by a linker. The flexibility of the linkers can affect the mobility of the fluorophore and affect directly the observed fluorescence anisotropy, even when attached to large macromolecules.

Fluorescence anisotropy is a versatile tool that can be used in a variety of sophisticated methods [75]. In alternative approaches, for example the interactions between biomolecules are monitored using anisotropy combined with microscopy in cells, such as in the study of the density distributions of membrane proteins or ligand-receptor binding [78].

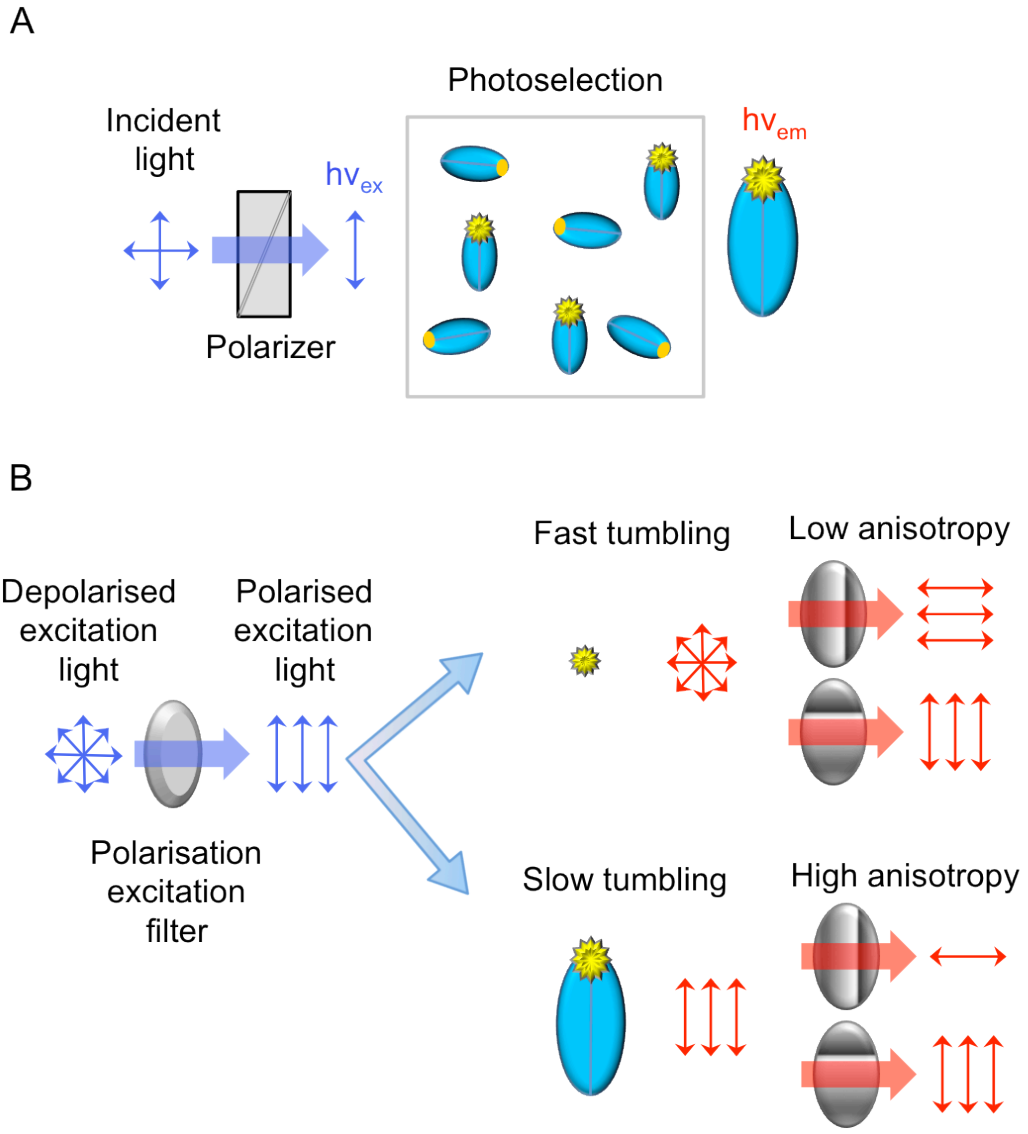

Figure 1.10. Fluorescence anisotropy in binding studies. (A) Photoselection. The incident light is separated in vertical and horizontal polarised light using a polarizer. Vertically polarised light then selectively excites the fluorophores with excitation transition dipoles which are oriented parallel to the excitation plane (as shown by the line in the diagram). (B) A sample containing fluorescently labeled species is excited with vertically polarized light. Fluorophores in the excited state tumble in solution within the fluorescence lifetime. The rate of tumbling is related to the size of the macromolecular complex. Emission is measured downstream through polarizers that are parallel and perpendicular to the plane of the excitation.

1.2.1.2. Förster Resonance Energy Transfer and fluorescence quenching

Förster (or Fluorescence) Resonance Energy Transfer occurs when the emission spectrum of one fluorophore (donor) overlaps with the absorbance spectrum of another fluorophore (acceptor) [74]. The excited donor molecule transfers its energy to the acceptor molecule through dipole-dipole interactions (Figure 1.11A). The efficiency of the energy transfer (E) depends on the distance between the donor and acceptor and is described by:

(4) $$E = \left[1 + \left(\frac{R}{R_0}\right)^6\right]^{-1}$$

Where R is the acceptor-donor distance and R_0, the so-called Förster distance, is the distance at which transfer efficiency is 50%. This represents a useful method to measure distances between biomolecules as well as conformational changes within a molecule. Thus, the extent of energy transfer depends on the distances between the two fluorophores on two different molecules or within the same molecule. The dipole-dipole interaction during energy transfer has an angular dependence, which is termed the orientation factor, K^2. The latter is often assumed to be two thirds, when both dyes are freely rotating [79]. However, in some cases this is not a valid assumption, and so a precise measure of the molecules distance is impaired by the uncertainty of the orientation factor.

In this thesis, FRET was used to detect binding of labelled deoxynucleotide to the polymerase, having the intrinsic protein tryptophan fluorescence as donor and a mant-labelled deoxynucleotide, mant-dATP, as acceptor.

Quenching of fluorescence consists of a decrease in the fluorescence intensity resulting from radiationless de-excitation of the fluorophore [72].

Environmental conditions extrinsic to the fluorophore can affect fluorescence and cause quenching. The latter can be achieved by static or dynamic collision (Figure 1.11B). The dynamic quenching occurs when a quencher molecule (Q) collides with the fluorophore (or reporter, R) while in its excited state, causing a rapid de-excitation without release of a photon. The dependence of fluorescence on Q is given by the Stern-Volmer equation:

$$\frac{F_0}{F} = 1 + k_q \tau_0 [Q] = 1 + K_D [Q] \quad (5)$$

Where F_0 and F are the fluorescence intensity respectively in the absence and in the presence of a quencher, k_q is the bimolecular quenching constant, τ_0 the lifetime of the excited state and [Q] the concentration of the quencher molecule.

Static quenching takes place when the reporter and quencher form a stable complex in the ground state before excitation can occur. The complex Q-R has its own properties, such as being non-fluorescent.

An alternative form of quenching, based on the distances between Q and R, is achieved via energy transfer. In this mechanism, excitation energy is transferred from R to Q via coupling between the emission dipole of R and the absorption dipole of Q.

The ability of fluorescent compounds to transfer absorbed energy to molecules in close proximity has been used to develop homogenous nucleic acid assays. A useful approach to monitor DNA helicase activity and DNA strand separation is the hybridization of two complementary oligonucleotide probes containing a pair of interactive labels located at their ends. In this thesis and in previous studies [80], the Cy3 group was used as fluorophore and the Dabcyl as quencher on short DNA junctions (20-40 bp). Thus, the designed DNA shows either successful fluorescence quenching, permitting energy transfer to occur while Q and R are close to each other in the duplex state or fluorescence increase during strand separation. Quenching using non-fluorescent dyes enables changes in the fluorescence intensity to be measured

more directly, rather than as an alteration in the shape of the emission spectrum.

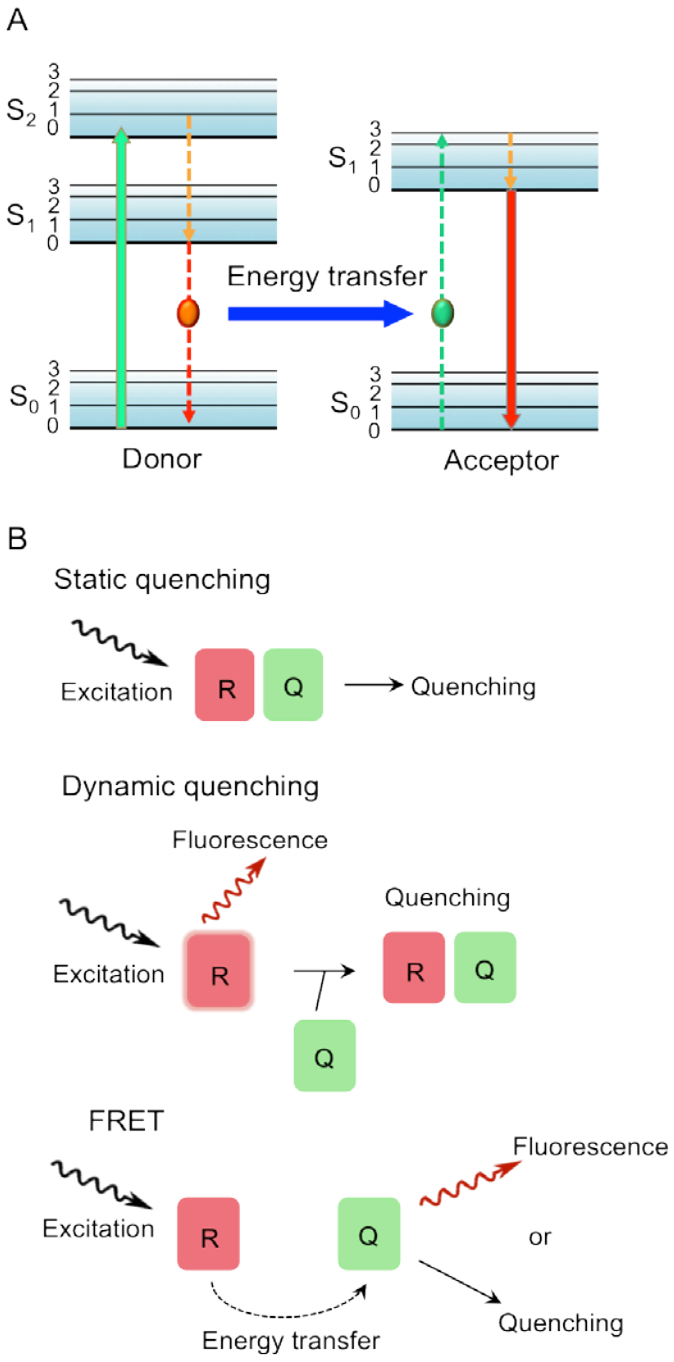

Figure 1.11. Schematic diagram of FRET and quenching. (A) Electronic transitions during dipole-dipole interaction and energy transfer between the donor in the excited state and an acceptor. (B) Quenching mechanisms between a quencher (Q) and a reporter (R). See text for details.

1.2.1.3. Fluorescent biosensors

Monitoring biological events and a range of important target substances both *in vivo* and *in vitro* has been a great challenge in chemical biology and biotechnology. Quantitative information on the cellular and subcellular dynamics of ions, signaling molecules, and metabolites is critical for functional understanding of organisms. Mass spectrometry is for example used for this approach; however, its temporal and spatial resolutions are limited.

A powerful tool has emerged to address these challenges with the design of fluorescent biosensors. These devices have high specificity for a particular process and can be developed from a wide range of compounds such as antibodies, nucleic acids, enzymes and other proteins [81, 82].

Proteins are good candidates for the design of a fluorescence-based biosensor as they can report the dynamic distribution of specific reactions, protein interactions but also the kinetics of a reaction. The protein biosensors consist of a polypeptide component that recognizes selectively a target, and a fluorescent component that gives fluorescence signals upon environmental changes. The latter can be a label attached to the protein to give extrinsic fluorescence or another protein that is intrinsically fluorescent [81].

There are several important requirements that need to be considered to design a successful protein-based biosensor. One of these is the specificity for the substrate and the ability to discriminate against similar molecules. The binding should be tight and rapid in order to allow rapid real time measurements. Reporting properties are also important. A number of strategies have been described for site-specific protein labelling. In one approach, cysteine residues can be introduced at specific positions known to be allosterically linked to the active site. In this case, the fluorophore label is typically attached in close proximity of the protein active site in order to report protein-activity-dependent spatial rearrengements. This represents a relatively simple way to generate a signal. However, difficulties can arise in choosing the ideal aminoacid positions that report a significant signal change.

This strategy was used to generate a sensitive probe for DNA by modification of *E. coli* SSB with an extrinsic fluorophore [83]. Another strategy would be to insert two fluorophores on the same protein. In this case, the two labels are arranged such that they exhibit molecular stacking that is perturbed on changing conformations upon target binding. In this way, the fluorescence changes in relation to the relative positions of the two labels. This strategy can be used to insert labels in protein subdomains that undergo large conformational change or also in case of multimeric proteins. It was used to generate a ADP biosensor, the rhodamine-ParM [84]. In the absence of ADP the fluorescence is quenched by the two rhodamines in close proximity. Nucleotide binding causes a loss of the rhodamines interaction and an increase in fluorescence.

Fluorescent-protein biosensors have been used in several assays in this investigation. A labeled phosphate binding protein, MDCC-PBP, was used as sensor for P_i production and the DCC-SSB to detect single stranded DNA [83, 85]. MDCC-PBP, used for real-time measurements of rapid inorganic phosphate production, was developed from the *E. coli* periplasmatic phosphate binding protein. This probe is labelled with a coumarin derivative, MDCC and gives a 6-fold change in fluorescence intensity upon P_i binding. P_i binds tightly (K_d approximately 70 nM, 5 °C) and causes a rapid conformational change (317 s^{-1}, 5 °C) [85]. MDCC-PBP has been used in real time ATP hydrolysis assays using DNA helicases as well as other ATP hydrolyzing motor proteins, such as myosin [49, 86].

DCC-SSB, used to detect single stranded DNA, is based on the tetrameric single-stranded-DNA binding protein from *E. coli* [83]. The exposure of ssDNA is a common event during replication, recombination and DNA repair and the SSB binding is essential to either protect the DNA from restriction enzyme activity and undesirable DNA reannealing. Binding is highly selective for ssDNA over dsDNA. It has also been shown that SSB can directly interact with numerous DNA replication proteins being crucial for successful DNA replication. The SSB sensor, labelled with a coumarin derivative on each monomer, DCC, provides a signal increase of ~ 6 fold when bound to the substrate. SSB binds

tightly and rapidly to ssDNA (K_d ~ 2.2 nM, 10^9 M^{-1} s^{-1} for dT70). However, the mechanism of binding is complex, as the binding is cooperative and the DNA interaction site size varies from 35 bases at low salt concentrations to 65 bases at high salt [87].

Typically, the use of DCC-SSB works well to monitor unwinding of large DNA molecules, rather than oligonucleotides, and so it has been used to measure ssDNA release from highly processive helicases such as AddAB and PcrA [48, 52, 83].

1.2.2. Rapid reaction techniques

Many biological reactions occur on a time scale of milliseconds and need to be measured. Unfortunately, for operational and technical reasons, most conventional spectrophotometers cannot be used to study reactions that are complete within less than few seconds. To study such processes, it is essential the use of rapid reaction techniques.

The methods used in this thesis to study rapid reactions include stopped-flow and quenched-flow techniques [88]. All flow techniques use a special mixing chamber designed to receive solutions being driven at high speed. Following rapid mixing, the solution can be monitored only after a certain time from mixing. The time taken to start monitoring the “aged” solution is called the “dead time” of the instrument.

1.2.2.1. Stopped-flow

Stopped-flow is a rapid mixing technique used to follow the kinetics of a reaction in solution, developed from the continuous flow method of Gibson (Figure 1.12) [89]. Reactants are rapidly and simultaneously injected in the mixing chamber where they start to react and then they quickly move to the spectrophotometer cell. The flow is stopped through a stopping syringe where the old mixture is displaced by the new solution. The instrument allows also the performance of double-mixing experiments in which two mixing reactions can be successively achieved. Firstly, two solutions are rapidly mixed and after a

defined time a third solution is mixed to the previous one. This approach is useful to study the formation of intermediates during enzyme reactions. The dead time of the stopped-flow is typically around 2-3 ms [88].

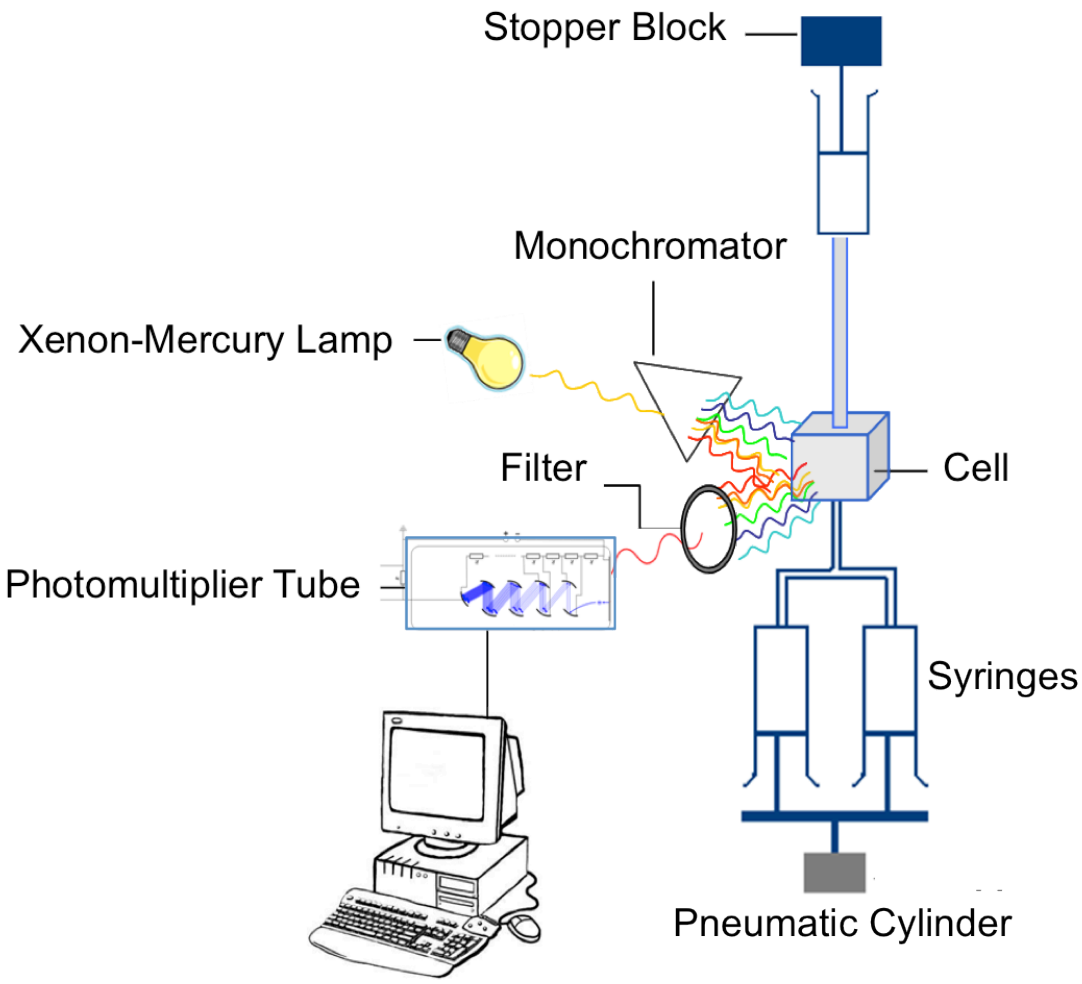

Figure 1.12. Schematic representation of a stopped-flow apparatus. Reactants A and B, incubated in the syringes, are rapidly mixed by a pneumatic cylinder and the flow is stopped using the stopper block. The fluorescence of the solution is measured in the cell. Solution is excited by a white light from a Xenon –Mercury lamp through a monochromator. Emission is measured at 90˚ through an emission cut off filter (Fλ), at the appropriate wavelength, and the intensity measured using a photomultiplier tube. A software converts this signal to fluorescence units.

1.2.2.2. Quenched-flow

The second method used to measure rapid-reactions in this investigation is quenched-flow. Quenched-flow allows the rate of a chemical process to be measured and correlated to fluorescent signals.

Similarly to the stopped-flow, the instrument consists of syringes containing the reactants of interest. The reaction under investigation is initiated by rapid mixing of two reactant solutions. The flow continues at a constant velocity through a delay line to a second mixer. At this point the reaction is quenched with chemicals. Prior to quenching, the reaction time can be controlled through the length of the delay loop and the speed of the stepper motor that mixes the solutions. The quenched reaction is then collected and analysed [88].

Generally, the analysis of the final solution defines concentrations of substrate and product. This is determined using a variety of techniques, such as chromatography or gel assays, which depend on the nature of the reactants under investigation. In this thesis, quenched-flow was used to determine the nicking rate of RepD on DNA plasmid. Using quenched solutions from a range of time points, an overall time course of the reaction can be obtained. The final products were then physically separated on an agarose gel for analysis.

1.2.3. Atomic force microscopy

Atomic force microscopy, AFM, is a scanning tool that provides topographical images of a sample surface and allows the investigation of morphological features of a surface area [90].

Advanced single molecule microscopy techniques are advantageous to study self-assembled DNA structures due to their small size and complexity. Since the invention of AFM, when it was described for the first time by Binnig et al. in 1986, it was clear that the strength of this method would rely in its resolution [91]. Since then AFM has enabled the imaging and analysis of a multitude of different biological samples ranging from single molecules such as proteins and nucleic acids to macromolecular assembly and cells (Figure 1.13) [90, 92, 93]. Its remarkable feature consists in “seeing” details at the molecular level, thus

increasing our understanding of how systems work and leading to new discoveries in many fields. Today, this versatile technique has been successfully applied in a variety of science branches including microbiology, DNA and RNA nanotechnology and even food science [94, 95].

There are several benefits that AFM brings to biology with its ability to investigate structures and dynamics on a nanometer scale. Besides morphology, the physical and mechanical properties and the molecular interactions between macromolecules can also be addressed through force spectroscopy experiments [96].

The applications of AFM instrument have extremely increased in recent years and a wide range of biological samples has been explored recently using AFM. The first biological samples imaged with AFM were bulk crystals of amino acids and polymers, followed by individual actin filaments in solution and soon after DNA samples at high resolution. Subsequently many studies have recently been conducted describing the organization of multi-protein assembly, living cells and nucleoprotein complexes. Currently AFM is routinely used to identify higher-order structures of DNA including supercoiling, formation of loops, as well as nucleosomes and chromatin [92].

Here, atomic force microscopy has been used to image distinctive steps of plasmid unwinding and replication by stopping the reaction at a desired time point and imaging the products. Topology changes in DNA, as well as protein-DNA and protein-protein interactions have been investigated. Furthermore, the combination of the AFM with Total Internal reflection fluorescence microscopy (TIRFM) enabled the simultaneous visualisation of fluorescently labelled proteins in a scanned sample. This technique is described below.

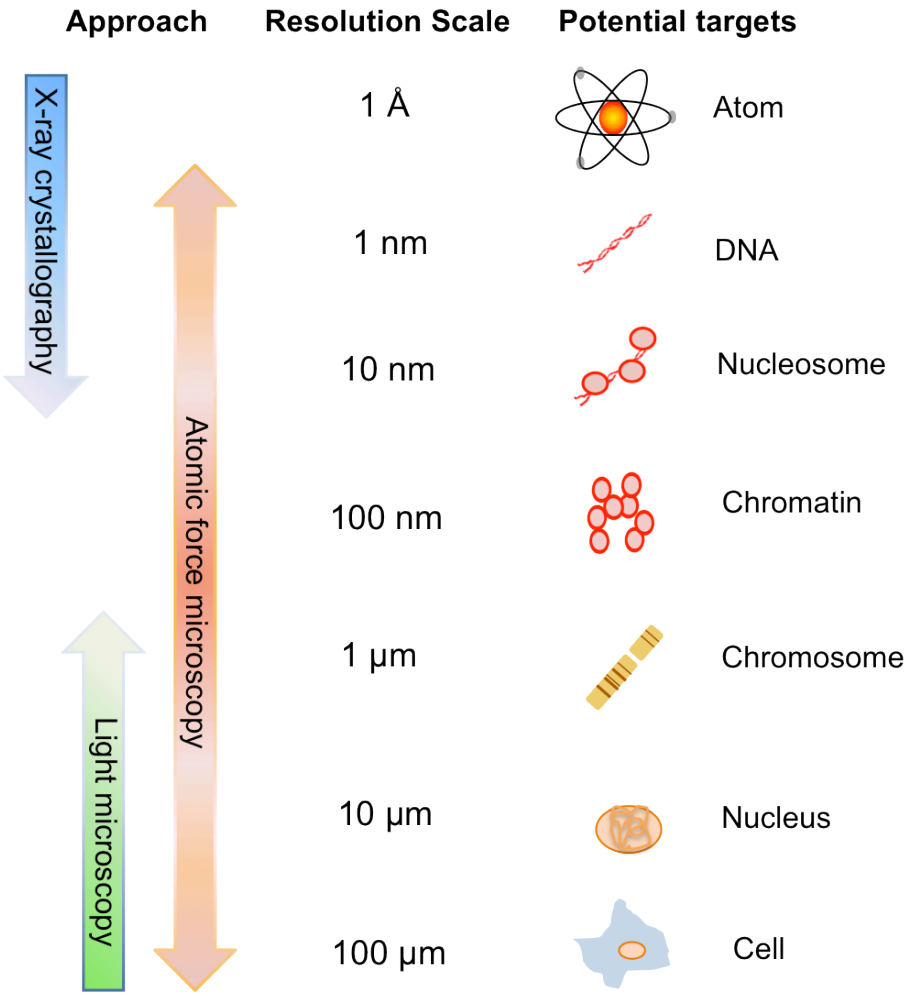

Figure 1.13. AFM applicability on macromolecules and assemblies.

1.2.3.1. Principles of AFM imaging

AFM reveals the surface topography through the interactions between a sharp tip and the sample while scanning across it (Figure 1.14). The microscope is composed of a photodiode, a cantilever, a laser and a piezo transducer [90]. The tip used to scan over the surface is mounted on a flexible cantilever and can "feel" the sample through its bending. This occurs according to the Hooke's Law:

$$F = \pm ks \qquad (6)$$

Where *F* is the force acting on the cantilever, *k* is the spring constant and *s* is the displacement. As the force F can be either attractive or repulsive, its value can be positive or negative, respectively.

This force is translated in deflection of the cantilever detected by a laser beam (Figure 1.14A). The latter is reflected from the top of the cantilever onto a photodiode. The angular displacement of the laser is then converted into an electric signal by the photodiode. The piezo transducer allows the movement of the scanner along the x, y and z directions to scan over a pre-determined surface area.

There are two main imaging modes that can be used with AFM, the contact and dynamic mode (Figure 1.14B). When using contact mode, the tip is constantly in contact with the sample surface and the cantilever is held at constant deflection through a feedback loop between the detector and the piezo. In the dynamic mode, the cantilever constantly oscillates at its resonance frequency during scanning. In both modes, three-dimensional surface topographies are obtained. However, Contact AFM is also used for measurements of sample properties such as adhesion, chemical binding, and electrical properties.

The dynamic mode is usually preferred for imaging very soft and fragile samples, because of the reduced frictional and adhesive forces of the cantilever during scanning [90].

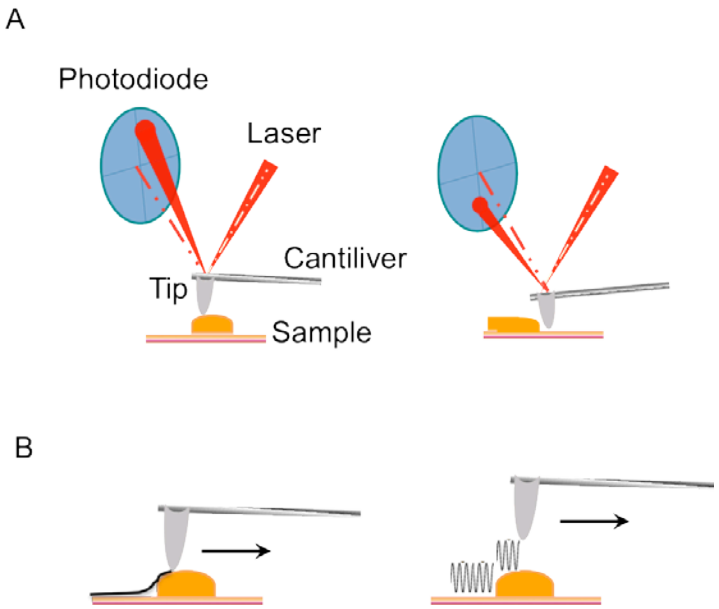

Figure 1.14. AFM principles. (A) Simplified illustration of AFM principle of function. The deflection of the laser beam upon surface scanning is shown. (B) AFM operating modes. On the left is the contact mode, on the right the dynamic mode. See text for more details.

1.2.3.2. Combining AFM with TIRFM

AFM can be combined with other complementary techniques to obtain more comprehensive information from biological samples. One advantageous strategy is to combine AFM with total internal reflection fluorescence microscopy (TIRFM) in order to image a sample and examine different properties of the components simultaneously.

Generally, molecules can be selectively labeled with fluorescent dyes to be seen by TIRFM. The advantages from the combination AFM with a fluorescence technique such as TIRFM are numerous. Whereas AFM provides high spatial resolution, fluorescence offers high temporal resolution, sensitivity to local physical chemistry and the possibility of functional imaging via specific labeling. Thus, this approach allows obtaining such data simultaneously. The combined information can then be used to identify and localize individual labelled species of interest in a complex system and characterize macromolecule interactions.

This combined approach was recently used to image fluorescently labelled actin filaments [97].

In this work, a synchronized TIRF and AFM system was used to detect protein-DNA interactions during replication. Specifically, we investigated binding of the fluorescently labeled Cy3B-SSB on ssDNA upon PcrA-helicase unwinding.

AFM-based measurements will continue to play an important role in the biological field and the possibility to combine AFM with other microscopy techniques is a powerful approach to understand structure-function relationships.

1.3. Aims of this investigation

The overall aim of the project is to study the protein interactions during asymmetric rolling circle replication of a staphylococcal plasmid. To achieve this goal, several questions are addressed concerning the mechanistic functions of the initiator protein RepD, the helicase PcrA and the replicative (α) subunit of the PolIIIC.

In more detail, one aim of the project is to analyse the kinetic mechanism of RepD-DNA interaction during initiation. The latter can be studied with measurements of binding and nicking kinetics of DNA. An active mutant of RepD, N189K RepD, was generated to study its function further and directly compare the nicking activity with the wild-type protein.

The interplay between DNA, RepD and PcrA will be further investigated in detail. It was previously shown that RepD is essential for PcrA processive unwinding [52]. Here, important factors relating to successful initiation and RepD-PcrA mediated unwinding will be examined. The use of N189K RepD-PcrA complex on different DNA substrates revealed the PcrA requirements for functional DNA unwinding.

A second aim of the project focuses on the PolC activity and its effects on PcrA helicase activity during plasmid unwinding. As described in the Introduction, DNA helicase activity can be modulated by other replicative enzymes. The kinetics of PcrA-mediated DNA separation *in vitro* have been determined in previous studies. At 30º C, the rate of unwinding of PcrA is ~ 30 bp s^{-1} and during translocation the coupling ratio is 1 ATP hydrolyzed per base pair separated by PcrA [47, 52]. Here, the PolC protein will be included in such assays to measure its effect on the PcrA unwinding rate. In addition, the polymerase activities including DNA template and nucleotide binding kinetics will be also investigated.

Another aim of the project is to visualise distinctive steps of plasmid replication through Atomic Force Microscopy. The structural information derived by the AFM experiments will provide insights into the dynamics of plasmid replication including DNA local and global rearrangements during unwinding and replication, as well as the macromolecular interactions of the replicative proteins.

A range of experimental techniques was used in this investigation, including quench-flow mixing, stopped-flow fluorescence, steady-state fluorescence measurements, atomic force microscopy and combined AFM-TIRFM.

These data could provide useful information to improve our understanding on the replication mechanisms occurring *in vivo* and how these processes can be potentially regulated and controlled. Elucidating the mechanisms behind successful initiation of a plasmid carrying antibiotic resistance genes is of high interest in the field of antibiotic drug design to identify novel targets and develop new powerful agents.

2. Materials and Methods

2.1. Chemicals and reagents

All chemicals were purchased from Sigma Aldrich Ltd. or Fisher unless specified. ATP (ultrapure) was dissolved in distilled-deionised water (ddH_2O) and then quantified using the extinction coefficient of 15400 M^{-1} cm^{-1} at 260 nm. dNTPs were from Fermentas and 2´(3´)-*O*-*N*-methylanthraniloyl-3´deoxyATP, mant-dATP, from Jena Bioscience. Purity of mant-dATP was checked by HPLC analysis by Gordon Reid, NIMR (purity >97%). Restriction enzymes were purchased from New England Biolabs. Phosphate binding protein (PBP) labeled with *N*-[2-(1- maleimidyl)ethyl]-7-diethylaminocoumarin-3-carboxamide, MDCC, and Single stranded binding protein (SSB) labeled with *N*-[2-(iodoacetamido)ethyl]-7-diethylaminocoumarin-3-carboxamide, IDCC, and Cy3B-SSB were made by colleagues (Colin Davis, and Lesley Southerden, NIMR) using the published protocols [83, 85].

2.2. Assay buffers

Assay buffers are indicated in figure legends for each experiment. Each assay buffer was used to match published assay conditions or particular reagent requirements.

K200 buffer: 50 mM Tris.HCl (pH 7.5), 200 mM KCl, 10 mM $MgCl_2$, 1 mM Ethylenediaminetetraacetic acid (EDTA), and 10% (v/v) Ethanediol. This buffer was used for all the unwinding experiments containing RepD, PcrA and DNA junctions.

K100 buffer: 50 mM Tris.HCl (pH 7.5), 100 mM KCl, 10 mM $MgCl_2$, 1 mM EDTA and 10% (v/v) Ethanediol.

K10 buffer: 50 mM Tris.HCl (pH 7.5), 10 mM KCl, 10 mM $MgCl_2$, 1 mM EDTA and 10% (v/v) Ethanediol.

AFM buffer: 50 mM Tris.HCl (pH 7.5), 100 mM KCl, 10 mM $MgCl_2$. This buffer was used for most AFM experiments. When a different buffer condition was used, this was stated in the figure legend.

2.3. DNA preparations

2.3.1. Plasmid DNA transformation

Different lengths of DNA plasmids, containing a single copy of *oriD* sequence (2437 bp, 3094 bp, 3650bp, 4907 bp, 6086 bp, 6642 bp), were used in this investigation. The DNA constructs were made by Andrew Slatter, NIMR [52]. Plasmid amplification was performed by transformation of the DNA into *E.coli* XL-1 Blue cells (Stratagene).

For protein expression, plasmids were transformed into *E.coli* B834 (λDE3), B834 (λDE3) pLysS cells or BL21 (DE3) pLysS cells (Novagen). Small aliquots of competent cells (50 µl) were thawed and transferred into pre-chilled 1.5 ml microcentrifuge tubes. The addition of 1 µl of pure plasmid DNA was followed by incubation for 30 min on ice. Following incubation, cells were heat shocked at 42 ˚C for 45 s and incubated on ice for 2 min. 800 µl of pre-warmed NZY or SOC media was added and incubated at 37 ˚C for 1 hour whilst shaking at 225 rpm. 200 µl of culture was plated on selective LB-Agar media with 100 µg/ml ampicillin, and 50 µg/ml ampicillin, and 34 µg/ml chloramphenicol for pLysS cells. Plates were inverted and incubated overnight at 37 ˚C and single colonies were used for cultures.

2.3.2. Plasmid DNA purification

Small scale, high copy number plasmid preparations from *E. coli* cultures were performed using the Qiagen kits according to the manufacturer's instructions. Plasmids were extracted from overnight cultures with the Qiaprep spin miniprep or maxiprep kit using a microcentrifuge, according to the Qiagen protocol. Supercoiled plasmid DNA was eluted in 30 µl of 10 mM Tris.HCl, pH 8.5, (Elution Buffer from Qiagen kit), and stored at -20 ˚C. DNA was quantified by absorbance spectroscopy using the following conversion factor for double stranded DNA: A_{260} of 1 cm^{-1}: 50 ng/µl DNA.

The quality of the DNA preparations was usually checked on a 1% agarose gel, and is shown in Figure 2.1.

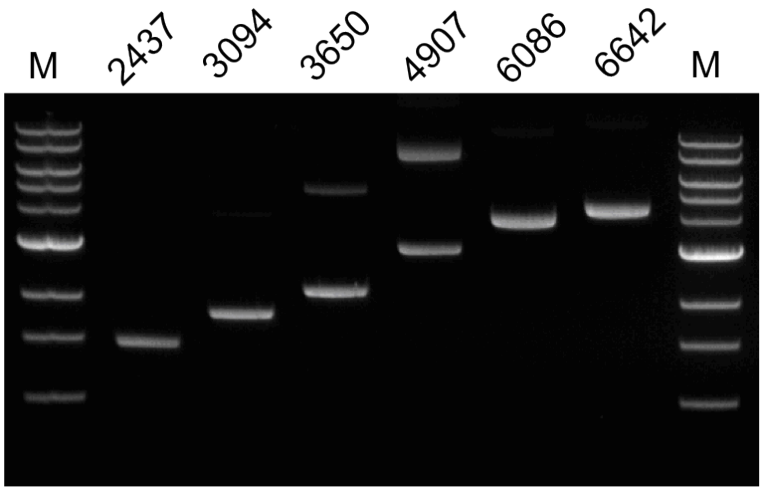

Figure 2.1. Agarose gel analysis of supercoiled pCERoriD plasmids. 100 ng of purified plasmids (indicated in bp) were loaded on a 1 % agarose gel and electrophoresed (see below for details on agarose gel electrophoresis). Molecular mass markers are in order from top to bottom 10, 8, 6, 5, 4, 3, 2, 1.5, and 1 kb, respectively. Additional contaminating bands are likely to be nicked plasmids.

2.3.3. Restriction digests

Linear DNA substrates were generated for the study of PcrA unwinding kinetics and the AFM experiments. Restriction digest reactions were carried out using commercially available restriction endonucleases (New England Biolabs). DNA plasmids were digested in the appropriate recommended conditions and buffers, HindIII and NdeI digestions in 10 mM Tris.HCl, 50 mM NaCl, 10 mM $MgCl_2$, 1 mM dithiothreitol DTT (pH 7.9, buffer 2, New England Biolabs) and NgoMIV in 10 mM Bis-Tris-Propane-HCl, 10 mM $MgCl_2$, 1 mM DTT (pH 7.0, buffer 1, New England Biolabs). Reactions were incubated at 37 ˚C for 2 hours.

The 3094 bp plasmid was digested with HindIII, whereas the 4907 bp plasmid was digested with NdeI, HindIII and NgoMIV. Digest reactions were mixed with 6 X loading buffer and ran on 1% agarose gels to separate the linear and supercoiled plasmids. DNA fragments were visualised, and removed from the gel using a scalpel, and purified using the QIAquick gel extraction kit (Qiagen).

2.3.4. Site-directed mutagenesis

Mutation of RepD gene was generated using QuikChange II site-directed mutagenesis kit and protocol (Stratagene). The primers containing the single mutation were designed in order to produce RepDN189K mutant (5′-CGTGACAGTGATAGATTTATTTGAATTTATAAAAAAAAACAAGAACG-3′, and 5′-GGCGTTATCTTTACGTTCTTGTTTTTTTTTATAAATTCTAATAAATC-3′, N189K reverse and N189K forward oligonucleotides, respectively).

RepD gene was amplified by PCR using the genomic DNA from *S. aureus*. The two primers annealed on the site containing the desired mutation. The polymerase then extends the template starting from the primers resulting in a circular DNA that contains the mutation. For PCR reactions, 10 ng pET11a-RepD was incubated with 125 ng N189K reverse and N189K forward primers, 1 µl of 10 mM dNTPs mix, 2.5 U of *Pfu* hot start DNA polymerase, 10 µl 5X *Pfu* hot start buffer and 1.5 µl 100% DMSO. PCR reactions were performed using 25 cycles consisting of a 20 s denaturation step at 98 °C, followed by a primer annealing step at 68 °C for 30 s and an extension step at 72 °C for 5 min. After 25 cycles, the reaction was incubated at 4 °C.
PCR final reactions were incubated with 10 U Dpn I at 37 °C for 2 h in order to eliminate the wild type DNA template. Reaction products were purified using the QIAquick PCR purification kit and the purified mutated vector was used to transform *E. coli* DH5α cells. The newly generated gene was sequenced by Geneservice, Ltd.

2.3.5. Oligonucleotides and DNA junctions

Oligonucleotides, either unlabelled or labelled with fluorescent dyes, were purchased from Eurofins MWG Operon, (Germany) or Sigma, Ltd. Oligonucleotides were dissolved in ddH_2O at the desired concentration and quantified by measuring absorbance at 260 nm using the given extinction coefficient.

DNA junctions were made by mixing two oligonucleotides in 50 mM Tris.HCl pH 7.5, 150 mM NaCl, and 3 mM $MgCl_2$ (1:2 ratio for Cy3:Dabcyl labeled oligonucleotides). DNA junctions were heated to 95 ˚C for 5 min and kept at room temperature for 2 h prior to storage at -20 ˚C. Oligonucleotides and DNA junctions used in this investigation are shown in Figures 2.2, 2.3, and 2.4.

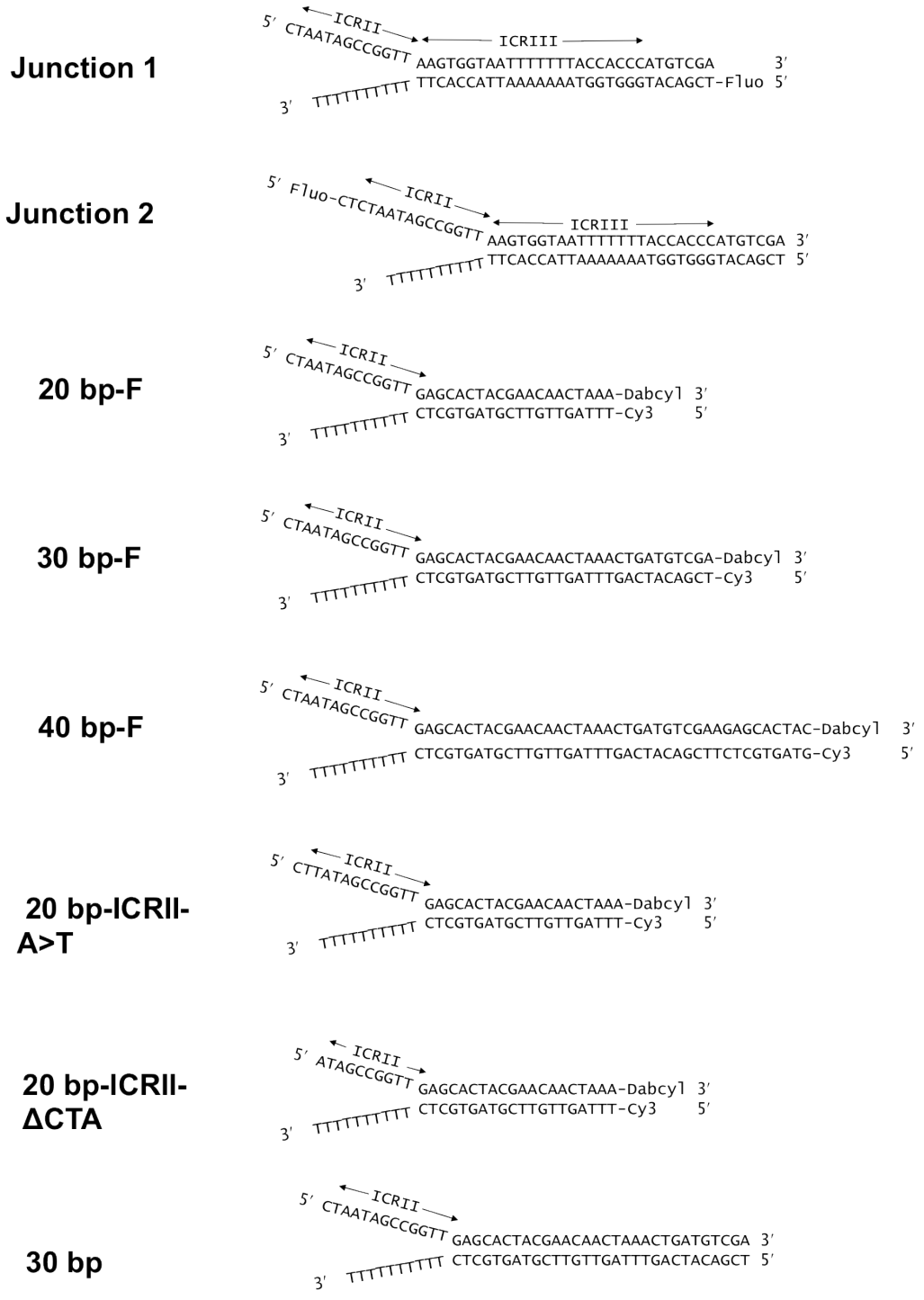

Figure 2.2. DNA junctions used for RepD and PcrA assays.

Junction 3	5′AAAAAAAAAAGAGCACTACGAACAACT 3′ 3′TTTTTTTTTTCTCGTGATGCTTGTTGATTTGACTACAGCTTCTCGTGAGT-Cy3 5′
Junction 4	5′AAAAAAAAAAGAGCACTACGAACAACT 3′ 3′TTTTTTTTTTCTCGTGATGCTTGTTGATTTGACTACAGCTTC 5′
Junction 5	5′CAGCTTCGACGATACTATCGCCATCAT 3′ 3′GTCGAAGCTGCTATGATAGCGGTAGTAAAAAAAAAAAAAAA 5′
Junction 6	5′CAGCTTCGACGATACTATCGCCATCAT 3′ 3′GTCGAAGCTGCTATGATAGCGGTAGTACCCCCCCCCCCCCC 5′
Junction 7	5′CAGCTTCGACGATACTATCGCCATCAT 3′ 3′GTCGAAGCTGCTATGATAGCGGTAGTATTTTTTTTTTTTTT 5′

Figure 2.3. DNA junctions used for PolC experiments.

dT10-2AP	5′ 2TTTTTTTTT 3′
dT16-2AP	5′ 2TTTTTTTTTTTTTTT 3′
dT30-2AP	5′ 2TTTTTTTTTTTTTTTTTTTTTTTTTTTTTT 3′
ICRII-wt	5′ CTAATAGCCGGTT 3′
ICRII-A>C	5′ CTCATAGCCGGTT 3′
ICRII-A>T	5′ CTTATAGCCGGTT 3′
ICRII-ΔCTA	5′ ATAGCCGGTT 3′
OriD-(+)	5′GCTTTAGACAATTTTTCTAAAACCGGCTACTCTAATAGC CGGTTAAGTGGTAATTTTTTTACCACCC 3′
OriD-(-)	5′GGGTGGTAAAAAAATTACCACTTAACCGGCTATTAGAGT AGCCGGTTTTAGAAAAATTGTCTAAAGC 3′

Figure 2.4. DNA oligonucleotides used in this investigation.

2.4. Protein preparations

2.4.1. Bacillus Stearothermophilus PcrA preparation

The over-expression and purification of *Bacillus Stearothermophilus* PcrA helicase has been published previously [98]. The method used here to purify PcrA is similar. *B. Stearothermophilus* PcrA in a pET22 vector (pET22-*Bst*PcrA, a gift from Dale Wigley, London Research Institute) was transformed into *E. coli* strain B834 (λDE3) (Novagen). A single colony from the plate was inoculated into the overnight culture of LB media (100 ml) with 100 µg/ml ampicillin, shaking at 225 rpm at 37 ˚C. 2 L of LB media (4 x 500 ml) with 100 µg/ml ampicillin were inoculated with 5 ml (1/100 dilution) of overnight culture, and grown shaking (220 rpm) at 37 ˚C. PcrA expression was induced with 1 mM Isopropyl-beta-D-thiogalactopyranoside, IPTG, when the optical density (OD_{595}) reached 0.5. Cells were further grown for 3 hours post-induction. Cultures were centrifuged at 4 ˚C, at 4000 rpm, in a JS 4.2 swing bucket rotor (Beckman Coulter) for 30 min. Cell pellets (2 x 500 ml of culture) were resuspended in 20 ml of buffer containing 50 mM Tris pH 7.5, 2mM EDTA, 1 mM DTT, and 200 mM NaCl, 10% (w/v) sucrose. Re-suspended cells were stored at -80 ˚C until purification.

For PcrA purification, cells were thawed, pooled, and phenylmethanesulfonylfluoride (PMSF) was added to final concentration of 0.1 mM. Cells were sonicated on ice for 4 x 30 second bursts using a probe sonicator, and centrifuged at 13200 rpm, at 4˚C for 20 min using a 45 Ti rotor (Beckman Coulter). The supernatant was measured and 0.7 times this volume of saturated $(NH_4)_2SO_4$ was added to precipitate PcrA gradually (over 5 min) whilst stirring at room temperature. Following $(NH_4)_2SO_4$ precipitation, centrifugation was performed at 13200 rpm, at 4˚C for 20 min using a 45 Ti rotor. The supernatant was removed and the pellet was resuspended in 20 ml of low salt buffer (50 mM Tris.HCl pH 7.5, 2 mM EDTA, 1 mM DTT and 100 mM NaCl). The conductivity of the protein sample was measured with a conductivity

meter (Mettler Toledo), and adjusted to match that of the resuspension buffer by adding a buffer containing 50 mM Tris.HCl pH 7.5, 2 mM EDTA, and 1 mM DTT. This sample was loaded onto a 20 ml heparin sepharose column (GE healthcare) equilibrated in 50 mM Tris.HCl pH 7.5, 2 mM EDTA, 1 mM DTT, and 100 mM NaCl at 1 ml/min at 4˚C using AKTA FPLC (GE healthcare). Following loading, the column was washed in a buffer containing 50 mM Tris.HCl pH 7.5, 2 mM EDTA, 1 mM DTT, and 100 mM NaCl until a baseline was reached at 280 nm absorbance.

PcrA was eluted in 50 mM Tris.HCl pH 7.5, 2 mM EDTA, and 1 mM DTT using a linear NaCl gradient starting from 100 mM NaCl to 700 mM NaCl, over a volume of 150 ml. PcrA elutes at ~350-400 mM NaCl, confirmed by SDS-PAGE analysis.

Fractions were pooled and concentrated using 20 ml 10 000 molecular weight cut-off (MWCO) vivaspin concentrator (Millipore). Samples were spun down at 4000 rpm at 4 °C in JS 4.2 swing bucket rotor. PcrA was quantified using the molar extinction coefficient of 75875 M^{-1} cm^{-1} at 280 nm (Chris Toseland, personal communication). PcrA was stored in aliquots at -80˚C after the addition of 10% glycerol (v/v). Typically, ~100 mg of protein was purified from 3 L of culture volume. Purified PcrA is shown in Figure 2.5 (section 2.5.2).

2.4.2. Staphylococcus aureus RepD preparation

The over-expression and purification of *Staphylococcus aureus* RepD has been published previously [25]. *S. aureus* RepD in a pET11a expression vector (pET11a-*Sa*RepD, a gift from Christopher D. Thomas, University of Leeds) was transformed into B834 (λDE3) pLysS. A single colony was inoculated into 100 ml of 2YT media with 1% glucose (w/v), 50 µg/ml ampicillin, and 10 µg/ml chloramphenicol and grown overnight by shaking at 225 rpm at 30 ˚C. 2 L of 2YT media (4 x 500 ml) with 50 µg/ml ampicillin, and 10 µg/ml chloramphenicol were inoculated with 5 mls (1/100 dilution) of overnight culture, and grown in 2L flasks at 30 ˚C in orbital shaker at 225 rpm until optical density (OD_{595}) reached 0.5. Cells were induced with 0.1 mM IPTG and grown further 6 hours. Cultures

were centrifuged at 4 ˚C, at 4000 rpm, in a JS 4.2 swing bucket rotor for 30 min. Cell pellets were resuspended in ~50 ml of a buffer containing 50 mM Tris.HCl pH 7.5, 1 mM EDTA, 10% (v/v) ethanediol, 500 mM KCl, 1 mM DTT, and frozen at -80 ˚C until purification.

Cell pellets were thawed adding 1 tablet of protease inhibitor cocktail (Santa Cruz biotechnology, complete). Cells were sonicated in ~50 ml aliquots on ice for 2 x 15 s bursts using a probe sonicator. Sonicated cells were centrifuged at 12000 rpm, at 15 ˚C for 30 min using a 45 Ti rotor (Beckman Coulter). The volume of the supernatant was measured and 2 times the volume of a buffer containing 50 mM Tris.HCl pH 7.5, 1 mM EDTA, 10% (v/v) ethanediol, and 3 M $(NH_4)_2SO_4$ was added and incubated on ice for 30 min. Following $(NH_4)_2SO_4$ precipitation, sample was centrifuged at 12000 rpm, at 4˚C for 30 min using a 45 Ti rotor (Beckman Coulter). After centrifugation, the pellets were resuspended in a buffer containing 50 mM Tris.HCl pH 7.5, 1 mM EDTA, 10% (v/v) ethanediol, and 500 mM KCl (~4 mls for each pellet). The conductivity of pooled resuspended pellets was measured and adjusted with a buffer containing 50 mM Tris.HCl pH 7.5, 1 mM EDTA, and 10% (v/v) ethanediol, to match that of a buffer containing 50 mM Tris.HCl pH 7.5, 200 mM KCl, 1 mM EDTA, and 10% (v/v) ethanediol. A further centrifugation step was done at 12000 rpm, 15˚C, for 30 min in a 45Ti rotor (Beckman Coulter). The soluble supernatant was first loaded on 6 ml Q-sepharose (GE healthcare), and then on a 20 ml heparin sepharose column (GE healthcare), both equilibrated in 50 mM Tris.HCl pH 7.5, 1 mM EDTA, 10% (v/v) ethanediol, and 200 mM KCl at 1 ml/min using AKTA FPLC (GE healthcare). Columns were washed in ~200 mls of the equilibration buffer before removal of the Q-sepharose column. A linear KCl gradient from 200 mM KCl to 700 mM over 200 ml was performed to elute RepD from the heparin sepharose column.

Fractions were analysed by SDS-PAGE analysis, and measured for absorbance at 260 nm, and 280 nm. Fractions with a 280/260 ratio of greater than 1.5 were pooled, and concentrated using 20 ml 10000 MWCO Vivaspin concentrator (Millipore) by centrifugation at 3000 rpm, at 4 °C in a JS 4.2 swing

bucket rotor. RepD dimer was quantified using an extinction coefficient of 119514 M^{-1} cm^{-1} at 280 nm (Andrew Slatter, personal communication). Typically, ~90 mg of protein was purified from 3 L of culture volume. Purified RepD proteins are shown in Figure 2.5 (section 2.5.2).

2.4.3. Staphylococcus aureus PolC preparation

The over-expression and purification of *Staphylococcus aureus* PolC has been published previously [64]. The method of purification used during this investigation is largely similar, but has some alterations from this published procedure. *Staphylococcus aureus* PolC in pET11a vector (pET11a-*Sa*PolC) was given by Andrew Slatter, NIMR. PolC was expressed and transformed into BL21 (DE3) pLysS cells. An overnight culture of M9ZB media with 50 µg/ml ampicillin and 10 µg/ml chloramphenicol, was grown shaking (225 rpm) at 29 ˚C, inoculated with a single colony from pET11a-*Sa*PolC in BL21 (λDE3) pLysS cells. 3 L of M9ZB media with 50 µg/ml ampicillin, and 10 µg/ml chloramphenicol (6 x 500 ml) were inoculated with 5 mls (1/100 dilution) of overnight culture, and grown shaking (225 rpm) at 29 ˚C to an OD of 1.0. The cells were induced by adding 1 mM IPTG and grown for 3 hours. Cultures were centrifuged at 4 ˚C, at 4000 rpm, in a JS 4.2 swing bucket rotor for 30 min. Cell pellet was resuspended in 50 mM Tris.HCl, pH 7.5, 0.1 % Triton X100, 1 mM EDTA, 20% glycerol (v/v) (25 ml of buffer each liter of culture) and stored at -80 ˚C.

Cell pellets were thawed adding 1 tablet of protease inhibitor cocktail (Santa Cruz biotechnology, complete). Cells were sonicated on ice for 3 x 15 s bursts using a probe sonicator. Sonicated cells were centrifuged at 12000 rpm, at 15 ˚C for 1 hour using a 45 Ti rotor (Beckman Coulter).

The supernatant was loaded onto a HiTrapQ column (5 ml, GE healthcare) that was equilibrated in 50 mM Tris.HCl, pH 7.4, 10% glycerol (v/v) and 1 mM EDTA (No Salt buffer). Following loading, the column was washed with 20 column volumes of buffer. PolC was eluted in 50 mM Tris.HCl, pH 7.4, 10% glycerol (v/v), and 1 mM EDTA using a linear NaCl gradient from 0 to 0.5 M and the

peak between 0.3 and 0.4 M NaCl was loaded onto a HiTrap Blue column. Before loading, the column was equilibrated in No Salt buffer. Following loading, the column was washed again with 10 column volumes of No Salt buffer. A linear NaCl gradient from 20 mM to 2 M over 250 ml was performed to elute PolC.

Fractions were analysed by SDS-PAGE analysis, and were pooled and concentrated using 10 ml 100 000 MWCO vivaspin concentrator (Millipore). Samples were spun down at 4000 rpm at 4 °C in JS 4.2 swing bucket rotor. PolC concentration was determined using an extinction coefficient of 112385 M^{-1} cm^{-1} at 280 nm (Andrew Slatter, personal communication). Typically, ~10 mg of protein was purified from 3 L of culture volume. Purified PolC is shown in Figure 2.5 (section 2.5.2).

2.5. DNA and protein gel electrophoresis

2.5.1. Agarose gel electrophoresis

Gel electrophoresis is used to separate molecules by size and topology. DNA was analysed by agarose gel electrophoresis. 1% agarose gels (w/v) were prepared by adding 1 g. agarose (Molecular biology grade-Biorad) to 100 ml of TAE buffer (40 mM Tris-acetate, and 1 mM EDTA). The agarose was dissolved by heating the solution and 1 µg/ml ethidium bromide was added before pouring into a cast and allowed to set for ~30 min at room temperature.

DNA samples, mixed with gel loading buffer (30 % (v/v) glycerol, 0.25 % (w/v) bromophenol blue), were loaded into gel wells and run in TAE buffer at 120 volts for 1 to 1.5 hours depending on the DNA separation. Visualisation was achieved by illumination using a UVItech trans-illuminator.

2.5.2. SDS-PAGE

The purity of proteins (PcrA, RepD, RepD N189K, and PolC) during over-expression and purification procedures was checked using a sodium dodecyl

sulfate polyacrylamide gel electrophoresis (SDS-PAGE, BioRad mini gel system, Figure 2.5).

For PcrA, a 15% running gel was made with 7.5 ml of 30 % (w/v) acrylamide and bis-acrylamide mix (37.5:1), 3.8 ml of 1.5 M Tris.HCl pH 8.8, 3.4 ml of dH_2O, and 150 µl 10 % SDS (w/v), setting was initiated by addition of 100 µl 10 % (w/v) ammonium persulfate, and 5 µl TEMED, and ~45 min are needed at room temperature for polymerization (total volume: 4 gels). 5% stacking gel was done with 1.7 ml of 30 % (w/v) acrylamide and bis-acrylamide mix (37.5:1), 1.25 ml of 1 M Tris.HCl pH 6.8, 6.8 ml of dH_2O, and 150 µl of 10 % SDS (w/v), and set with 100 µl of 10 % (w/v) ammonium persulfate, and 5 µl TEMED. Stacking gel mix was poured on the main gel and the well comb was used to set for ~30 min before use. For RepD and PolC, the running gel was made of 12 % (w/v) acrylamide/bis mix.

Protein samples were mixed with sample buffer (125 mM Tris.HCl pH 6.8, 4% SDS, 20 % (v/v) glycerol, 10% (v/v) 2-mercaptoethanol, and 0.25 mg/ml bromophenol blue), loaded onto wells, and ran in running buffer (25 mM Tris, 1.44 % (w/v) glycine, and 0.1 % SDS) at 200 volts for ~1 hour. Gels were stained with coomassie brilliant blue R-250 stain (BioRad) for ~20 min at room temperature, and destained with destain mix (10 % (v/v) acetic acid, 50 % (v/v) methanol) for 2-3 hours.

SDS-PAGE was also used to analyse RepD nicking on DNA. Each reaction contained 1 µM RepD and 10 µM of DNA in a total volume of 20 µl of K200 buffer. The reactions were incubated for 10 min at 30°C, prior mixing with 20 µl of sample buffer (see above), which stops the nicking reaction through protein denaturation. 20 µl reactions were loaded on a 12% SDS-PAGE gel, and run at 200 volts for 1 h. Gel staining was performed as described above. The band sizes were quantified using UVIpro software.

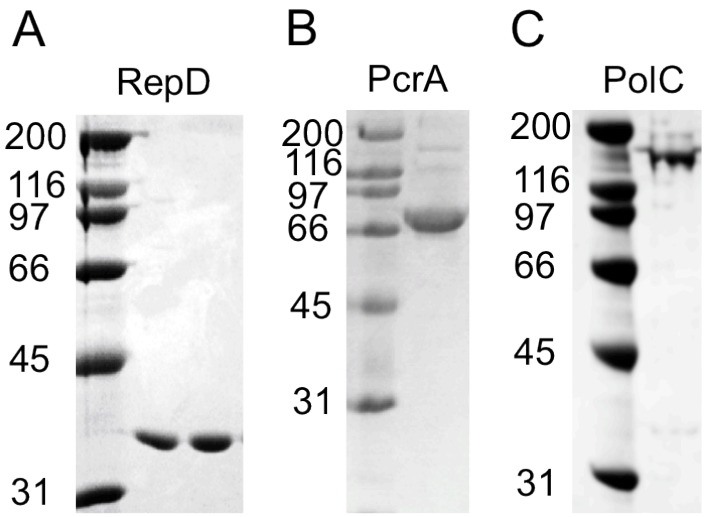

Figure 2.5. SDS-PAGE analysis of protein purifications. (A) 5 µg of RepD (37.3 kDa), wt (lane 2) and N189K RepD (lane 3). (B) 7 µg of PcrA (82.8 kDa). (C) 5 µg PolC (162 kDa). Proteins were purified according to protocols stated in the Methods (see above for details). Markers are indicated in kDa.

2.5.3. Non-denaturating PAGE

Non-denaturating PAGE was generally used to evaluate protein-DNA interactions, as well as the quality of DNA junctions.

A gel shift assay was used to study the binding of RepD either to the *oriD* sequence (made by annealing OriD-(+) and OriD-(-) oligonucleotides, Figure 2.3) or to DNA junctions (20bp-ICRII-A>T, 20bp-ICRII-ΔCTA, Figure 2.1), and PolC binding to a DNA template (Junction 4, Figure 2.2) (Eurogentec, Ltd.).

Mini gels were done with the BioRad mini gel system (10 cm x 8 cm, and 0.75 mm thickness). 6% polyacrilamide native gels were made with 3.5 ml of dH_2O, 0.5 ml TBE 10X, 1 ml Acrylamide/Bis solution (30 % (w/v) 29:1), 5 µl TEMED, and 50 µl of 10 % (w/v) ammonium persulfate.

Binding reactions were carried out at 4 ˚C for 15 min. Reactants and concentrations are indicated in the figure legends. Binding reactions were loaded onto wells (typically 10 µl), and ran in TBE 1X buffer (89 mM Tris base, 89 mM Boric acid, 2 mM EDTA) at 120 volts for ~30 min. Gels were stained with SYBR-gold dye for ~30 min at room temperature and visualised using a UVItech trans-illuminator.

The DNA junctions used for PolC binding and polymerization assays were checked on a 20% polyacrylamide gel under non-denaturating conditions (Figure 2.6). The gel was made with 0.5 ml of dH_2O, 0.5 ml TBE 10X, 3.3 ml Acrylamide/Bis solution (30 % (w/v) 29:1), 5 µl TEMED, and 50 µl of 10 % (w/v) ammonium persulfate. 10 µl of a 1 µM DNA solution was loaded on the gel and ran in TBE 1X buffer (89 mM Tris base, 89 mM Boric acid, 2 mM EDTA) at 120 volts for ~45 min. Staining and visualisation were performed with SYBR-gold dye, as described above.

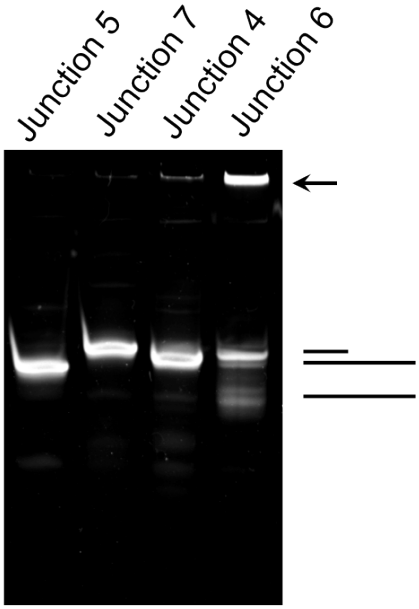

Figure 2.6. PAGE analysis of DNA junctions used in the DNA replication assay. The DNA junctions (see Figure 2.2 for sequences) were loaded on a 20% polyacrylamide native gel and run in non-denaturating conditions. The Junction 6, formed by a stretch of dGNP had an additional band, corresponding to the residual template oligonucleotide. The position of the partial DNA junction and the bottom oligonucleotide shown with a cartoon, the arrow indicates DNA cross-linking, resulting from the inter- and intramolecular G-quadruplexes.

2.6. Fluorescence-based assays

2.6.1. Fluorescence intensity measurements

Fluorescence intensity measurements were performed at 30 °C using a CARY Eclipse fluorometer (Varien). For these measurements, a xenon light source was used with 2.5 mm slits on excitation and emission with an averaging time of 1 second. Solution volumes were 60 µl in a quartz cuvette (Hellma). The experimental conditions and further parameters are given in the text.

MDCC-PBP biosensor (excitation wavelength 436 nm and emission wavelength 455 nm) was used as Pi biosensor in order to monitor PolC activity during synthesis of a DNA template (see details in section 2.6.2). The mant-dATP (excitation wavelength 366 nm and emission wavelength 430 nm) was used to assess PolC binding to the substrate.

2.6.2. DNA replication assay

PolC activity was analysed using an inorganic pyrophosphatase, PPase (Sigma), and MDCC-PBP as biosensor to detect the P_i. The overall reaction can be described, with generation of PP_i from PolC activity (step 1) and pyrophosphatase conversion (step 2), as follows:

(1) PolC + DNA template (n) + dNTPs → DNA template (n+1) + PP_i + PolC
(2) PP_i + Pyrophosphatase → P_i

For this assay, partial DNA junctions have been used (Sigma-Aldrich) (Figure 2.3, DNA junctions 4-7). Solutions (60 µl: total volume cuvette) were left to equilibrate for few min at the desired temperature prior to measurements. Reactions contained 10 nM PolC, 500 nM DNA (Eurogentec Ltd), 0.1 U inorganic pyrophosphatase, 20 µM of MDCC-PBP, and different concentrations of dNTPs (as indicated in the Figure legend), and were prepared in 10 mM Tris.HCl pH 7.5, 50 mM KCl, and 10 mM $MgCl_2$, and 2 mM EDTA, pH 7.5. The fluorescence signal was calibrated using known concentrations of inorganic

phosphate (usually in the μM range, see Appendix for details). V_{max}, k_m, and K_{cat} were determined from these measurements.

2.6.3. Fluorescence anisotropy measurements

Fluorescence anisotropy titration experiments were performed at 30℃ using an ISS PC1 Photon Counting Spectrofluorometer with a xenon light source. A solution of total volume 300 μl was prepared in a cuvette and left to equilibrate to 30℃ for 5 min prior to measurements. Fluorescence anisotropy measurements were taken every 30 sec, exciting with vertically polarized light; with emission read through both parallel and perpendicular polarisers in L-format using 1 nm slit widths, and an averaging time of 3 sec. Fluorescein was used in these measurements with an excitation wavelength of 492 nm and emission of 512 nm. Anisotropy is calculated and fitted to data using equations outlined in the Appendix of this thesis. Solution conditions are described in individual figure legends.

2.6.4. Stopped-flow measurements

These measurements were performed using a Hi-Tech stopped-flow apparatus with a xenon-mercury lamp (TgK Scientific, UK). In all the experiments described, the stated concentrations are those in the mixing chamber, which are half the concentrations of the syringes solutions, and reactions were done at 30 °C unless stated. Solution conditions and concentrations for measurements are indicated in figure legends.
Cy3 was excited at 548 nm, with a 570 nm cutoff filter (Schott glass) on the emission. 2-aminopurine was excited at 313 nm, with a 360-nm cutoff filter. Fluorescein was excited at 497 nm with a 515 nm cutoff filter.

PcrA unwinding activity on DNA junctions was tested using a stopped-flow apparatus (TgK scientific Ltd, Figure 1.12), in which reactant solutions can be mixed rapidly in a flow in order to start measurement of the optical signal. Different length DNA junctions (20-30-40 bp-F, 20 bp-ICRIIA>T, 20 bp-ICRII-ΔCTA; Eurogentec Ltd, Figure 2.2), labelled with Cy3 and Dabcyl, were used as

substrate for these reactions. Each reaction (typically 400 ul) had 100 nM PcrA, 2.5 µM RepD, 500 nM DNA, rapidly mixed with 200 µM ATP in K200 buffer. RepD was manually incubated with DNA solution for 5 min at 30 ˚C. PcrA was then added to the reaction and incubated for further 5 min. The pre-formed complex was then mixed rapidly with ATP using the stopped-flow apparatus (at 30 ˚C). Data were analysed with Grafit 6 software and unwinding rate for PcrA was calculated.

PcrA, RepD, and PolC were also used to monitor the unwinding of different length DNA plasmids using a stopped-flow apparatus. Wt RepD was manually mixed with the supercoiled plasmid DNA substrate for 30 s, whereas N189K RepD for 10 min to allow nicking (at 30 ˚C). PcrA was then added in the same reaction and left for further 30 s before starting mixing with ATP using the stopped-flow instrument. For these experiments, DCC-SSB was used to measure the ssDNA production. For DCC-SSB fluorescence, the excitation wavelength used was 436 nm with a 455-nm cutoff filter (Schott glass). The experimental conditions and concentrations are given in the text.

Fluorescence anisotropy measurements were performed in the stopped-flow instrument using additional polarisers for excitation and dual channel emission. Anisotropy was measured with the T format set-up of the instrument, allowing simultaneous acquisition of parallel ($I_{//}$) and perpendicular ($I_{\perp}$) components. This enabled anisotropy $(I_{//} - I_{\perp})/(I_{//} + 2I_{\perp})$, and intensity $(I_{//} + 2I_{\perp})$ to be calculated from the same reaction profile [88]. Anisotropy measurements are complicated by the different response of the detection systems to light of the same intensity but of different polarisation. Therefore, a correction has to be carried out in order to equalise the detection system which consists of two photomultipliers with parallel or perpendicular polarisation filters. This correction is carried out by first exciting the fluorophore with horizontally polarised light. Due to symmetry, there is an equal chance of the emitted light being polarised in parallel or perpendicular planes. Any difference between the parallel and perpendicular detectors can then be corrected by altering the photomultiplier voltage. This normalisation factor is often referred to as the G-factor.

Reaction conditions are indicated in the text. Fluorescence data were analysed on Kinetic studio (TgK Scientific, UK) or Grafit software.

2.7. Quench-flow experiment

Quench-flow experiments were performed using the Hi-Tech Rapid Quench Flow system RQF-63 (TgK Scientific, UK) to measure the nicking kinetics of plasmid DNA by RepD. 30 nM of 3650 bp pCERoriD was mixed with 150 nM RepD (concentrations after mixing) in 50 mM Tris·HCl pH 7.5, 100 mM KCl, 10 mM $MgCl_2$, 1 mM EDTA, and 10 % ethanediol and then reaction was quenched with 25 mM EDTA, pH 7.5, at 30 °C. Reaction products were collected and analysed on a 1% agarose gel.

2.8. AFM imaging

Imaging experiments were carried out at room temperature in contact mode using an atomic force microscope (NanoWizard, JPK Instruments, Germany). Silicon nitride cantilevers were employed for soft contact imaging (chipsize 3.4 x 1.6 x 0.45 mm, gold/chromium coated 70 nm thickness, 100 × 200 µm cantilever length, 0.27 N m^{-1}, tip radius < 15 nm, SiNi probes, BudgetSensors). Mica sheets (~2 x 2 cm large, SPI® supplies) were attached on a microscope glass slide of 3 x 40 mm using UV glue, and were used as substrates to attach the DNA.

Reactions were typically prepared at 30 °C. A freshly cleaved mica surface was treated with 2 mM $MgCl_2$, followed by washing with a solution containing 10 % (v/v) PBS supplemented and 2 mM $MgCl_2$ (washing is repeated three times). For samples containing only DNA plasmids, the DNA stock solution was diluted in either buffer or water, and deposited directly on the surface.

For samples containing proteins and DNA, reactions were mixed manually, incubated at 30 °C, and after the desired incubation time was diluted (100X) in 2 mM MgCl2. 10 µl of the DNA sample was deposited on the mica surface (typically ~ 20 ng of DNA), and left to adsorb for 1 minute. The surface was

rinsed with ddH_2O water for three times. Following washing, the specimen was dried under compressed air prior imaging. Solutions and conditions are indicated in the figure legend.

To reduce binding of the AFM tip to the sample, new cantilevers were irradiated for 20 min by a 254 nm, 5 watt mercury lamp (UVP, Cambridge, UK) prior to the experiment.

Image acquisition was performed using the JPK Nanowizard software. The scan line frequency was typically 2 Hz at 512 x 512 resolution. Contour lengths, height, and width were measured from the magnified images captured, using the tools of the nanoscope software (JPK, Nanowizard).

For combined TIRF-AFM experiments, round borosilicate glass coverslips (12 mm dia, 0.13 - 0.17 mm thick, GE Healthcare) were used as surfaces in these experiments. The coverslips were coated with aminosilane groups. Glass surfaces were mounted in a slide holder (Teflon coverslip holder) and ultrasonicated in a glass bath for 5 min in a solution containing 15 g KOH, 20 ml ddH_2O and 300 ml of ethanol. The surfaces were then washed in ddH_2O and ultrasonicated for 5 min x 3. Following washing, glass surfaces were treated and ultrasonicated for 5 min with a solution containing 200 µl (3-(2-(2-aminoethylamino)ethylamino)propyl trimethoxysilane (DETA), 20 µl glacial acetic acid, and 300 ml ddH_2O. This was then followed by a further step of washing with ddH_2O (ultrasonication for 5 min x 3). The excess of water is removed and the coverslips are dried in oven at 80 °C for 30 min. The procedure converts the glass surface from negative to positive, and so it allows DNA absorption. The glass coverslips were then mounted on a microscope specimen holder prior sample deposition.

Samples were prepared as described above and allowed to adsorb for 1 min before washing (ddH_2O X 3) and drying. Reactions and conditions are indicated in the figure legends.

Fluorescently images were visualised using a digital camera (ORCA–FLASH 4.0, C114440, Hamamatsu, Japan) with the use of the HCImage software (Hamamatsu, Japan). Images were taken with a resolution of 1024 x 1024 pixels (binning 2), with an exposure time of 0.3 s. AFM images were taken at

regions of interest determined from the TIRF images based on the known tip location as shown from the brightfield imaging of the cantilever.

3. Formation of the Initiation Complex

3.1. Introduction

The initial events of the replication process specifically require interactions between the supercoiled plasmid and the plasmid-encoded initiator protein, which is RepD for the pC221 plasmid. Initiation is achieved through RepD binding ICRIII and nicking ICRII sequence at the origin of the replication [25]. Through nicking a short ssDNA stretch is opened that allows the loading of the motor proteins, the helicase and polymerase.

In this chapter, the initiation step was investigated in terms of RepD-DNA complex formation prior PcrA helicase recruitment on the *oriD*. An important approach towards the elucidation of the mechanism of initiation involves the determination of RepD nicking kinetics on DNA containing critical sequences for its recognition.

Two main strategies were adopted to study the overall process of initiation and involve the use of two different DNA substrates (Figure 3.1). In one, synthetic, fluorescently labeled oligonucleotides with essential parts of *ori*D such as ICRII and ICRIII sequences are used. These junctions are designed to have a Y-shaped conformation with two short ssDNA arms given by annealing of two partially complementary oligonucleotides. Thus, their structures ensure RepD binding on the ICRII ssDNA arm and PcrA loading on a short ssDNA-tail. These junctions were previously used as synthetic DNA substrates to successfully monitor PcrA-RepD mediated unwinding in fluorescent-based assays [52]. Alternatively, DNA plasmids containing the *oriD* sequence are useful tools to investigate initiation and translocation by RepD and PcrA complex along DNA. In this case, the benefits of using these substrates are that a close comparison can be made to events occurring *in vivo,* and more events can be examined such as the religation step performed by RepD, which is an essential activity during the termination process. On a practical point of view, these substrates are easily produced with a highly productive *E. coli* strain harboring the DNA and purification usually results in optimal yields for the use in biochemical assays.

An additional approach to study initiation is to design RepD variants and compare the binding and nicking activities with the wild type protein. A variant of

RepD, N189K RepD, retaining a mutation within the active site of the protein was generated in order to study the effects of such modification on RepD nicking and binding activites. The crystal structure of RepD has not been solved yet, however several mutants of Rep proteins have been previously described delineating its activity. Such mutants were useful for the design of the N189K mutation. The reactive tyrosine (Y188 in RepD), involved in the covalent attachment to the DNA, was initially identified through isolation and amino acid sequence analysis of a labeled peptide-oligonucleotide fragment. This tyrosine residue is conserved in all Rep proteins, and its importance in Rep nicking was also confirmed through mutational analysis and the production of the Y188F variant [25]. Another variant RepD was described previously, R186K (published using a different numbering system as R189K), having the mutation at -2 from the active tyrosine. This mutant is able to nick the DNA but is not able to catalyze the reverse reaction of religation forming a more stable RepD-DNA complex [99]. Clearly, substitutions of an aminoacid in the active site have an effect on the RepD-mediated DNA cleavage. Based on the RepD mutations previously published and in the absence of any structural information for RepD, one mutation in the active site of RepD was attempted to study its activity. Similarly to the R186K mutant, a lysine was choosen to be inserted at position 189, close to the active tyrosine. The mutation N189K is located at +1 from the tyrosine group involved in the RepD covalent attachment and may actively assist the transesterification reaction. A direct comparison of the two initiator proteins activity was made.

Firstly, the RepD variant, N189K, was generated to study RepD nicking activity. The nicking kinetics of RepD on a supercoiled pCERoriD plasmid were determined, and the binding, nicking and translocation activities of the active mutant, N189K RepD, were investigated. The mutant showed similar DNA binding activity to the wild type but a rather different nicking activity. The latter was significantly affected by the DNA structure.

Additional features of RepD were then studied such as its function of being part of the translocation complex with PcrA during unwinding. It was previously shown that RepD recruits and activates PcrA helicase by forming a stable complex at the origin that allows processive unwinding [52]. This function of RepD might be achieved through direct interactions with the helicase. However,

the exact molecular interactions between RepD and PcrA are still not completely clear. The ability to form a functional translocation complex with PcrA was further investigated here using the N189K RepD. Such studies were performed using a variety of fluorescent-based assays, gel assays combined with rapid-reaction techniques.

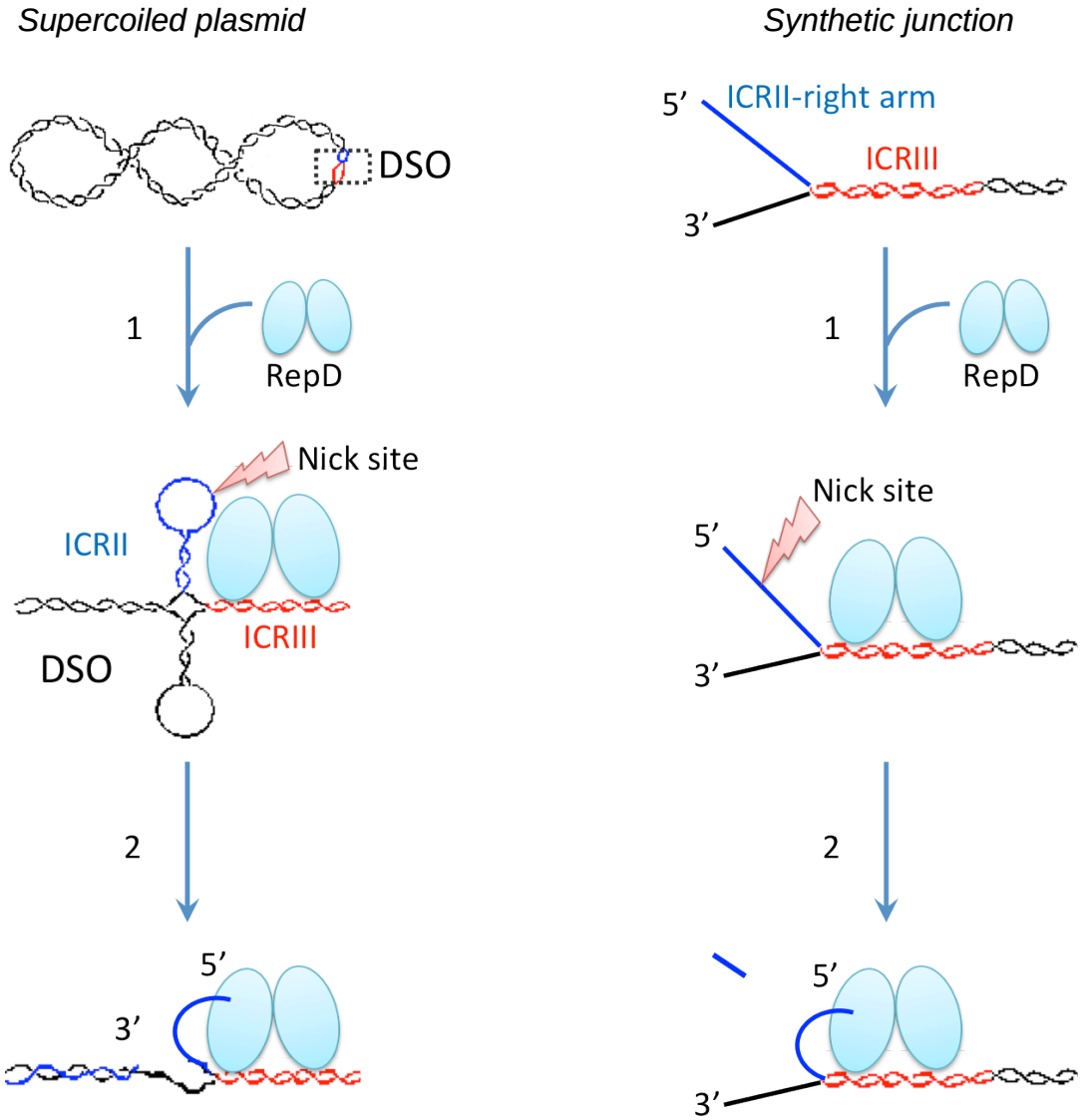

Figure 3.1. Schematic models of RepD-mediated initiation. RepD dimer, ICRIII and ICRII sequences of the (+) strand are shown respectively in azure, red and blue. The nick site is indicated. RepD binds the ICRIII (step 1) and nicks the ICRII site forming a covalent bond with the 5’-end of the nicked DNA (step 2). In the supercoiled plasmid, the whole origin of replication can form a cruciform structure due to the inverted repeated sequences. Nicking activity by RepD induces release of supercoiling in the native plasmid. In the Y-junction model, the right arm of the ICRII sequence is used and nicking results in DNA cleavage and release of a small DNA.

3.2. RepD nicking activity on supercoiled plasmids

3.2.1. Kinetics of RepD nicking and religation pCERoriD plasmid

As previously mentioned, initiation of replication starts with RepD binding and nicking the plasmid. It has previously been shown that RepD is able to nick and religate pC221 and pCERoriD plasmids *in vitro* [25]. Here, the RepD nicking kinetics were studied to elucidate the mechanisms of the initial steps in replication. The nicking reaction catalyzed by RepD requires DNA containing its cognate *oriD* and Mg^{2+} ions. The overall reaction is a transesterification resulting in a phosphodiester bond between the 5' of the (+)-strand at *oriD* and the active tyrosine of RepD. The reaction is reversible and a second transesterification can occur resulting in resealing of the nicked DNA strand (for details of the nicking reaction see the Introduction).

Considering the biological effects of RepD nicking activity, a change in the plasmid topology when using a supercoiled substrate (SC) occurred. Because of its ability to release the supercoiling of DNA, it has also been called topoisomerase I-like activity. The relaxation reaction is shown in Figure 3.2. RepD binding of SC is followed by nicking with conversion of the supercoiled plasmid into an open circular form (OC) having RepD covalently attached (steps 1 and 2, Figure 3.2). From this OC intermediate, RepD can religate to produce a relaxed, covalently closed plasmid (CC) in step 3 (Figure 3.2). Following religation, RepD is released in an unaltered form (step 4, Figure 3.2). Release of supercoiling is irreversible and can be restored only upon the activity of a DNA gyrase.

The assay used here to investigate RepD nicking kinetics is based on the analysis of these plasmid topological forms. The use of such assay was previously described to study the activity of several topoisomerase enzymes *in vitro* [100]. In this assay, the substrate (SC), the open circular (OC) and the closed circular product (CC) produced by the nicking/religation reaction between RepD and the plasmid run differently on an agarose gel and were

visualised as three discrete bands following electrophoresis. Thus, reactions were analysed for DNA topology. However, this approach has several limitations, because it does not allow a separate calculation for plasmid binding of RepD (step 1), or distinguish between the religation of the OC form (step 3) and RepD dissociation from the CC form (step 4, Figure 3.2).

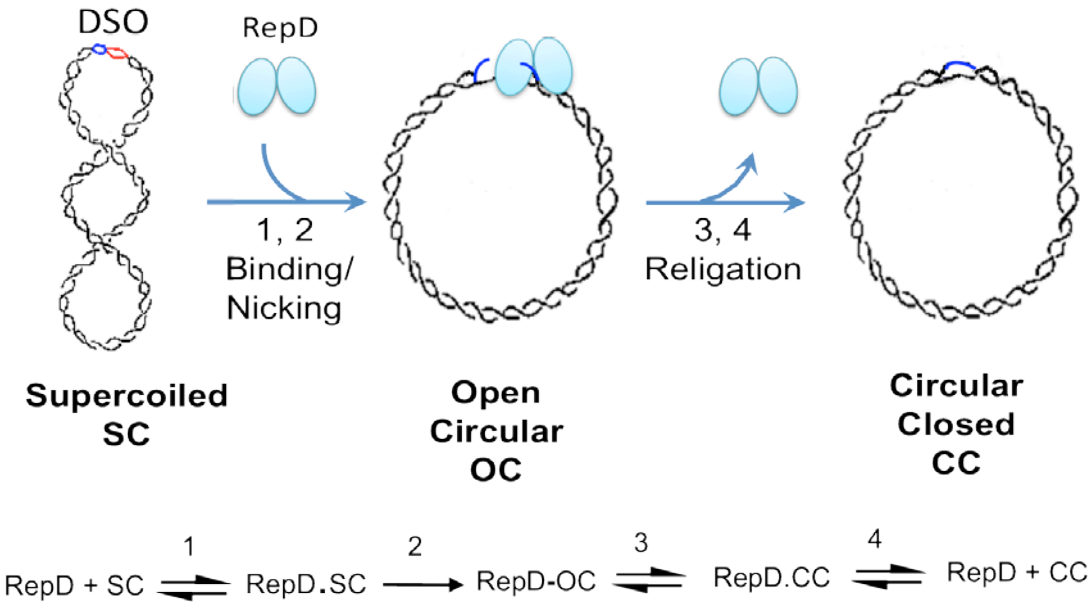

Figure 3.2. Relaxation activity of RepD on a supercoiled plasmid. Cartoon of the RepD nicking/closing activity and relative topology changes in a DNA plasmid, and reaction scheme of the DNA relaxation. RepD interacts with a supercoiled plasmid within the DSO (step 1) and then nicks the (+)-strand of the ICRII (step 2). Plasmid relaxation is concomitant with DNA cleavage. The latter can be followed by religation (step 3) and RepD dissociation (step 4).

A negatively supercoiled plasmid containing the whole *oriD* sequence (pCERoriD, 3.6 kb) was used as substrate for RepD. Requirement of Mg^{2+} by RepD was a useful tool in order to control and preferentially stop the reaction at a desired time using a chelating agent such as EDTA. Thus, a time course reaction was performed to assess RepD nicking/closing activities and the final products of this reaction were analysed on an agarose gel (Figure 3.3).

The activity of wt RepD on pCER*oriD* was assayed over 30 min. The relative band intensities of the SC, OC and RC were measured at fixed time points. Manual mixing of the nicking reaction showed rapid and essentially complete

nicking to form the open relaxed structure. After only 5 s the complete plasmid reacted to form the open circular form. On a longer time scale (2-30 min) a new gel band appeared, corresponding to a closed circular plasmid (CC, Figure 3.3) formed by religation of the DNA ends. The closed circular plasmid form migrates ahead of the supercoiled plasmid under these electrophoretic conditions. This is due to the presence of ethidium bromide that can intercalate in the DNA and affect the overall topology of the circular close plasmid. Thus, positive superhelical twists can be introduced in the DNA by the intercalation of ethidium bromide in relaxed closed plasmid [101]. The religation resulted in 23% closed, relaxed plasmid at apparent equilibrium with nicked, open DNA (Figure 3.3B). Quantitation of the gel bands as function of time gives a rate constant of 0.0037 s^{-1} for this religation (Figure 3.3B).

As the shortest time analysed in the manual mixing experiment was 5 s, an accurate estimate of the nicking rate could not be achieved with this approach. So, a quench-flow mixing experiment was then designed and used to get higher time resolution (Figure 3.4A). Wt RepD and the supercoiled plasmid were rapidly mixed, and then quenched with EDTA at the defined times and the reaction products were analysed on an agarose gel (Figure 3.4B). Quantification of the bands is shown in Figure 3.4C. Nicking kinetics was biphasic. So data were fitted with a double exponential. The time course of the nicking reaction show a rapid burst that occurs >25 s^{-1} with a 35% amplitude followed by a slower phase at 2.5 s^{-1} with a further 50% reaction. The initial burst was too fast to be measured precisely because the quenched-flow dead time. Nicking experiments was also repeated in presence of PcrA to evaluate possible effects of the helicase on the nicking and religation rates. Results showed that PcrA does not have a significant effect on RepD nicking-closing activities (see the Appendix of this thesis).

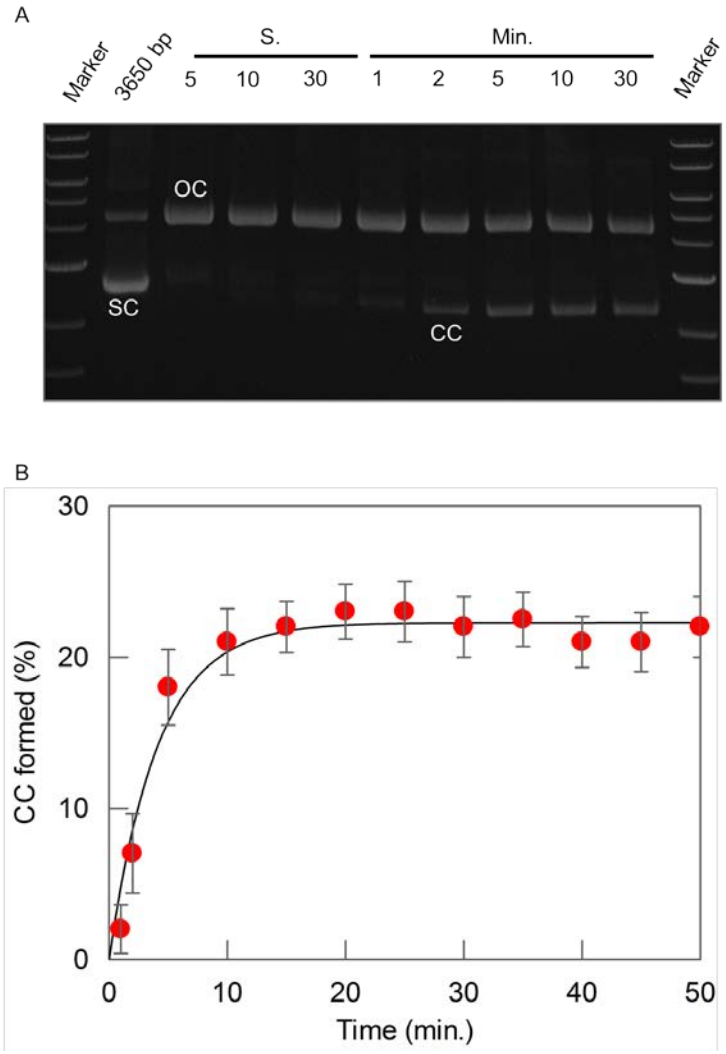

Figure 3.3. RepD nicking/closing activities on a supercoiled pCERoriD plasmid. (A) Time course of RepD products generated from a manual mixing reaction analysed on a 1% agarose gel. 15 nM pCERoriD (3.6 kb), and 60 nM RepD were pre-incubated in K100 buffer at 30˚C. At the time points indicated (in s and min), samples were quenched by addition of 50 mM EDTA. Additional details can be found in Methods. Molecular weight markers are from top to bottom 10, 8, 6, 5, 4, 3, 2, 1.5 kb. Plasmid topology indicated above relevant bands, in either supercoiled (SC), open circular (OC), and closed circular (CC) forms. (B) Kinetics of formation of the relaxed, closed plasmid (CC) from relaxed, open plasmid. The data points were obtained by integration of the gel bands. The line is the best fit exponential, giving a rate constant of ~0.0037 (± 0.0006) s^{-1}. Error bars indicate standard deviations among three independent experiments.

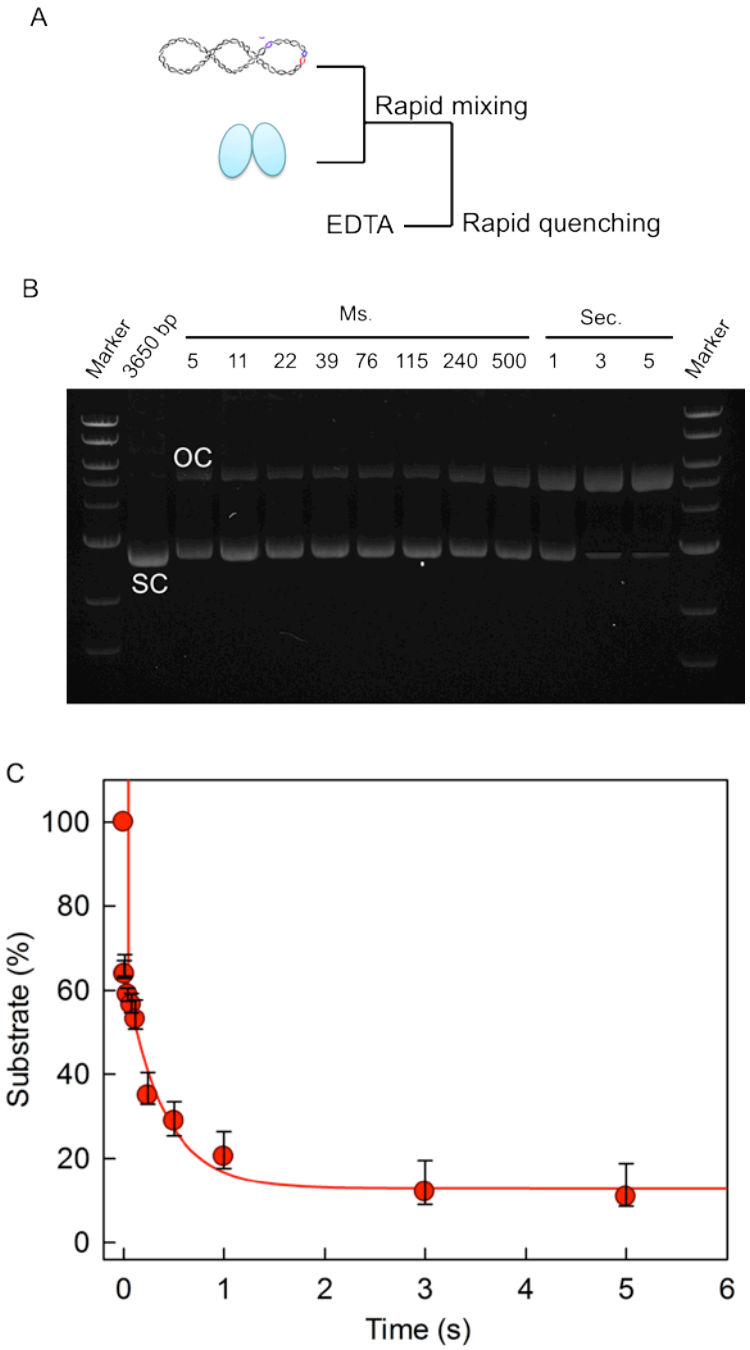

Figure 3.4. Kinetics of RepD nicking a supercoiled pCERoriD plasmid. (A) The quench-flow experimental set-up. (B) Time course of the nicking reaction analysed on a 1% agarose gel. 30 nM plasmid (pCERoriD, 3.6 kb) was mixed with 150 nM RepD (concentrations after mixing) and then the reaction was quenched with 25 mM EDTA (pH 7.5) at 30 °C as shown in (A). Additional details are in Methods. Molecular weight markers are as in Figure 3.3. (C) Agarose gel analysis of the plasmid substrate relaxed over time by RepD. The line is the best fit exponential for the slow phase that follows a burst. The burst at >25 s^{-1} has ~35% amplitude followed by a slow phase at ~2.6 ± 0.4 s^{-1} with a further 50% reaction. Error bars indicate standard deviations among three independent experiments. Repeats are found in the Appendix of this thesis.

The same approach was undertaken with N189K RepD mutant in order to further investigate the RepD nicking reaction. In contrast to wt RepD, N189K RepD nicking of supercoiled plasmid was much slower. Thus, a manual mixing approach was used to measure its nicking kinetics. The activity of N189K RepD on pCER*oriD* was assayed over 30 min in order to get the nicking rate (Figure 3.5A). The integration of the bands gives a nicking rate constant of 0.003 s^{-1} (Figure 3.5C). In order to measure religation kinetics, reaction was assayed over a longer time scale (incubation time > 30 min, Figure 3.5B). A band was detected for the closed circular form after 30 min. The intensity of such a band increased at a rate of 0.00039 s^{-1} and remained constant reaching an equilibrium between the closed relaxed and the open nicked DNA, similar to wt RepD (24%, Figure 3.5D). N189K RepD showed nicking occurring at a rate ~ 1000-fold slower than the wt protein and also slower religation (~ 10-fold). For both RepD proteins, the relief of supercoiling resulted in the high extend of product formation.

In the progress of plasmid replication, the next step of plasmid replication is PcrA binding to the exposed ssDNA and this process is much faster than the religation and so it might affect the religation rate of plasmid [48]. However, when performing the nicking reaction in the presence of PcrA, the helicase had no measurable effect on nicking nor on re-ligation kinetics (data not shown).

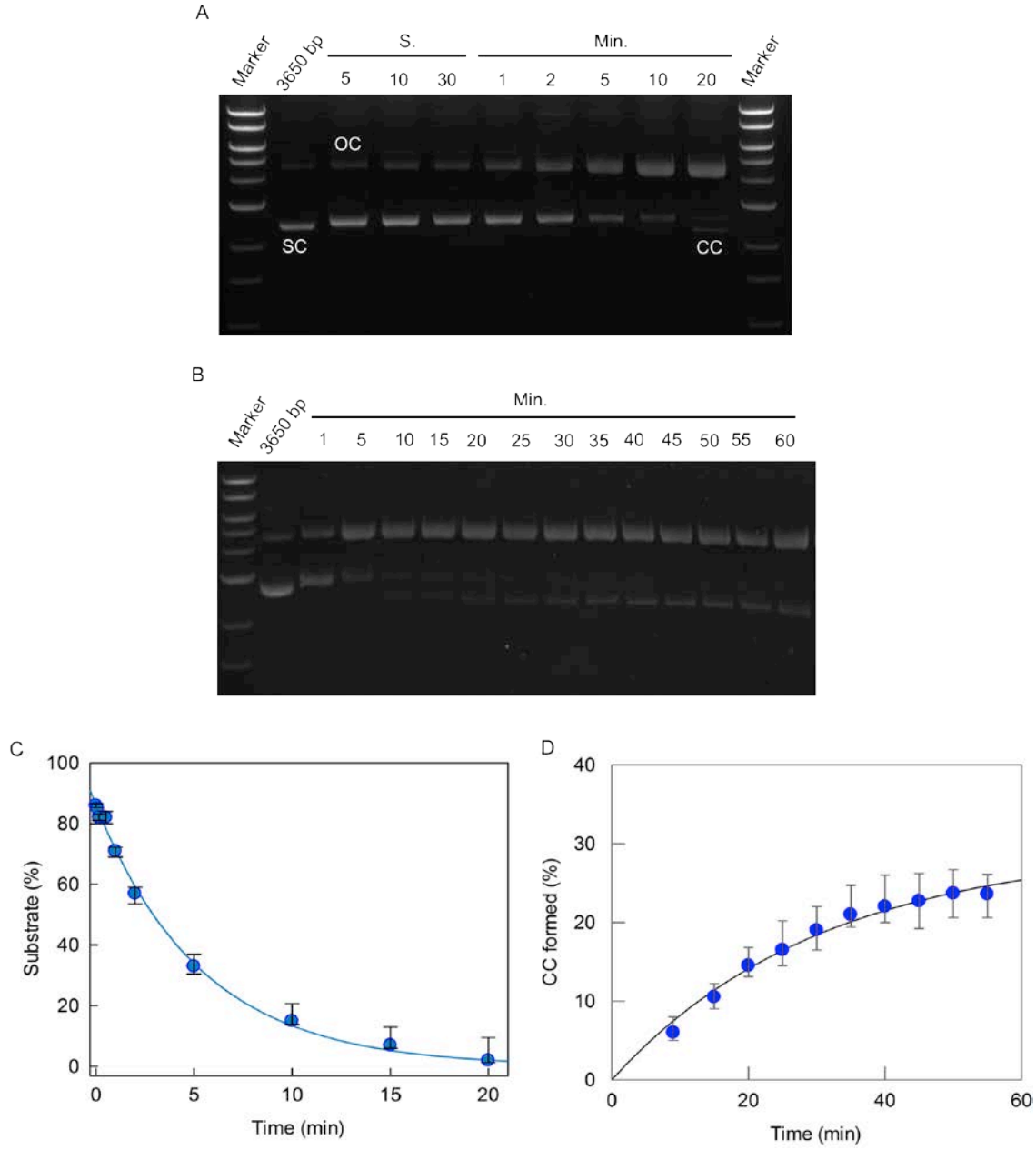

Figure 3.5. N189K RepD nicking/closing activity on a supercoiled pCERoriD plasmid. (A-B) Manual mixing experiment and agarose gel analysis of the DNA topology. (C) Quantification over time of the bands corresponding to the supercoiled substrate. Data were fitted to a single exponential, giving a rate of 0.003 s^{-1}. (D) Formation of the circular closed plasmid by N189K RepD religation activity. Data were fitted to a single exponential, giving a rate of 0.00039 s^{-1}. For solutions and conditions see Figure 3.3. Error bars indicate standard deviations among three independent experiments.

3.2.2. The requirement of divalent cations for nicking

Metal ion cofactors and especially divalent ions are important modulators of the catalytic activity of enzymes. They are involved in a wide range of chemical reactions such as redox and non-redox catalysis. In this perspective, a special case is represented by magnesium ion, which is largely utilized for electrostatic stabilization and for activaton of substrates. *In vivo*, magnesium represents an abundant species, as it is found in cells in the millimolar range. It is by far the most frequently found metal ion cofactor in the enzymatic systems due mainly to its ability to form stable complexes with phosphate-containing molecules.

The DNA cleavage performed by RepD requires Mg^{2+} for full catalytic activity. The requirement seems to be crucial for the chemistry as the ions may actively participate to the reaction in several ways [102]. Mg^{2+} could activate the attacking tyrosine group, and stabilize the negatively charged transition state and/or interact with the leaving group (for details about the nicking reaction see Introduction). Thus, such ions can affect the catalytic protein activity during the reaction. It has been shown that the use of different divalent cations affected RepD nicking and religation activities. In particular, substitution of Mg^{2+} with Ba^{2+} ions permits RepD mediated cleavage but promotes neither a stable covalent linkage nor relegation [25].

The effects of the interactions between three different divalent cations with RepD are further investigated here. The ability of Mn^{2+}, Mg^{2+} or Ca^{2+} to support RepD-mediated nicking of a supercoiled plasmid was monitored. These ions possess distinctive chemical features such as ionic size, hardness and geometry. Within this series, Mn^{2+} is the softest metal. Generally, hard metal ions usually coordinate more readily with oxygen and soft metals often prefer sulfur. So, in the transesterification reaction less rapid DNA cleavage should be generated in reaction containing soft metals.

DNA cleavage was measured upon incubation of wt or N189K RepD with the 3.6 kb supercoiled plasmid and increasing concentrations of cofactors. Such measurements allow the investigation of a differential use of ions by RepD and can provide an idea of their overall affinities. Reactions were incubated for 1

min for the wild-type and 10 min for the mutant prior quenching, and then ran on a 1% agarose gel. The bands corresponding to the relaxed DNA plasmids were quantified (Figure 3.6). A positive relationship was found between the relaxation activity of RepD and the concentration of Mg^{2+}, with near complete nicking at around 500 µM for wt RepD and 5 mM for N189K mutant (Figure 3.6A, D). For wt RepD, an initial burst phase occurred at the lowest concentrations of Mg^{2+} (in the nM range), where the level of DNA cleavage reached ~ 60%, implying an apparent K_{app} value < 41 nM. Substitution of Mg^{2+} as catalytic cofactor had an effect on the extent of RepD nicking. Ca^{2+} supported efficient nicking of wt RepD with formation of the near complete relaxed product between 6-10 mM (Figure 3.6C). Unlike wt RepD, the mutant RepD did not nick the plasmid in the presence of Ca^{2+}, even at high concentrations (Figure 3.6E). Lower levels of nicked plasmid over time were detected for both wt RepD and N189K when using Mn^{2+} (70% even at high concentrations of cofactor, 10 mM) and religation of the relaxed form was favoured (data not shown). So, it is likely that the ions affect the kinetics of nicking and religation, which were not determined here as only one time point of the reaction was examined.

Clearly, wt RepD was able to use all the three ions and the highest level of DNA scission was observed when using the hard cations as cofactors (Mg^{2+} and Ca^{2+}). However, the apparent affinity for such ions decreased in the following order Mg^{2+}>Mn^{2+}>Ca^{2+} (Table 3.1). Whereas, N189K RepD could support cleavage only with Mg^{2+} and Mn^{2+}, with a lower affinity for these ions compared to the wt protein.

	K_{app} Mg^{2+}	K_{app} Mn^{2+}	K_{app} Ca^{2+}
Wt RepD	*< 41 nM*	*260 ± 39 µM*	*1.0 ± 0.4 mM*
N189K RepD	*1.1 ± 0.3 mM*	*316 ± 97µM*	-

Table 3.1. RepD affinities to different divalent ions.

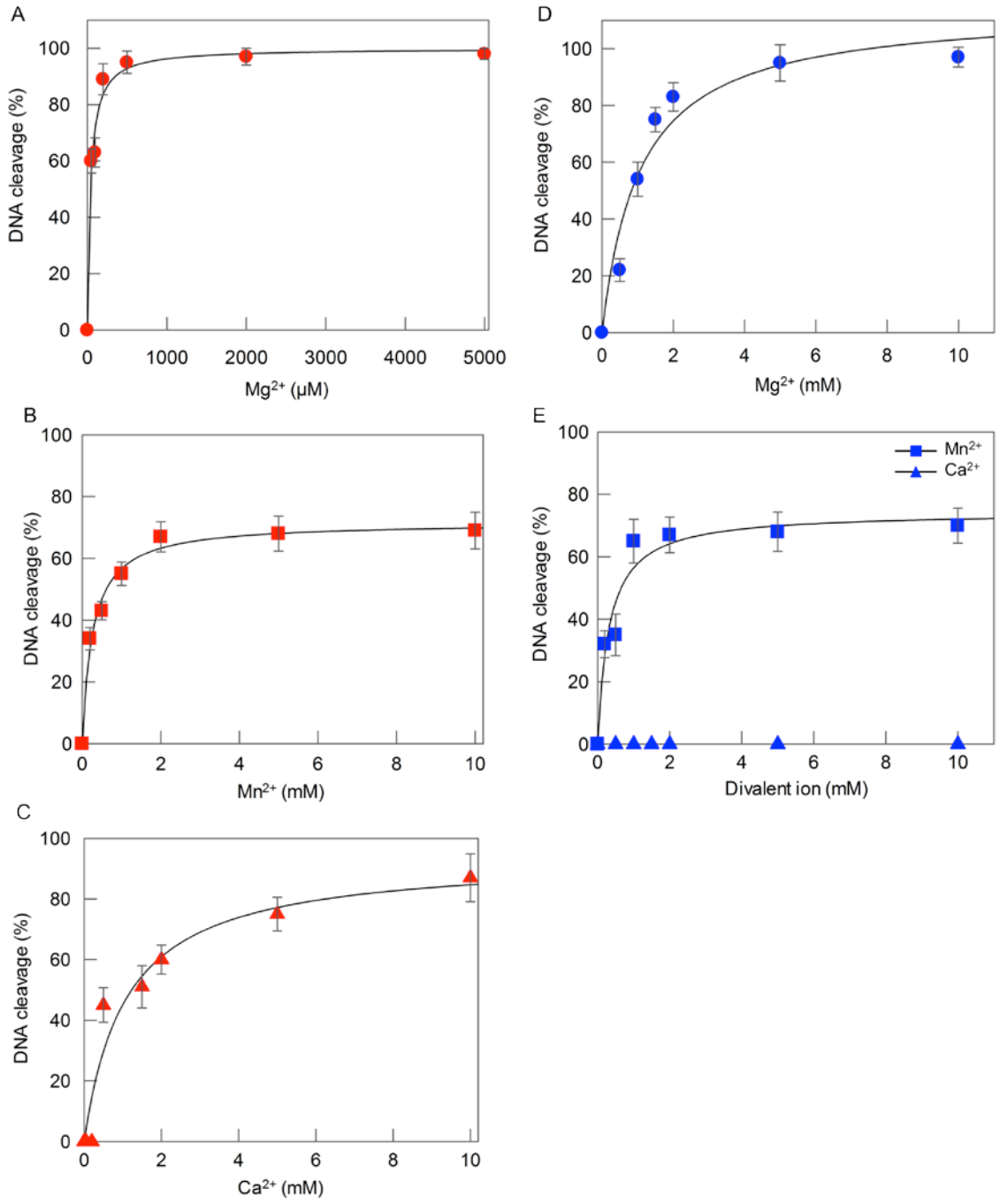

Figure 3.6. Effect of divalent ions on RepD catalysis. Agarose gel analysis of DNA cleavage by RepD upon increasing concentrations of divalent ions. Either wt (A-B-C) or N189K RepD (D-E) was incubated with a supercoiled plasmid and increasing concentration of ions and the relaxed plasmid formed was quantified by integration of the bands. Reactions were incubated for 1 min for wt RepD and 10 min for N189K prior EDTA mixing in order to allow complete nicking. Data were fitted to a hyperbola and values of K_{app} obtained from these titration experiments are summarized in Table 3.1. Solutions and conditions are as Figure 3.3. Error bars indicate standard deviations among three independent experiments.

3.3. PcrA-RepD mediated plasmid unwinding

3.3.1. Unwinding of supercoiled DNA plasmids

Unwinding of plasmid performed by the PcrA-RepD complex follows initiation. The activity of N189K RepD with PcrA during unwinding was investigated here. Several methods have been reported previously in order to measure in real time helicase unwinding of long DNA substrates such as plasmids. A good approach to quantify the unwinding activity is measuring a fluorescence signal change over time correlated with the production of ssDNA or the disappearance of dsDNA from the helicase activity. Fluorescent dyes have been widely used as reporter molecules for DNA unwinding. Fluorescent probes for nucleic acids such as DAPI and Hoechst 33258, display high fluorescence when bound to the dsDNA and low fluorescence when the fluorophore is either in solution or bound to the ssDNA. The dyes mentioned above were used in fluorometric assay to monitor the activity of RecBCD helicase [103]. Several limitations are correlated with these assays such as the possibility of reannealing of the unwound ssDNA.

The use of labeled SSB to measure unwinding overcomes several limitations of the assays described above. Firstly, the DNA length is virtually unconstrained allowing the study of processive helicases. In addition, SSB protein can trap the unwound ssDNA preventing reannealing. Binding of SSB is rapid and tight and so it is suitable for a real-time kinetic assay. SSB was labeled with a coumarin derivative (DCC-SSB) providing around 6-fold increase in fluorescence when bound to ssDNA. DCC-SSB has been successfully used in real-time to determine the kinetics of unwinding of AddAB and PcrA helicases [48, 52].

The assay used here to measure PcrA unwinding was performed in the presence of DCC-SSB using a stopped-flow instrument (Figure 3.7). In this assay, RepD and PcrA were incubated with a pCERoriD plasmid to allow the formation of the initiation complex, and then the solution was rapidly mixed with ATP to start unwinding in a stopped-flow apparatus. The newly generated ssDNA was substrate for the labeled SSB, causing an increase in the fluorescence intensity (Figure 3.7).

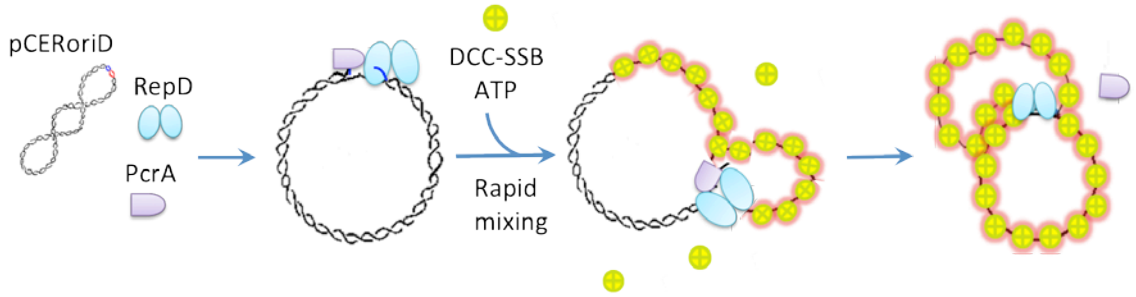

Figure 3.7. Cartoon showing the dynamics of supercoiled plasmid unwinding monitored in real time with DCC-SSB assay. A supercoiled pCERoriD plasmid is incubated with RepD and PcrA, RepD nicks and relaxes the plasmid and PcrA is recruited on the generated ssDNA tail. This solution is then rapidly mixed on the stopped-flow with a solution containing ATP, in presence of DCC-SSB. PcrA can start DNA unwinding with the hydrolysis of ATP and the produced ssDNA is bound by the DCC-SSB causing an increase in fluorescence.

Using the assay described above, it was previously shown that RepD activity is essential for processive unwinding by PcrA helicase [52]. Here, the assay is used to investigate the activity of the N189K RepD-PcrA unwinding complex. Different length pCERoriD plasmids were used in the DCC-SSB assay to monitor PcrA-unwinding and measure an average rate of unwinding. Unwinding of six plasmid lengths with the PcrA-N189K RepD complex is shown in Figure 3.8. Qualitatively, traces were similar to those observed with wt RepD (see the Appendix of this thesis). For the majority of the plasmids, a small lag phase is followed by an increase in fluorescence intensity and then a final flat phase. The difference in DNA length does not affect the initial lag phase which might be caused by the initial DNA-protein interactions or initial competition between PcrA and the SSB for the the ssDNA generated through RepD-mediated nicking. The increase in fluorescence is consistent with SSB binding ssDNA during unwinding. The amplitude of the traces linearly increases with the plasmid length, which is consistent with a higher amount of SSB bound on longer DNA once unwinding is complete (Figure 3.8C). However, the amplitudes varied, as they're proportional to the amount of supercoiled DNA in the solution and the efficiency of RepD nicking. The duration of unwinding also depends linearly on the size of the plasmid and the unwinding time (or break-

point) of the traces is used for the analysis. The slope of the linear fit of the duration of the unwinding phase in function of the DNA length gives a rate of unwinding of 19 bp s^{-1} for N189K RepD-PcrA complex (Figure 3.8B). This is similar, although a little slower than the rate (30 bp s^{-1}) observed with wt RepD (see the Appendix of this thesis).

Despite the slow nicking kinetics on the supercoiled plasmid of the mutant RepD, a functional unwinding complex with N189K-PcrA could be made and successful and processive unwinding could be achieved.

One feature of the plasmid unwinding assay is that a decrease in the amplitudes of the traces was observed for longer incubation times of the wt RepD-PcrA-DNA complex. Fluorescence traces of an aged complex using a 2437 pCERoriD plasmid are shown in Figure 3.9. This is likely to be caused by RepD religation events of the nicked plasmids over time.

However, when using N189K RepD the complete unwinding complex with this protein was normally incubated for 10 min before starting unwinding (wt RepD is incubated for only 60 s), because of a slower nicking activity of N189K RepD. This is the time taken by the mutant to achieve complete nicking of the supercoiled DNA. For incubation times >10 min the amplitudes of the traces were constant (Figure 3.9B, C). These observations suggest that a more stable RepD-DNA complex is formed with N189K over relatively long time. This is consistent with the slow religation kinetics of N189K RepD determined above.

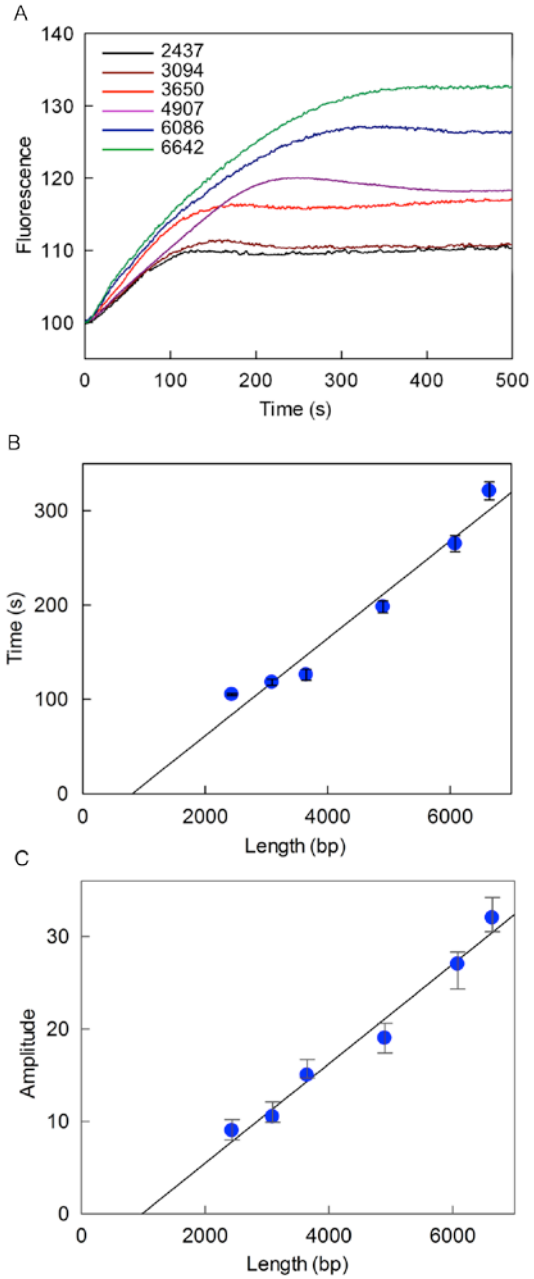

Figure 3.8. Unwinding of different length supercoiled plasmids monitored in real time using the DCC-SSB fluorescence assay. (A) Fluorescence time course for unwinding of plasmids of different lengths (shown in base pairs) with PcrA and N189K RepD. The assay performed in a stopped-flow apparatus is shown in Figure 3.7. Final concentrations after mixing in K100 buffer at 30 °C were 0.5 nM plasmid, 95 nM PcrA, 2 nM RepD, 1 mM ATP, and 200 nM DCC-SSB tetramers. The fluorescence has arbitrary units, normalized to start at 100. (B) Dependence of unwinding time on plasmid length, as described in the text. The linear fit gives a rate constant of 19 ± 2 bp s^{-1} for unwinding. (C) Dependence of the amplitude of the unwinding phases on the plasmid length. Error bars indicate standard deviations among three independent experiments. Examples of fitting are shown in the Appendix of this thesis.

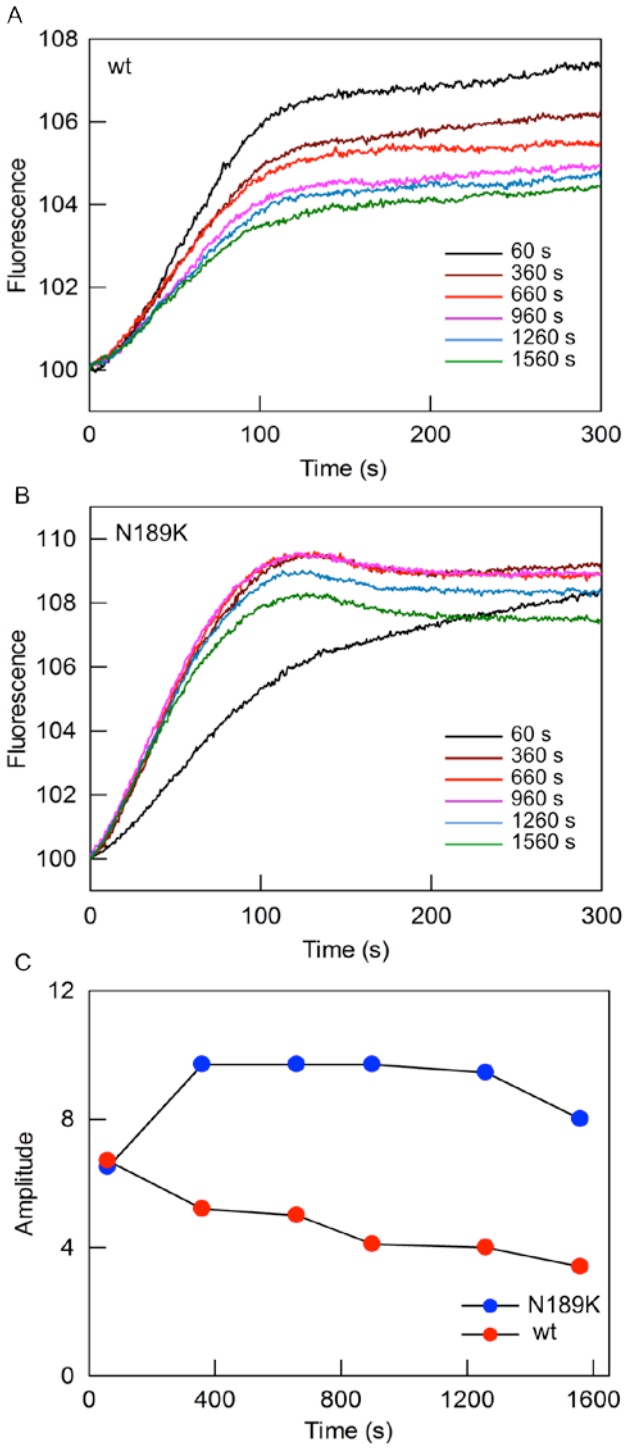

Figure 3.9. Unwinding of a supercoiled pCERoriD plasmid as a function of pre-incubation time. Comparison of unwinding traces of an aged solution containing a pCERoriD plasmid (2.4 kb) and wt RepD (A), or N189K RepD (B). RepD was incubated with the plasmid at the time indicated, and then unwinding was monitored using the DCC-SSB fluorescence assay (as described in Figure 3.7). The times taken to unwind were independent of the age time, but the amplitudes varied. The fluorescence has arbitrary units, normalized to start at 100. (C) The amplitudes of fluorescence in function of the incubation time.

3.3.2. Unwinding of a linear DNA plasmid

Unwinding was also measured on a linear DNA plasmid. The pCERoriD plasmids contain various sites for different restriction enzymes. Plasmid digestion was performed to generate linear DNA substrates. RepD nicking on the *oriD* is followed by PcrA helicase directional unwinding of the linear DNA substrate [51]. Unwinding traces for linear plasmid unwinding using the DCC-SSB biosensor are shown in Figure 3.10. A 3094 pCERoriD plasmid was digested to produce linear DNA placing the *oriD* at the initial end of the plasmid (the HindIII-3094, Figure 3.10A).

A direct comparison with a supercoiled substrate showed that the use of linear DNA had a negative effect on RepD nicking as the amplitudes of the traces were significantly reduced (Figure 3.10B). For this reason, the protein was incubated with this DNA substrate over several min prior unwinding. Fluorescence traces of linear DNA displayed an increase in signal for wt RepD but the phases were not distinctive and so the break point was not as well defined as when using supercoiling substrates (Figure 3.10B). A small increase in the amplitude was observed for longer incubation times of the RepD-DNA complex. This would be caused by slow nicking and an increase in the nicked linear DNA over longer time. These results suggested that supercoiling may play a significant role in RepD nicking activity.

Unwinding of such linear plasmids was also monitored with N189K RepD-PcrA complex (Figure 3.10C). Traces showed no change in fluorescence and similar results were observed with other linear plasmids (data not shown). These results indicated that N189K RepD-PcrA complex did not support unwinding of linear DNA. However, supercoiled plasmids are successful substrates for unwinding, so possibly one or more functions between binding, nicking and translocation activities were compromised in the RepD mutant.

The functions of N189K RepD mentioned above will be further investigated in this chapter in order to elucidate this mechanism.

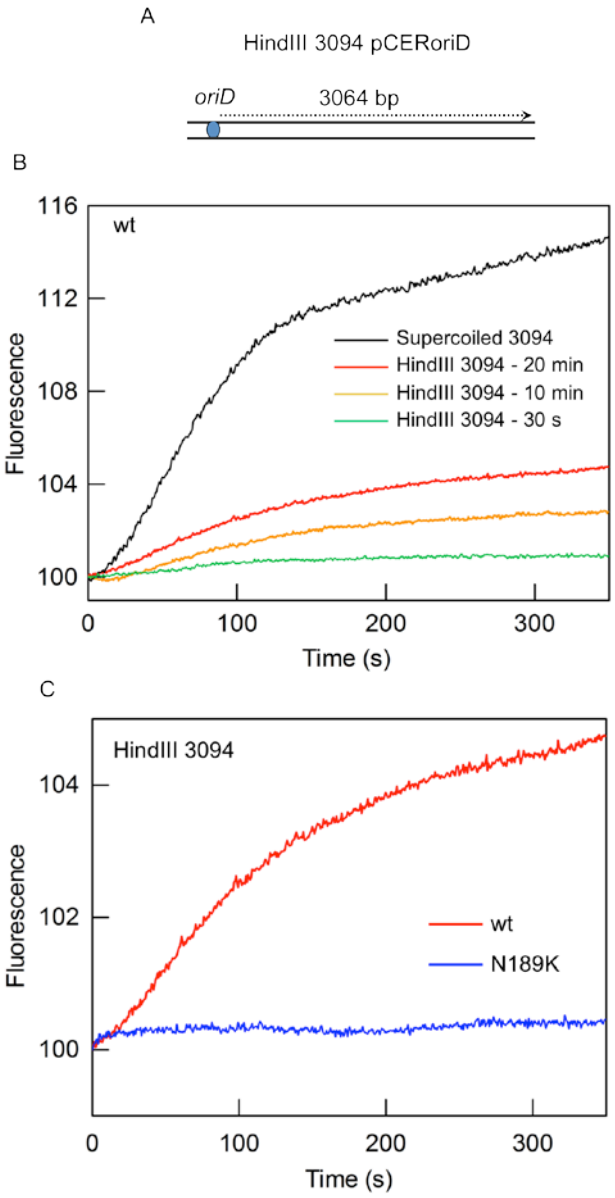

Figure 3.10. Unwinding of linear pCERoriD plasmid monitored in real time with the DCC-SSB assay. (A) Schematic of the linear pCERoriD plasmid (HindIII-cut 3094) used showing the location of the *oriD* sequence. (B) Comparison of the unwinding traces of a 3094 supercoiled plasmid (30 s incubation time) and the digested linear DNA (different incubation times) by wt RepD-PcrA complex. The effect of aging complex (30s, 10 and 20 min.) is shown for the linear plasmid. (C) Fluorescence traces of the HindIII 3094 plasmid unwound by either wt or N189K RepD-PcrA complex. Complexes were aged for 20 min prior unwinding. Solutions and conditions were as Figure 3.8.

3.4. RepD binding activity on partial DNA junctions

3.4.1. Anisotropy titrations of RepD binding partial DNA junction

The difference in the unwinding activity of the N189K RepD-PcrA complex of linear plasmids stimulated a further investigation of the mutant RepD function in initiation using linear DNA. An initial approach represented the exploration of binding to short labeled DNA junctions through anisotropy experiments.

Generally, a change in the fluorescence properties of a fluorophore accompanies binding and formation of macromolecular complexes and it can be used to quantitatively monitor such interactions. Fluorescence anisotropy can give useful information about the molecular mass of the probe in relation to its rotational correlation time (details on fluorescence anisotropy can be found in Chapter 1). Anisotropy measurements were described in a previous study with RepD and the Y-shaped junction [52]. These showed that wt RepD binds with high affinity to its recognition sites. Fluorescence anisotropy was used here to detect binding of wt RepD and N189K RepD variant to a partial DNA junction containing the right arm of the ICRII sequence and the complete ICRIII (junction 1, Figure 2.2 for structure and sequence). The 5'-end of one oligonucleotide of the duplex was labeled with fluorescein in order to locate the probe on the terminal part of the DNA junction and opposite to the protein binding site. Fluorescein is a useful probe for anisotropy measurements because of its fluorescence lifetime (~ 4 ns).

Titrations of wt RepD and N189K RepD in a solution containing the junction 1 were performed by monitoring the anisotropy changes in real time. The anisotropy increases upon RepD addition to the solution as binding to the DNA substrate occurs until it reaches saturation (Figure 3.11). The increase in anisotropy is accompanied with a relatively small decrease in the fluorescence intensity. This can be caused by a direct effect on the fluorescein presumably by direct interaction with RepD or conformational changes during complex formation. The change in fluorescence intensity may well be caused by a change in the fluorescence lifetime of the fluorescein, and for this reason the observed anisotropy is therefore apparent.

The change in anisotropy was plotted versus protein concentration and the measurements were fitted for reversible binding, gaving an apparent equilibrium constant, K_{app}, of 50 nM for wt RepD and 484 nM for N189K RepD (Figure 3.11). These values represent an approximate assessment of affinity due to the sensitivity of the method and the nature of the experimental approach.

Considering that these measurements were carried out in the presence of Mg^{2+}, the values obtained do not distinguish between the non-covalent and covalent interactions for wt RepD. However, it is anticipated that N189K RepD is not able to nick linear DNA so its apparent affinity constant would reflect only the noncovalent binding step.

In order to investigate the role of Mg^{2+} on DNA binding affinities, an alternative way to perform the measurements is to exclude Mg^{2+} from the buffer solution and include a chelating agent, such as EDTA, to remove any ion contamination. Under these conditions, the covalent linkage does not occur for wt RepD and the effect of Mg^{2+} on binding can be examined. Measurements of the K_{app} values were 90 nM for wt RepD and 484 nM for N189K (Figure 3.11, insets). In the absence of the catalytic ion, the K_{app} did not change significantly for either protein. These results suggest that mutation N189K may reduce RepD affinity to the DNA junction by ~6 fold.

The affinities of wt and N189K RepD to partial duplex DNA are further investigated in this chapter. The change in fluorescence intensity observed in the anisotropy measurements will be useful for supplementary binding studies. The effects of magnesium and other divalent cations on RepD activities are further examined. Additional aspects of the formation of the initiation complex, and a more direct comparison of the activity of the two RepD proteins will be made in the Discussion section.

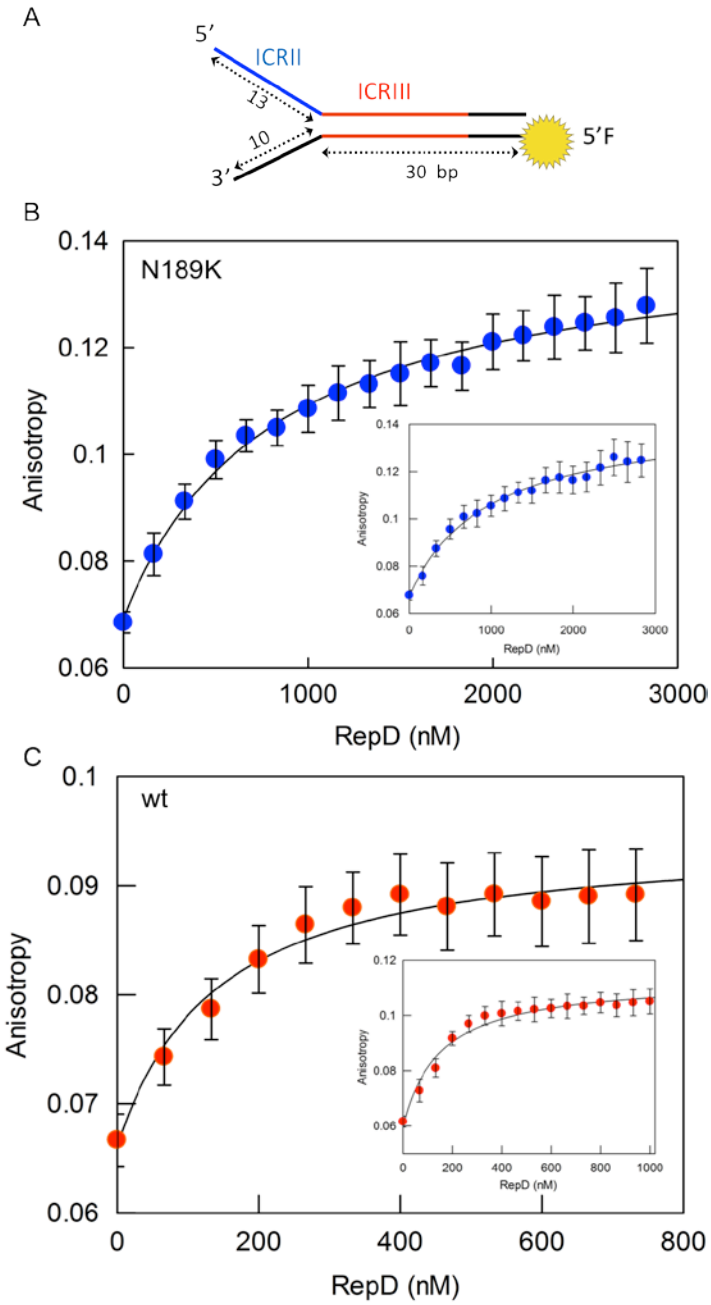

Figure 3.11. Fluorescence anisotropy analysis of DNA binding equilibrium by RepD. The structure of the Y-junction used in this assay and the position of the fluorescein (F) is shown in the top image (junction 1, Figure 2.2). Measurements were made in K200 buffer at 30 °C, exciting with vertically polarized light at 497 nm, and emission measured using a 515 nm cut off filter. Individual example titrations with wt RepD (B) and N189K RepD (B) giving a K_{app} of 50 nM and 484 nM respectively (DNA concentration is 200 nM). Titrations performed in Mg^{2+} free buffer (K200 without Mg) are shown in the insets giving a K_{app} of 90 nM for wt RepD and 484 nM for N189K RepD. Error bars indicate standard deviations among three independent experiments. Intensity changes are in the Appendix of this thesis.

3.4.2 RepD binding kinetics to a partial DNA junction

The fluorescence intensity signal generated by the fluorescein junction was used to further investigate DNA binding by RepD. The signal generated upon complex formation with a labeled molecule enables the determination of association and dissociation rate constants. Thus, the association kinetics of wt and N189K RepD are examined here under pseudo-first-order conditions by monitoring in real-time the fluorescence intensity of the fluorescein-labeled junction (junction 1, Figure 2.2).

The binding reaction is represented by scheme 1 with a single-step reversible model of binding.

Scheme 1:

$$\text{RepD} + \text{DNA} \underset{k_{-1}}{\overset{k_{+1}}{\rightleftharpoons}} \text{RepD.DNA}$$

In this model, the observed rate constant, k_{obs}, is given by the equation 6, where k_{+1} and k_{-1} represent the association and dissociation rates respectively. These measurements enable the calculation of the dissociation constant for the overall reaction, $K_{d\ (overall)}$, using equation 7:

(6) $$k_{obs} = k_{+1}\,[\text{RepD}] + k_{-1}$$

(7) $$K_d = k_{-1}/k_{+1}$$

The binding experiment was performed by mixing the DNA junction with increasing concentration of wt and N189K RepD using a stopped-flow apparatus (Figure 3.12A). The DNA substrate provides a significant signal change when bound to RepD. Addition of either wt or N189K RepD to the DNA solution causes a decrease in fluorescein fluorescence intensity consistent with rapid binding (Figures 3.12B-C). The traces are fit to single exponentials and

there is a linear dependence between the observed rate constants and RepD concentration.

Traces were fitted to single exponentials and linear data fitting give a slope (k_{+1}) of 83 $\mu M^{-1}s^{-1}$ and intercept of 12 s^{-1} for wt RepD, and 77 $\mu M^{-1}s^{-1}$ and an intercept of 19 s^{-1} for N189K RepD (Figure 3.12D). The value for wt RepD is similar to that observed previously [52]. RepD proteins show similar association kinetics.

Generally, the dissociation constant (K_d) may be estimated from the association kinetics experiments by using the intercept value (k_{off}) of linear fit to k_{obs} versus ligand concentration. The values of the intercepts obtained here are not accurate estimates of the dissociation rates as they are close to 0 and can be largely affected by fitting error. In this circumstance a more accurate measurement of k_{off} was needed. The latter can be determined through a displacement experiment performed using a stopped-flow instrument (Figure 3.13). Initially, RepD was allowed to bind the fluorescein junction until equilibrium was reached. At that point, the RepD-DNA complex was rapidly mixed with an excess of unlabeled junction. The resulting trace has an opposite fluorescence signal to binding and in this experiment is observed as an increase in fluorescein fluorescence (Figure 3.13). The traces were fitted to single exponential and the rate constants were independent from the unlabeled DNA concentration (2-50 μM). The dissociation rates were 1.3 s^{-1} for wt RepD and 6 s^{-1} for N189K variant.

The K_d values obtained from the k_{+1} and k_{-1} measurements are collected in Table 3.2.

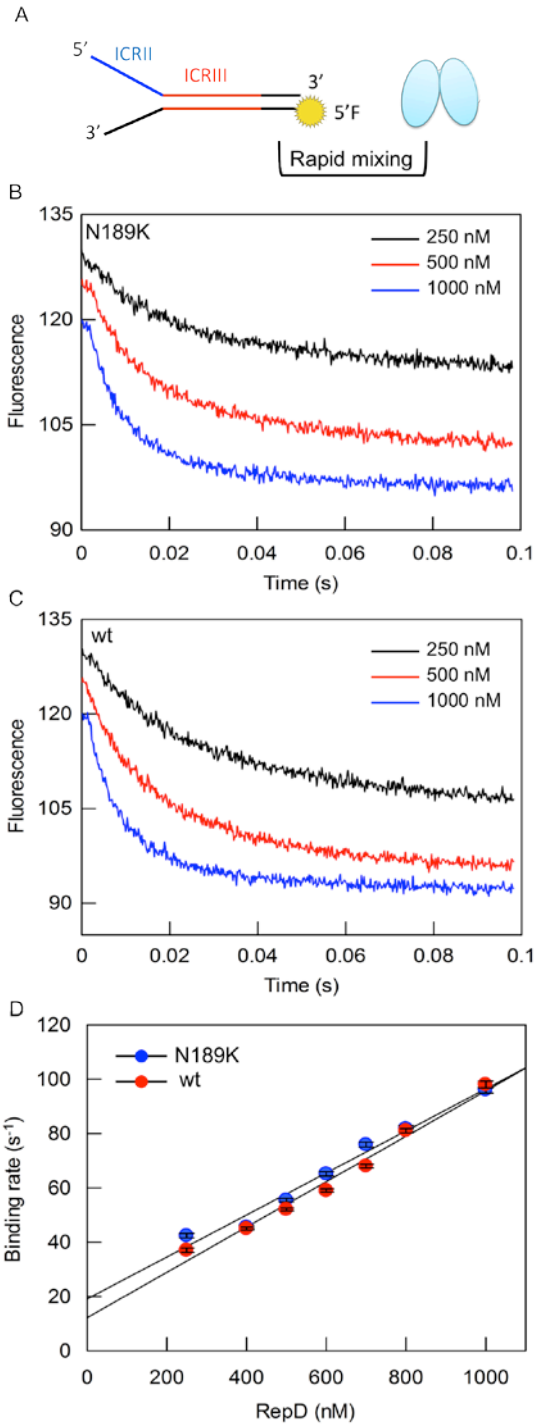

Figure 3.12. Binding kinetics of RepD to a DNA junction. (A) Binding experiment on a stopped-flow apparatus showing the structure of the junction 1, labeled with fluorescein (Figure 2.2). (B) Examples of fluorescence intensity traces of a range of concentrations of wild-type, and N189K RepD (C), mixed with the junction 1 (100 nM) in K200 buffer. (D) Linear data fitting gives a slope of 83 (±3) $\mu M^{-1}s^{-1}$ and intercept of 12 (±2) s^{-1} for wt RepD. N189K RepD binding to the junction gave a slope of 77 (±5) $\mu M^{-1}s^{-1}$ and intercept of 19 (±3) s^{-1} (30 °C). Error bars indicate standard errors from each fit. Individual fits are shown in the Appendix of this thesis.

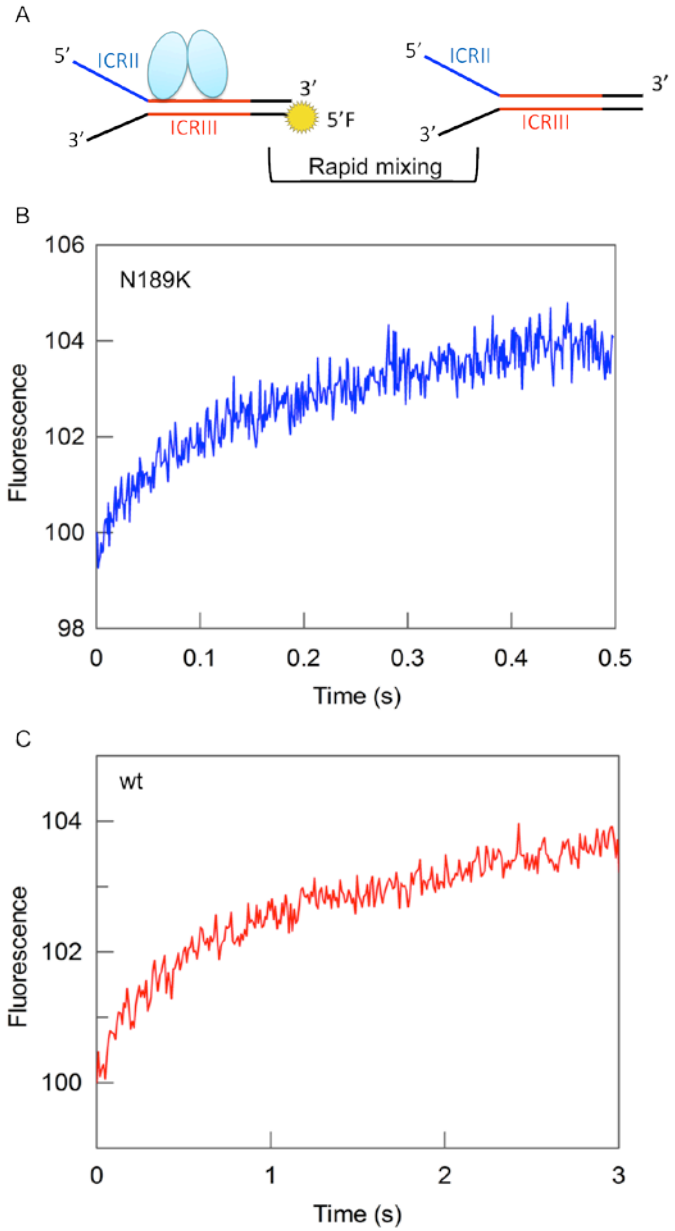

Figure 3.13. RepD dissociation kinetics from a DNA junction. 100 nM junction 1 and 200 nM RepD were rapidly mixed with 10 µM of unlabelled junction as shown in (A). Resulting dissociation traces of N189K RepD (B) and wt RepD (C) are fit to single exponentials giving rates of 1.9 s^{-1}, and 6 s^{-1}. Details of fits and errors can be found in the Appendix of this thesis.

3.4.3. Effect of magnesium on RepD binding kinetics to a partial DNA junction

Association and dissociation experiments were also performed in the absence of Mg^{2+} to evaluate its effect on RepD binding kinetics (Figure 3.14). Fluorescence traces were noisier compared to those observed in the presence

of Mg^{2+}, as shown above (Figure 3.14A). The association rate for wt RepD was 104 $\mu M^{-1}s^{-1}$ and 84 $\mu M^{-1}s^{-1}$ for N189K (Figure 3.14B, D). The k_{off} were 2.3 s^{-1} and 8.8 s^{-1} for wt and N189K, respectively (Figure 3.14C). There was no significant difference in RepD binding kinetics in the presence and the absence of Mg^{2+}.

The measurements of k_{+1} and k_{-1} enabled the calculation of K_d values for the RepD affinity to the junction 1 (equation 6) and are summarised in Table 3.2.

These results indicated that the mutation N189K did not have a dramatic effect on RepD binding activity. However, the K_d values for the mutant RepD were slightly higher than the wild type. Thus, N189K RepD affinity to DNA was reduced by ~ 5-fold. Furthermore, removal of Mg^{2+} that is necessary for RepD catalytic reaction did not have a significant effect on the protein binding kinetics and affinity.

These data are consistent with that obtained from the anisotropy measurements. The differences between wt and N189K binding affinity were confirmed, however more accurate estimates were obtained from the fluorescence intensity experiments.

	Wt RepD (Mg^{2+})	Wt RepD (No Mg^{2+})	N189K RepD (Mg^{2+})	N189K RepD (No Mg^{2+})
k_{on} ($\mu M^{-1}s^{-1}$)	*83 ± 3*	*104 ± 5*	*77 ± 5*	*84 ± 6*
k_{off} (s^{-1})	*1.3 ± 0.2*	*2.3 ± 0.2*	*6.0 ± 0.2*	*8.8 ± 0.3*
K_d (nM)	*15 ± 2*	*22 ± 1*	*78 ± 3*	*104 ± 5*

Table 3.2. RepD binding kinetics and affinity to a partial DNA junction.

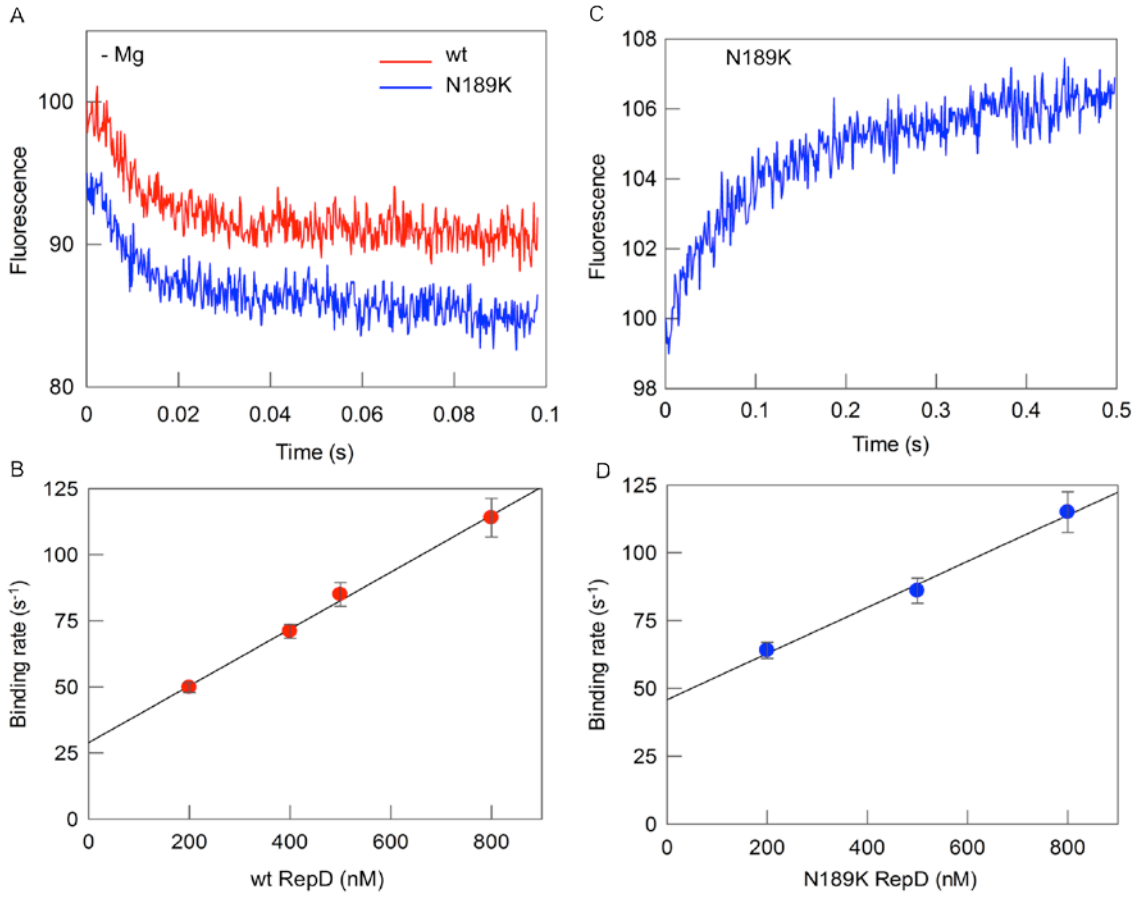

Figure 3.14. RepD binding kinetics to a DNA junction in the absence of Mg^{2+}. (A) Examples of fluorescence intensity traces mixing 500 nM RepD and 100 nM DNA junction 1. Measurements were carried out in K200 buffer without magnesium. Traces are fit to single exponentials. (B) Linear data fitting gives a slope of 104 ± 5 $\mu M^{-1}s^{-1}$ and an intercept of 31 ± 9 s^{-1} for wt RepD. (D) N189K RepD binding to the Y-junction gave a slope of 84 ± 6 $\mu M^{-1}s^{-1}$ and an intercept of 47 ±12 s^{-1} (30 °C). Error bars indicate standard errors from each fit. (C) Dissociation kinetics for N189K RepD. Trace is fitted to a single exponential giving a rate constant of 8.8 s^{-1}. For reactions and conditions see Figure 3.13.

3.5. RepD nicking activity on linear DNA

3.5.1. Kinetics of RepD binding/nicking a partial DNA junction

Additional information on binding and nicking steps can be obtained with anisotropy. Fluorescence anisotropy was used to assess RepD binding and nicking a fluorescein-labeled junction with a rapid mixing experiment using the stopped-flow instrument. The partial DNA junction contained part of the ICRII sequence including the nick site as ssDNA arm, the fluorescein on the 5' end of

this arm, and the ICRIII sequence within the duplex region (junction 2, Figure 2.2).

It has already been shown that the structure of this junction and the fluorescein label location are useful to gain information about RepD binding and nicking [52]. When RepD binds the DNA junction a change in the fluorescence anisotropy is expected as a higher molecular mass complex is formed. Upon RepD binding, nicking on ICRII occurs and the consequent release of the fluorescein with four bases attached causes a decrease in the observed anisotropy (Figure 3.15A).

RepD was mixed with the fluorescein-labelled junction to get a time course of anisotropy (Figure 3.15). As expected, traces were biphasic when mixing wt RepD to the junction and the changes in fluorescence anisotropy were consistent with changes in the molecular mass of the fluorophore. The rapid increase (150 s^{-1}) is followed by a slower phase occurring at a rate of 2.1 s^{-1} which would represent the apparent rate of nicking for this junction. Although this measurement provides a good estimate of the RepD nicking rate, a quantitative analysis of the extent of nicked DNA by RepD cannot be achieved using anisotropy. The RepD mutant trace showed a rapid rise in anisotropy consistent with binding of the junction but no subsequent decrease (Figure 3.15B). The lack of the second phase suggested that the DNA was not nicked and so the fluorescein was not released. The effect of Mg^{2+} on the anisotropy trace was also measured with wt RepD (Figure 3.15C). RepD was mixed with the junction 2 using a Mg^{2+} free buffer, and so nicking was prevented. Under these conditions, the wt RepD trace was qualitatively similar to that of the N189K RepD.

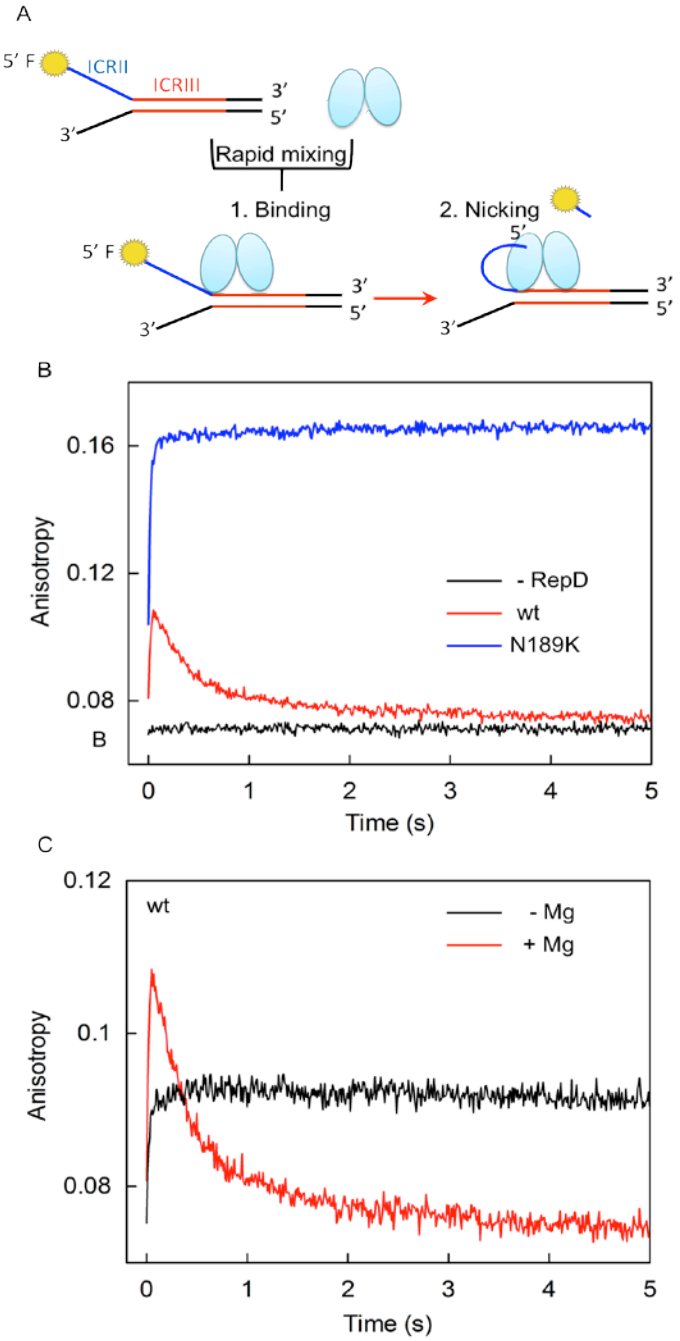

Figure 3.15. Anisotropy time-course following mixing of RepD with a DNA junction. (A) Binding/nicking experiment with RepD. See text for details. (B) Comparison of wt and N189K RepD anisotropy traces. Solutions contained 100 nM of junction 2 (Figure 2.2) and 800 nM RepD (wt or N189K) in K200 buffer at 30 °C. The control without RepD is also shown. (C) Effect of Mg^{2+} on the anisotropy signal. Wt RepD and the junction 1 were mixed as described in B. For the - Mg trace, magnesium was removed from the K200 buffer (in black).

Increasing concentrations of N189K RepD were used in order to measure the association kinetics to the DNA junction 2 (Figure 3.16A), and compare these results with the binding measurements described above. Individual traces were fitted well with single exponentials, and the average rate constants were fit to a linear relationship with the concentration of RepD with the slope giving a second order binding constant of 75 $\mu M^{-1}s^{-1}$ (Figure 3.16B). These results were consistent with the binding kinetics measured with the DNA junction 1 (Figure 3.12).

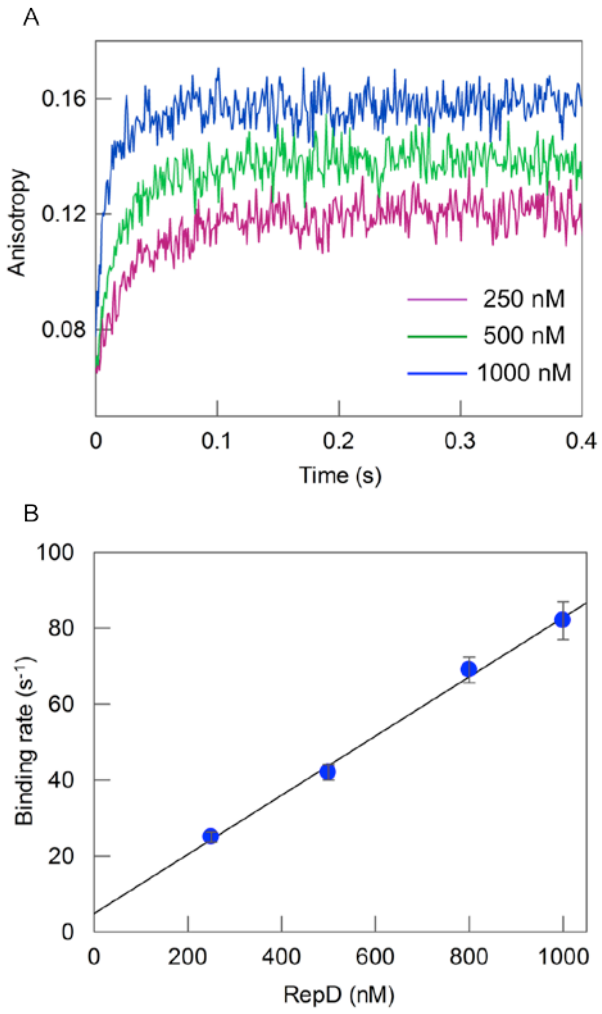

Figure 3.16. Anisotropy time-course following mixing a DNA junction over a range of N189K RepD concentrations. (A) Examples of anisotropy traces at three different concentration of RepD with 100 nM junction 2. Solutions and conditions were as Figure 3.15. Traces were fitted to single exponentials. (B) Linear data fitting gives a slope of 75 ± 4 $\mu M^{-1}s^{-1}$ and intercept of 7.4 ± 2 s^{-1} for the junction 2. Error bars indicate standard errors from each fit. Fits and errors are shown in the Appendix of this thesis.

3.5.2. RepD nicking activity analysis using a gel assay

Anisotropy data indicated that nicking on linear DNA was abolished for N189K RepD. A further analysis of RepD nicking different DNA substrates was performed on SDS-PAGE to confirm the anisotropy results. In this assay, RepD subunits covalently bound to the DNA migrate behind the unbound monomers (cartoons in Figure 3.17). RepD acts as dimer while nicking, however protein denaturation occurred upon incubation with SDS so that just one subunit of the active dimer was attached to the DNA. The separation of the two different subunits was then achieved through electrophoresis allowing separation of the different molecular weights.

A range of different lengths oligonucleotides, including the *oriD* sequence and DNA junctions were used in the assay to assess N189K nicking ability (Figure 3.17). Gel analysis showed that wt RepD was able to nick all the different DNA structure used. The amount of free and bound RepD subunits (%) was calculated from the quantification of the bands (Figure 3.17B). Nicking efficiency of wt RepD in its dimeric active form is between 40% and 70% on the oligonucleotides used. N189K RepD did not show nicking on a variety range of DNA substrates (Figure 3.17A) being 100% inactive on such linear DNA (Figure 3.17B).

These results confirmed the anisotropy measurements and will be further reviewed in the Discussion section.

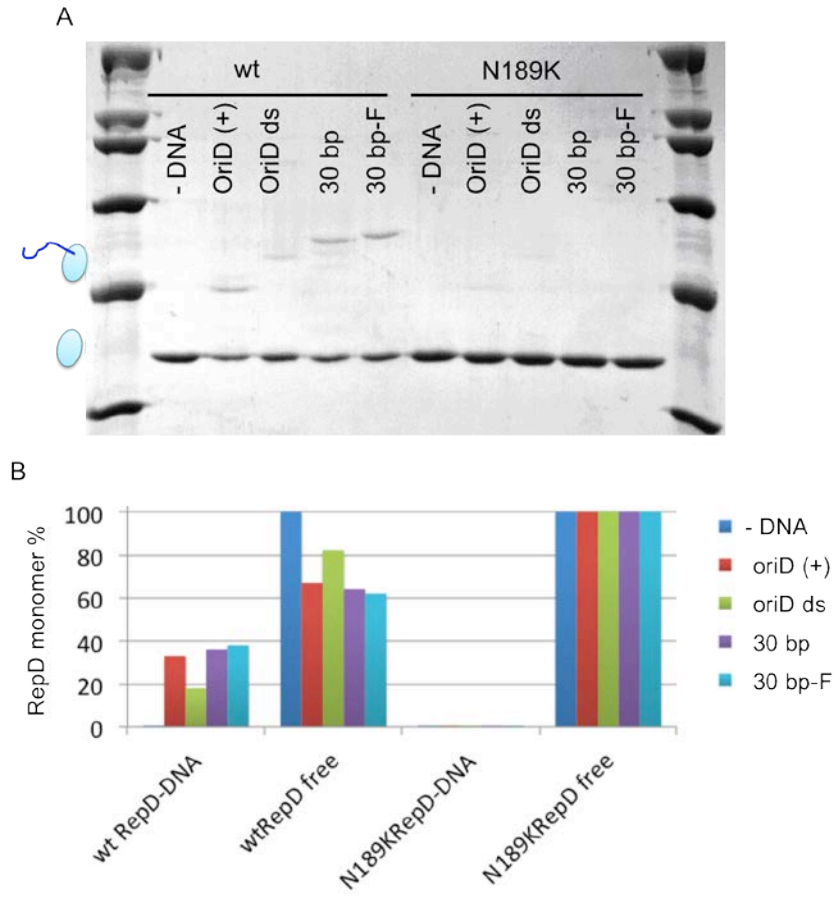

Figure 3.17. RepD nicking different DNA substrates, monitored by SDS-PAGE. (A) SDS-PAGE gel of the nicking reactions done with wt RepD and with N189K RepD. OriD (+) represents the (+) strand of the *oriD* sequence, OriD ds is the double stranded origin made of equimolar OriD-(+) and OriD-(-). "30 bp" and "30 bp–F" are DNA junctions (see Figures 2.2 and 2.4 for DNA sequences). Reactions were incubated at 30 °C for 10 min. Additional details are in Methods. (B) SDS-PAGE analysis by quantification of the bands corresponding to the RepD subunits.

3.6. PcrA-RepD mediated DNA junction unwinding

From an initial characterization of N189K RepD activity presented above, a singular feature of the variant was revealed. Its nicking activity was strictly depending on the presence of supercoiling in DNA substrates and failed on linear DNA. The observation of a different nicking ability of N189K RepD compared to the wild-type protein led to a broader investigation of its function.

As nicking was not observed on linear DNA, its ability to translocate with PcrA on such DNA substrates was monitored using the DNA junction unwinding

assay described in Figure 3.18. Such DNA, in this assay, is labeled with adjacent 5'-Cy3 and 3'-Dabcyl groups away from the initial DNA-protein complex interactions. In the duplex state, the Dabcyl group quenches Cy3 fluorescence. Upon complete duplex unwinding by PcrA-RepD, the Cy3 group dissociates from Dabcyl and a fluorescence intensity increase is observed (Figure 3.18). The DNA junctions contained the right arm of the ICRII sequence for RepD binding, a ssDNA stretch for PcrA binding and then random sequence forming the duplex region to mimic translocation during pseudo-steady-state plasmid unwinding (junctions 20 bp-F, 30 bp-F, and 40 bp-F, Figure 2.2). The use of such junctions to study unwinding kinetics of RepD-PcrA complex was previously described [52]. This system has been shown to provide sufficient signal to measure duplex separation and so helicase unwinding activity. With this assay, it was also demonstrated that PcrA alone is not able to unwind short DNA duplexes and that needs an activator, which is the initiator protein RepD.

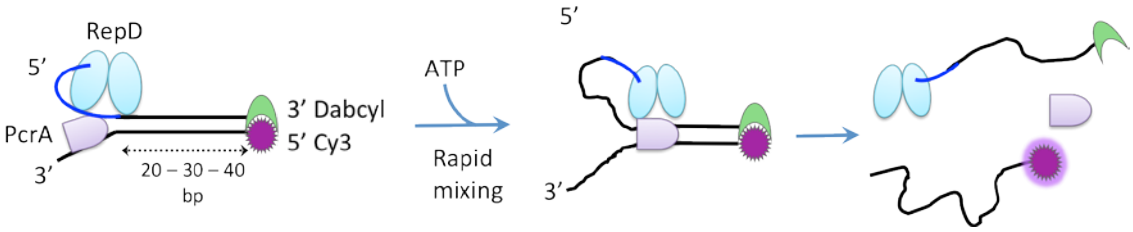

Figure 3.18. Cartoon of the DNA junction unwinding by RepD-PcrA complex. Three different lengths of duplexes (20, 30 and 40 bp) containing the ICRII sequence are used to measure PcrA unwinding kinetics. Cy3 fluorescence is quenched by the Dabcyl group until its dissociation occurs upon unwinding. See text for details.

As described above, the linear plasmids were not unwound by the N189K RepD-PcrA complex. Here, the function of the RepD-PcrA unwinding complex was evaluated on DNA junctions having an opened structure so that a loading site was available for PcrA. The unwinding reaction was monitored in real time by rapid mixing the pre-formed complex RepD-DNA.PcrA with ATP using a stopped-flow apparatus, as shown in Figure 3.18. The DNA-RepD complex was assembled with either wt or N189K protein. In this assay, an excess of RepD

was used over the DNA to allow full loading of RepD on the DNA, and then the Rep-DNA complex was in excess of PcrA. Under these conditions, it is likely that the majority of DNA will have only one PcrA molecule bound. Mixing with ATP caused an increase in fluorescence signal due to unwinding and release of the Cy3-group (Figure 3.19). Qualitatively, fluorescence traces of N189K RepD-PcrA complex were similar to that observed with wt RepD indicating that N189K supported unwinding of linear DNA junctions. An initial lag phase was followed by an increase in the fluorescence intensity. The rise in fluorescence was consistent with DNA unwinding (Figure 3.19A). There was a further increase in fluorescence that occurred at a slower rate that is likely to be caused by PcrA dissociating and then binding and unwinding other RepD-DNA complexes, which are present in solution in steady state conditions.

The duration of the lag phase represents the time required by PcrA to fully unwind the DNA junction (Figure 3.19A). This time increased with the duplex length and using different length of DNA duplexes allowed the calculation of an average of the unwinding rate (Figure 3.19B). The latter is given by the slope of the linear fit from the plot of the lag phase time in function of DNA lengths (Figure 3.19C). The amplitude of the traces varied between the different length junctions, and such a difference may be caused by the excess of Dabcyl oligonucleotide in the DNA solution which can be a potential binding substrate for PcrA. This results in less helicase available for the RepD-DNA complexes. However, a direct comparison cannot be easily made as differences may intrinsically arise from small errors in DNA stock concentrations.

For N189K RepD-PcrA complex unwinding occurred at a rate of 47 bp s^{-1}, similar to that of wt RepD-PcrA complex, 54 bp s^{-1}, measured here and in a previous study (Figure 3.19C, Slatter et al). These data indicated that N189K RepD efficiently activated PcrA helicase in a similar way of wt RepD and that loss of nicking on these substrates does not have significant effects on its ability to efficiently translocate with PcrA during unwinding.

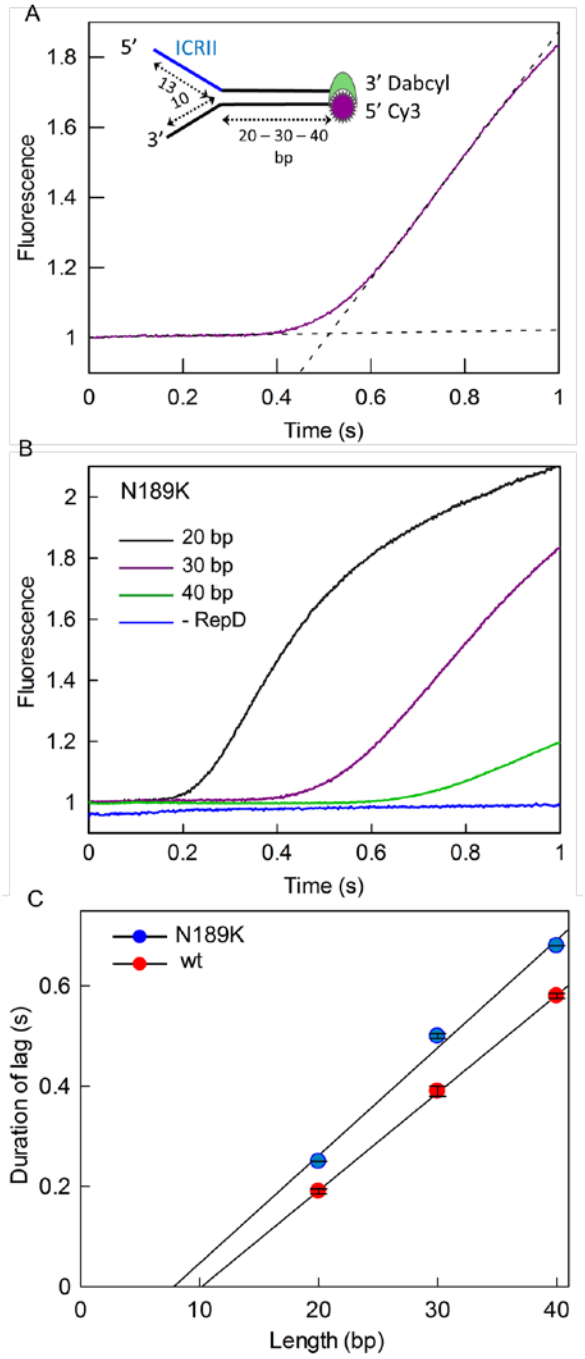

Figure 3.19. Unwinding kinetics of different length DNA junctions by RepD-PcrA complex. (A) Example of fluorescence trace for the 20 bp-F junction, showing the linear fits used to measure the duration of lag. (B) N189K RepD-PcrA mediated unwinding of three different lengths of DNA junctions. Traces were normalized to 1. 500 nM of junction, 100 nM PcrA, and 2.5 μM RepD were rapidly mixed with 200 μM ATP at 30 °C, in K200 buffer. The control reaction without RepD is also shown. (C) Dependence of the lag time on DNA lengths. The slope of the linear fit gives a rate of unwinding of 47 ± 4 bp s^{-1} for N189K RepD-PcrA and 54 ± 9 bp s^{-1} for wt RepD-PcrA complex. Error bars indicate standard deviation among two independent experiments. Fits and errors are in the Appendix of this thesis.

3.7. The PcrA-RepD translocation complex

The functional studies previously described in this chapter using a fluorescent approach and gel assays have shown that N189K is not able to nick linear DNA but can promote unwinding by PcrA of such substrates. This suggested that nicking *per se* was not needed for functional translocation. In order to confirm this hypothesis, the unwinding kinetics were further monitored here under conditions where nicking was prevented.

One approach to limit nicking is to design mutations in the ICRII region that could abolish the cleavage reaction but preserve protein binding. Two main strategies were taken. One mutation deleted the 5′-side of the nicking site by removing 1-3 positions on the right arm of ICRII so that there is no phosphodiester in the correct position for transesterification by RepD. The others consisted in substitution of the adenine base involved in the covalent attachment with RepD. The activity of the RepD and the function of RepD-PcrA complex were investigated on such mutated DNA.

The first set of experiments established the ability of wt RepD to nick short ICRII-mutated oligonucleotides (ICRII-A>T, A>C, ΔCTA, Figure 2.4 for sequences). Incubation of wt RepD with all mutated ICRII sequences showed loss of DNA nicking from an SDS-page gel analysis (Figure 3.20B). With this assay, binding could not be discriminated as it is performed in denaturating conditions. However, binding was assessed through a gel shift assay. In the latter, the DNA and the DNA-protein complex run differently on a gel according to their molecular weights in nondenaturating conditions. An excess of RepD was incubated with the DNA junctions containing the ICRII mutations (20bp-ICRII-A>T, 20-bp-ICRII-ΔCTA, Figure 2.2), and the formed DNA-RepD complex was detected on the gel (Figure 3.20A). These results indicated that despite the lack of nicking caused by modifications in the ICRII sequence, protein binding was still preserved on such DNA.

The ability to form a functional translocating complex by RepD-PcrA was then investigated on these mutated ICRII DNA junctions (Figure 3.21). This experiment is based on the Cy3-Dabcyl assay described above (Figure 3.18). As described for the gel shift assay above, the partial DNA junctions contained

either the ΔCTA deletion or the substitution A>T (20bp-ICRII-A>T, 20-bp-ICRII-ΔCTA, Figure 2.2). Qualitatively, the unwinding traces for both DNA junctions were similar to those obtained with the wt ICRII sequence, a lag phase followed by a fluorescence increase consistent with PcrA unwinding. These data supported the idea that the nicking activity and the translocation activity are separate and a complete active translocation complex is possible in the absence of DNA nicking.

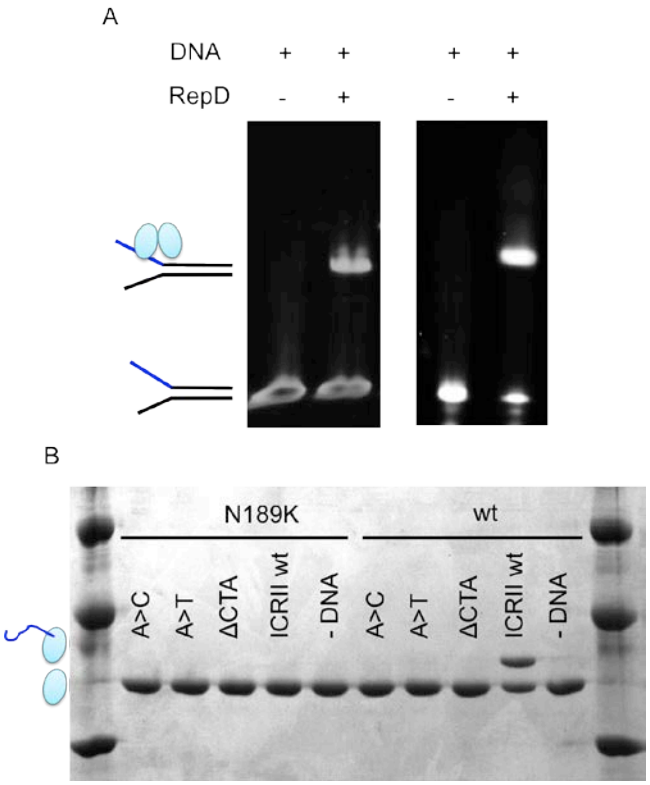

Figure 3.20. RepD binding and nicking activities on ICRII mutated DNA. (A) Gel shift analysis of RepD binding ICRII-mutated DNA junctions. Solutions contained 1 μM of DNA (20bp-ICRII-A>T on the left, and 20-bp-ICRII-ΔCTA on the right) +/- 1 μM wt RepD, as indicated. (B) SDS-PAGE gel analysis of the nicking reaction following incubation of RepD with a range of ICRII oligonucleotides (see Figure 2.4 for sequences). The control without DNA is also shown (- DNA). Reactions and conditions were as in Figure 3.17. Cartoons on the left side of the gels represent the molecular interactions corresponding to the relative bands. Details on the gel assays can be found in Methods.

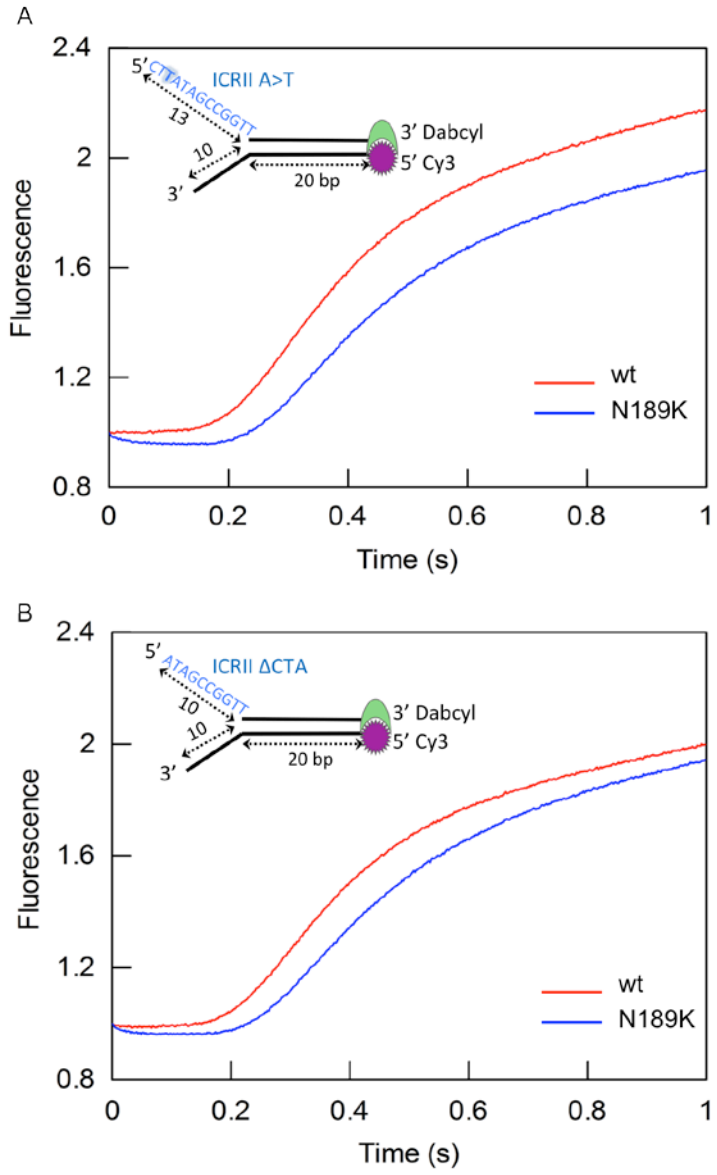

Figure 3.21. Unwinding of ICRII mutated DNA junctions by RepD-PcrA complex monitored in real time by Cy3 fluorescence. (A) Unwinding of 20bp-ICRII-A>T junction and (B) 20bp-ICRII-ΔCTA junction. Reactions, conditions and analysis are as Figure 3.19. The DNA junctions with the mutated ICRII sequence are schematically shown in the insets.

3.8. Discussion

3.8.1. Formation of the initiation complex

The work described in this chapter, addresses the factors that are involved in ensuring that RepD successfully initiates plasmid replication. In particular, this was achieved by examining the kinetics of the nicking reaction and how this is related to subsequent unwinding. The investigation of RepD function is also extended with the use of the active N189K RepD variant.

Inverted complementary repeats are essential both for RepD recognition and for formation of the initiation complex [16, 17]. These elements were introduced into DNA junctions that were prepared from oligonucleotides and used in several biochemical assays. In particular, real-time measurements of nicking kinetics show how features of the DNA are important for different steps of formation of the initiation complex. In addition, some measurements were taken on the whole plasmid using discontinuous real-time assays, for example, using the quench-flow technique.

The initiation events involving the formation of the RepD-DNA complex can be described considering elementary chemical steps by the simplified scheme:

Scheme 2:

$$\text{RepD} + \text{A-B} \underset{k_{-1}}{\overset{k_{+1}}{\rightleftharpoons}} \text{RepD.A-B} \underset{k_{+2}}{\overset{k_{+2}}{\rightleftharpoons}} \text{A.RepD-B} \underset{k_{-3}}{\overset{k_{+3}}{\rightleftharpoons}} \text{A} + \text{RepD-B}$$

In Scheme 2, the DNA is shown as A-B with A being the 3'-end and B the 5'-end of the DNA nick site. Steps are shown with the relative rate constants of the forward and reverse reaction. RepD binding (step 1) is followed by the chemical step 2. The rapid nicking results in the covalent attachment of the protein to the 5'-end of the cleaved DNA. This is an intermediate shown as a non-covalent complex between the RepD–DNA complex and the nicked DNA. There may be interactions of RepD with the nicked DNA as well as potential remnant base

pairing of the nicked DNA with the covalently bound part of ICRII. Finally, in step 3, the 3′-end of the nicked DNA dissociates to provide the structure with a stretch of ssDNA to which PcrA binds. This dissociation could be complete separation in the case of some oligonucleotide junctions, or just removal from the RepD binding site in the case with the complete *ori*D. Apart from inhomogeneities that may occur in any biochemical reactions, such as partially damaged proteins, further inhomogeneity could arise in this type of reaction because DNA with inverted complementary repeats might take up various structures, particularly hairpins. Such inhomogeneity could add to the complexity of the measured kinetic transients.

The binding kinetics of RepD that were measured by fluorescence intensity (Figure 3.12) depend largely on the presence of ICRIII and vary little with the structure of the neighboring ICRII sequence. This binding (k_{+1}) is fairly rapid 83 $\mu M^{-1}s^{-1}$ (Table 3.2), and it is also independent of whether subsequent nicking occurs on the junction, as shown using N189K RepD (with a value of 77 $\mu M^{-1}s^{-1}$). Nicking on ICRII then follows the binding step. The extent of nicking reaction was almost quantitative when a single-stranded ICRII is used as substrate, either as a ssDNA oligonucleotide or as part of a DNA junction (Figures 3.17). Note that only one RepD subunit becomes covalently linked via its active site tyrosine to the 5′-end of the DNA. The nicking kinetics with such DNA were not measured, but the reaction with a fluorescein-labelled DNA junction (junction 2) indicates that single-stranded ICRII is nicked slowly (~2 s^{-1}, Figure 3.15). In this case, it is likely that nicking is followed by rapid dissociation of the small DNA product (step 3, Scheme 2).

The direct measurement of nicking kinetics, using quench flow, suggests that both thermodynamic equilibria and kinetics play a part in the observed time courses (Figure 3.4). The nicking kinetics of the whole plasmid are complex because of the slow release of the nicked DNA end from RepD and reversibility of the nicking step. The plasmid nicking kinetics are multiphasic, and show a rapid phase (k_{+2}: >25 s^{-1}) with a 35% amplitude followed by a slow phase (k_{+3}: ~2.5 s^{-1}, Figure 3.4). Gel analysis of plasmid nicking on a longer time scale shows the slow religation of the DNA to give a relaxed, closed plasmid at an observed rate constant of 0.0037 s^{-1} with an equilibrium constant of 0.3 (Figure

3.3). It seems likely that RepD remains bound to the relaxed, closed plasmid, based on the dissociation constant of RepD from the DNA junction, so this is a direct measurement of the equilibrium constant for the nicking reaction.

The nicking reaction is formation and breakdown of a phosphodiester bond, and this equilibrium might be expected in the absence of other factors to be close to unity. Both the free energy of supercoiling in the intact plasmid and RepD binding could drive the formation of the cruciform extrusion of palindromic sequences contained within *ori*D [15, 16, 104].

The formation of the cruciform has been shown to be dependent on superhelicity, as the torsional stress of supercoiling leads to a decrease in the activation energy of the reaction, followed by conformational changes in DNA structure that favor the formation of cruciform structures. In the absence of enzymes, this occurs only very slowly, even when thermodynamically favored [105]. However, RepD might enhance and stabilize the extrusion on the supercoiled plasmid through binding on supercoiled but not linear DNA. This then exposes the nick site as a single-stranded loop as the target site for RepD nicking activity. Supercoiling could also be the cause of a larger k_{+3}, thereby shifting the equilibrium toward “product release” by physically separating the 3′-end of the nicked DNA from the RepD active site resulting in the high extent of product formation. In this model, the supercoiling has little effect on step 2 (Scheme 2).

3.8.2. The activity of N189K RepD

The site-specific nick results in a phosphodiester bond at Tyr188 [25]. N189K RepD activity was examined for its ability to nick DNA and support unwinding by PcrA. Position 189 is likely to be within the active site of RepD and as described above, its mutation has some effects on the protein functionality.

Firstly, the mutation affects RepD ability to nick linear DNA (Figures 3.17, 3.15). A range of linear constructs containing ICRIII and the nicking site were not substrates for this mutant (Figure 3.17). Secondly, nicking kinetics on a supercoiled plasmid were affected as this occurred at a rate 3 orders of magnitude slower than that of wt RepD (Figure 3.5). However, only the supercoiled plasmid showed significant nicking (Figures 3.5, 3.17). This again

illustrates the importance of supercoiling in driving the nicking to completion. The combined wild type data with the mutant RepD suggest that K_2 and k_{+2} (Scheme 2) are greatly reduced by the mutation. Only the effect of supercoiling is driving the reaction to completion.

As conformational changes in the DNA–RepD complex are essential for nicking, it is possible that mutation N189 might reduce bending activity. One interpretation of such results is that the RepD mutant could not efficiently enhance the secondary structure causing a very slow nicking reaction for supercoiled plasmid and an absent nicking for linear DNA.

A similar situation was reported previously for the RepC protein, a RepD homologue that acts on the *ori*C. The heterodimer, RepC·RepC–oligonucleotide, in which one subunit has a short oligonucleotide bound to its tyrosine, is able to bind but not to induce melting of *ori*C [32]. Thus, this could also be the case of N189K RepD. However, this cannot be the complete effect, as the mutation reduces the rate of nicking of supercoiled substrates, suggesting that either the DNA at the nick site cannot assume the correct conformation or the nicking itself is impaired.

According to the lack of nicking of linear substrates, linearized plasmids DNA did not support PcrA-mediated unwinding (Figure 3.10). However, unwinding was successful on short DNA junction containing ssDNA tail for PcrA loading (Figure 3.19). On such DNA structures nicking is not needed to open up a short stretch for the helicase binding, and so unwinding can be effectively performed. These data indicated that, despite nicking, N189K is able to form a functional unwinding complex and this activity does not depend on the DNA structures.

3.8.3. The effect of divalent ions on RepD activity

The nicking reaction performed by RepD consists in a transesterification in which Mg^{2+} plays an essential role. Binding to the DNA is not affected by the removal of this ion from the reaction. The absence of Mg^{2+} has not a significant effect on DNA binding kinetics and affinity (Figure 3.14). The requirement of Mg^{2+} is for catalysis (Figures 3.3, 3.6, 3.15). A titration of Mg^{2+} in a RepD-DNA solution shows complete plasmid nicking at a concentration of ~1 mM (Figure 3.6). The high affinity for Mg^{2+} is translated in ~60% of cleaved DNA at a

concentration of only ~100 nM Mg^{2+}. For N189K RepD almost complete nicking is reached at 10 mM Mg^{2+} (Figure 3.6). However, a single time point was performed in such measurements, and it is likely that nicking is slower at lower Mg^{2+} concentrations.

The lower affinity to the ion compared to the wild type protein might be due to a different ability of the mutant to interact with the positively charged cofactor. The N189K mutation introduces a positive charge in the active site of RepD and might weaken this binding. In addition, substitution of Mg^{2+} with other divalent cations such as Mn^{2+} and Ca^{2+} has a significant effect on DNA relaxation. In particular, Ca^{2+} did not support DNA cleavage for N189K RepD (Figure 3.6). One possibility of this effect is the difference in their ionic radius, confirming the importance of the interactions between the cofactors and RepD during catalysis.

These results would suggest a functional role of Mg^{2+} in binding the protein active site that possibly induces the conformational change required for catalysis and DNA relaxation. However, currently there is no crystal structure of RepD and so no available information of the specific contacts between RepD-metal-DNA as well as the metal ion:enzyme stoichiometry. Also there is a lack of mechanistic details of the reaction and the specific roles of the ion during conformational changes and cleaving.

3.8.4. Functionality of the unwinding complex

RepD is essential for the initiation of asymmetric, rolling circle replication of plasmids containing the DSO, *ori*D. In this work, most of the data relate to the interaction of RepD with DNA, although there is also information about how such interaction affects the PcrA-driven unwinding.

The ability to form a functional PcrA-RepD unwinding complex was investigated on supercoiled and linear DNA substrates. The data do not address directly the interactions of PcrA with RepD, although this remains an unclear aspect of RepD. Because of this, it remains valid to use *B. stearothermophilus* PcrA, although the RepD is from *S. aureus*. This PcrA allows comparison of unwinding with different RepD variants and different DNA constructs, even though it is possible that precise protein–protein interactions are not completely optimal.

The study of the N189K RepD activity led to the observation that DNA structures that had a ssDNA region in the appropriate place for PcrA binding were unwound with little or no modification of kinetics (Figure 3.19). Supercoiled plasmids were suitable substrates for nicking and so were unwound with kinetics very similar to those of wt RepD (Figure 3.8). Linearized plasmid DNA structures that did not provide a site for PcrA to bind, were not nicked by N189K RepD and also not unwound (Figure 3.10). Thus, loss of supercoiling in such DNA affects nicking and consequently unwinding.

The use of linear DNA junction with an opened structure containing most of the ICRII for RepD binding and a ssDNA tail for PcrA loading would overcome the need of nicking to make the DNA accessible to PcrA. These DNA were unwound with similar kinetics to the wt RepD (Figure 3.19). This was suggesting that the function of nicking was not required for unwinding.

Complementary data were obtained by introducing mutations into ICRII to prevent nicking. Again, when there is a site for PcrA and RepD (wt or N189K) to bind, then the DNA is unwound approximately as with unimpaired ICRII (Figures 3.20, 3.21). The nicking activity *per se* and the presence of the covalent DNA bonding with RepD are not essential for the role of RepD in enhancing PcrA processivity in DNA unwinding (Figure 3.21).

Acknowledging the above, the separate functions of RepD in plasmid replication will be further discussed in Chapter 6.

3.9. Summary

In summary, detailed examination of the kinetics of RepD binding and nicking for a variety of DNA structures has shown that, while binding is usually rapid, the nicking rate constant is very dependent on the way in which the nicking site is presented. Although the equilibrium constant for the nicking is close to unity, supercoiling favors product formation and increases the overall rate of nicking. The activity of the mutant N189K was investigated here and a direct comparison with wt RepD was made. In particular, mutation N189K had two main consequences on RepD function. The nicking/closing kinetics were slower and nicking was impaired with the supercoiled DNA being the only substrate for

RepD. The use of different divalent ions showed a different preference between the ions suggesting active roles of such ions in protein interaction.

Interestingly, the separation of nicking function of RepD from its role in assisting strand separation is clearly demonstrated by the measurement of translocation rates in situations where nicking does not occur. However, it is intriguing that RepD can increase the processivity of PcrA during unwinding, so it presumably must maintain interaction with the PcrA·DNA junction throughout. The fact that covalent attachment of DNA to RepD is not apparently essential means that this factor is not crucial in maintaining RepD at the junction. Furthermore, once unwinding is underway, RepD cannot be in contact with its tight-binding ICRIII site. The interactions of RepD with DNA and PcrA during unwinding remain to be elucidated as well as factors that maintain tight interaction of RepD with DNA once unwinding has progressed beyond ICRIII.

4. DNA Polymerase III Function During Plasmid Replication

4.1. Introduction

Staphylococcal pC221 plasmid replication is a complex process that requires the coordination of the replicative proteins, which are the initiator protein RepD, the helicase PcrA, and the DNA polymerase III. The individual activities of these proteins have to be timely and orderly synchronized in order to succeed in each biochemical stages of initiation, elongation and termination of a successful replication event. It is important to elucidate the mechanism and dynamics of DNA synthesis and unwinding in order to understand how closely the replicative enzymes work in a plasmid replication system.

The molecular details of initiation involving RepD and its cognate *oriD* are described in Chapter 3 with particular emphasis on the initiator binding and nicking activity, and its function of forming the translocation complex with PcrA helicase. Following initiation of replication, the elongation process begins with unwinding of the dsDNA by PcrA and DNA synthesis by the DNA polymerase III starting from the 3′ of the nicked DNA generated by RepD. The polymerase follows the helicase using the unwound (-)-strand as template for the synthesis of the (+) strand and incorporation of nucleotides occurs in the same direction of the helicase unwinding (3’ > 5’ direction) [10].

In this chapter, the activity of the replicative subunit (α) of the DNA polymerase III from *S. aureus,* known as PolC, is presented and its effect in modulating PcrA kinetics during plasmid replication is studied using a variety of biochemical assays.

The investigation starts with a general PolC characterization. In particular, the early binding events occuring before DNA polymerization are investigated using a fluorescence-based approach. Rapid-mixing experiments were designed to study the kinetics of DNA and nucleotide binding. In such experiments, fluorescent probes are ideally suited to report changes in their environment that result in complex formation or subsequent conformational changes upon binding. The fluorescent reporter, Cy3, was attached on the DNA template, to the 5’-end of the ssDNA tail to measure the PolC binding kinetics to the DNA template. Association and dissociation kinetics to a fluorescently

labelled nucleotide were also determined to further investigate PolC binding activity.

In addition to the pre-chemistry studies, steady-state measurements were performed on a primed DNA in order to measure the rate of DNA extension with a fluorescence-based assay, using the MDCC-PBP biosensor. This assay allows the determination of the k_{cat} and K_M parameters for dNTPs. Steady-state measurements can also be useful to measure the k_{cat}/K_M ratio which estimates the specificity for each substrate.

PolC activity was subsequently investigated in the plasmid replication process. The information provided by the initial PolC characterization were useful to generate optimal conditions in a more complex assay involving a set of proteins used to generate the complete replication system.

Here, PolC effect on PcrA helicase activity was measured in the presence of the initiator protein RepD. There have been several studies demonstrating that the replicative helicases can work closely to the DNA polymerases and the other components of the replisome and their coordination generally modulate the unwiding or the synthesis kinetics of one of the enzymes.

Studies of the monomeric PcrA helicase in the recent years have provided deeper insights into the mechanisms of unwinding as well as in determining its unwinding kinetics. Biochemical studies have also shown that PcrA requires its partner RepD for processive unwinding [52]. Here, the study of the helicase activity was extended with measurements of PcrA unwinding kinetics in the presence of PolC.

Measurements of the activity of the helicase in a complete replicating system define more precisely their mechanisms and provide new insights into the complete replication process by revealing potential physical and/or functional couplings between motor proteins.

4.2. DNA polymerase binding activity to DNA

The first high-resolution crystal structure of a replicative DNA from a Gram-positive bacterium was recently resolved (see also the Introduction of this thesis). This is the DNA polymerase III from the *G. kaustophilus* organism [62].

The structure of the PolC bound to a primed DNA shows the residues and the protein domains involved in the DNA interaction. PolC interacts extensively with the DNA substrate further away from the active site making contacts with the duplex at -8 from the template base and reaching the +13 position from the nascent base in the ssDNA tail.

This structural information was used to design potential DNA substrates for PolC. Partial DNA duplexes were made by annealing of two different lenght oligonucleotides to create a DNA template structure. The final product was a DNA with a free 3'-OH available for PolC activity (Figure 2.3). The use of such synthetic primed junctions allowed the analysis of protein activities such as binding and catalysis.

4.2.1. DNA Polymerase binding activity to a partial DNA junction

Firstly, PolC binding to a partial DNA junction (junction 4, Figure 2.3) was assessed through a gel shift assay (Figure 4.1). In this assay, the binding of PolC to the DNA is monitored on a gel under nondenaturating conditions. Increasing concentrations of PolC were incubated with the DNA and a faint, single-shifted band was detected, indicating binding. The retarded band was not detected in the absence of protein (Figure 4.1A). The appearing of the band was consistent with the formation of PolC-DNA complex of a higher molecular weight compared to the unbound DNA molecule.

The DNA binding was also investigated incubating the complex in the absence of the divalent ion (Figure 4.1B). This experiment showed similar results to the reaction containing Mg^{2+}. However, it should be noted that the electrophoresis buffer contained EDTA, which can bind the Mg^{2+} upon sample loading. This adds difficulties in the interpretation of the results obtained from the reactions prepared with 10 mM $MgCl_2$ (Figure 4.1A). For these reasons, the effect of Mg^{2+} on DNA binding could not be investigated under these conditions. The increasing PolC concentrations generated different ionic strength conditions between the binding reactions, which in turn caused a slightly different migration of each sample on the gel. Such an effect was more evident when samples were prepared in the presence of 10 mM Mg^{2+} (Figure 4.1A), as

a result of an increased ionic strength. The low intensity of the bands corresponding to the DNA-protein complex indicated that PolC binding to the partial DNA junction occured with a relatively low affinity. Such a value could not be estimated with this assay due to the sensitivity of this approach and the need of high concentrations of PolC. However, this could be addressed with binding kinetics measurements (section 4.2.2).

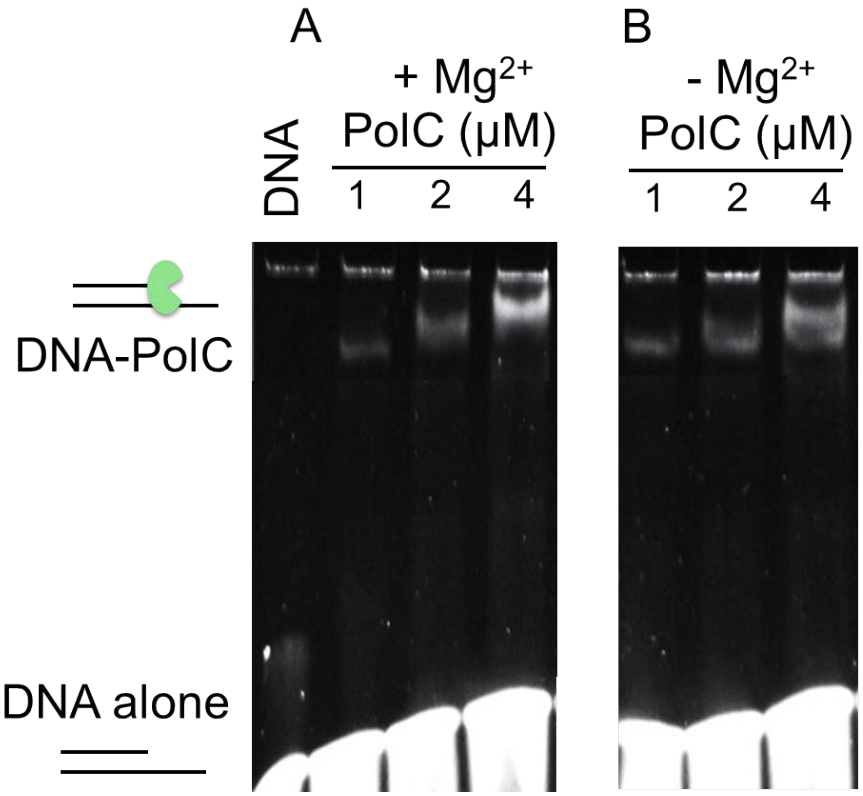

Figure 4.1. Gel mobility shift assay of PolC binding to a partial DNA junction. 15μL of binding reactions contained 1 μM of DNA junction 4 and increasing concentrations of PolC, in K100 buffer +/- 10 mM $MgCl_2$ (as indicated). Reactants were incubated for 5 minutes at 4 °C. Solutions were ran on 6% native polyacrilamide gels. Detection of the bands was achieved with SYBR-gold staining. A new band appears, of higher molecular weight, when PolC interacted with the DNA template. However, the effect of Mg on binding could not be clarified because the samples were run in a EDTA containing buffer (TBE buffer), and so the reaction conditions change drammatically upon sample loading.

4.2.2. DNA polymerase association kinetics to a partial DNA junction

A more sensitive approach to investigate binding was taken using fluorescently labelled DNA. A Cy3 probe was attached at the 5' terminal end of a template strand, away from the free 3'-OH (junction 3, Figure 2.3). An initial assessment of binding was perfomed with the gel shift shown in Figure 4.1 showing that the partial DNA junction would potentially be a good substrate to investigate the PolC binding kinetics.

The association kinetics were investigated by rapid-mixing experiments, monitoring in real-time the fluorescence intensity produced by the Cy3 labelled DNA in a stopped-flow apparatus (Figure 4.2A). Using a single step binding model as in Scheme 3, the observed rate constants (k_{obs}) is given by equation (8), with the second order rate constant (k_{+1}), and the first order rate constant (k_{-1}) representing effective 'on' and 'off' rates for Polymerase (Pol) binding under pseudo first order conditions:

Scheme 3:

$$\text{Pol} + \text{DNA} \underset{k_{-1}}{\overset{k_{+1}}{\rightleftharpoons}} \text{Pol.DNA}$$

(8) $$k_{obs} = k_{+1}[\text{Pol}] + k_{-1}$$

An initial experiment was carried out using an excess of PolC over the DNA junction 3 (Figure 4.2A). Upon mixing, a rapid increase in the fluorescence intensity was detected on a millisecond time scale. This phase is likely to represent protein binding as the observed rate constants increased with the PolC concentration. The fluorescence rise was particularly fast at high PolC concentrations and the amplitudes of traces linearly increased with the protein concentration (Figure 4.2C). Fluorescence traces were fitted to single exponentials, and the resulting k_{obs} are shown in function of the PolC

concentration. The linear fit gave a value of the second order rate constant (k_{+1}) of 118 $\mu M^{-1}s^{-1}$ and an intercept of 37 s^{-1} (k_{-1}) (Figure 4.2B).

The measurements of the k_{-1} and k_{+1} values allowed the calculation of the K_d (using equation 6, Chapter 3). Such value was 313 nM for junction 3.

The effects of Mg^{2+} and the dNTPs on DNA binding were also investigated. Firstly, an excess of PolC was rapidly mixed with the DNA junction in a free-Mg^{2+} solution (Figure 4.3A). Similarly to the Mg^{2+} containing reaction, the rapid fluorescence increase is observed occuring at a similar rate. These results indicated that removal of the divalent ion from the reaction had no significant effect on DNA binding, consistent with the DNA binding analysis performed on the gel shift assay (Figure 4.1). On a longer time scale, the fluorescence traces showed a slow decrease occuring with a rate of 1 s^{-1}. Such phase was independent on PolC concentrations (data not shown), and was not detected for the free Mg^{2+} reaction (Figure 4.3B).

In a similar experiment, an excess of PolC was rapidly mixed with a solution containing the Cy3 labelled DNA and dNTPs in presence of Mg^{2+} (Figure 4.3B). Under these conditions, the increase in fluorescence was replaced by a more rapid decrease in signal with an amplitude of around 50% occuring at a rate of ~ 3 s^{-1}. The slow decreasing phase might be interpretated as possible interaction with the Cy3 probe as result of PolC catalytic-induced conformational changes.

4.2.3. DNA polymerases dissociation kinetics to a partial DNA junction

In order to measure the affinity of PolC to the DNA, the PolC dissociation kinetics (k_{-1}) from the DNA junction 3 (Figure 2.3) were determined more accurately from the displacement assay performed using a stopped-flow apparatus. In this assay, the polymerase was loaded on the primed DNA and then rapidly mixed with high concentration of unlabelled DNA (Figure 4.4A).

Dissociation was detected as a decrease in the fluorescence intensity (Figure 4.4B). As expected, this phase anticorrelates with the fluorescence signal obtained from the association experiments (Figure 4.2). The fluorescence trace generated was fitted to a single exponential, giving a k_{-1} of 10 s^{-1} for PolC. The

observed rates were not dependent on the unlabelled DNA concentration (Figure 4.4C).

From the measurements of the k_{+1} and k_{-1} and using the equation 6, the PolC K_d value for the junction 3 was 83 nM.

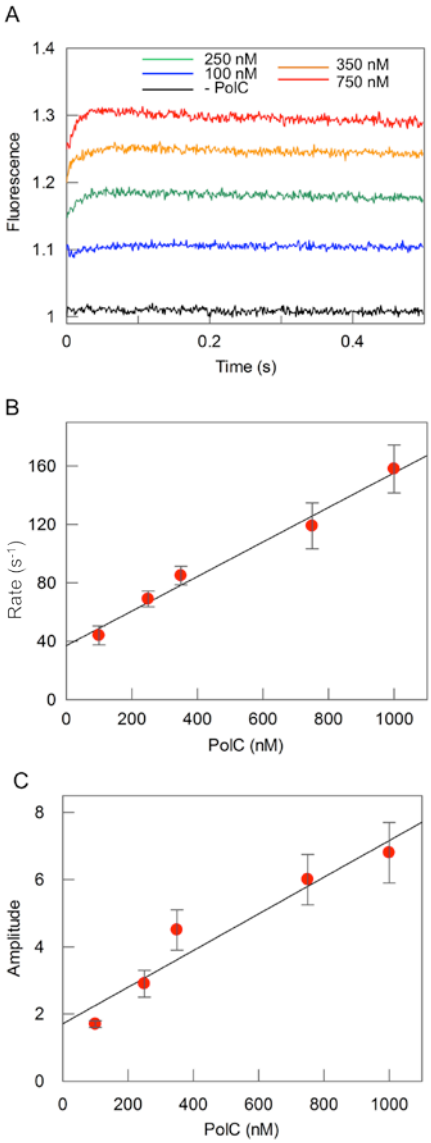

Figure 4.2. PolC association kinetics to a partial DNA junction. (A) Examples of fluorescence intensity traces from rapid mixing in a stopped-flow apparatus the junction 3 (50 nM) with a range of PolC concentration (as indicated) in K100 buffer. Fluorescence traces (shown offset for clarity) were fitted to single exponentials. (B) Dependence of the observed rate constants on the polymerase concentration. The linear fit gives a slope of 118 ± 8 (S. e.) $\mu M^{-1}s^{-1}$ and an intercept of 37 s^{-1}. Error bars indicate standard errors from each fit. (C) Amplitudes of the fluorescence traces. Error bars indicate standard deviations from independent experiments. Details of fitting and errors are shown in the Appendix of this thesis.

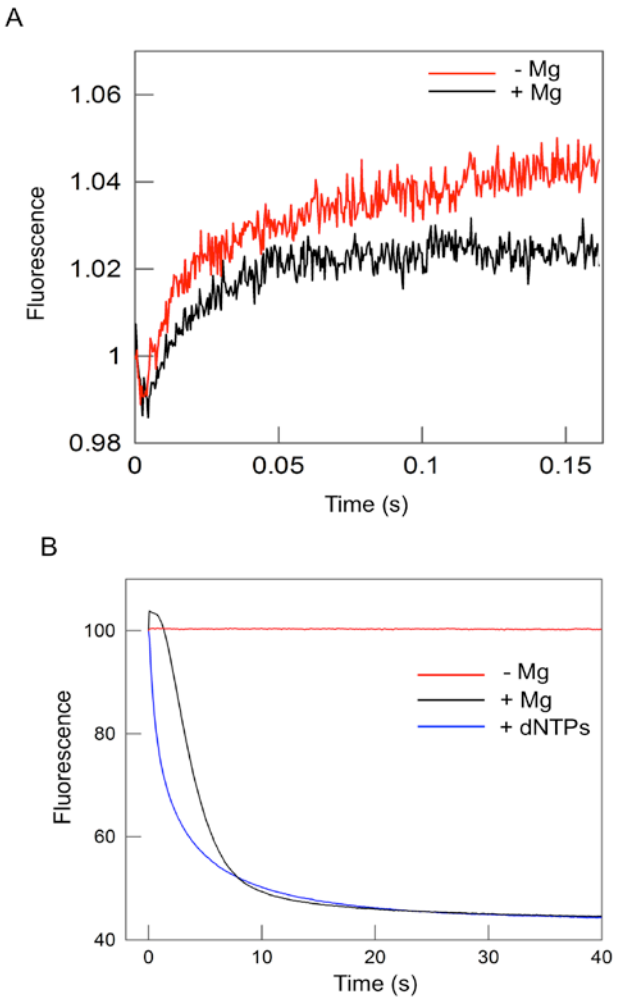

Figure 4.3. Fluorescence traces upon mixing PolC with a partial DNA junction. The DNA junction 3 (50 nM) was mixed with 250 nM PolC in the stopped-flow apparatus in the same condition as Figure 4.2. (A) Effect of Mg^{2+} on the PolC binding (0.5 s. trace). Traces were fit to single exponentials giving rates of 52 s^{-1} (for the + Mg trace) and 54 s^{-1} (for the - Mg trace). (B) Effect of Mg^{2+} and dNTPs on the binding reaction monitored on a longer time scale. Reaction conditions for black and red traces were as in (A). The blue trace contained 1 mM dNTPs. The decreasing phases were fit to single exponentials giving rates of 1 s^{-1} (black) and 3 s^{-1} (blue trace).

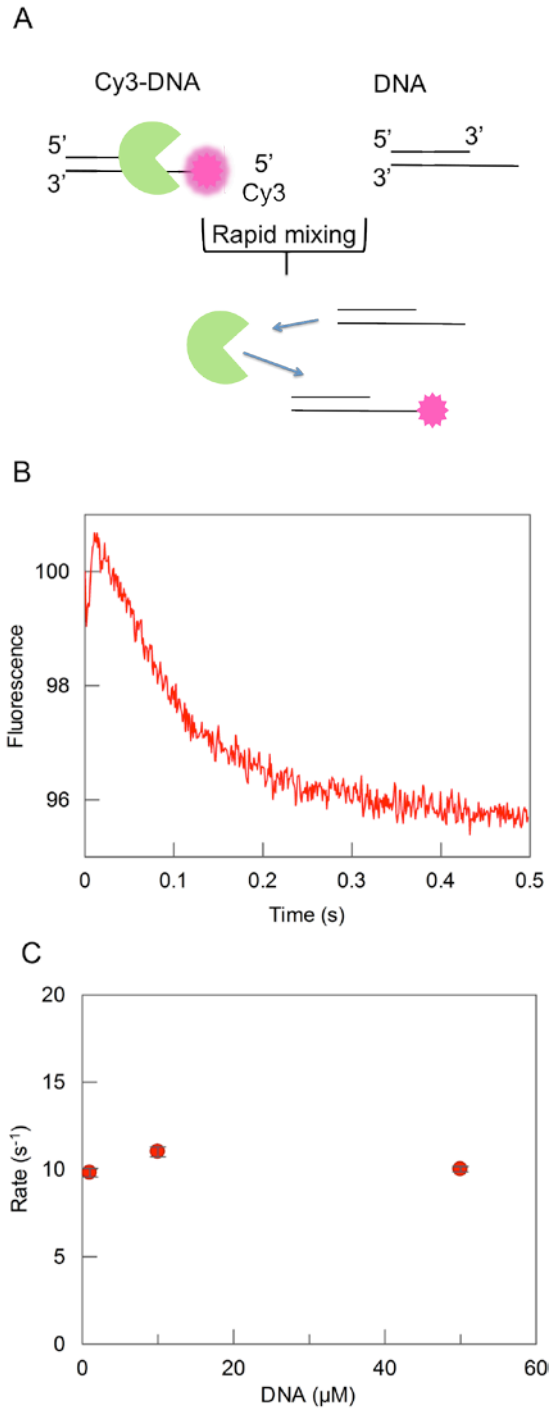

Figure 4.4. PolC dissociation kinetics from a partial DNA junction. (A) The competition assay performed in a stopped-flow apparatus by mixing a preformed complex of polymerase and junction 3 with an excess of unlabelled DNA junction 3. (B) Fluorescence trace generated by PolC dissociation from junction 3. Solutions contained 50 nM DNA, 250 nM PolC, 5 μM unlabeled DNA in K100 buffer. A single exponential fit of the fluorescence trace gives a rate of 10 s^{-1} at 30 °C. Details of fitting and errors are shown in the Appendix of this thesis. (C) Dependence of the observed rates from the unlabelled DNA concentration. Error bars indicate standard errors from each fit.

4.3. PolC binding to a fluorescently labelled nucleotide

4.3.1. Assessment of mant-dATP as ligand

Generally, fluorescently labelled nucleotides can be modified with fluorophores and used to investigate kinetics of association and hydrolysis steps of enzymes. These allow the use of low concentration reagents in such experiments [106]. The use of fluorescently labelled deoxyribonucleotides allows the investigation of PolC binding activity to these substrates.

Modifications can be placed at different locations on the structure of the nucleotide. Purine ring modifications can be made, as in the case of Cy3-dCTP, but these changes may affect the protein-nucleotide interactions due to selectivity of the base.

Sugar modifications are often the most successful whereby the analogue closely mimics the unmodified nucleotide. Examples of such modifications are the ATP analogues, mant-ATP and mant-ADP, which enabled measurements of binding and release kinetics for PcrA helicase [49].

Here, the fluorescent mant nucleotide, mant-dATP shown in Figure 4.5, was chosen to investigate PolC binding kinetics. The main reasons of selecting mant-dATP are the compact nature of the mant probe and its environmental sensitivity. However, such modifications interfere with the polymerization reaction as the mant is located at the 3'-OH position.

Prior to measuring the binding and release kinetics, it is important to have a fluorescence change in response to nucleotide binding. In order to assess the fluorescence change, fluorescence spectra were measured with an excess of PolC over mant-dATP for mant fluorescence (Figure 4.6). A two-fold increase in mant fluorescence was observed upon mixing with polymerase. By monitoring the fluorescence of the nucleotide, the increase in the fluorescence signal directly relates to nucleotide binding rather than a conformation change in the

protein. The fluorescence enhancement obtained upon mant-dATP binding can provide a useful signal to study the association and dissociation kinetics of PolC.

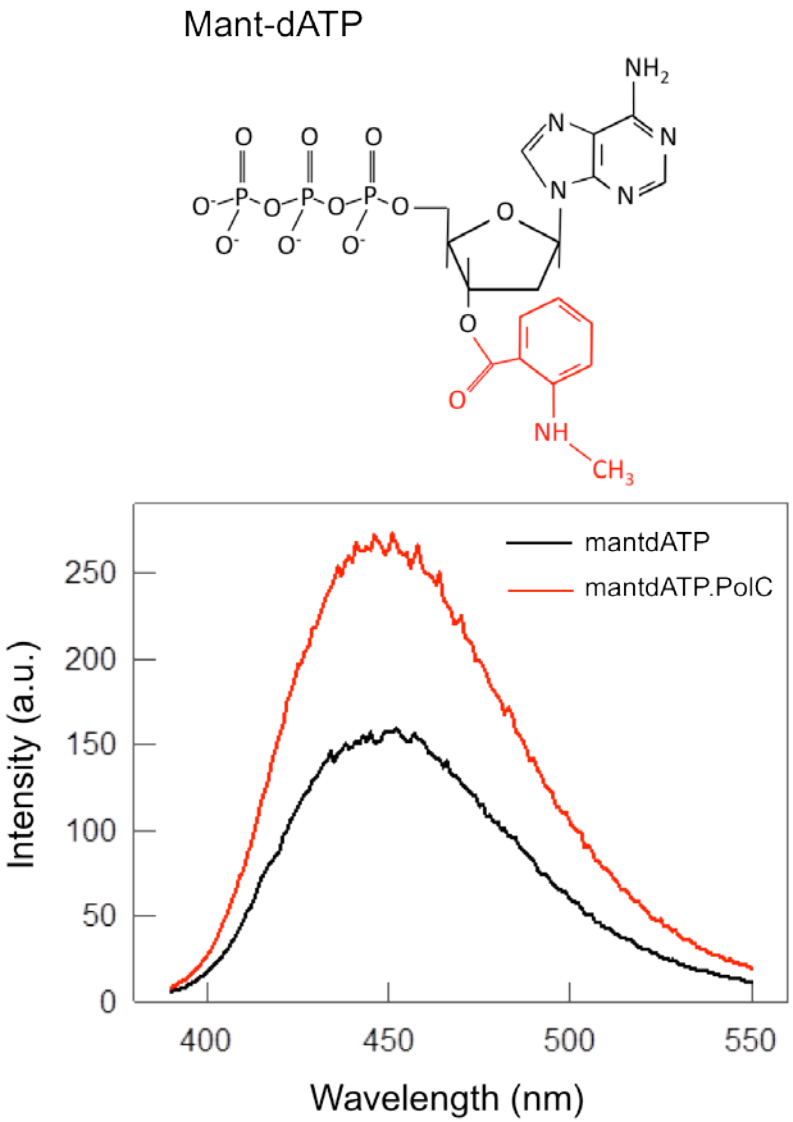

Figure 4.5. Mant-dATP fluorescence spectra. Fluorescence emission spectra of mant-dATP (structure shown in the top panel with the modification highlighted in red), with and without PolC, were recorded between 390 nm to 550 nm while exciting at 350 nm. Solutions contained 0.5 µM mant-dATP +/- 10 µM PolC in K100 buffer, at 30 °C.

4.3.2. PolC association kinetics to mant-dATP

Once the ability of mant-dATP to bind PolC was assessed, the nucleotide substrate was then used in rapid mixing experiments to investigate the binding kinetics. For such measurements, PolC was used as a reactant rather than a catalyst. This is achieved performing the experiments in the absence of a DNA template. In this situation, the observed fluorescent changes and rate constants will not be affected by the step of nucleotide incorporation or any conformational changes due to the formation of a ternary complex.

In an initial experiment, an excess of mant-dATP has been used in rapid mixing experiments (Figure 4.6A). Due to the excess of mant-dATP conditions, direct mant excitation gave a high background signal. Therefore, the fluorescence signal was monitored by exciting tryptophan at 290 nm and measuring FRET to mant, using a 400 nm cut-off filter. With the FRET assay, which is based on proximity between donor and acceptor, only the initial binding event is investigated and not a subsequent fluorescence change due to a local conformational change. Upon mixing, an increase in fluorescence was observed (Figure 4.6B). Fluorescence traces were fitted to single exponential and the k_{obs} increased linearly with the substrate concentration (Figure 4.6C). Interpreting the increase in terms of single step binding, the slope of the linear fit gave a second order rate constant (k_{+1}) of 0.44 $\mu M^{-1}s^{-1}$ and an intercept of 6.1 s^{-1} (k_{-1}).

The effect on the fluorescence signal was investigated by removing the free Mg^{2+}. Binding measurements were performed adding EDTA in the reaction (Figure 4.7A). The trace showed no change in fluorescence. This suggested that nucleotide binding occurred in Mg^{2+}-dependent manner, consistent with previous observation that the nucleotide binds to the polymerase as a Mg^{2+}-dNTP complex (Wang et al., 2009).

In another experiment, PolC binding to mant-dATP was examined in presence of the DNA template (junction 5, Figure 2.3). MantFRET fluorescence was followed over time upon rapid mixing the PolC solution with an excess of

mant-dATP and DNA (Figure 4.7B). Similarly to the free DNA reaction, an increase in fluorescence was observed upon mixing and the single exponential fit gave a rate of 7.4 s^{-1}, suggesting that the presence of DNA did not have a significant effect on the observed rate and so on nucleotide binding. Thus, the experiment was not performed using different concentrations of DNA.

4.3.3. PolC dissociation kinetics to mant-dATP

The FRET to mant was used to analyse PolC dissociation kinetics in a displacement assay. A solution containing a preformed complex of Polymerase and mant-dATP was rapidly mixed with an excess of unlabelled dATP (Figure 4.8A). The traces showed a decrease in mant fluorescence over time, consistent with dissociation of the labelled specie.

The fluorescence trace was fitted to a single exponential and gave a rate constant of 2 s^{-1} (k_{-1}) (Figure 4.8B). Rate constants were independent of ATP concentration in the range of 200 – 1000 μM (Figure 4.8C).

Calculation of the association and dissociation constants allowed the measurement of the binding affinity, K_d, which was 4.5 μM for mant-dATP.

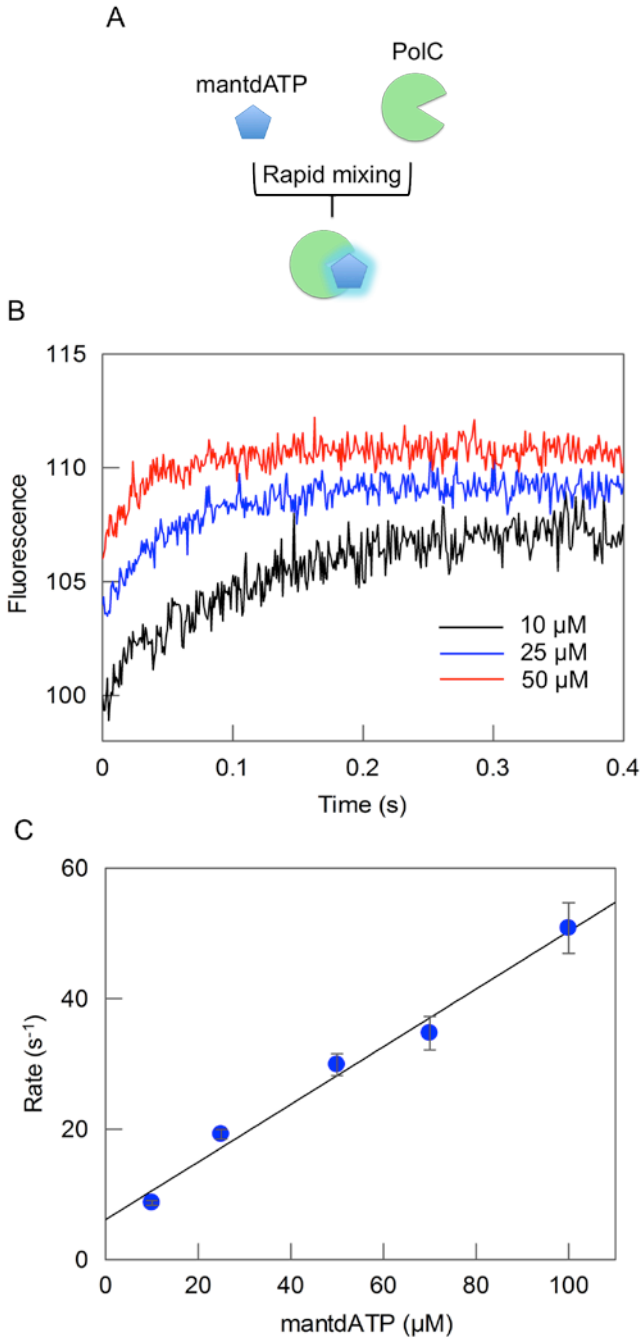

Figure 4.6. PolC association kinetics with an excess of mant-dATP. (A) FRET mant-dATP binding assay was performed by rapid mixing an excess of the labelled nucleotide with the PolC in the stopped flow apparatus. (B) Increasing concentrations of mant-dATP were mixed with 0.5 µM PolC in K100 buffer at 30 °C. The fluorescence signal was measured by exciting tryptophan at 290 nm and measuring the FRET to mant using a 400 nm cut-off filter. Traces shown are offset for clarity. Individual traces were fit to single exponentials. (C) Linear relationship between the rate constants and mant-dATP concentration gives a slope of 0.44 ± 0.03 (S. e.) $\mu M^{-1}s^{-1}$ and an intercept of 6.1 s^{-1}. Error bars indicate standard errors from each fit. Fits are shown in the Appendix of this thesis.

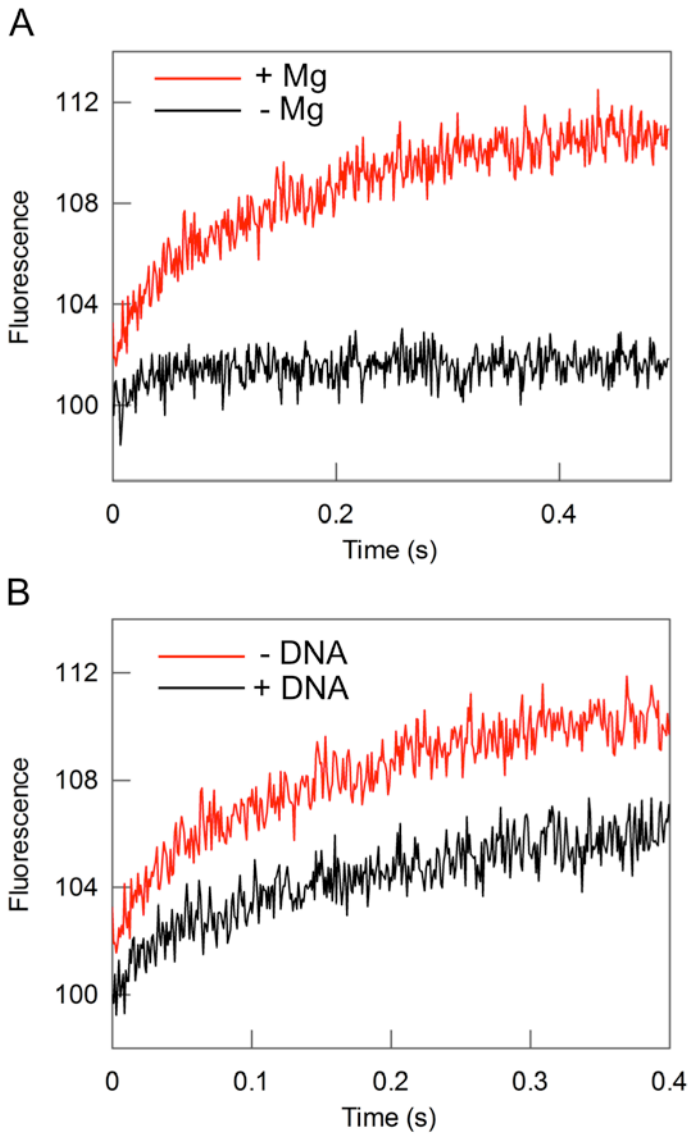

Figure 4.7. PolC association to mant-dATP under different conditions. (A) Effect of $MgCl_2$ removal on the FRET fluorescence signal to mant. 500 nM PolC with a solution containing an excess of mant-dATP (10 μM). Solutions contained either Mg^{2+} (K100 buffer for the red trace) or EDTA (K100 - $MgCl_2$ buffer for the black trace). The red trace (+ Mg) was fitted to a single exponential. (B) MantFRET signal upon mixing 500 nM PolC with a solution containing an excess of mant-dATP (10 μM) and DNA (10 μM). Traces were fitted to single exponentials, giving rates of ~7.4 s^{-1}. Solution conditions were as Figure 4.6.

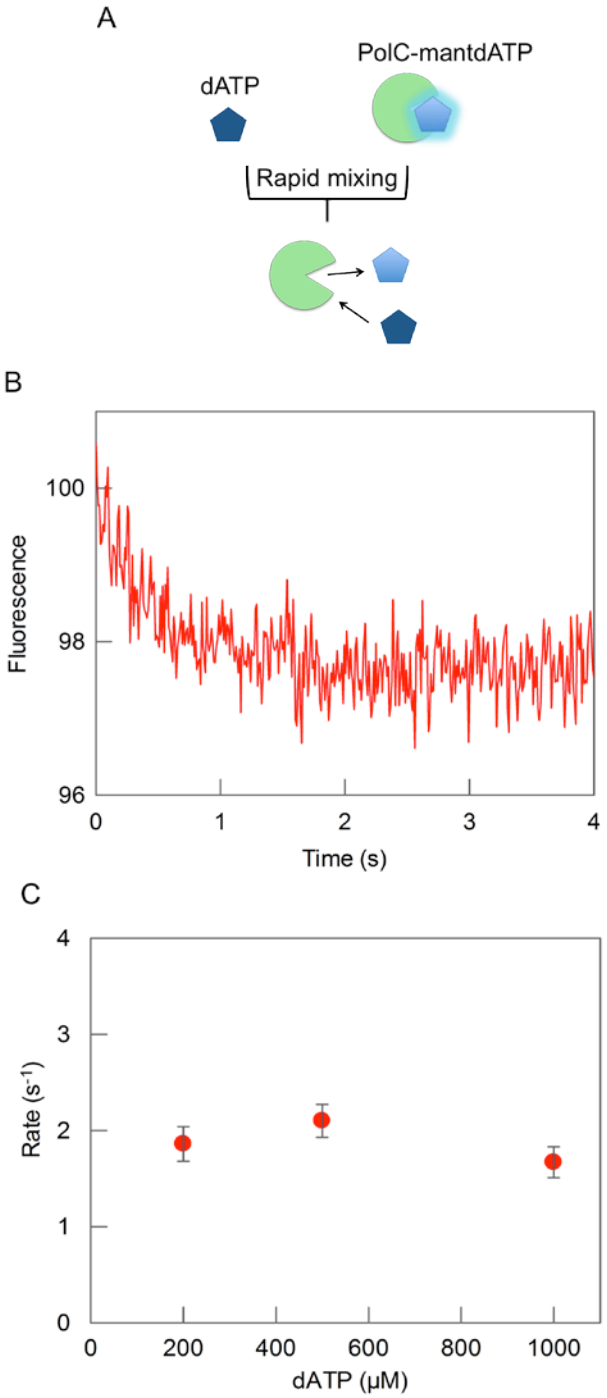

Figure 4.8. PolC dissociation kinetics from mant-dATP. (A) The displacement assay. A preformed mant-dATP-PolC complex was mixed with an excess of unlabelled dATP in the stopped-flow apparatus. (B) Example of fluorescence trace obtained from pre-mixing 0.5 μM with 10 μM mantATP before rapid mixing with 250 μM ATP under the same conditions as Figure 4.6. The resulting curves were fitted to single exponentials for different concentrations of ATP. (B) Rate constants (~2 s^{-1}) were independent of ATP concentration in the range of 250 μM – 5 mM. Error bars indicate standard errors from each fit. Details of fitting are shown in the Appendix of this thesis.

4.4. Steady-state kinetics of the DNA polymerase reaction

Early non-covalent transitions and conformational changes occuring upon PolC binding to its DNA and dNTP substrates are followed by the chemistry of nucleotide insertion (see Introduction for more details). One approach to investigate the DNA polymerase activity is based on measuring the rate of extension on a 3'-OH primed DNA *in vitro*.

The main strategy used here to assay PolC activity is given by the possibility to detect the inorganic pyrophosphate produced upon dNTP incorporation in a continous enzyme-coupled assay *in vitro* (Figure 4.9). This uses a fluorescently labelled PBP, the MDCC-PBP, as biosensor for phosphate to determine the rate of P_i production. The incorporation of dNTP into a primer DNA generates PP_i that can be hydrolyzed into phosphate by a pyrophosphatase. As PP_i does not induce a significant change in PBP fluorescence, fluorescence is monitored as P_i production by the pyrophosphatase using the MDCC-PBP.

Previous studies showed that the PPase and PBP were efficiently coupled to monitor PP_i production for a real-time assay [107].

Here, the overall experiment was designed so that the concentrations of PPase and PBP are in excess over the expected concentration of the PP_i produced form the total reaction. The activity of the PPase was first assessed in presence of inorganic pyrophosphate before its use (see the Appendix of this thesis). The PP_i hydrolysis was rapid and phosphate binding reflected the amount of PP_i providing an accurate assessment of real time activity of PolC.

Measurements were performed under steady-state conditions to gain information of the overall synthesis reaction and determine the affinities of various PolC substrates by measuring the k_{cat} and K_M parameters.

Such measurements have the advantage of being simple to carry out as the DNA substrate is present in large excess over the polymerase and so precious material is conserved. In addition, the assay is sensitive and allows working even at relatively low concentrations of dNTPs. As multiple enzyme turnovers occur during the reaction these experiments do not require the use of rapid kinetics instrumentation. Conversely, the main disadvantage of the assay is that

the steady-state rate, k_{cat}, is an overall rate and is dominated by the slowest step of the reaction cycle. The ratio k_{cat}/K_M is a useful measure of the enzyme specificity for the substrates.

The polymerase activity was assayed over a range of substrate concentrations. The Michaelis-Menten equation was used to determine the k_{cat} and K_m values for the reactions. In this assay, the short ssDNA tail of the primed DNA was made of either just one type of deoxyribonucleotide or all the four dNTPs (junctions 4-7, Figure 2.3). Figure 4.10 shows the rate of P_i production as a function of dNTP concentrations. The best fit of these data gave K_m values of 3.4 μM for dATP, 7.2 μM for dGTP, 45 μM for dTTP and 7.4 μM for a mixture of dNTPs. Results are collected in Table 4.1.

Measurements with the dCTP could not be performed because the DNA template for these measurements showed formation of secondary structures through a polyacrylamide gel analysis (see Methods, Figure 2.6). This was possibly caused by the ability of dGTP stretches to form G-quadruplexes. The K_m value for dATP was similar to the affinity obtained for mant-dATP (K_d: 4.5 μM). The parameter k_{cat}/K_m is the apparent second order rate constant for nucleotide incorporation when dNTP is bound in the Pol.DNA complex (Table 4.1).

The assay was also performed by varying the DNA template concentration (junction 4, Figure 2.3) in presence of an excess of dNTPs. This experiment gave a K_m value of 250 nM and a k_{cat} of 7 s^{-1} (Table 4.1). The K_m value was higher than that obtained with the binding kinetics measurements (~80 nM).

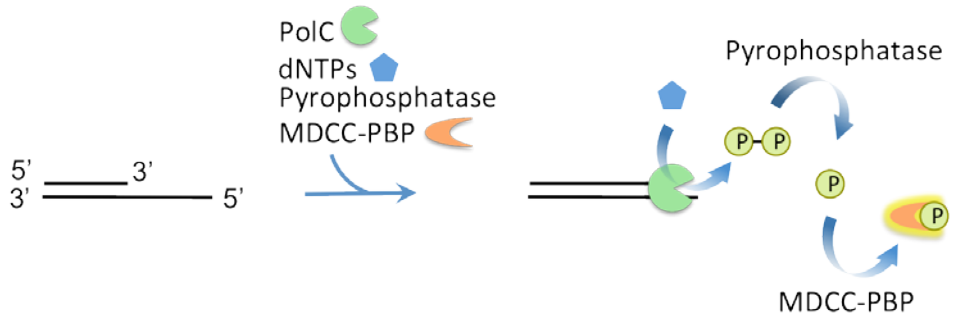

Figure 4.9. DNA polymerase synthesis assay using a pyrophosphatase and the MDCC-PBP. See text for details.

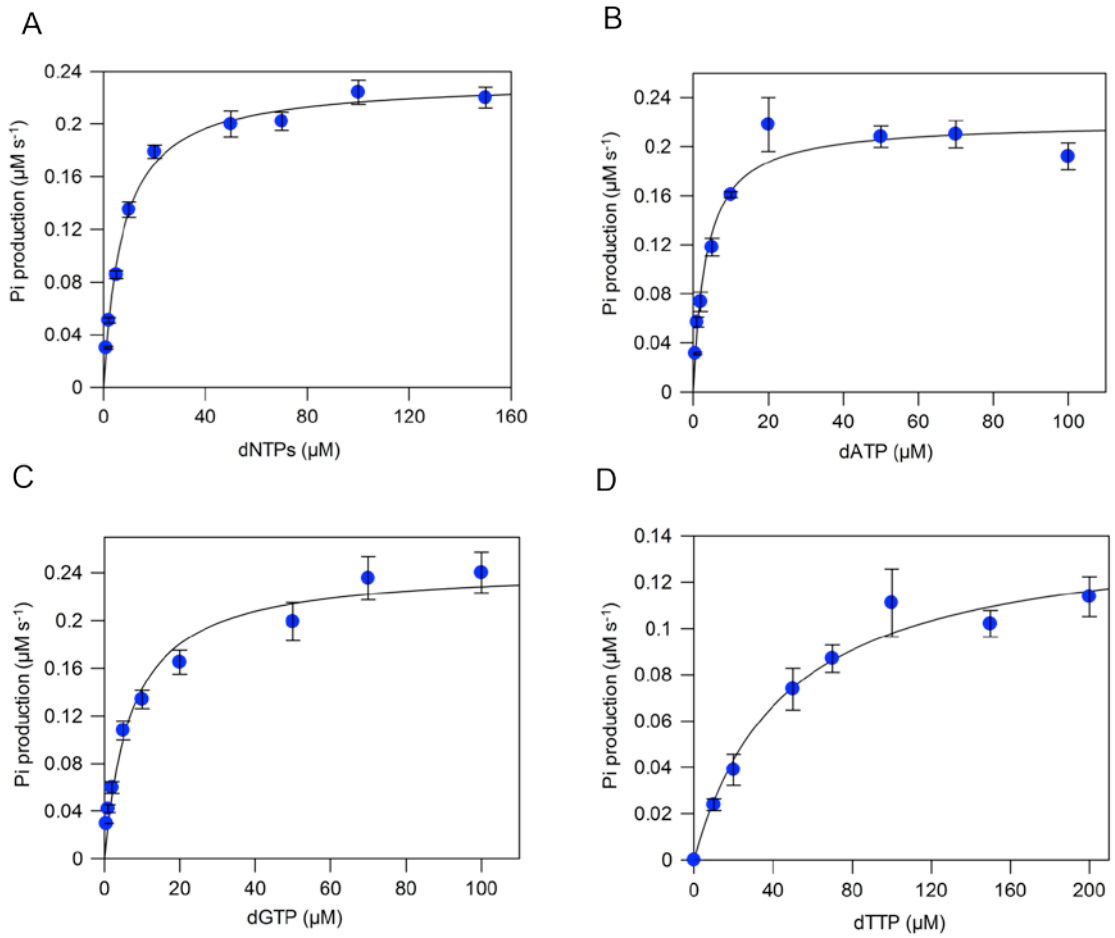

Figure 4.10. Steady-state measurements of PolC DNA synthesis activity. Data show the P_i produced as a function of substrate concentration. The lines are best fits to the Michaelis-Menten equation to give K_m and k_{cat} values (Table 4.1). Measurements were carried out at 30 °C in K10 buffer. 500 nM DNA (see junctions 4-7, Figure 2.3), 0.001 U/μL Inorganic Pyrophosphatase and 20 μM MDCC-PBP and the nucleotides at the indicated concentrations. P_i biosensor was calibrated in same reaction mix using known phosphate concentration. Error bars indicate standard deviations among three independent experiments. Examples of raw data and fits are in the Appendix of this thesis.

Substrate	Parameter		
	K_m (μM)	k_{cat} (s^{-1})	k_{cat}/K_m ($\mu M^{-1}s^{-1}$)
dNTPs	7.4 ± 0.6	11.6 ± 0.2	1.6 ± 0.1
dATP	3.4 ± 0.7	10.9 ± 0.5	3.2 ± 0.5
dGTP	7.2 ± 1.2	12.2 ± 0.6	1.7 ± 0.2
dTTP	45.0 ± 9.2	7.5 ± 0.5	0.2 ± 0.3
DNA	0.25 ± 0.07	7.0 ± 0.7	28.0 ± 5

Table 4.1. Steady-state kinetic parameters of PolC for various substrates. Errors and repeats are in the Appendix of this thesis.

4.5. DNA polymerase exonuclease activity

The abilitity of DNA polymerases to hydrolyze DNA by removing nucleotides is termed exonuclease activity. It is an instrinsic property of several DNA polymerases and plays a primary role in removing “errors” in a DNA template .

From structural analysis, native PolC shows an intrinsic exonuclease domain, which is conserved among the PolC type DNA polymerases [62]. From analysis of the aminoacid sequence alignment, a segment of around 163 amino acids in the PolC enzyme displays homology with the exonuclease domain of the *G. kaustiphylus* PolC.

Gel assays were used to investigate the PolC exonuclease activity. In this assay, the enzyme was incubated with a primed DNA (junction 4, Figure 2.3) and the final products were analysed on a native polyacrylamide gel (Figure 4.12). Upon PolC incubation, the intensity of the band corresponding to the intact DNA duplex decreased over time and a new band appears of lower molecular weight (Figure 4.12A). This corresponded to the template strand forming the annealed primed DNA template as shown from the oligo control. This result clearly confirmed that the purified PolC protein retains 3′-exonuclease activity. Similar to other nucleases, this activity was dependent upon a divalent cation. In this case, when Mg^{2+} was removed from the solution

(in presence of a EDTA-buffer), the exonuclease activity was inhibited (Figure 4.12B).

The polymerase exonuclease activity would be modulated by the concentration of dNTPs, since an abundance of dNTPs would favour DNA synthesis over hydrolysis (Figure 4.11) [108]. In this model, decreasing the availability of dNTPs should stabilize single-stranded gaps and favor DNA repair. An experiment was conceived to investigate potential inhibitory effects on the exonuclease activity due to the presence of dNTP pools in solution. The PolC and the primed DNA were incubated with increasing concentrations of dNTPs (Figure 4.12C). The gel showed that the intensity of the DNA band did not decrease and additional bands of digested products were not detected for dNTPs concentrations between 0.5 – 50 µM.

These results suggested that in the absence of dNTPs or under limiting concentration, the exonuclease/sunthesis balance of PolC is strongly shifted towards exonucleolytic hydrolysis instead of DNA polymerization and a gradual increase of dNTP concentration in the reaction mixture altered the balance in favor of DNA polymerization.

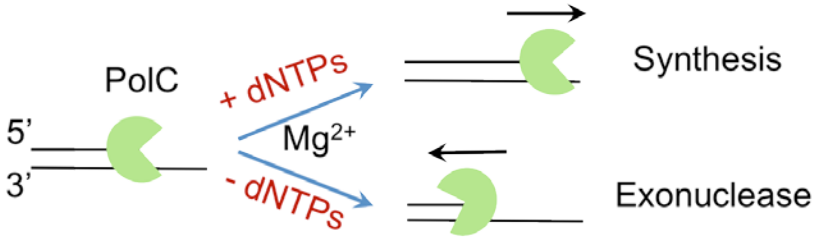

Figure 4.11. Schematic illustration of synthesis and exonuclease activities of PolC. PolC switches from the synthesis to the exonuclease activity according to the abundance of dNTPs. See text for details.

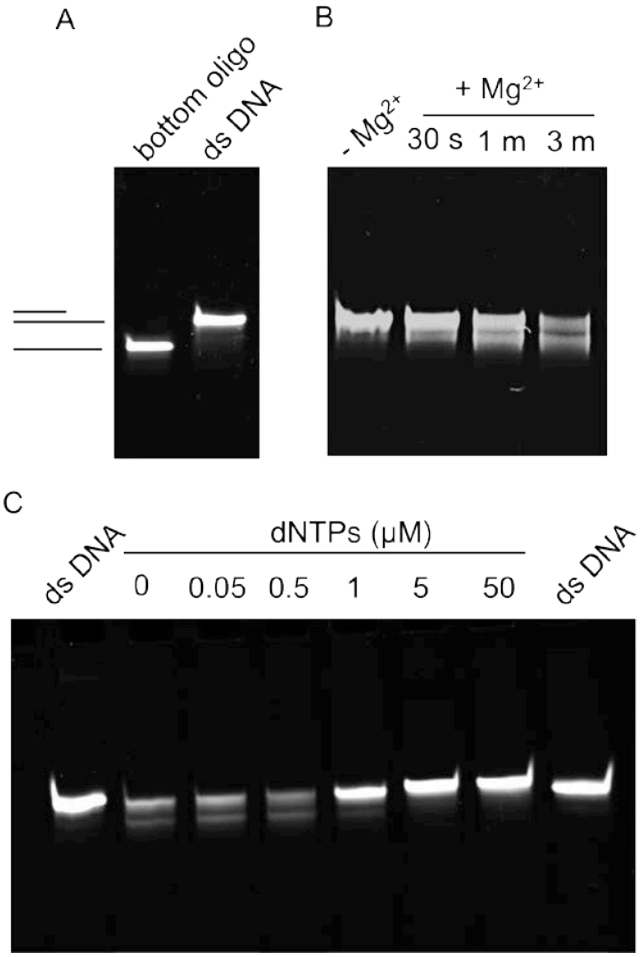

Figure 4.12. Exonuclease activity assay on a PAGE gel. (A) 0.5 μM junction 4 was loaded on a gel. The bands corresponds to the bottom oligonucleotide (lane 1, bottom oligo) of the primed DNA (lane 2, ds DNA) as showed by the cartoon. (B) Time course of the nuclease digestion. The no Mg^{2+} reaction is also shown. (C) Effect of dNTPs concentration (shown in μM) on DNA digestion. Reactions contained 1 μM junction 4 and 50 nM PolC in K10 buffer, and were quenched with 50 mM EDTA at the desired time points. Incubation times were 5 minutes unless stated.

4.6. PcrA helicase activity on DNA

Experiments performed in Chapter 3 explored the activity of PcrA helicase in complex with RepD in terms of PcrA unwinding speed using different dsDNA structures. Prior to investigating the effect of PolC on PcrA activity, the helicase translocation rate on ssDNA was measured in order to allow the comparison of a complete set of the kinetics data.

PcrA translocation was measured using an oligonucleotide having a fluorescent base analogue 2-aminopurine (2AP) at its 5'-end (dT10-2AP, Figure 2.4). Upon rapid mixing the preformed PcrA-DNA complex with ATP using a stopped-flow apparatus, the fluorescence trace consisted of two main phases, an initial rise in the fluorescence up to a maximum followed by an exponential decrease (Figure 4.14A). The initial increasing phase represents PcrA translocating to the 5'-end of the oligonucleotides with a maximum signal when the helicase interacts with the 2AP group (step 1, and 2, Figure 4.13). PcrA then dissociates causing the decrease in fluorescence (step 3, Figure 4.13). Following the first translocation event, the helicase enters a steady-state of multiple binding and translocation cycles (Figure 4.13). The time taken to reach maximum fluorescence gives a measure of the translocation speed. As control, removal of ATP caused no changes in fluorescence (Figure 4.14A).

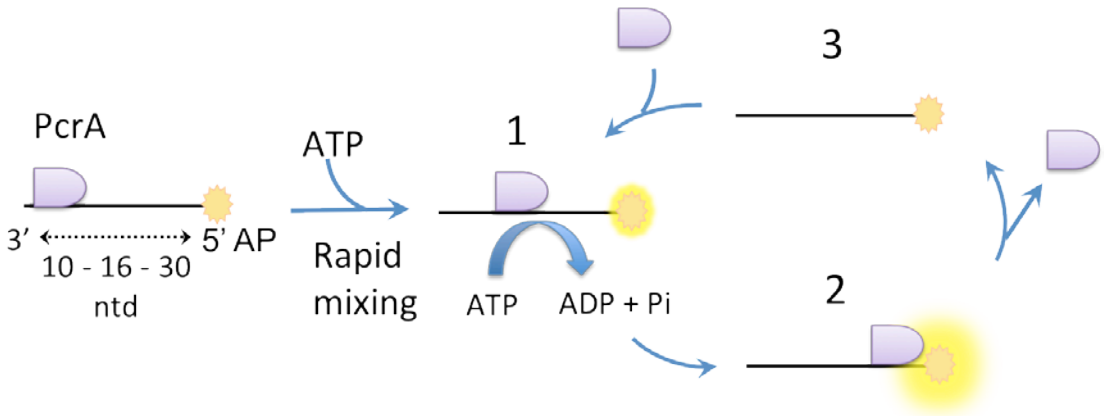

Figure 4.13. PcrA translocation assay on ssDNA. See text for details

To calculate an average of PcrA translocation rate, the experiment was also performed using different length oligonucleotides from 10 to 30 bases (dT10-2AP, dT16-2AP, and dT30-2AP, Figure 2.3). The time taken to reach the maximum of fluorescence increased with the DNA length (Figure 4.14B). These results are consistent with the increase in the time taken by PcrA to reach the 5'-end for longer DNA. The slope of the linear relationship between the DNA length and the time required to reach the maximum fluorescence gives an average of translocation rate of 227 nucleotides s^{-1} on single stranded DNA

(Figure 4.14C). The data also indicate that PcrA translocates unidirectionally from 3′ to 5′.

These observations were consistent with the proposed mechanism of PcrA translocation [48]. The PcrA translocation rate determined here was higher due to a different temperature condition (20 °C), but rather similar to that observed in a recent study using a labeled PcrA helicase, MDCC-PcrA (30 °C) [53].

The PcrA ssDNA translocation rate was significantly higher than the measured DNA unwinding rate for PcrA-RepD complex (Chapter 3). Such a difference will be further examined in the Discussion section.

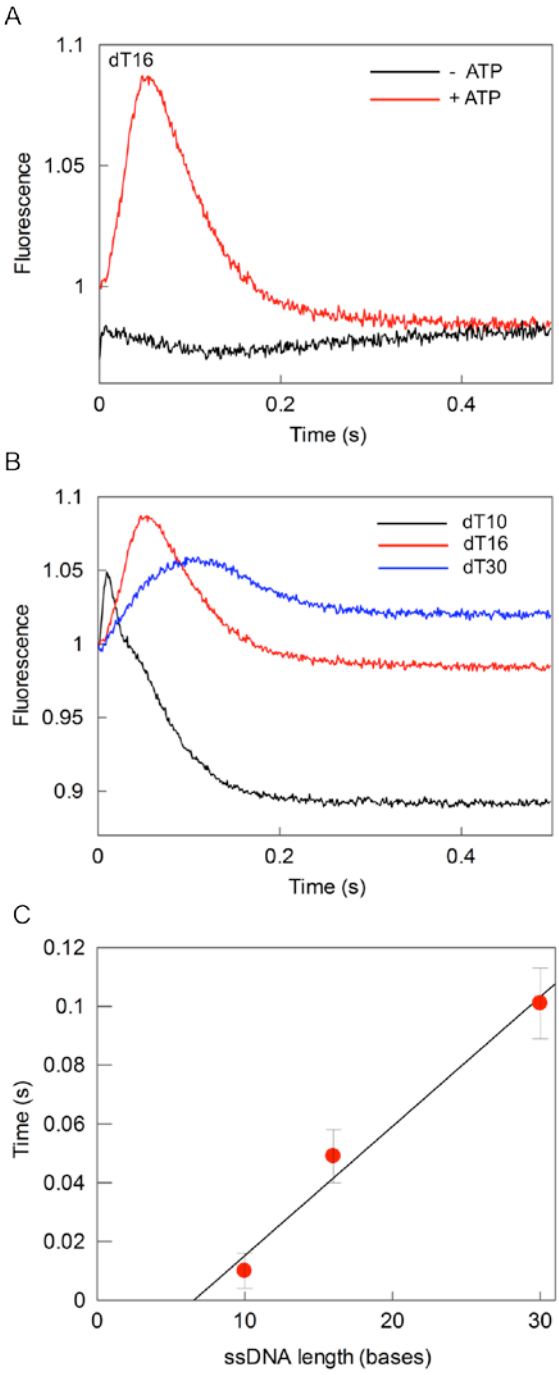

Figure 4.14. PcrA translocation activity on ssDNA monitored in a stopped-flow instrument. (A) Fluorescence traces of the ATP-dependent PcrA translocation along a dT16-2AP oligo (Figure 2.3). (B) Fluorescence traces upon PcrA translocation along different length oligonucleotides (dt10-2AP, dT16-2AP, dT30-2AP). (C) Relationship between the time of maximum fluorescence and ssDNA length. The linear fit gives a slope of 227 ntd s^{-1} at 30 °C. Error bars indicate standard deviations among three independent experiments. Solutions contained 500 nM PcrA, 2.5 μM DNA and 500 μM ATP in K100 buffer. Further details are in the Methods. Rapid mixing was performed at 30 °C as described in Figure 4.13.

4.7. PolC activity during staphylococcal plasmid replication

4.7.1. Effect of PolC on RepD nicking activity

A key step in measuring the kinetics of plasmid replication is to re-constitute the complete set of purified proteins involved. The investigation started with the analysis of the PolC effects on RepD binding/nicking activities on a supercoiled plasmid.

This was achieved performing the RepD nicking assay (described in Chapter 3) in a solution containing the PolC enzyme (Figure 4.15). Firstly, the supercoiled pCERoriD plasmid was incubated with RepD in the presence of PolC and the nicking reaction was followed over time (Figure 4.15A). The agarose gel analysis of the final products showed formation of the OC (open circular) band gel indicating rapid RepD-mediated nicking. However, a second band of lower molecular weight was also detected. The intensity of such band increases over time and with concomitant decrease of the OC band intensity. This was likely to be a DNA intermediated produced by the PolC exonuclease activity on the nicked plasmid.

In order to assess this hypothesis, a second experiment was designed investigating the effects of dNTPs on PolC activity. From experiments described above, it was shown that PolC exonuclease activity is inhibited by high concentrations of dNTPs substrates. The nicking reactions were incubated with increasing concentrations of dNTPs (Figure 4.15B). At low dNTPs concentrations or in their absence, the agarose gel showed formation of the two bands. At higher dNTPs concentrations only the OC band of maximum intensity was detected.

These results confirmed that PolC retains exonuclease activity on a nicked plasmid. The data are consistent with exonuclease inhibition by dNTPs as observed on a primed DNA junction.

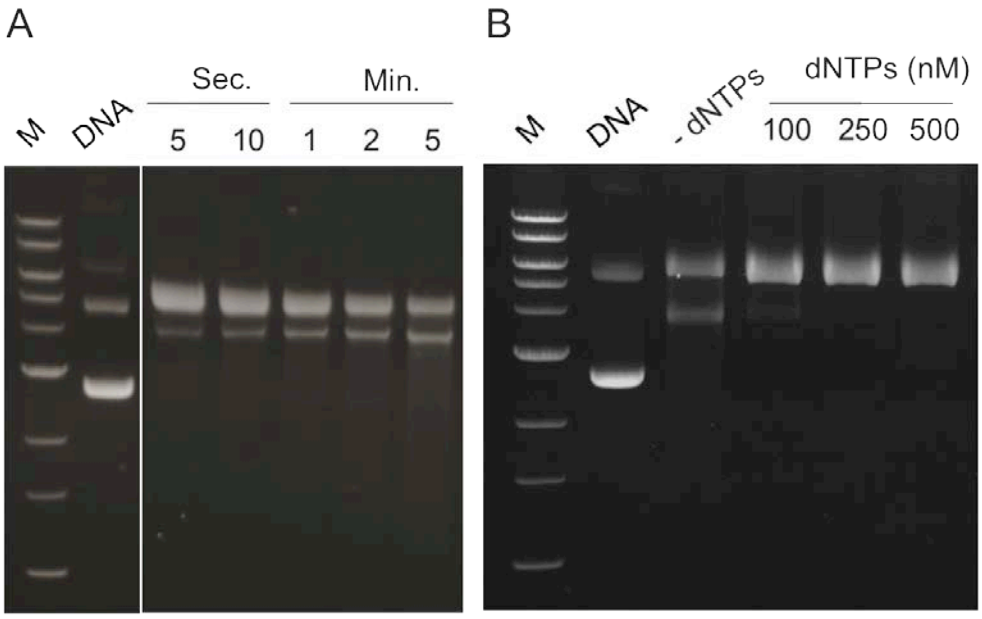

Figure 4.15. PolC effect on RepD nicking a supercoiled pCERoriD plasmid. Reactions contained 15 nM pCERoriD, 60 nM RepD, 100 nM PolC and +/- dNTPs. Solutions were incubated at 30 °C in K100 buffer and quenched with EDTA at the time indicated. (A) Time course of RepD nicking a supercoiled substrate in presence of PolC. (B) Effect of increasing concentrations of dNTPs (as indicated in nM) during RepD-mediated nicking in presence of PolC. Reactions were incubated for 5 minutes prior quenching with EDTA unless stated.

4.7.2. Effect of PolC on PcrA-RepD mediated plasmid unwinding

The kinetics of RepD-PcrA mediated unwinding DNA plasmids were examined here, as described in Chapter 3. The investigation of PolC role and effect on PcrA unwinding activity requires the inclusion of the polymerase in the plasmid unwinding assay described in Chapter 3. In such assay, the fluorescence signal is monitored in real time in a stopped-flow apparatus with the use of the DCC-SSB ssDNA biosensor. In a complete unwinding reaction of an intact DNA plasmid, PcrA helicase generates two ssDNA strands that are trapped by the fluorescently labelled SSB.

Upon PolC introduction in the assay, the strand having the free 3'-OH generated by RepD nicking and used by PcrA for translocation is the substrate for PolC-mediated synthesis (Figure 4.16). Under these conditions, only one

single stranded DNA strand would be available for the SSB binding and so the fluorescence intensity increase generated by the DCC-SSB is expected to be around half compared to that without PolC.

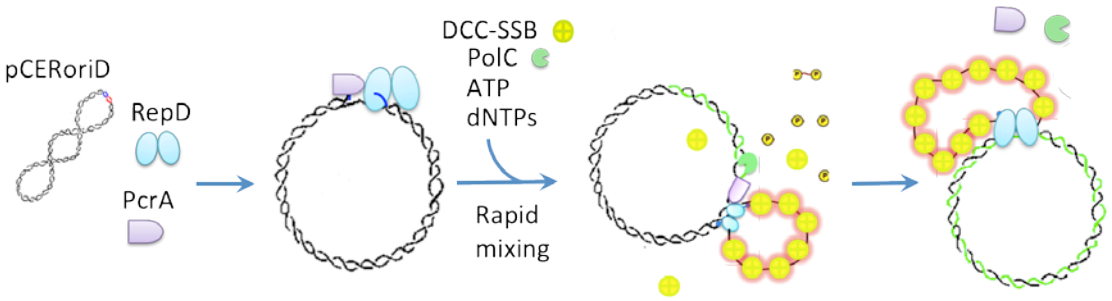

Figure 4.16. Cartoon showing the dynamics of plasmid unwinding and replication monitored in real time with DCC-SSB assay. The supercoiled pCERoriD plasmid is manually incubated with RepD and PcrA. RepD nicks and relaxes the plasmid and PcrA is recruited on the generated ssDNA tail. This solution is then rapidly mixed with a solution containing ATP, dNTPs, PolC and DCC-SSB using a stopped-flow apparatus. PcrA starts DNA unwinding with the hydrolysis of ATP and the PolC elongates the nicked strand behind PcrA. The displaced ssDNA is bound by the DCC-SSB causing an increase in fluorescence.

The PolC data obtained in previous assays were used to generate the optimal conditions in the plasmid unwinding assay. As described above, PolC retains exonuclease activity in the absence of dNTPs. This activity was also exhibited on a nicked DNA plasmid. Thus, in the stopped-flow experiments described below PolC was incubated with the dNTPs pool separately from the RepD-DNA solution to prevent digestion of the nicked DNA plasmid.

An initial experiment was performed to assess the effect of increasing concentrations of PolC on the fluorescence traces (Figure 4.17). The 2437 bp plasmid was preincubated with RepD and PcrA and then rapidly mixed with a range of PolC concentrations to examine whether the plasmid was saturated. Similarly to the PcrA traces, the one obtained in the presence of Polymerase showed a rapid increase in fluorescence followed by a small decreasing phase (Figure 4.17A). The initial lag phase varied between different measurements.

Qualitatively, PolC inclusion in the plasmid unwinding reaction had two major effects on the fluorescence trace. Both the amplitudes of the fluorescence

increase phase and the apparent unwinding durations were affected by PolC concentration (Figure 4.17B-C).

In the absence of PolC, the amplitude of the trace was at its maximum as the whole ssDNA generated by PcrA was available for SSB binding. PolC caused a reduction of the amplititude, expecially at high PolC concentrations (250 nM), suggesting that in this range the plasmid was saturated. The linear decrease in the amplitude with PolC concentration is consistent with less ssDNA available for DCC-SSB binding as a result of PolC-mediated strand synthesis. The break point of the trace was also affected by increasing PolC concentrations (Figure 4.17C). The shift in the break-point from ~ 80 s to ~ 45 s for the 2kb plasmid suggested that PolC had a positive effect on PcrA unwinding speed. For PolC concentrations > 250 nM no further changes in the traces were observed confirming that plasmid substrate saturation was reached.

The effect of PolC on PcrA activity was further investigated by measuring an avarage of unwinding rate using different lenght DNA plasmids in the DCC-SSB assay. Unwinding of four plasmid lengths is shown in Figure 4.18. Qualitatively, fluorescence traces were similar for the majority of the plasmids. The rapid increase in fluorescence was consistent with SSB binding ssDNA during PcrA-mediated unwinding. The amplitude of the increase linearly increased with the DNA length (Figure 4.18C). This phase was then followed by a slow decrease in signal. The final phase could be interpretated as interaction of the free PcrA molecules with the SSB-coated-strand following complete uwinding and replication.

The duration of unwinding linearly depended on the plasmid size and the unwinding times were measured as described in Chapter 3. The slope of the linear fit of the duration of the unwinding phase in function of the DNA length gives a rate of unwinding of 71 bp s^{-1} for PcrA (Figure 4.18B).

These data showed that PcrA activity was modulated by the presence of other replicative proteins. A complete set of PcrA kinetic data determined in this investigation is collected in Table 4.2.

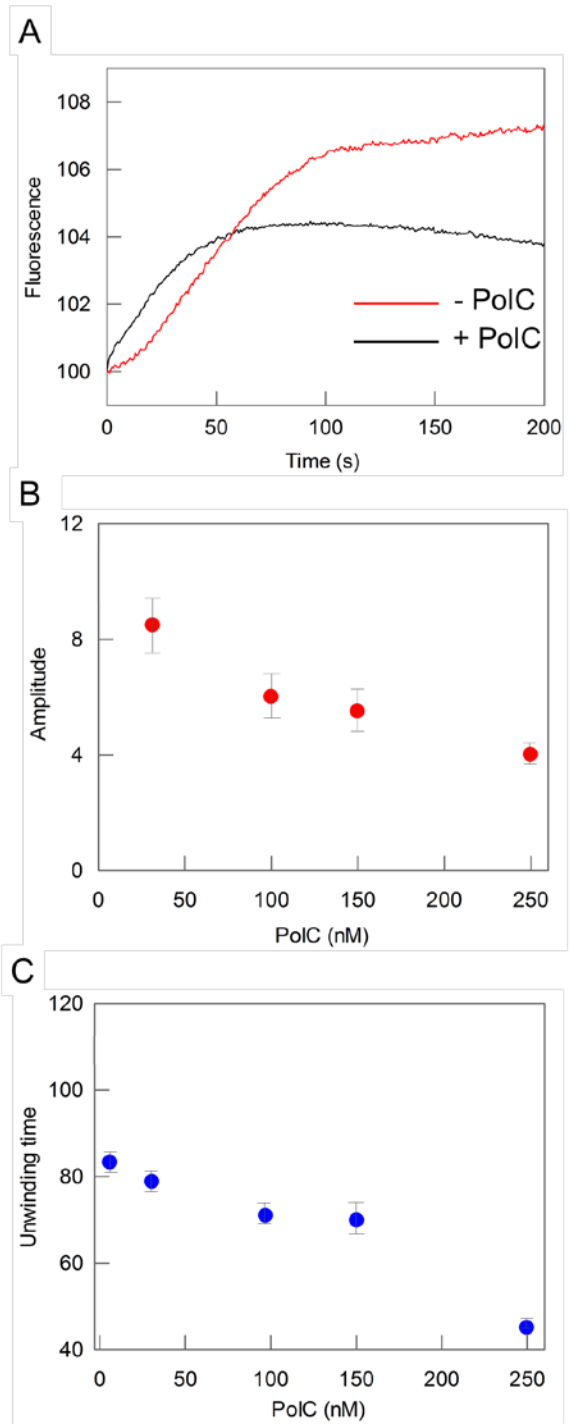

Figure 4.17. Effect of PolC on PcrA-mediated plasmid unwinding. The plasmid was preincubated with RepD, PcrA and then rapidly mixed with PolC as illustrated in Figure 4.17. (A) Examples of fluorescence time course for unwinding traces with (black) and without PolC (red). The fluorescence has arbitrary units, normalized to start at 100. Traces were analysed as described previously. (B) Dependence of the amplitudes on PolC concentrations. (C) Dependence of the break point on PolC concentrations. Reactions contained 0.5 nM pCERoriD plasmid (2437 bp), 2 nM RepD, 95 nM PcrA, 200 nM DCC-SSB (tetramers), ± PolC, 500 µM ATP and ± 500 µM dNTPs in K100 buffer at 30 °C. Error bars indicate standard deviations among two experiments.

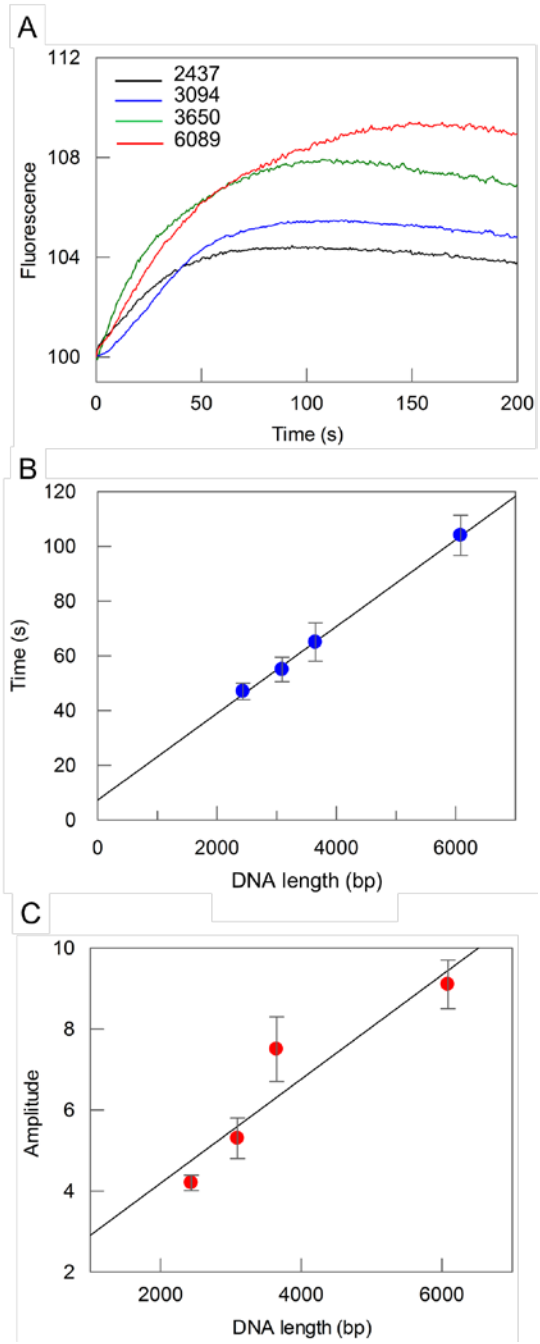

Figure 4.18. Unwinding traces of different length supercoiled plasmids by PcrA in presence of PolC. (A) Fluorescence time course for unwinding of different plasmid lengths (shown in base pairs). Reactions were made of 0.5 nM plasmid (size in bp), 2 nM RepD, 100 nM PcrA, 200 nM DCC-SSB (tetramers), 250 nM PolC, 500 µM ATP and 500 µM dNTPs in K100 buffer. The assay performed on a stopped-flow apparatus is shown in Figure 4.17. Traces were analysed as described previously. (B) Dependence of unwinding time on plasmid length. The linear fit gives a rate constant of 71 ± 3 bp s^{-1} for unwinding. (C) Dependence of the amplitude of the unwinding phases on the plasmid length. Error bars indicate standard deviations among three independent experiments. Examples of fitting are shown in the Appendix of this thesis.

PcrA activity	PcrA helicase	RepD-PcrA	N189K RepD-PcrA	RepD-PcrA-PolC
Translocation on ssDNA ($nt\ s^{-1}$)	227 ± 31	-	-	-
Plasmid unwinding ($bp\ s^{-1}$)	-	27 ± 2	19 ± 2	71 ± 3
DNA junction unwinding ($bp\ s^{-1}$)	-	54 ± 9	47 ± 4	-

Table 4.2. PcrA activities and interactions with replicative proteins *in vitro*. The rates of PcrA translocation on ssDNA and DNA unwinding were measured at 30 °C in solution.

4.8. Discussion

4.8.1. DNA polymerase activity

The analysis of the staphylococcal replicative DNA polymerase activities was presented in this chapter, providing information on both the kinetics of early non-covalent and covalent chemistry. This was achieved combining a fluorescence-based approach with gel assays.

Structural and functional studies of a number of DNA polymerases have been previously performed to improve our understanding of the mechanisms underlying their novel properties. Collectively, data from kinetic, mutational and structural studies of high-fidelity DNA polymerases have been used to describe a common ordered multi-step kinetic mechanism for an incorporation event of a correct nucleotide (Figure 4.19) [65]. This is based on the general assumption that the DNA polymerase initially binds the DNA template and then the correct dNTP substrate. The formed ternary complex then undergoes to a conformational change to allow a correct alignment of the template with the incoming dNTP. This is followed by the catalytic step of incorporation and PP_i release.

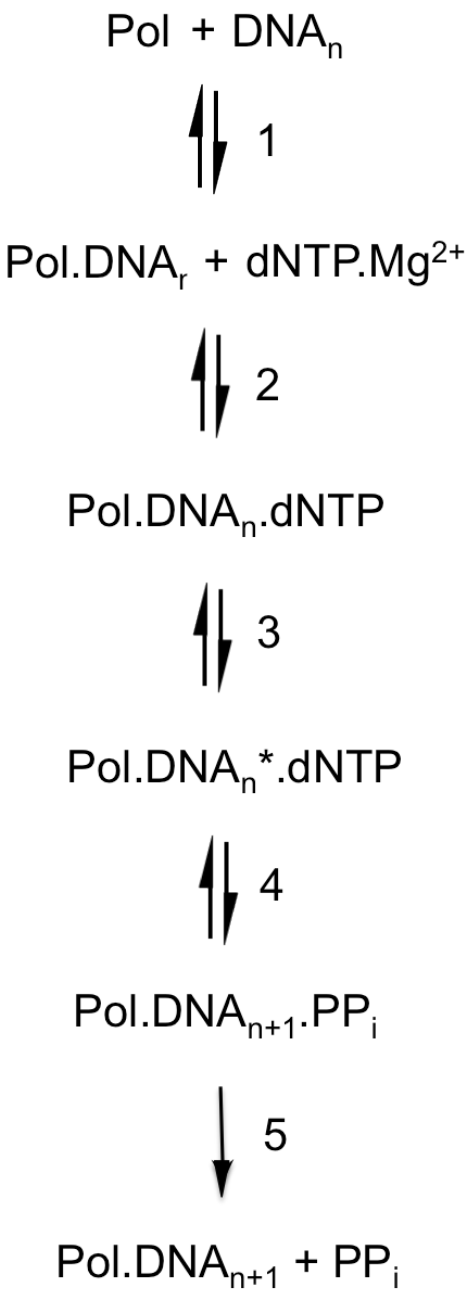

Figure 4.19. Overall kinetic scheme of an incorporation event of a correct incoming dNTP catalysed by a polymerase. The DNA polymerase binds a primed DNA (step 1). A complementary dNTP is then recruited in the active site to form a ternary complex (step 2). After nucleotide binding, a conformational change occurs (step 3) that leads to the optimal alignment of the catalytic residues in a precise conformation to promote incorporation (step 4). This is followed by subsequent PP_i release (step 5). At this stage, the polymerase can continue the synthesis by moving on the next template position or dissociate from the DNA to act on another substrate.

Stopped-flow rapid mixing experiments allowed measurements of PolC binding kinetics to the substrates and the determination of the binding affinities. In the kinetic scheme proposed above, DNA.PolC complex formation is the first event. PolC binding to DNA was relatively rapid (k_{+1}: ~1.2 $\times 10^8$ $M^{-1}s^{-1}$, Figure 4.2), and such binding was Mg^{2+}-independent and did not show DNA sequence specificity (Figures 4.1, 4.3). Measurements of the k_{-1} allowed the calculation of the dissociation constant for such primed DNA (~10 s^{-1}, Figure 4.4). Most DNA polymerases show K_d values varying from 5 to 70 nM) [109-111], and PolC displayed a slightly weaker affinity for DNA (K_d: 83 nM).

The following event in the kinetic scheme is nucleotide binding. The fluorescently labelled mant-dATP was used as main nucleotide to investigate binding kinetics and, for simplicity, PolC binding was initially monitored in the absence of DNA template. However, the observed rate constant upon mant-dATP association was independent on whether or not DNA was present (Figure 4.7). In its absence, the K_d value from binding kinetics experiments was 4.5 μM for mant-dATP. The latter was similar to the affinity value obtained for dATP incorporation in steady-state measurements (K_m: 3.4, Figure 4.10). The similar affinity values for mant-dATP and dATP suggested that mant-dATP is an excellent ATP analogue as the mant modification had no significant effects on PolC binding.

The overall kinetic data obtained with the nucleotide and DNA substrates indicated that PolC binds tighter and faster to the DNA. These results supported the idea that the DNA is the first PolC substrate according to the sequential binding proposed for the high-fidelity polymerases.

The kinetic parameters, k_{cat} and K_m, governing nucleotide incorporation were determined in steady-state experiments (Table 4.1). The values of the K_m are an overall guide to nucleotide affinities of the PolC.DNA complex for the incoming substrate and ranged between 3.5-45 μM for the dNTPs. PolC binding was tighter for the purine bases in the following order dATP > dGTP > dTTP (Figure 4.10). Similarly to PolC, K_m values for replicative polymerases incorporating a correct dNTP in a DNA template are ~10 μM [109-111].

The maximal rate, k_{cat}, representing the rate of polymerization, k_{pol}, was measured as a function of dNTP concentration and a gave value of ~12 s^{-1} for

dNTPs (at 30 °C). Such value was independent on the type of nucleotide and ssDNA template used (Figure 4.10). In such experiments, the interpetration of the synthesis rate is complex as it is an estimate of the overall reaction cycle and depends strongly by one or more elementary steps. In this case, the k_{pol} might be dominated by the rate-limiting step of PolC dissociation (k_{-1}) from DNA product that takes place to process many DNA molecules and so the value might not reflect the "true" rate of synthesis.

Using a gel-based approach, it has been previously shown that *S. aureus* PolC fully extends a primed site around a circular ssDNA plasmid at a speed of 80–120 nucleotides s^{-1} (at 37 °C) [112]. This rate is ~10 fold faster than the value determined here, albeit in different temperature conditions and experimental approach, such as the presence of SSB, and the use of a long DNA template (~7 kb).

4.8.2. PcrA helicase activity

The kinetics of PcrA DNA unwinding and translocation were investigated here and in Chapter 3 using a fluorescence-based approach. The main sets of rate constants from rapid mixing experiments are summarized in Table 4.2. PcrA helicase showed different rates depending on the nature of the DNA and the effect of the initiator protein RepD.

As previously shown, PcrA alone is not a processive helicase and requires the activation of its partner, RepD, which enables PcrA to processively unwind DNA. Unwinding occurs at a relatively slow rate for the RepD-PcrA complex (~30 bp s^{-1} at 30 °C).

The kinetics of PcrA translocation along ssDNA were measured here using labelled DNA. This process was much faster than dsDNA unwinding and gave an average rate of 223 bases s^{-1} (Figure 4.15). PcrA translocation rate on single stranded DNA was measured in previous studies. Such rate was 80 bases s^{-1} using the assay described here at 20 ˚C [48]. In a more recent study, MDCC-PcrA, a labelled cysteine mutant of PcrA with identical catalytic activity to the wild type was used to measure translocation. With this approach, a similar rate was obtained at 20 ˚C (99 bases s^{-1}) and increased to 299 bases s^{-1} for measurements done at 30 °C, which is similar to the rate reported here [53].

It is clear that PcrA average rate of unwinding was several-fold slower than the PcrA translocation rate on ssDNA. One interpretation of such activity was that PcrA-mediated DNA unwinding could occur with a partially passive mechanism [53]. However, despite the different rates observed, it has been shown that the coupling between the ATP hydrolysis reaction and PcrA base translocation is one ATP per base for both ssDNA translocation and dsDNA unwinding [48].

Measurements of DNA unwinding can only be performed in presence of RepD protein. The functional interaction between RepD and PcrA occurring during initiation and unwinding has no significant effect on PcrA ATPase activity [48]. As described in Chapter 3, PcrA in complex with the mutant N189K RepD unwinds DNA plasmids at a speed of 19 bp s^{-1} and short DNA duplexes at a rate of 47 bp s^{-1}. The values are slightly reduced than that obtained with wt RepD-PcrA complex (Table 4.2).

There have also been evidences of a physical interaction between the two proteins as they remain associated forming a functional unwinding complex until termination, and so it is possible that RepD might also play a role in modulating PcrA motor activity.

4.8.3. Polymerase interaction with PcrA?

So far studies of the staphylococcal plasmid replication mechanisms have been mainly focused on the activity of the PcrA helicase and RepD protein. The activity of PolC in a complete replicating system was investigated here. There have been several examples in the literature of helicase activity regulation by other proteins such as polymerases (see Introduction for details on the coupled activity of the motor proteins).

Efforts were made here to characterize the activities of the α-subunit of the *Staphylococcus aureus* polymerase, in order to insert the enzyme in a full plasmid replication system *in vitro*. In such a complex scenario, there are multiple replicative proteins processing a single DNA plasmid molecule in a coordinated manner including RepD, PcrA, PolIII and the SSB.

Firstly, the activity of RepD was investigated to assess the extent of plasmid nicking in presence of polymerase (Figure 4.16). RepD relaxation activity was

found to be unaffected by PolC. This means that plasmid initiation can successfully occur under these conditions. However, PolC retained exonuclease activity on DNA and so on the nicked plasmid (Figure 4.16). DNA digestion occurred as long as a primed DNA was present in solution. Exonuclease inhibition was achieved using a high excess nucleotide concentration (Figures 4.13, 4.16).

The unwinding activity of PcrA was then measured including PolC in the plasmid unwinding assay. Upon mixing increasing concentrations of PolC the fluorescence signal decreased (Figure 4.17), which was consistent with unwinding followed by synthesis of the (+)-strand and less ssDNA available for SSB binding. The extent of DNA synthesis was highest at 250 nM PolC where the amplitude was around half compared to that in the absence of PolC. At such PolC concentration, the plasmid substrate reached saturation. This was in agreement with the DNA affinity value K_m (250 nM) determined in steady-state measurements, albeit ~3 fold lower than the measured K_d (~ 80 nM).

Another interesting observation was that the 'break-point' of the traces occurred earlier with the PolC, giving a PcrA average rate of unwinding of 71 bp s^{-1} (30 ˚C) (Figure 4.19). This was few fold faster than the rate observed with PcrA alone (30 bp s^{-1}, 30 ˚C), and the PolC synthesis rate (12 ntd s^{-1}, 30 °C, Table 4.1), albeit the latter was measured under different assay conditions and in the absence of other replicative proteins. The increase in PcrA unwinding speed might result from interactions between the two motor proteins during nucleic acid unwinding/replication. One interpretation of the different unwinding/translocation/synthesis rates might be that PolC could activate PcrA to perform unwinding at a rate more close to its translocation speed (~200 ntd s^{-1}), albeit limited by the slow PolC synthesis rate. When both motors are moving around the plasmid during replication, PcrA would pull the PolC and dictate the overall speed of DNA unwinding-synthesis. However, proteins used in this investigation are from different bacteria (*B. stearothermophilus* PcrA and *S. aureus* RepD is from *S. aureus*), and only the replicative polymerase subunit of the holoenzyme was used and so protein–protein interactions might not completely reflect the *in vivo* scenario.

Currently, there are no structural studies of the initiator protein in complex with the *oriD* and or PcrA helicase. The length of the ssDNA stretch formed by

RepD nicking as well as the motor proteins disposition on the *oriD* during initiation would provide insights into how such enzymes are assembled during replication.

There have been several studies reporting functional coupling between helicases and polymerases showing that their interaction resulted in a faster helicase movement through the dsDNA, as occurs for the phage T7 replication system [70]. However, the exact mechanisms of functional coupling between the motor proteins are yet to be elucidated.

4.9. Summary

In this chapter, the activities of the *S. aureus* PolC were analysed using rapid-mixing experiments combined with gel assays. Kinetic rate constants have been measured for various steps in the formation of PolC, DNA and dNTP complexes. The complete kinetic scheme of the PolC incorpotation reaction for a correct dNTP in a DNA template has not been fully characterised here, but important steps have been determined. Fluorescently labelled substrates have been used to determine the PolC binding kinetics. Kinetic analysis showed that PolC rapidly binds DNA in a Mg^{2+}-independent way and this is followed by a more slow Mg^{2+}-dependent nucleotide interaction. These observations were in agreement with the model of sequential substrate binding proposed for the high-fidelity polymerases, such as T7 DNA polymerase.

From the prospective of understanding how the activity of the replicative proteins is coordinated during replication, PcrA activitiy on DNA was investigated as single motor and in association with other proteins. Kinetic measurements showed that the helicase moved on DNA at higher speed compared to DNA duplex unwinding. The latter, occuring only in presence of the RepD initiator protein, was few fold faster in the presence of PolC. These results indicated that PcrA properties such as processivity and unwinding speed were different modulated by partner proteins. The unwinding data also suggested a functional interaction between PcrA and PolC during coordinate plasmid unwinding and replication.

Studies of the protein interactions within the replisome need to be extended in the future with structural determinations to provide the greatest understanding of these molecular machines.

5. Observing DNA Replication Using Atomic Force Microscopy

5.1. Introduction

Atomic Force Microscopy has been extensively used in the study of the biomolecular structures, as it can provide a deeper understanding into several biological processes like DNA-protein interactions and enzymatic activities through their direct visualisation on a surface (see Introduction for details on AFM). Previously studies reported AFM images of fundamental processes of DNA metabolism, such as rolling circle synthesis of *E. coli* phage φX174 viral DNA, interactions between the protein-DNA complexes, and the movement of RNA polymerases on DNA [113, 114].

In this chapter, AFM imaging was used to visualise directly the events of the asymmetric rolling circle plasmid replication of a Gram-positive system. Events relating unwinding and synthesis of the plasmid pCER*oriD* have been investigated by AFM using the initiatior protein RepD, *B. stearothermophilus* PcrA, *S. aureus* PolC, and *E. coli* SSB. Previous work described the directional unwinding of a pCERoriD plasmid by AFM [51]. Here, a more detailed structural analysis of biomolecular complexes is reported. In addition, the whole replication system, with the inclusion of the polymerase, is also investigated.

The overall process is characterised by a series of defined events that can be investigated including protein-induced changes to the local and the global structure of DNA that were both quantitatively and qualitatively recorded with AFM. In these experiments the plasmid pCERoriD was used in the supercoiled or in linear form, and different length plasmids were employed in some measurements. The 3.6 kb DNA plasmid was used throughout the various steps of replication, as its relative short size was convenient for imaging a relatively small area on the surface, and also the analysis was easier for the reduced intramolecular crossings.

Firstly, the DNA plasmid could be visualised in its native state, and its topological changes caused by RepD nicking activity were also analysed. Accordingly to the results shown in Chapter 3, RepD was able to relax the majority of negatively supercoiled plasmids. Such an event allows the plasmid to be accessible to the replicative proteins. Following initiation, PcrA-mediated unwinding of linear and supercoiled DNA substrates was monitored with and

without SSB. Strong evidences supporting a physical interaction and dynamic coupling between PcrA helicase and RepD during plasmid unwinding were found through the analysis of the macromolecule complexes.
PolC inclusion in the unwinding reaction allowed imaging of the final products generated by a complete replication system. Upon complete replication, newly synthethised circular plasmids were found along ssDNA molecules.

To better understand the morphology of molecules, a quantitative description of the surface topography must be carried out, and this was achieved extending the two-dimensional data analysis by measuring the heights of the surface features. A simultaneous analysis of the initiation stage products was also performed using gel assays. However, the gel approach was used only for a plasmid topology analysis because transient states and intermediates that may form during a reaction as well as structural information of protein and DNA are not detectable.

The use of AFM for imaging has several advantages. The DNA preparation and deposition on the surface does not require special treatments such as contrasting agents and staining mainly used in other types of microscopy.

The surface used here is the muscovite mica that was freshly cleaved to allow a straightforward deposition of the sample. The mica surface has a layered structure of aluminum silicate sheets weakly bonded together by layers of potassium ions. The potassium ions occupy large holes between oxygen atoms. The electrostatic interaction between potassium and oxygen is rather weak allowing ceavage along the basal plane of the surface. Upon cleavage, potassium ions are evenly distributed along the two surfaces. In aqueous solution the potassium ions will dissociate and the surface acquires a negative charge. The absorption of negatively charged molecules like DNA is promoted through Mg^{2+} surface treatment for an efficient interaction with the negatively charged phosphates of the nucleic acid backbone. This strategy is necessary to prevent the movement of DNA molecules upon interaction with the tip whilst scanning, which would result in a severely distorted image.

Reactions in this investigation were carried out in solution and samples were deposited on mica, dried onto the surface and imaged. This is less demanding

than imaging with an aqueous layer on the mica, which requires buffer conditions optimization and functionalized surfaces for sample immobilization. AFM images presented here have been generated using the contact mode.

In addition, a combined Total Internal Reflection Fluorescence and Atomic Force Microscopy (TIRF-AFM) approach was used here in order to identify labeled SSB proteins on DNA (see Introduction for details on TIRF-AFM). In this experiment, the fluorescently labelled Cy3B-SSB was used in the unwinding reaction and the ssDNA produced by PcrA helicase was substrate for the labelled SSB protein allowing the visualisation of fluorescence images from the TIRFM. Such fluorescence images were combined with the topography analysis obtained from AFM to identify the DNA-protein complexes.

The study presented here provides a comprehensive set of information in the general mechanisms of a complete plasmid replication system, including low-resolution structural data of the initiation complex, and the interactions occurring during unwinding and replication.

5.2. Supercoiled pCERoriD plasmids

The first step in the study of the dynamics of plasmid replication events was given by the acquisition of the purified plasmid substrate images in its native state. An initial experiment was performed to analyse the surface used in these measurements. The freshly cleaved mica surface was imaged in the absence of any solution (see the Appendix of this thesis). The topography analysis showed a clean surface with no detectable structures and an exceptional smooth surface. These properties make the mica a valuable substrate to examine nucleic acid and proteins.

A solution containing the pCERoriD plasmid was immobilized on the mica surface previously treated with Mg^{2+}, followed by drying and scanning. A typical image of the DNA plasmid molecules absorbed on the surface is shown in Figure 5.1. It has been previously shown that imaging supercoiled DNA samples in air gives similar images to those in liquid [112]. The scanned DNA plasmid molecules clearly showed basic features of DNA supercoiling known as

plectonemic superhelices. In such a DNA geometry, the DNA molecule winds helically up and back down in an imaginary cylinder (Figure 5.1). These results were consistent with the geometry of bacterial plasmid DNA *in vivo*, where the dominant DNA form is a plectoneme [115]. The three-dimensional analysis of the molecules, shown in Figure 5.1C, revealed that the height of the DNA molecule varied from 1.2 to 2.5 nm depending on the superhelical twist superimposed on the secondary helical winding.

The topology analysis performed over 50 DNA molecules from AFM imaging is shown in Figure 5.2A. The stock solution contained a tiny population of relaxed DNA form. This indicated that a freshly purified DNA sample contained ~ 97% of intact supercoiled molecules. An agarose gel analysis of the DNA sample confirmed the high purity of the DNA (Figure 5.2B). The presence of circular structure is possibly caused either by degradation during the DNA purification process or by the sample storage conditions. Agarose gel analysis of DNA showed variability of the amount of relaxed plasmid between different DNA preparations (data not shown).

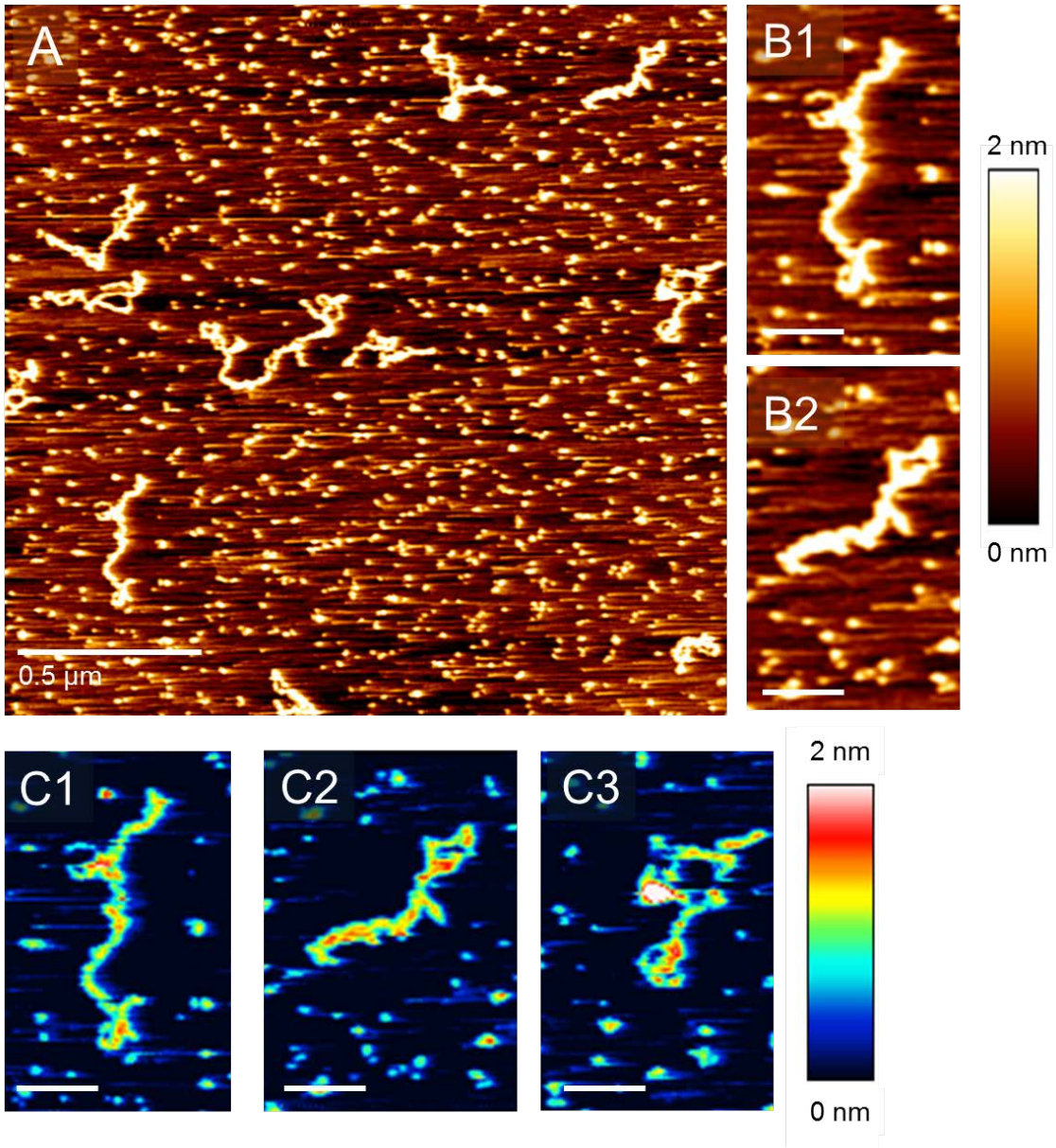

Figure 5.1. AFM images of the supercoiled pCERoriD plasmids. DNA (3.6 kb) was deposited in a solution containing 50 mM Tris.HCl, and 100 mM KCl. (A) Typical AFM image of the pCER*oriD* plasmid (2 x 2 µm field of view). The purified plasmids were in a negatively supercoiled form. (B-C) Software zooms of two individual molecules from (A). (C) Rainbow color scale indicating the heights measured from black (minimum height) to white (maximum height) of three supercoiled plasmids. The white scale bars represent 0.12 µm.

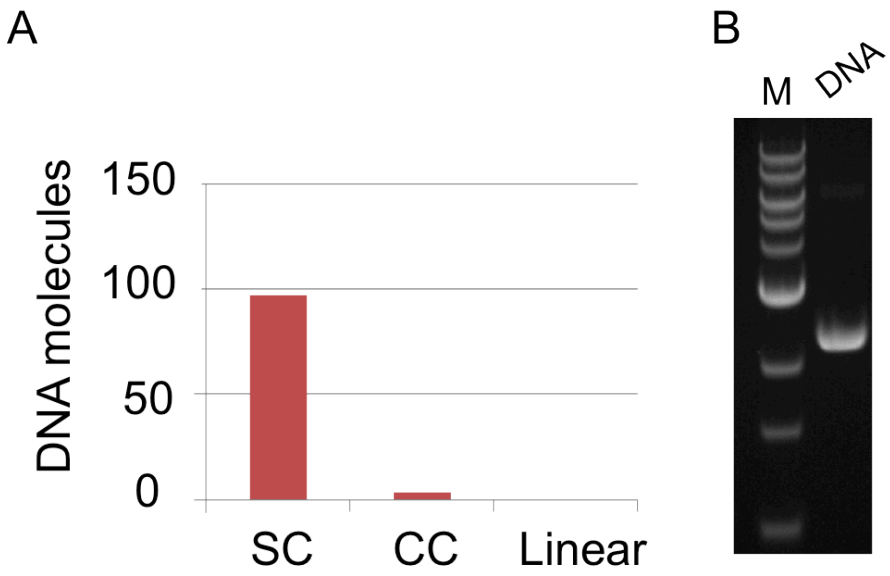

Figure 5.2. DNA topology analysis of a supercoiled plasmid sample. (A) Single plasmid DNA molecules imaged with AFM imaging, as shown in Figure 5.1, were analysed for their conformations. Analysis was performed over 100 DNA molecules. 97 DNA plasmids were negatively supercoiled (SC), 3 plasmids were closed circular (CC) and no linear DNA was detected. (B) Agarose gel analysis of plasmid topology. The DNA plasmid used in AFM experiments (Figure 5.1) was run on a 1% agarose gel. The gel band (DNA lane) indicates the supercoiled pCERoriD plasmid.

5.2.1. Effect of ionic conditions on DNA topology

The DNA samples described in the previous experiment were prepared in the absence of $MgCl_2$ and in moderate salt conditions. However, in the following experiments Mg^{2+} was introduced in the buffer as cofactor for the proteins. As previous works have shown that DNA conformation depends on environmental conditions and in particular on the ionic strength [116], another experiment was performed to investigate the effect of ionic conditions on the DNA conformation.

The DNA plasmids were prepared and absorbed on the mica at different salt conditions (Figure 5.3). In no salt condition, an obvious change in the supercoiled DNA geometry was observed, since the molecules became almost invariably irregular and folded with no defined superhelix axis (Figure 5.3A). This change is likely to be caused by the inhibition of spatial re-arrangements. The tightly twisted geometry typical of a conventional supercoiled DNA, seen at

higher salt conditions (Figure 5.3B-C, 100 mM KCl), was less evident compared to the DNA prepared at no salt conditions. Addition of Mg^{2+} in the high salt buffer sample improved the absorption of the supercoiled DNA on mica (Figure 5.3C). The axis of the supercoiled molecule was more defined and the DNA was tightly underwound. Typically, molecules assumed a branched "Y" shape, and the length of each branch randomly varied between molecules.

These results showed that the geometry of supercoiled DNA molecules was different depending on the environmental ionic strength. The high salt condition favored interhelical and intramolecular interactions. These observations were consistent with previous systematic theoretical studies, and with AFM studies showing that DNA conformations depend on the ionic conditions [116, 117].

The reaction buffer for the following AFM experiments reported in this investigation contained both KCl and $MgCl_2$ for an optimal activity of RepD. Accordingly with these results, the supercoiled DNA typically adopted the conformations showed in Figure 5.3C.

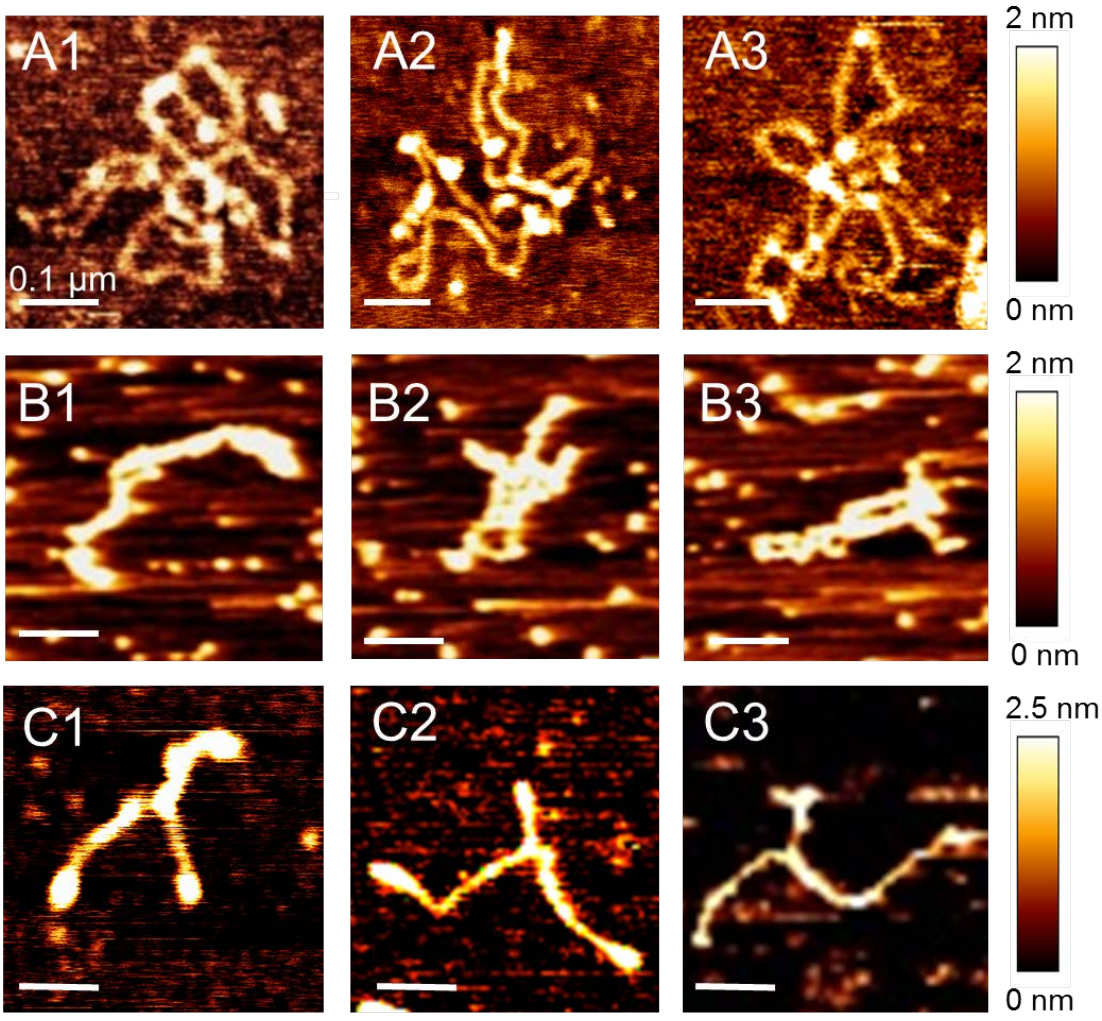

Figure 5.3. Effect of ionic strength on the plasmid DNA conformation. (A) DNA molecules absorbed on the surface in the presence of ddH_2O (no salt). The sample was then dried and scanned. Molecules appeared irregular, with random coiling and the presence of loose loops. (B) DNA sample prepared in same buffer conditions as shown in Figure 5.1. (C) DNA molecules absorbed on the surface in the presence of 50 mM Tris.HCl, 100 mM KCl and 10 mM $MgCl_2$. Larger field of view for each reaction are shown in the Appendix of this thesis.

5.3. RepD-mediated relaxation of supercoiled plasmids

As previously described, the supercoiled plasmid is the main substrate for RepD nicking activity. The initiator protein binds to the oriD sequence and relaxes the DNA plasmid through its topoisomerase-like activity (Figure 5.4A).

Here, the change in DNA topology caused by RepD activity was observed by imaging the final products of the relaxation reaction (Figure 5.4B). In this

experiment, an excess of RepD protein was incubated with a 3.6 kb supercoiled plasmid for 2 min to allow complete nicking. The reaction was then deposited on the mica surface for 30 s for absorption. The excess solution was removed, followed by washing with water and drying prior imaging. AFM images revealed the presence of relaxed plasmid DNA as extended circular molecules on the mica surface (Figure 5.4B). This was consistent with a previous study showing the relaxation products of the RepD-mediated reaction [51].

The RepD reaction products of a relaxation reaction were analysed for the DNA topology, and a frequency histogram was obtained from 100 plasmids as shown in Figure 5.5. The majority of the DNA molecules, ~96%, adopted the shape of unconstrained freely fluctuating rings without any intramolecular crossings (Figures 5.4B and 5.5). Some relaxed plasmids presented an “eight” shape. This alternative DNA conformation was likely to be produced during sample deposition and/or surface drying. The majority of the relaxed circular plasmids showed a single, high globular feature at a unique location on the DNA (Figures 5.5A2, 5.6A1). This was interpreted as the RepD protein covalently attached on the *oriD* (Figures 5.4B, B1). A small amount of unreacted plasmids, ~ 4%, could also be seen in their supercoiling state (Figures 5.4B, B2 and 5.5). The reaction also contained partially relaxed DNA molecules with local supercoiling (Figures 5.4B, B3). These molecules were interpreted as circular closed products (CC), as nicking and relegation events might also occur after sample deposition and/or during washing. Following deposition, the release of DNA supercoiling in such molecules might be limited by the interactions with the charged surface inhibiting a global relaxation of the DNA. Alternatively, RepD might partially relax the DNA as result of nicking and rapid religation. Such an activity might result from the buffer switching on the surface during sample preparation. Non-covalent binding of RepD on these molecules could not be distinguished due to the presence of coiling. Upon RepD incubation for 2 min, the amount of CC plasmids detected was ~ 36% (Figure 5.5B). However, DNA topology analysis of this reaction on a gel assay showed that the CC form was ~ 7% (Figure 5.5C). It is likely that sample preparation on the surface affect the RepD religation activity.

5.3.1. The RepD-DNA complex

In the previous section the effect of RepD on DNA topology was clearly demonstrated. As expected from a nicking reaction, RepD protein could be found attached on the relaxed DNA molecules (Figure 5.5A2). A rainbow color scale for height analysis allows a more clear visualisation of the RepD-DNA complex formation during a nicking reaction (Figure 5.6). The differences in heights between the dsDNA and RepD allowed a straightforward detection of the protein on the relaxed molecules.

The height analysis of the protein complex gave a value of ~ 2 nm (Figures 5.6B2-B3). Rarely, more than one RepD protein could be found attached on the plasmid (Figure 5.6A4). This was likely to be caused by the presence of potentially three RepD-binding sites (ICR I–III) within *oriD.* The binding of multiple RepD molecules at the *oriD* was also confirmed with a gel shift assay (see Appendix of this thesis).

These results are consistent with previous studies showing that RepD is able to bind at the different ICR sequences, albeit with different specificity [99].

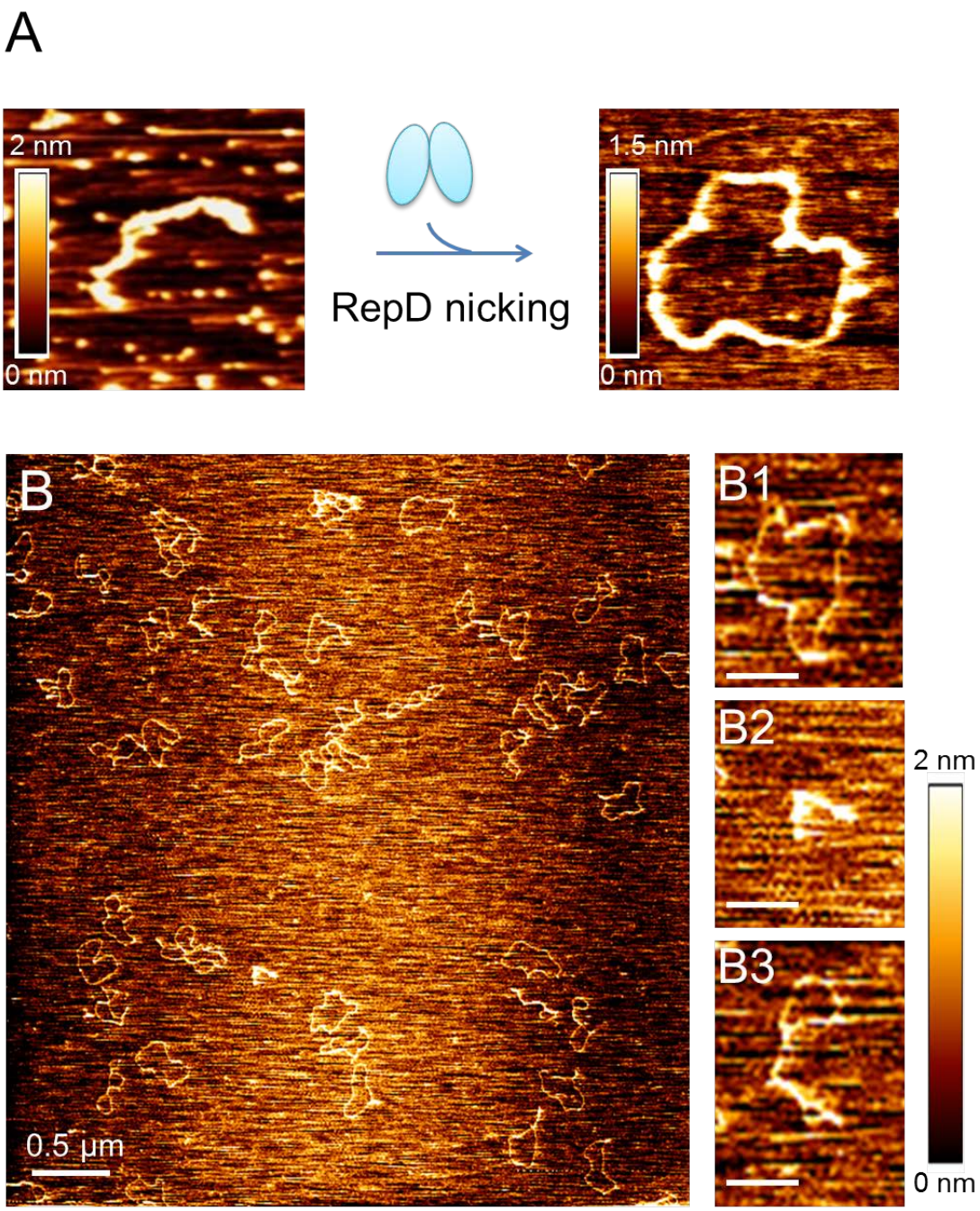

Figure 5.4. AFM images of the RepD-mediated relaxation of supercoiled pCERoriD plasmids. (A) The supercoiled pCERoriD plasmid is the native RepD substrate for nicking. The reaction causes release of supercoiling and so formation of a relaxed circular DNA. (B) A typical AFM image of plasmids products from a 2 min incubation with RepD. (B1-B3) Zooms of individual plasmids shown in (B) showing the different DNA topology. 10 µl of a solution containing 10 nM pCERoriD plasmid (3.6 kb) and 30 nM RepD, in 50 mM Tris.HCl, 10 mM MgCl2 and 100 mM KCl, was deposited on a freshly cleaved mica surface following 2 min incubation of the reaction.

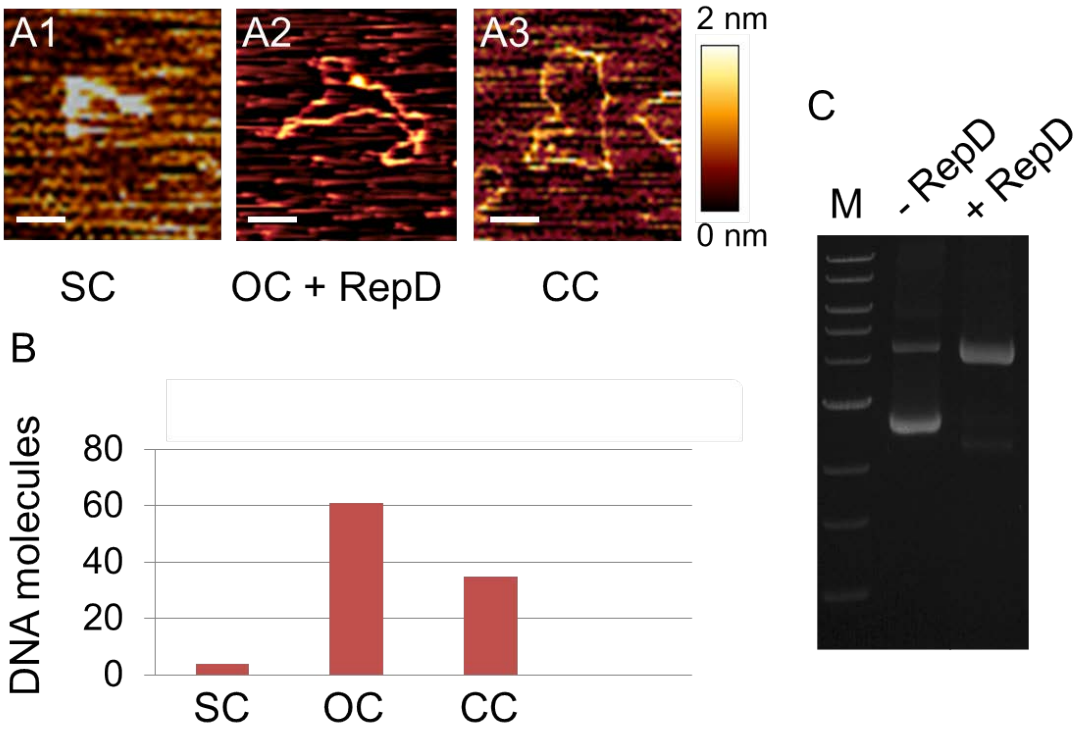

Figure 5.5. DNA topology analysis of a nicking reaction performed by RepD on supercoiled pCERoriD plasmids. (A) Typical images of the plasmid topology of the RepD-mediated relaxation products. (B) Histogram representation of the DNA topology analysis performed over 100 DNA molecules imaged by AFM. SC: residual unreacted supercoiled plasmids as shown in (A1); OC: open circular relaxed plasmid with a visible RepD molecule attached as shown in (A2); CC: circular closed relaxed plasmids as shown in (A3). (C) Agarose gel analysis of the nicking reaction. Upon RepD incubation for 2 min, ~91% of OC plasmid is produced (+ RepD lane). The SC plasmid substrate used as RepD substrate is also shown (- RepD lane).

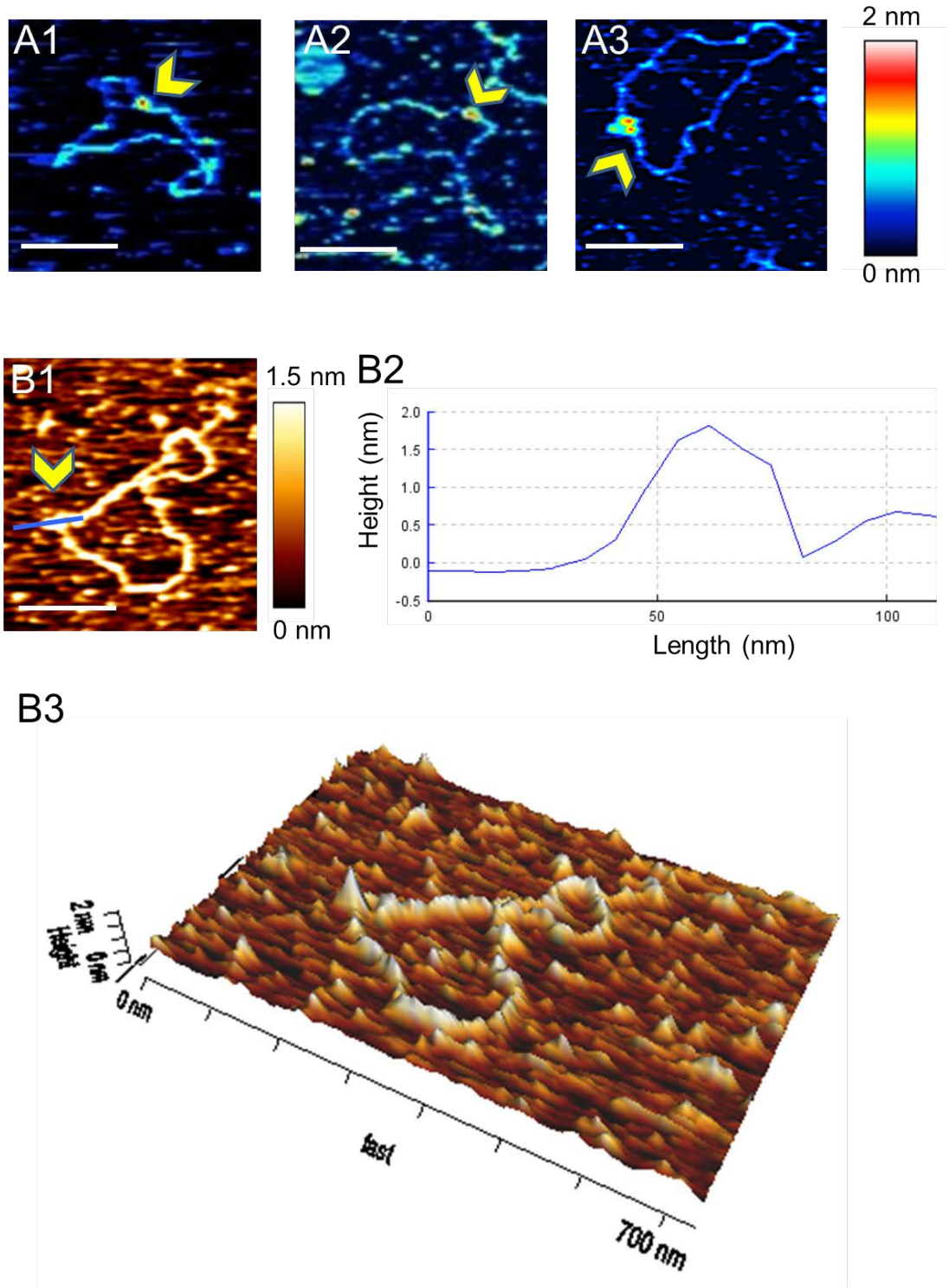

Figure 5.6. Visualisation of the RepD-DNA initiation complex by AFM. (A1-A3) Colour scale representation of RepD (in red) bound to relaxed pCERoriD plasmids (3.6 kb). Individual red dots represent RepD dimers. (B1-B2) Cross section and corresponding height profile and three-dimensional representation (B3) of the RepD-DNA complex. The height was 1.8 ± 0.3 nm (width: ~ 20 nm for one RepD dimer). Reactions were prepared as described in Figure 5.4. The scale bar represents 200 nm.

5.4. Different length DNA plasmids

Two different lengths of pCERoriD plasmid, the 3.6 kb and 6 kb plasmids, have been imaged in order to calculate an average of the DNA length and compare their geometrical conformations. A direct comparison of the plasmid images in their supercoiled and relaxed forms is shown in Figure 5.7. Despite their difference in the DNA size, the plasmids presented a similar conformation on the surface. As described previously for the 3.6 kb plasmid, the 6 kb supercoiled plasmid also showed a "Y" shape with three main arms and a central knot (Figure 5.7 A), whereas the relaxed plasmids formed random rings (Figure 5.7 B-C).

The length of the DNA axis was relatively uniform between the DNA molecules of a plasmid population of a certain length. The average lengths calculated from 50 molecules were 0.36 µm for the 3.6 kb and 0.6 µm for the 6 kb in their supercoiled form (Figure 5.8A-B), and 0.95 µm for the 3.6 kb and 1.87 µm for the 6 kb in their relaxed form (Figure 5.8C-D).

Some DNA binding proteins can change the contour length of DNA. For example, the RecA protein elongates a DNA molecule by 50% when it is completely covered [118]. However, only up to three RepD dimers can bind the *oriD*, so protein binding should not affect significantly the DNA length. To investigate this, the contour length of circular DNA molecules with attached RepD proteins was measured. There was no significant change in the DNA contour length between the open (+ RepD) and closed (- RepD) circular plasmids, and so binding of RepD does not have a major effect (Figures 5.7B1, C1)

Such measurements allowed the calculation of the base spacing values, which gave similar results for both plasmid DNA lengths with a value 0.1 nm bp^{-1} for supercoiled DNA and of 0.3 nm bp^{-1} from relaxed double-helical molecules. The latter value is similar to that measured in previous studies (0.28–0.34 nm bp^{-1}, and is consistent with the expected value of the B-form DNA, which is the most common physiological form of DNA [113]. The reduced value of the base spacing in the supercoiled DNA compared to the relaxed molecule is consistent with the packaging role of supercoiling.

For both plasmids, the height and the width were fairly uniform along the DNA fibre. The height of the dsDNA fibre had a value of 1.2 ± 0.2 nm, which is smaller than the theoretical value of the B-form DNA (~2 nm). Such a difference is likely to be caused by the tip-sample interactions and the force applied by the tip during scanning that can compress the molecules.

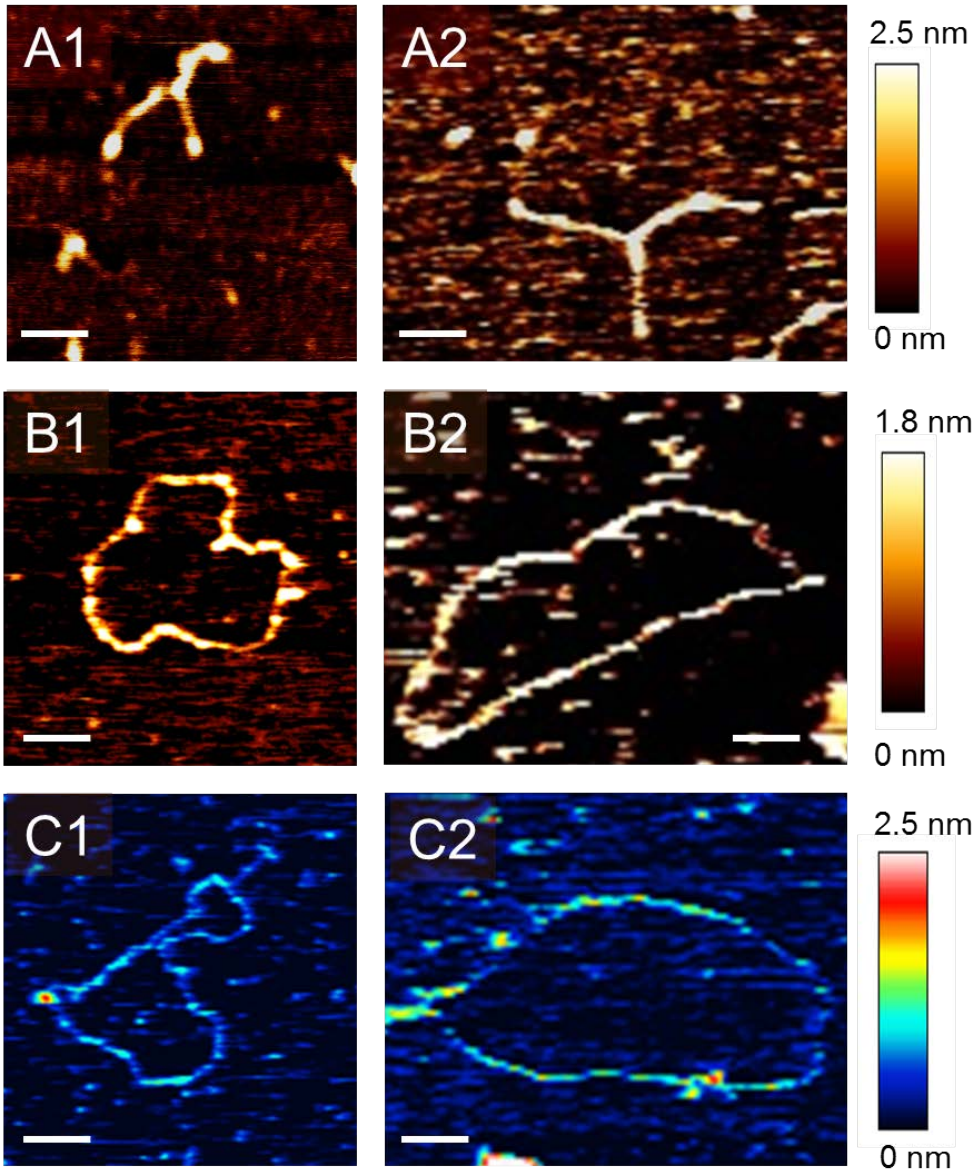

Figure 5.7. Direct comparison of different length pCER*oriD* plasmids visualised by AFM. (A1-B1) 3.6 kb plasmid in its supercoiled and relaxed circular form respectively. (A2-B2) 6 kb plasmid in its supercoiled and relaxed form respectively. Colour scale representation of the RepD protein (red dot) on the 3.6 kb plasmid (C1) and the 6 kb plasmid (C2). Solutions were prepared as described in Figures 5.3C and 5.4.

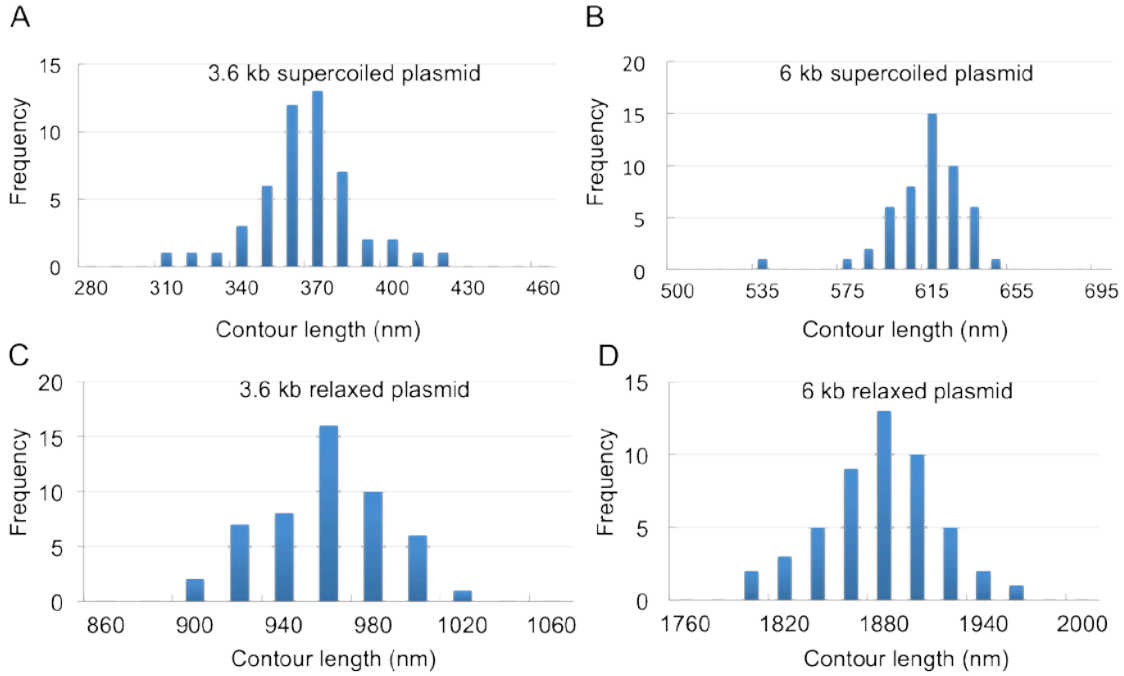

Figure 5.8. Histograms of DNA contour length measured from two different length plasmids with or without supercoiling. All DNA length measurements were from images collected from one deposition of molecules from one reaction mixture. Measurements of contour length of a 3.6 kb (A and C) and 6 kb plasmid (B and D). The average lengths calculated from 50 molecules (mean value ± standard deviation) were 0.36 ± 0.02 μm for the 3.6 kb and 0.6 ± 0.01 μm for the 6 kb in their supercoiled form, and 0.95 ± 0.03 μm for the 3.6 kb and 1.87 ± 0.03 μm for the 6 kb in their relaxed form. In these measurements, the contour length is referred as a measure of the linear distance between the two endpoints of a DNA molecule, and it differs by the standard definition of the contour length which defines the distance along the curved DNA backbone.

5.5. Unwinding of supercoiled pCERoriD plasmids by PcrA and RepD

5.5.1. Unwinding of supercoiled plasmids without SSB

Following RepD-mediated nicking, the supercoiled plasmid is converted in its relaxed form, which is the accessible to the replicative helicase, PcrA.

In an effort to explore the dynamics of PcrA-mediated plasmid unwinding, the pCERoriD plasmid was incubated with RepD, PcrA, and ATP, in the absence of SSB, and the reaction products were imaged by AFM.

Unwinding reactions were initiated in solution and then two different time points (~30 s and 2 min) were quickly collected and stopped by dilution in buffer. These were than deposited onto a mica surface and dried. With this procedure, partial and complete unwinding events could be visualised in order to monitor the progress of DNA unwinding catalyzed by PcrA.

Upon a relatively short incubation time of the reaction (~ 30 s), two main populations of plasmids were imaged (Figures 5.9 and 5.10). Some relaxed circular plasmids showed a single globular feature at a unique location (Figure 5.9). The three-dimensional analysis of this structure revealed a double peak with a main height at 3.5 nm with a shoulder at ~ 2 nm. This is likely to represent the PcrA-RepD initiation complex since RepD alone on DNA has a similar height of the shoulder (~ 1.8 nm, Figure 5.6). The latter was a usual feature detected for the complexes found on DNA plasmids and analysis of additional complexes is found in the Appendix of this thesis.

In addition, various plasmids were found at early stages of unwinding. Recruitment of PcrA by RepD as shown in Figure 5.9 is then followed by DNA unwinding (Figure 5.10). DNA plasmids had globular structures of various dimensions flanking the DNA axis. These represented the partially coiled ssDNA produced by PcrA, and their measured heights were ~1.5 nm. On such plasmids, the PcrA-RepD complex was also visible (indicated by the yellow arrows in Figure 5.10B-C). These had comparable height profiles to those observed in Figure 5.9.

These results indicated that PcrA helicase could be loaded onto a nicked relaxed plasmid and most interestingly the RepD-PcrA complexes were formed during initiation and early unwinding.

As mentioned above, a longer reaction incubation time was also analysed in order to image the final unwinding products (~2 min., Figure 5.11). Interestingly, PcrA-mediated unwinding produced plasmids with “web-like” shapes. As shown from the heights analysis, the PcrA-RepD complex could be detected on some plasmids (Figure 5.11). In some occasions, molecules had loops emerging out

of a central condensed knot representing RepD-PcrA complex (Figures 5.11A1 and C1). Other plasmid molecules had loops randomly alternated with ssDNA (Figure 5.11C2-C3), and occasionally the unwinding complex could be found freely along the DNA axis of such plasmids (Figure 5.11C2). The number of loops and their distribution along the DNA varied between molecules. These structures are likely to be generated, in the absence of SSB, by PcrA-mediated unwinding and partial reannealing occurring randomly after passage of the helicase. Thus, the DNA structures were caused by the topological constraints of the (-)-strand of the circular plasmids, which, upon unwinding, had to rotate in order to reanneal. This could also explain the different DNA conformations assumed around the RepD-PcrA complex at different stages of unwinding. The RepD-PcrA complex was found at the condensed center of the plasmid molecule for uncompleted unwinding events. Plasmid unwinding resulted in either dissociation of the complex (Figure 5.11B2-C3), or its location on a stretch of dsDNA at termination (Figure 5.11B1-C2). More rarely, the formation of condensed ssDNA irregular structures was evident (Figure 5.11A1). These were possibly produced by inhibition of DNA reannealing through extra PcrA molecules binding and/or translocating along ssDNA stretches produced upon unwinding.

These results indicated that helicase-mediated plasmid unwinding could be performed in the absence of SSB. Thus, SSB is not an absolute requirement for efficient unwinding and stimulation of PcrA by RepD occurs independently by the presence of SSB protein. However, it is still unclear whether the presence of SSB could affect PcrA unwinding speed and/or the helicase forward movement along DNA.

From a direct comparison between the two unwinding times analysed above, it is clear that early deposition of the DNA on the surface inhibited the formation of loops favoring the appearance of ssDNA condensed structures along the DNA (Figures 5.10 and 5.11). The presence of ssDNA could be caused by unwinding events occurring on partially immobilized molecules over the surface, and so the ssDNA formed *in situ* would be locally trapped by interactions with the surface whilst inhibiting reannealing.

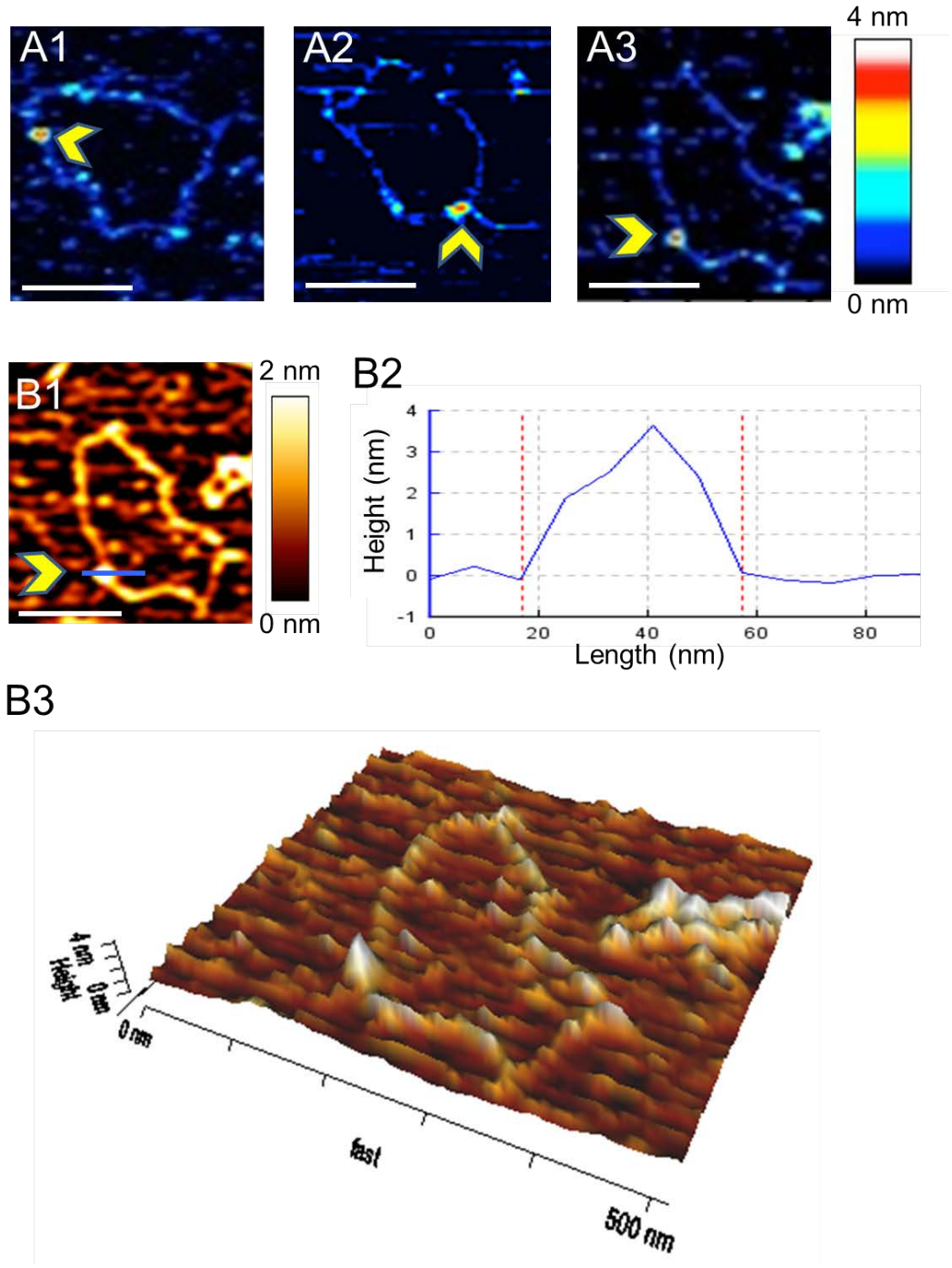

Figure 5.9. Visualisation of the RepD-DNA-PcrA complex by AFM. (A1-A3) Colour scale representation of the complex, in red, bound to a relaxed pCERoriD plasmid (3.6 kb), formed in a 30 s incubation time reaction. (B1-B2) Cross section and corresponding height profile and three-dimensional representation (B3) of the PcrA-RepD complex. The height measurement showed a peak of maximum height at 3.5 nm with a shoulder ~ 2 nm was observed for the complex (width: ~40 nm). The scale bar represents 200 nm.

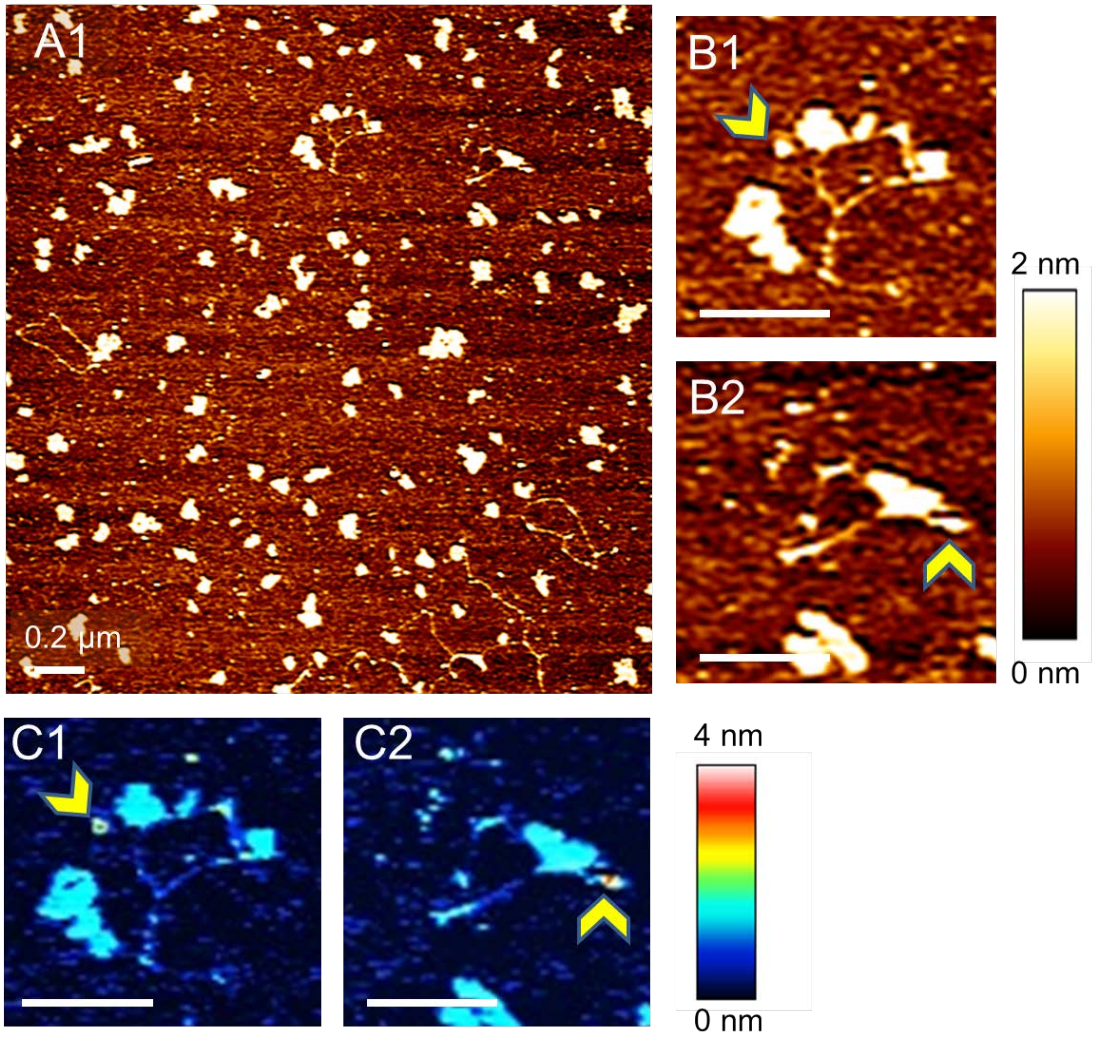

Figure 5.10. Visualisation of early plasmid unwinding events by RepD-PcrA complex. Reaction contained 10 nM plasmid (pCERoriD, 3.6 kb), 60 nM RepD, 90 nM PcrA, and 1 mM ATP, and was incubated for 30 s prior sample deposition. (A1) AFM topographical image of the unwinding reaction products. (B1-B2) Zooms of two DNA plasmids having the PcrA-RepD complex. (C1-C2) Colour scale representation of the plasmids showed in (B). In red, indicated by the arrows, is the RepD-PcrA complexes bound to the pCERoriD plasmids (3.6 kb). The condensed structures represent ssDNA wrapped along the circular plasmid. The scale bar represents 200 nm.

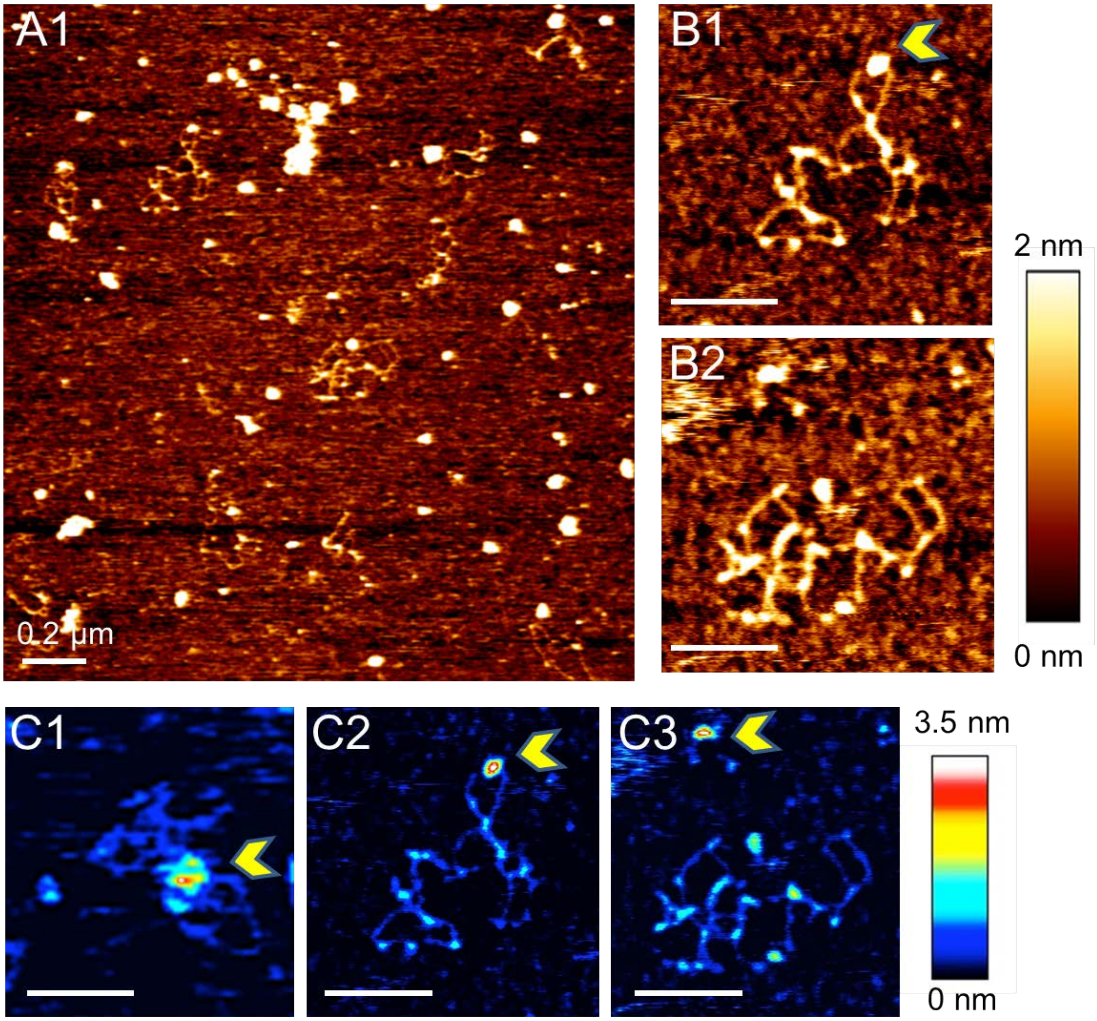

Figure 5.11. Visualisation of late plasmid unwinding events by RepD-PcrA complex. Reaction contained 10 nM plasmid (pCERoriD, 3.6 kb), 60 nM RepD, 90 nM PcrA, and 1 mM ATP, and was incubated for 2 min prior sample deposition on mica. (A1) AFM topographical image of the unwinding reaction products. (B1-B2) Zooms of two DNA plasmids having the typical "web-like" conformation. (C1-C3) Colour scale representation of the unwound plasmids. In white, indicated by the arrows, is the RepD-PcrA unwinding complex. The condensed structures represent wrapped ssDNA along the circular plasmids. The scale bar represents 200 nm.

5.5.2. Unwinding of supercoiled plasmids with SSB

The AFM experiments described above were performed in the absence of SSB. *In vivo*, the SSB participates in the replication event by sequestering the ssDNA produced through the helicase activity. In order to simulate the *in vivo*

conditions, the intermediates of DNA unwinding in the presence of SSB were visualised by AFM. Thus, pCERoriD was treated with RepD and incubated with PcrA and ATP, in the presence of SSB. Reaction products from two time points were then scanned (30 s and 2 min). With this strategy, early PcrA unwinding should occur by the first time point (30 s) and be near to completion for the second time point were expected as expected from the PcrA unwinding speed measurements described in Chapter 3.

Typical AFM images obtained from such reactions are shown in Figures 5.12 and 5.13. Upon incubation of the reaction for 30 s, PcrA-RepD-mediated unwinding of DNA plasmids was detected and SSB coating of the ssDNA produced was clearly visible (Figure 5.12A). The analysis of the SSB coated regions of DNA displayed divergent heights depending on the amount of SSB bound to the region (from 4 nm, Figure 5.12C). This was caused by poor absorption of the complexes on the mica possibly due to interactions between adjacent SSB tetramers. There was some heterogeneity in the extent of dsDNA unwound between molecules (Figure 5.12C). However, the majority of the DNA molecules presented the conformation showed in Figure 5.12B. The presence of DNA plasmids at slightly different stages of unwinding is possibly caused either by late nicking events or complex pausing during unwinding.

On a longer incubation time (2 min), complete plasmid unwinding should occur, and this was detected as disappearance of dsDNA and presence of condensed structures representing SSB molecules on ssDNA (Figure 5.13). Only a small fraction of plasmids had some residual dsDNA due to late unwinding events (Figures 5.13B1-C1-C2). In the presence of SSB, the RepD-PcrA complex could not be detected on the plasmids.

These results showed that rapid SSB binding follows unwinding and ssDNA production by PcrA. The presence of SSB promoted progressive unwinding and release of the two single stranded DNA molecules.

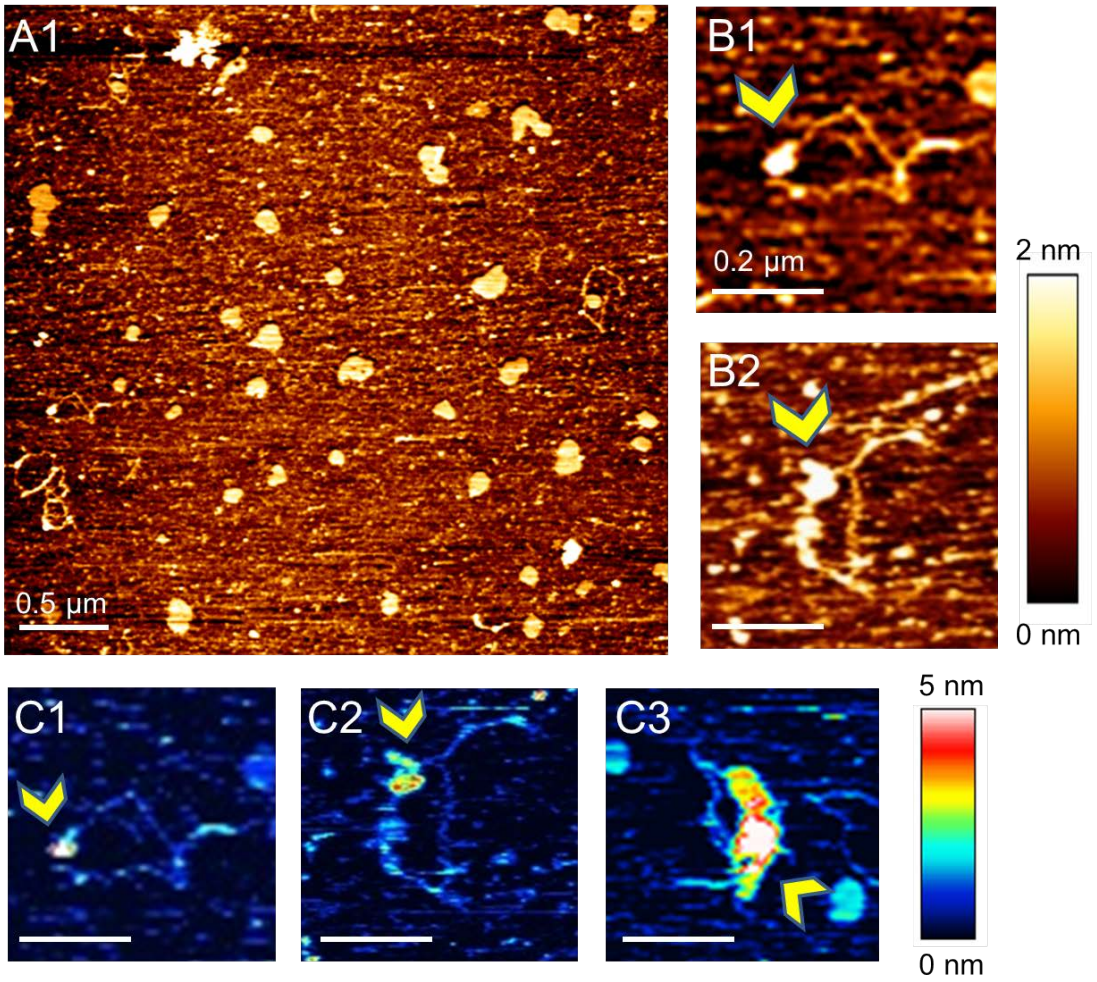

Figure 5.12. Visualisation of early plasmid unwinding events by RepD-PcrA complex in the presence of SSB. Reaction contained 10 nM plasmid (pCERoriD, 3.6 kb), 60nM RepD, 90nM PcrA, 500 nM SSB, and 1 mM ATP, and was incubated for 30 s prior sample deposition. (A1) AFM image of the unwinding reaction products. (B1-B2) Zooms of two DNA plasmids with the SSB bound. (C1-C3) Colour scale representation of the unwound plasmids. In white and red, indicated by the arrows, are the SSB-DNA complexes on the pCERoriD plasmids.

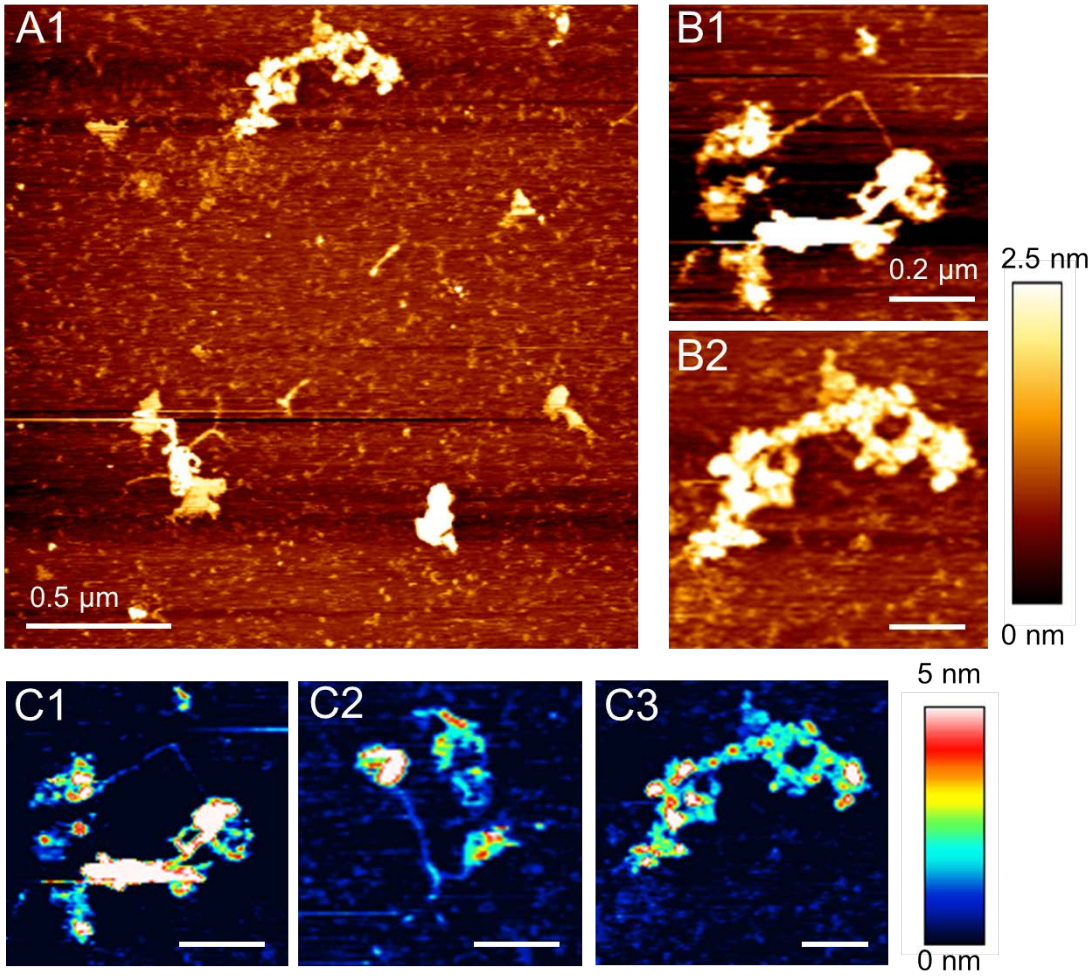

Figure 5.13. Visualisation of late plasmid unwinding events by RepD-PcrA complex with SSB. Reaction contained 10 nM plasmid (pCERoriD, 3.6 kb), 60nM RepD, 90nM PcrA, 500 nM SSB, and 1 mM ATP, and was incubated for 2 min prior sample deposition. (A1) AFM image of the unwinding reaction products. (B1-B2) Zooms of two DNA plasmids with the SSB bound. (C1-C3) Colour scale representation of the unwound plasmids. In white and red, indicated by the arrows, are the SSB-DNA complexes on the pCERoriD plasmids. The scale bar represents 200 nm.

5.6. PcrA-RepD mediated unwinding of linear plasmids

AFM experiments using linear DNA substrates were carried out to study PcrA ability to perform unidirectional unwinding. A supercoiled 4.9 kb pCERoriD plasmid was used as substrate to produce linear DNA by restriction enzyme digestion.

Typically, linear DNA molecules were generally rope-like in shape with random conformations when absorbed on the surface (Figure 5.14A1). The average length of the molecules was 1.38 ± 0.02 μm, consistent with measurements of the DNA duplex length showed in section 5.4.

Linearising the DNA plasmid with HindIII placed the *ori*D at the 5′ -end of the (+)-strand (Figure 5.15). Formation of the RepD-PcrA complex on the HindIII-cut plasmid was observed from detection of a distinctive feature at this location (Figures 5.14A2-A3). The height analysis showed similar results to those measured on circular plasmids (section 5.5.1). Upon ATP-dependent unwinding and in the absence of SSB, a loop was detected on the linear DNA. The linear DNA decreased in length as the loop increased (Figures 5.14B2-B3). A simple interpretation of these results is that the loop structure resulted from the forward movement of the helicase along DNA upon duplex unwinding and subsequent reannealing (Figure 5.15B). A condensed globular feature was found on the linear DNA axis and it is believed to be the RepD-PcrA complex with condensed newly generated ssDNA located at the unwinding fork (Figure 5.15B).

Unwinding of the linear DNA was also monitored in a reaction containing SSB (Figure 5.15C). AFM images showed relatively large condensed structures representing ssDNA molecules, products of complete plasmid unwinding from the origin. The overall conformation and the heights of such molecules were similar to those formed during unwinding of circular plasmids described above. Several unreacted linear plasmids were detected in the unwinding solutions (~36%). The presence of such a significant plasmid population was possibly caused by a lower extent of the RepD-mediated nicking on linear DNA substrates. This is consistent with the unwinding measurements performed with linear DNA and described in Chapter 3.

Previous work has established that PcrA displays unwinding only in the 3′ > 5′ direction [51, 98]. Here, linear DNA plasmids having the *ori*D placed at different positions along the DNA were generated in order to investigate further PcrA directional loading and unwinding. The three linear pCERoriD plasmid substrates used in this experiment and the final unwound products are shown in Figure 5.15. AFM images of the HindIII-cut plasmid are already shown in Figure

5.14. Linearising the plasmid with NdeI and NgoMVI places the *ori*D at around half and a close position relative to the 3′ -end of the (+)-strand, respectively. AFM images of the unwinding reactions of such substrates are shown in Figure 5.16. On some plasmids, the RepD-PcrA complex was evident and was found at the *ori*D (indicated by yellow arrows, Figures 5.16A2-B2-C2). The amount of ssDNA produced was consistent with the distance between the *ori*D and the 3′-end of the (+)-strand. The NgoMVI-digested plasmid was mainly detected in its double stranded form with an apparent short unwound tail (Figures 5.16A1-A3). The NdeI-cut plasmid was around half of its length unwound (Figures 5.16B1-B3). The HindIII-digested plasmid was fully unwound, as described above (Figure 5.16C1-C3).

These results confirmed the unidirectional (3′ > 5′) unwinding mechanism of PcrA helicase, and were consistent with previous observations [51].

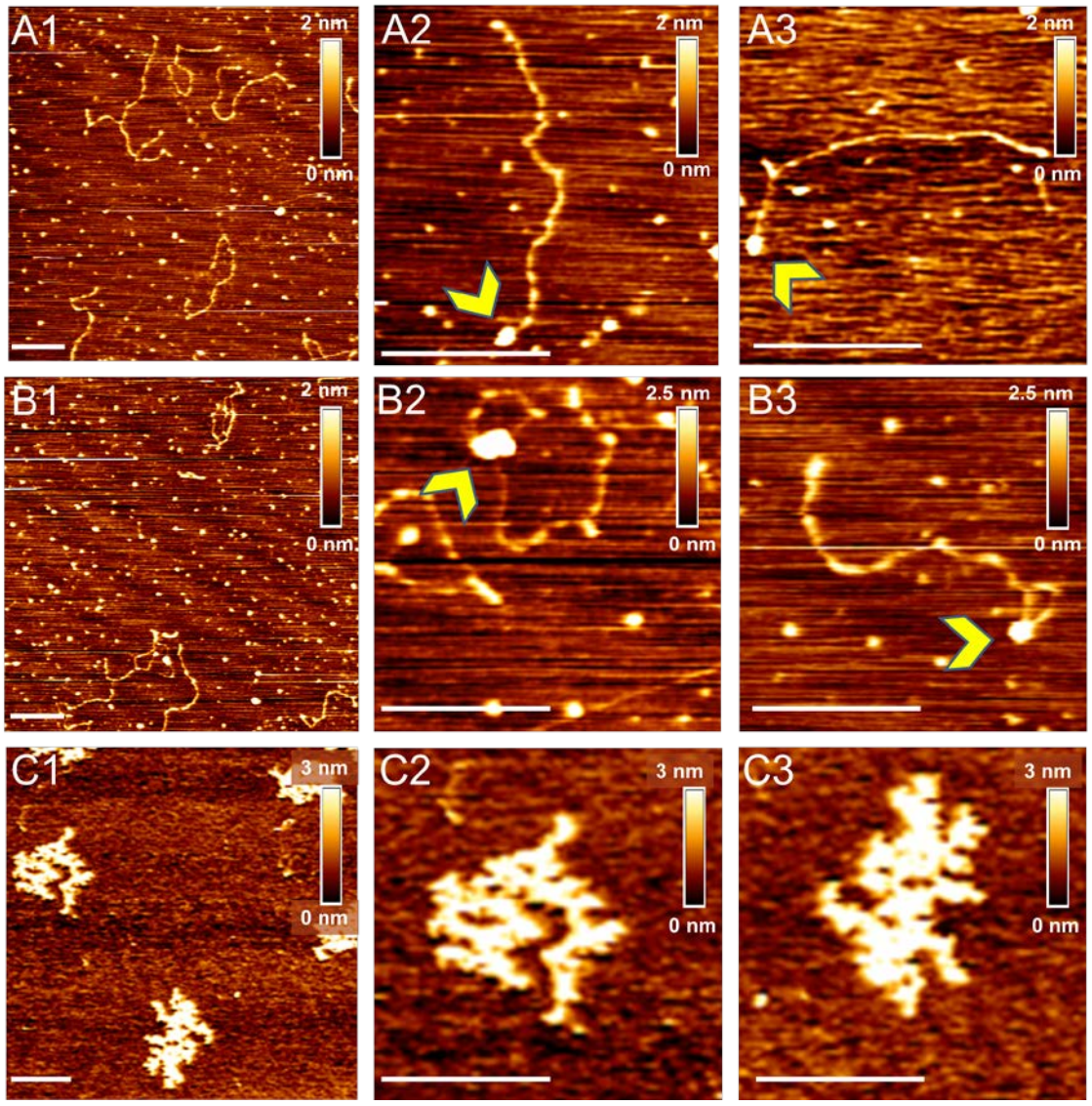

Figure 5.14. AFM visualisation of RepD-PcrA-mediated unwinding of HindIII-cut pCERoriD. (A1) Linearised pCERoriD 4.9 kb plasmid molecules. (A2-3) Formation of the RepD-PcrA initiation complex on linear DNA. (B1-B3) PcrA-mediated partial unwinding of linear plasmids in the absence of SSB. 10 nM plasmid, 60 nM RepD, 90 nM PcrA, were incubated for 10 min prior starting the reaction with 1 mM ATP. Reaction were taken and deposited on the surface after ~ 10 s. of unwinding reaction. (C) PcrA-mediated unwinding of linear plasmids in the presence of SSB. The scale bars represent 500 nm. Unwinding reaction contained 10 nM plasmid, 60nM RepD, 90nM PcrA, 100 nM SSB, 1 mM ATP, and was incubated for 10 min prior sample deposition and scanning.

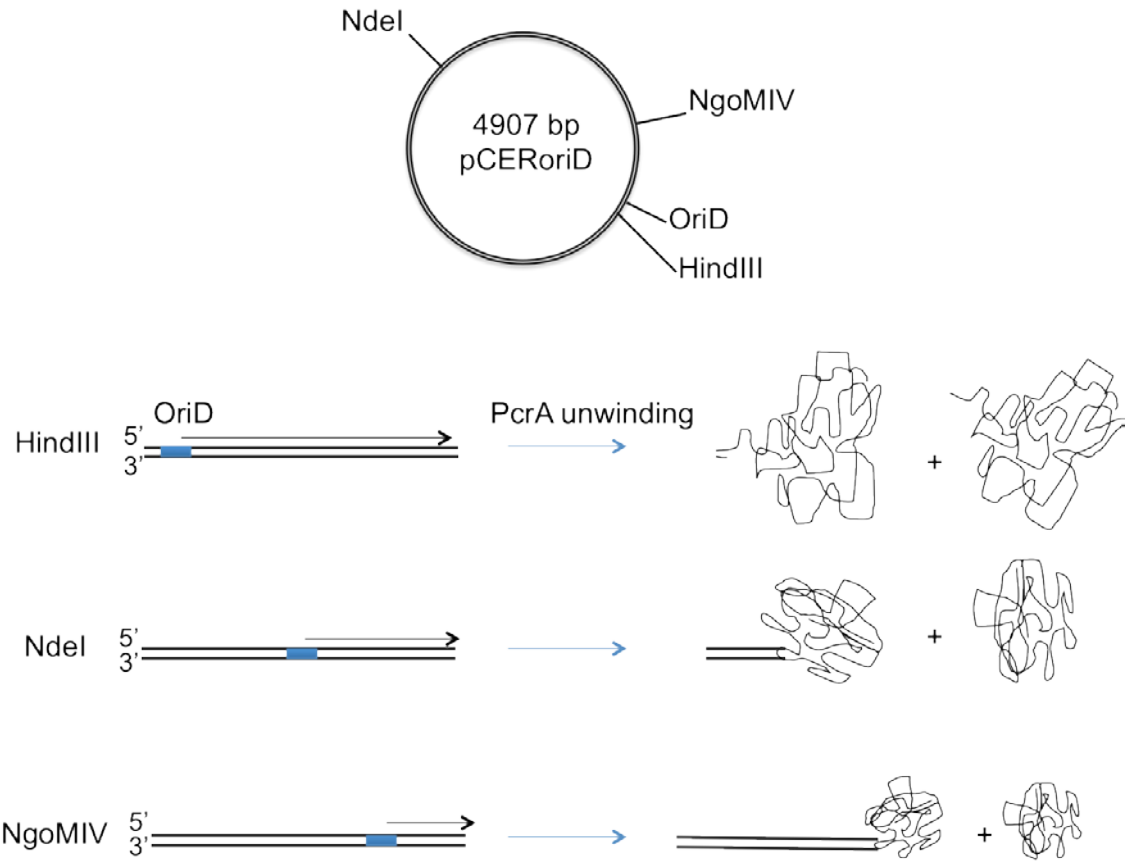

Figure 5.15. Unidirectional RepD-PcrA mediated unwinding of linear pCERoriD plasmids. Schematic representation of the 4.9 kb pCERoriD plasmid used to generate the linear DNA substrates. Digestion of the plasmid with different restriction enzymes placed the *oriD* at different positions in respect to the 3′ -end of the (+)-strand. This strategy allows monitoring unidirectional unwinding (3′ > 5′) from the *oriD* by PcrA helicase.

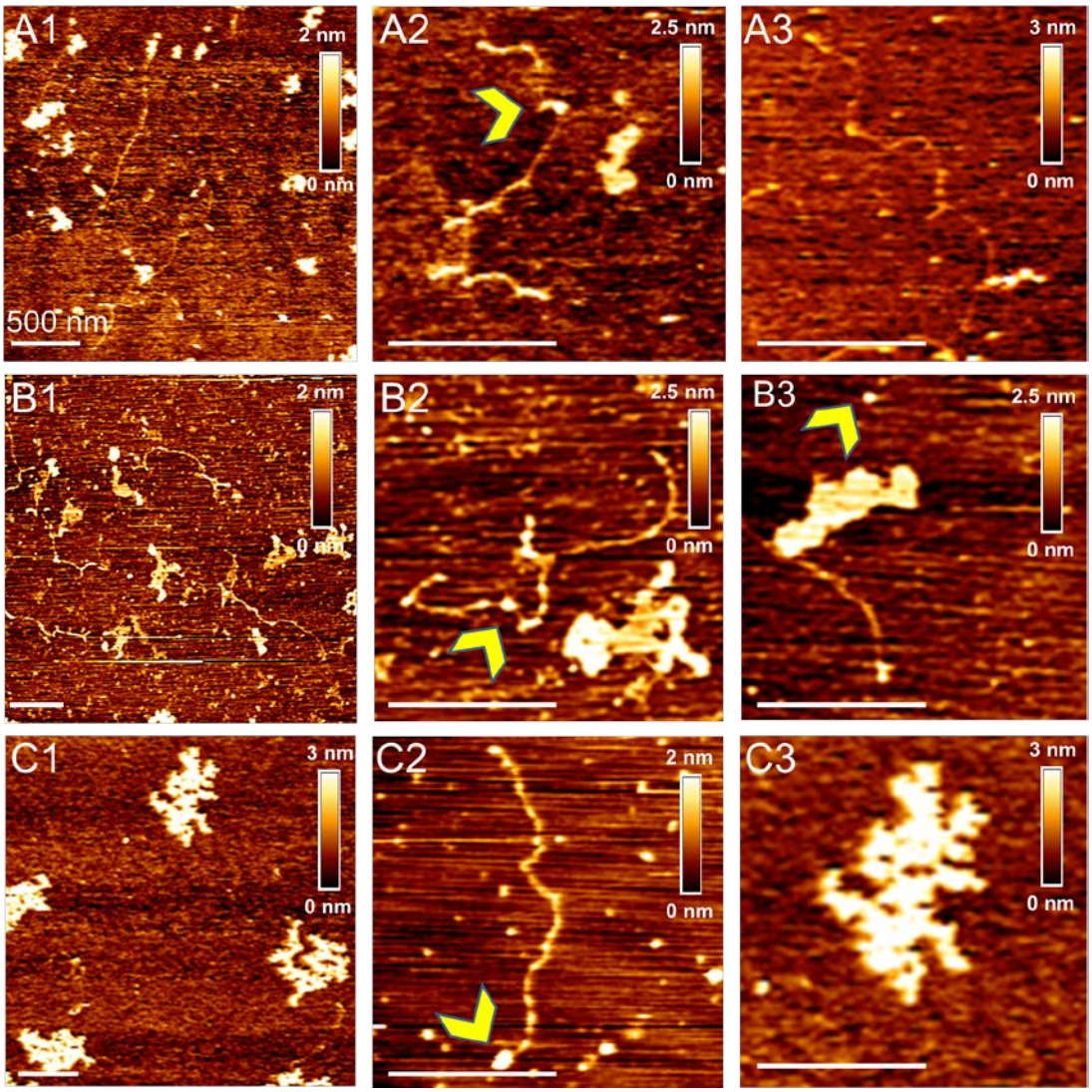

Figure 5.16. AFM visualisation of RepD-PcrA-mediated unwinding of linear pCERoriD plasmids. The 4.9 kb pCERoriD plasmid was digested with NgoMVI (A), NdeI (B), or HindIII (C). Field (A-C1) and zooms images (A-C-3) of the final unwinding products. (A-C2) Images showing the RepD-PcrA unwinding complex on linear DNA at the *oriD* located at different positions (yellow arrows). Formation of the unwound condensed ssDNA was detected. Samples were prepared as described in Figure 5.14C. The scale bars represent 500 nm.

5.7. Replication of supercoiled pCERoriD plasmid

Plasmid replication requires the activity of a high-fidelity DNA polymerase in order to produce a copy of the template strand. Experiments described above were performed in the absence of DNA polymerase in order to investigate the unwinding mechanisms and the helicase interactions. Presently, only few AFM

studies have shown the final products of DNA replication. In such studies, DNA polymerases were assayed via replication of the single-stranded ϕX-174 [113, 114]. Here, the intermediates of pCERoriD plasmid replication were investigated.

As described in the Introduction, in such a replication mechanism, PolC extends the (+)-strand using the (-)-strand as template for DNA synthesis. At the end of the process, a circular ssDNA and a new dsDNA plasmid molecule are produced. To investigate this process directly, the supercoiled plasmid (3.6 kb pCERoriD) was treated with RepD, PcrA, PolC, and SSB, and then the reaction was taken at two different incubation times (~10 s. and 1 min.) and imaged. Imaging the replication intermediates was demanding as large condensed complexes could be found in close proximity of the DNA, and so low PolC and SSB protein concentrations were used in this experiment to improve imaging.

Typical AFM images of the reaction products are shown in Figures 5.17 and 5.18. Upon a short incubation time, the majority of plasmids had a relatively large feature at a unique location along the DNA (Figure 5.17A). This structure had a maximum height of 9 nm, and presented two adjacent peaks of 6 and 2.5 nm (Figure 5.17C). The presence of several peaks suggested that this structure was a multiprotein complex. This was interpreted as the replisome complex, with the PolC neighbouring the RepD-PcrA complex at the replication fork. In some occasions, additional structures were found in close proximity of the big complex (Figure 5.17B). The simplest interpretation of such structures was that, as DNA unwinding and replication proceeded; the SSB protein trapped the displaced (+)-strand behind the replisome. However, the details of such an intermediate could not be clearly imaged as the large protein complex could partially “hide” the DNA structure, leading to lower-quality images.

A longer incubation time of the reaction was also analysed in order to visualise the final DNA products following synthesis (Figure 5.18). Two main populations of DNA were detected on the surface: circular DNA plasmids and ssDNA molecule were evident. These products were consistent with complete replication of the plasmid and release of the parental (+)-strand, in agreement

with the asymmetric model of synthesis. In some occasions, a large complex could be seen on the DNA plasmid (Figures 5.18B2-C2). This had a height value similar to those observed in Figure 5.17, and was thought to be the replisome complex. A globular structure was found in the close proximitiy of few circular DNA molecules, as shown in Figure 5.18C3. Its height was ~8 nm, and was interpreted as a released PolC protein following complete replication.

The overall reaction contained a similar number of ssDNA and circular molecules, albeit with few more ssDNA molecules. The increased amount of ssDNA compared to relaxed DNA was possibly caused by the non-saturating concentration of PolC used in this experiment in order to control the sample heterogeneity conditions and prevent the sticking of giant messy macromolecular complexes on the surface.

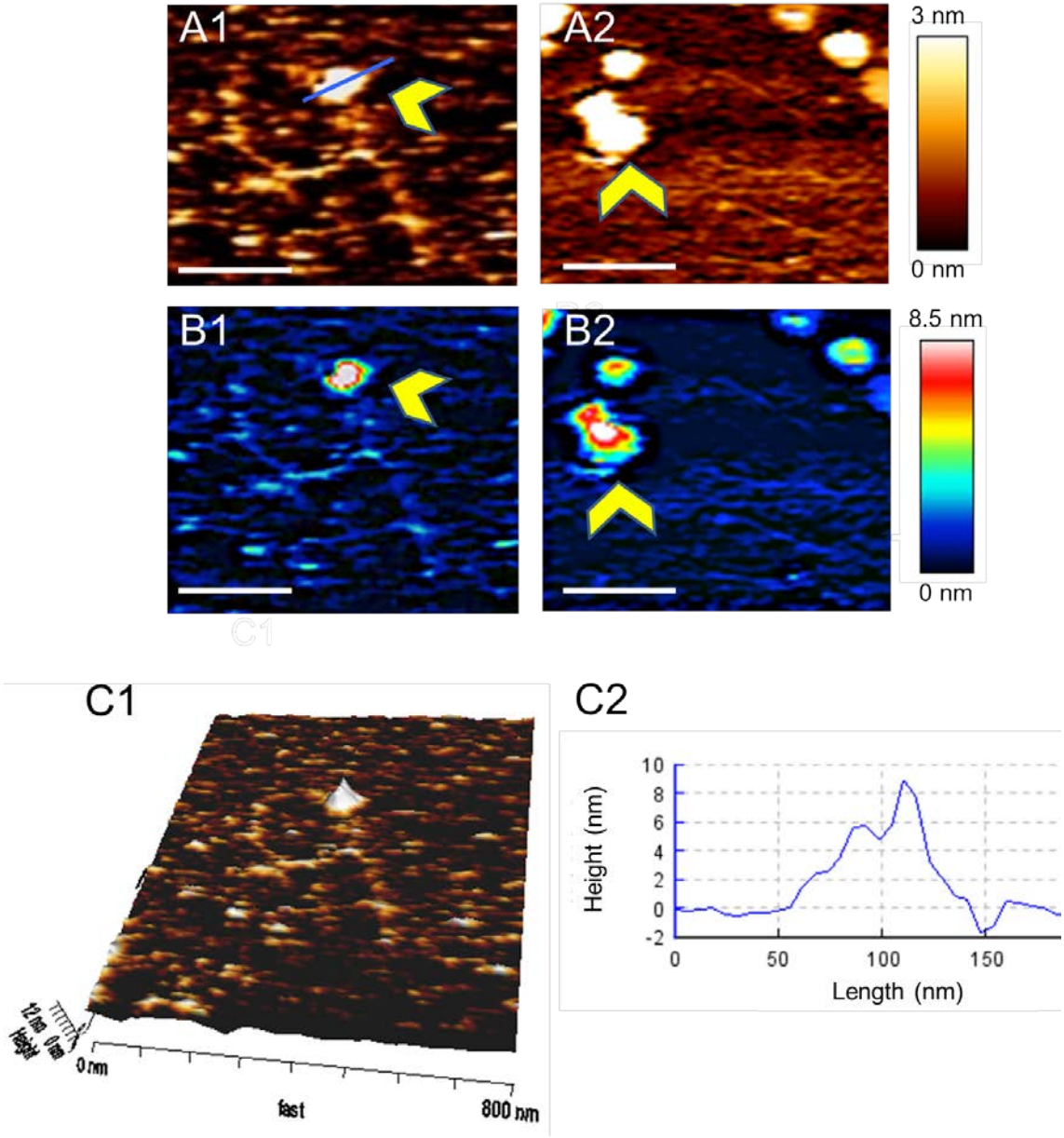

Figure 5.17. AFM visualisation of plasmids during the initial stages of replication. 10 nM plasmid, 60 nM RepD, 90 nM PcrA, 200 nM PolC, 100 nM SSB, 1 mM ATP, 1 mM dNTPs were incubated for 10 s. prior sample deposition and scanning. (A1-A2) AFM images of plasmids with a condensed structure bound on the DNA duplex (yellow arrows). (B1-B2) Colour scale representation of the plasmids displayed in A showing the relative heights of the surface. (C) 3D surface plot of A1 (C1) and the height profile of the complex (C2) of the cross section shown in A1. This had typically three adjacent peaks with a maximum height value of 9 ± 0.5 nm (width: ~90 nm). This was thougth to be the multiprotein replisome complex formed by RepD-PcrA and PolC. The scale bar represents 200 nm.

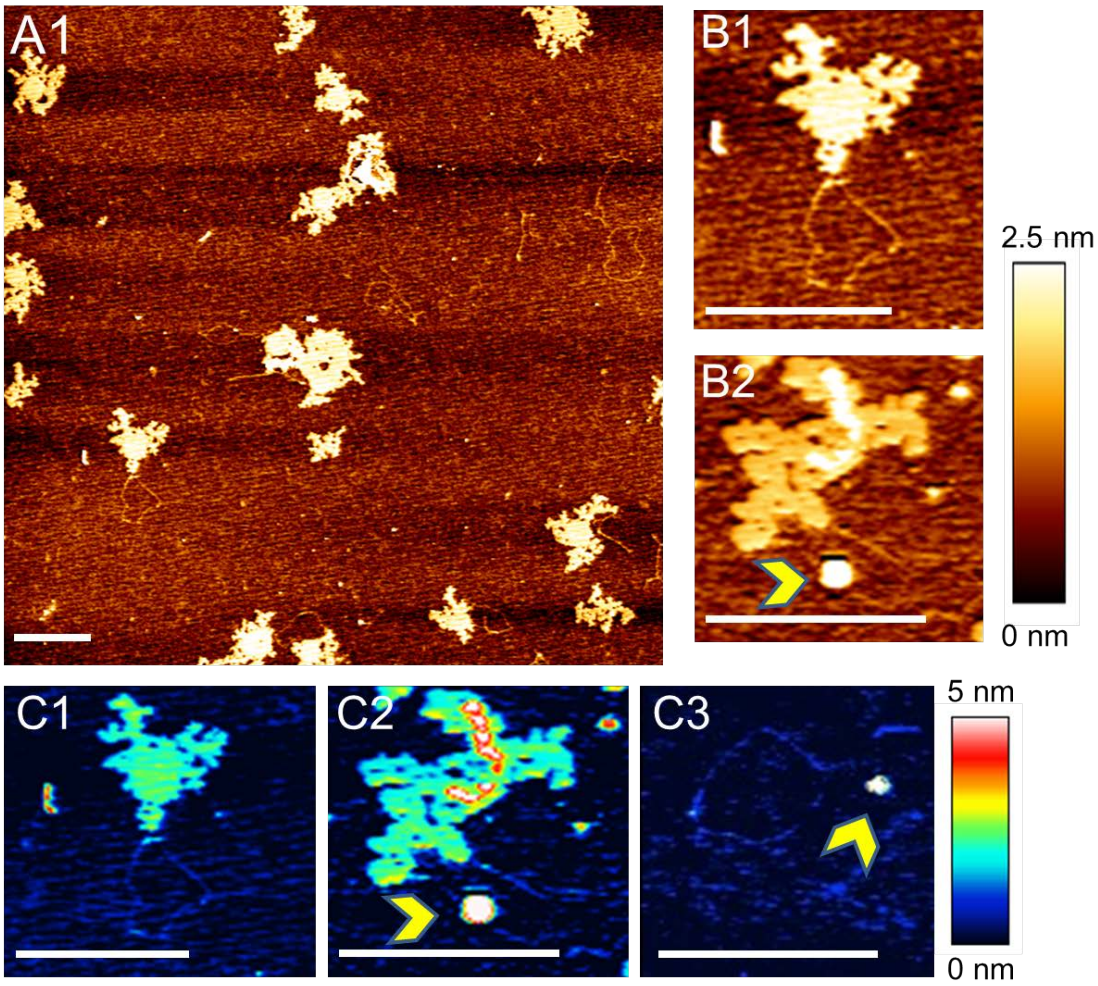

Figure 5.18. AFM visualisation of pCERoriD plasmid replication products. 10 nM plasmid (pCERoriD, 3.6 kb), 60nM RepD, 90nM PcrA, 200nM PolC, 100 nM SSB, 1mM ATP, 1mM dNTPs were incubated for 1 minute prior sample deposition and scanning. (A1) Typical field of view of the DNA products following replication. (B1-B2) Zoom images of two synthesized plasmids. The yellow arrow indicates the big complex on the DNA duplex. (C1-C3) Colour scale representation of the plasmids. The heights reached a value of 9.5 ± 0.5 nm for the complex indicated by the yellow arrow in C2 and 8 ± 0.3 nm for that in C3. The scale bar represents 500 nm. Supplementary data and heights analysis are shown in the Appendix of this thesis.

5.8. Identification of Cy3B-SSB by TIRF-AFM

As mentioned in the Introduction, single molecule imaging by fluorescence has been achieved with a number of systems and there have been several attempts to combine the AFM with fluorescence imaging [97, 119]. In this

approach, individual fluorescently labelled molecules can be visualised by fluorescence and their morphology can be imaged with AFM. The combination of these two techniques allows the identification and localization of biomolecules. Myosin filaments have been analysed by cross-correlation of TIRF and AFM previously [120].

Here, a spatially and temporally synchronized TIRF and AFM approach was validated and used to correlate topography and fluorescence images produced by Cy3B-SSB bound to unwound DNA.

In a first experiment, fluorescently labeled nanoparticles were analysed with both microscopes in order to test the simultaneous acquisition of topography and fluorescence information and validate the effective functionality of the assembled setup. The beads were absorbed on a borosilicate glass surface treated with bovine serum albumin (BSA) prior imaging. Their use offered strong and stable fluorescence, and a convenient size for AFM scanning (less than 30 nm in diameter). Fluorescence and AFM images of the fluorescent particles showed spots at matching positions (Figure 5.19). Differences in the spot locations could be detected only rarely (indicated by arrows, Figure 5.19), as result of poor absorption of the beads on the surface and thus displacement by the tip movement. Nevertheless, the agreement between the two methods was clear and the experiment confirmed that this method could be extended to the detection of fluorescent biomolecules.

Following the control experiment, full unwinding of a pCERoriD plasmid was imaged using the fluorescently labeled Cy3B-SSB. Such a protein has been recently employed to monitor real-time unwinding of plasmids by RepD-PcrA complex using a TIRFM [49]. SSB binds ssDNA as tetramer and each protein has 4 Cy3B fluorophores attached allowing the generation of bright fluorescence images. A supercoiled pCERoriD plasmid (3.6 kb) was first incubated with RepD and PcrA and an excess of Cy3B-SSB, allowing complete unwinding. The DNA was then allowed to adhere to a clean amino silane treated glass surface, and then dried prior imaging.

Typical AFM and TIRF images of a surface area are shown in Figure 5.20. Upon PcrA-mediated unwinding, bright spots could be observed by TIRF

(Figure 5.20C). When the same region was imaged with AFM, condensed structures were detected on the surface (Figures 5.20A, B). These represented Cy3B-SSB bound to the ssDNA molecules and were similar to the images observed with wt SSB. The shape of such structures could overlay with the bright spots observed by TIRF. Thus, these were confirmed to be the nucleoprotein complexes. AFM data analysis revealed a distribution of heights for these features (Figure 5.20B), in agreement with fluorescence intensities of the different spot observed by TIRF (Figure 5.20C). This was likely to be caused by their ability to form clusters along the DNA and so a relatively high level of packaging of the Cy3B-SSB molecules on ssDNA, in agreement with previous observations of highly clustered SSB binding to long ssDNA as visualised by electron microscopy and by AFM [121, 122].

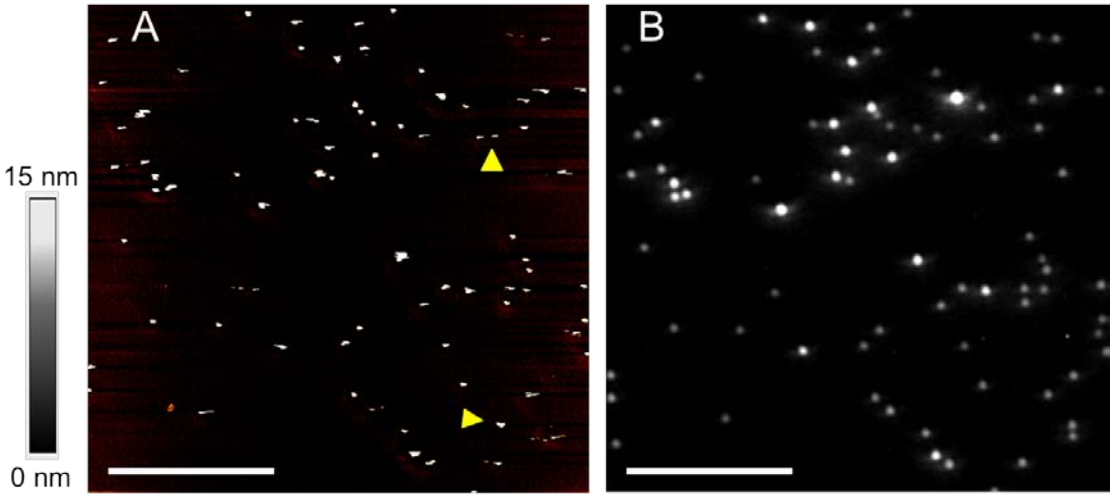

Figure 5.19. Images of fluorescent nanoparticles acquired with synchronized TIRF-AFM. (A) AFM topography of beads deposited on a glass surface. (B) Fluorescence image generated with TIRFM. Scale bars represent 10 μm. The majority of spots (~98%) matched between the AFM and TIRF images, with only few differences (indicated by the yellow arrows). The latter may well be caused by the tip displacement or sample degradation effects while scanning.

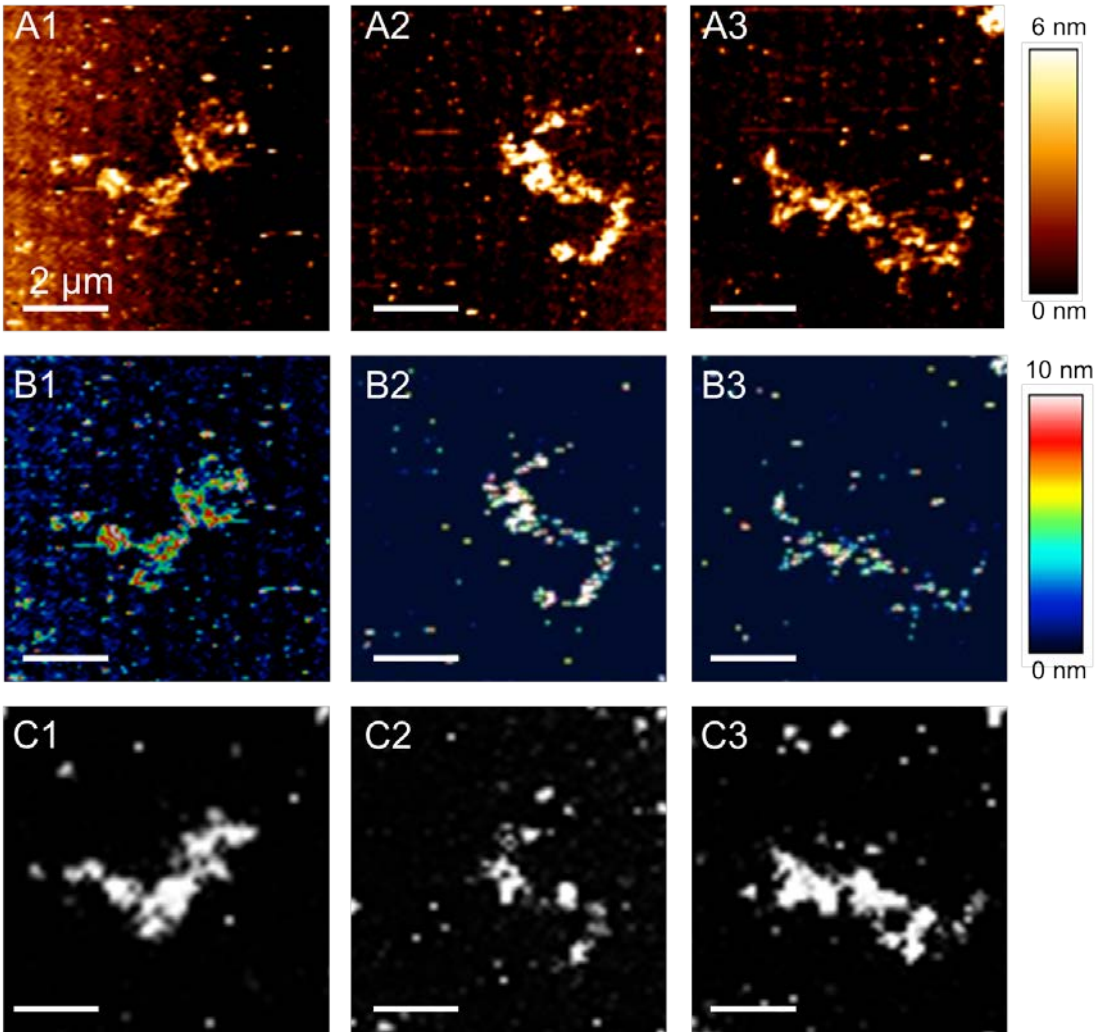

Figure 5.20. Zoom images of Cy3B-SSB-ssDNA complexes acquired with synchronized TIRF-AFM. Reactions were prepared as described in Figure 5.13. (A-B) AFM topographical images of unwound plasmids coated with SSB. Heights of the SSB-DNA varied along the ssDNA molecule. (C) Fluorescence images generated with TIRFM. Scale bars represent 2 µm.

5.9. Discussion

5.9.1. AFM imaging of plasmid replication

As stated above, protein-DNA interactions can be visualised with the AFM, which makes it a key tool in elucidating the role of various proteins in numerous biological processes. Here, AFM was mainly employed to visualise intermediate stages of plasmid replication performed by the initiator protein RepD, PcrA helicase, PolC and SSB.

Firstly, the pCERoriD plasmid substrate in its supercoiled state was imaged revealing the characteristic negative twisting of the DNA (Figure 5.1). This was consistent with the undertwisted plasmid conformation found *in vivo* [123]. In bacteria, the negative supercoiling is directly introduced into a relaxed DNA by the ATP-hydrolysis-driven action of the DNA gyrase. However, the level of supercoiling of a plasmid preparation *in vitro* may differ from that *in vivo*. As the DNA is a highly negatively charged polymer, contacts between DNA regions are inhibited by the electrostatic repulsion of the helices. Hence, the cations can have an effect on such interactions. This was directly observed here by imaging the DNA plasmid in a range of environmental conditions. In particular, the DNA conformation was affected by the ionic conditions (Figure 5.3). Condensed superhelical DNA molecules with close helix-helix contacts were found at high salt conditions (Figure 5.3C). These observations were consistent with previous AFM studies on DNA topology [112].

The supercoiled plasmid conformations in close to physiological salt concentrations (100 mM KCl) also displayed local bending resulting in a Y-shaped plasmid with variable arm lengths (Figures 5.3C and 5.7A). DNA branching is an important structural feature of supercoiled DNA involved interactions between distantly separated DNA regions. A previous study suggested that the interaction between such sites could be regulated *via* DNA branching, which could depend on the cruciform structure formation as well [104].

The DNA supercoiling itself plays a key role in a number of biological processes. Firstly, it reduces the number of base pairs per DNA turn allowing DNA packaging. Secondly, it can regulate DNA-protein interactions by bringing two distant sites into proximity. The latter function represents a first level of control for downstream pathways like DNA replication.

To initiate replication, the supercoiling must be resolved to make the DNA accessible to the replicative enzymes. This is achieved through the activity of the initiator protein. Incubation of the native pCERoriD plasmid with RepD induces a drastic shift of DNA conformation from a supercoiled to a relaxed state (Figures 5.4 and 5.5). The local binding of RepD to the origin of replication could also be observed, and the complex had a height of ~ 2nm (Figure 5.6). Relaxed molecules without RepD and/or with local coiling were also found, and

these represented the circular closed molecules. These results were in agreement with our understanding of RepD role *in vivo*, and the nicking/closing activities of RepD observed *in vitro* (see Chapter 3) [47]. A topology analysis of the relaxation reaction was performed from the AFM images and simultaneously on an agarose gel assay (Figure 5.5). Both assays showed a similar degree of DNA relaxation (~90% of circular plasmids), albeit a higher number of circular closed plasmids were found in the AFM approach. This was possibly caused by a different stability of the RepD-DNA complex on the surface due to buffer switching and washing steps during the sample preparation.

From the data reported in this investigation, it is clear that supercoiling can promote RepD protein interaction (Chapter 3), this phenomenon would also explain the optimal nicking activity of RepD in moderate-high salt condition as result of increased coiling in the DNA substrate and formation of an ideal DNA conformation (Figure 5.3).

Plasmid relaxation allowed the measurements of DNA contour length using different DNA plasmid lengths (Figure 5.7). The base spacing values (0.3 nm bp^{-1}) were similar to that previously reported in AFM studies (0.28–0.34 nm bp^{-1}), in agreement with the expected value of the B-form DNA [113]. However, heights measured smaller than 2 nm, which is the helix diameter of B-DNA. Although, DNA heights reported in previous AFM studies are almost always <2 nm, and vary from 0.5 to 1.9 nm in air and propanol, which are similar to the value measured here (0.8 nm ± 0.2, Figure 5.6) [113] .

Upon plasmid nicking and relaxation, RepD produces a short ssDNA stretch, which is the recruitment site for PcrA helicase. Loading of PcrA by RepD onto the (-)-strand of *ori*D has been previously demonstrated [47]. Here, PcrA and RepD were detected as a single complex binding at a unique position on the relaxed DNA molecules (Figure 5.9). From the 3D analysis, the complex showed a maximum height at 3.5 nm and a shoulder at 2 nm (Figure 5.9). Such a complex could also be found on both linear and relaxed DNA plasmids during initiation and unwinding, indicating that the proteins remain associated and co-translocate along the DNA during unwinding (Figures 5.10, 5.11, and 5.16). Previous studies have suggested that RepD and PcrA might physically interact forming a complex [48, 47]. The AFM results reported here provide the first low-resolution structural data of the RepD-PcrA complex.

Recruitment of the helicase by RepD at the oriD is followed by directional DNA unwinding (Figure 5.16). In the absence of the SSB protein, unwinding by PcrA-RepD resulted in formation of loops due to reannealing of the unwound strands (Figures 5.11 and 5.14B,). In some occasions, the unwinding complex could be found at a central condensed knot retaining the loops, representing incomplete unwinding (Figure 5.11C2). Alternatively the complex was on a duplex stretch of a loop or released (Figure 5.11C2, C3). RepD-PcrA complex position could reflect different unwinding stages.

The observation of ssDNA structures and loop formation upon helicase-mediated unwinding indicated that the SSB protein is not required for DNA strand separation *per se* (Figures 5.10 and 5.11). This is consistent with the unwinding measurements of labeled DNA junctions performed in the absence of SSB (Chapter 3). However, *in vivo* SSB is expected to bind the displaced (+)-strand during asymmetric replication. Presently, several studies showed that SSB can physically interact with the replicative proteins, and such an interaction can have an effect in modulating the helicase activity. One example is the stimulation of PriA-catalysed unwinding by contact with the *E.coli* SSB [124]. Currently, potential functional and/or physical interactions between PcrA and SSB still need to be investigated.

The inclusion of SSB in the unwinding reaction revealed formation of nucleoprotein complexes, consistent with binding of the emerging ssDNA produced by PcrA (Figure 5.12). At moderate salt conditions (100 mM KCl) collapsed, wrapped SSB–DNA complexes were detected, reflecting formation of the SSB-dT_{65} binding mode (Figure 5.13). Such behaviour was previously visualised by electron microscopy [121, 122]. The excess of SSB led to the formation of highly condensed structures possibly caused by ssDNA coating and interactions between neighboring tetramers. However, alternative rearrangements of the SSB binding mode could potentially occur during sample preparation on the surface.

A complete replication system could be achieved by the addition of PolC. This caused the formation of a big condensed globular feature on the DNA plasmid (~ 9 nm in height, Figure 5.17). Such an assembly contained three spherical structures of different heights (2, 6 and 9 nm, Figure 5.17C), which

were interpreted as the RepD, PcrA and PolC proteins at the replication fork. Measurements of PcrA unwinding kinetics reported in Chapter 4, showed that PolC increases PcrA unwinding speed. Thus, such a functional coupling might be achieved through a direct interaction. In the AFM images reported here, the proteins were found in close proximity during DNA replication and the low-resolution structural data indicated the formation of a multiprotein assembly.

Upon complete unwinding and replication, circular DNA plasmids and ssDNA molecules were observed (Figure 5.18). Such a result is consistent with plasmid product release following coordinated asymmetric DNA synthesis.

The structural analysis of the protein complexes formed at various stages of the plasmid replication showed formation of bigger structures when all the proteins where bound to the DNA. The heights and volumes increased progressively. However, while the height analysis is generally more accurate, the estimates of the complex width can be affected by the tip-sample convolution effect.

5.9.2. Identification of labelled proteins by combined TIRF-AFM

A cross-correlated TIRF-AFM provided complementary information for sample characterization. The combined TIRF-AFM has been used only recently to identify labeled proteins and cells. Here, the SSB-ssDNA complexes were specifically identified through TIRF-AFM. The unwinding reaction contained Cy3B-SSB protein, and the final products of unwinding were imaged with both techniques (Figure 5.20). The results confirmed the structural and morphology data initially observed with the wt SSB-ssDNA complexes (Figure 5.13).

Although performing the experiment with Cy3B-SSB was relatively straitghforward, initial efforts to identify the labeled PcrA helicase along the plasmids were unsuccessful. There were two main limits: the lower resolution of TIRF compared to the AFM and a relatively rapid photobleaching of the single fluophores during scanning. Further attempts are required to accomplish this task and perform a successful experiment. Nevertheless, this method could be employed in future with other fluorescently labeled macromolecular structures.

5.10. Summary

AFM is a powerful imaging tool for the analysis of biological structures. The AFM studies reported here represent the first complete investigation of the intermediates formed during asymmetric replication of a staphylococcal plasmid. Many aspects of such a process were uncovered; including the biomolecular interactions like the formation of the initiation complex, as well as the stages of RepD-PcrA-mediated unwinding and replisome-mediated replication.

In addition, a synchronized TIRF-AFM system was successfully tested and validated by imaging fluorescently labelled SSB proteins.

6. Concluding Remarks

6.1. Introduction

This thesis has been based on the investigation of several aspects of the asymmetric rolling circle replication of the pC221 plasmid. The work has centered on the function of the interactions during replication between a replication plasmid initiator protein, *S. aureus* RepD, with PcrA from *B. stearothermophilus* and the *S. aureus* PolC. A model plasmid, the pCER*oriD*, has been used in these *in vitro* studies. There are a number of conclusions that can be drawn from the data presented in this thesis and this is further discussed below.

6.2. RepD functions in plasmid replication

As previously described, RepD is essential for the initiation of asymmetric, rolling circle plasmid replication of plasmids containing the DSO, *ori*D, prior to PcrA helicase binding. The role of RepD and similar proteins in replication can be considered in several distinct but related parts. First, it ensures that copying the (−)-strand starts and ends at the DSO. This is achieved by specific interaction with the inverted complementary repeat sequence, ICRIII, carried by the plasmid within the DSO. Other pairs of Rep initiators and ICRIII provide their own specificity for this family of plasmids. The kinetics of RepD binding to a DNA containing the ICRII and ICRIII sequences showed relatively rapid binding with high affinity to such *oriD* elements (section 3.4). The RepD was found at a unique location on the DNA plasmids through AFM imaging (section 5.3).

The second part of the function of RepD is to nick one strand within ICRII [25], which causes a change in the DNA topology with relief of supercoiling. RepD-mediated nicking and plasmid relaxation was visualised through AFM, and the kinetics of nicking were measured here (sections 5.3, 3.2). Plasmid nicking occurred with a rate constant of > 25 s^{-1} at 30 °C (section 3.2). Once the covalent attachment is rapidly formed, the transesterification is reversible leading to DNA resealing and the formation of a relaxed closed DNA molecule (section 3.2). Such DNA products were visualised by AFM. Upon a short incubation time of RepD with the supercoiled plasmid (~ 30 s), most plasmids (~

93%) were imaged in their relaxed circular forms. These AFM data were in agreement with the plasmid nicking kinetics and the observation of complete DNA relaxation after only few s of reaction (section 3.2). The reaction catalysed by RepD requires a supercoiled plasmid, which is the main substrate *in vivo*, and divalent ions as cofactors for catalysis, like many proteins that break and rejoin nucleic acids (sections 3.2, 3.2.2). However, the cofactors are not essential for non-covalent DNA binding (section 3.4.3). Mg^{2+} appears to be the physiological metal ion used. However, other metal ions, such as Ca^{2+} and Mn^{2+}, also supported nicking (section 3.2.2). The nicked DNA-protein complex exhibits a relatively long half-life, which is likely to be of biological significance in terms of control of replication. RepD does not efficiently nick relaxed circular plasmids *in vitro* (personal communication Dr. Gerard Lynch, unpublished data), so it is likely that a supercoiled plasmid has only a single chance to enter in replication. The latter also needs to be coordinated with the activity of the host replicative proteins for a successful replication event.

It is clear from the results reported here that factors such as the DNA structure or the use of a specific cofactor can affect the nicking kinetics and the formation of a functional initiation complex. Firstly, the extent of the nicking reaction is highly dependent on the DNA topology and the relief of supercoiling results in a high extent of relaxed DNA formation. Both the free energy of supercoiling in the intact plasmid and RepD binding could drive the formation of the cruciform extrusion of palindromic sequences contained within *ori*D. The formation of the cruciform has been shown to be dependent on superhelicity: the torsional stress of supercoiling leads to a decrease in the activation energy of the reaction followed by conformational changes in DNA structure that favor the formation of cruciform structures. In the absence of proteins, this occurs only very slowly, even when thermodynamically favored. However, RepD might enhance and stabilize the extrusion on the supercoiled plasmid through binding on supercoiled but not linear DNA. This then exposes the nick site as a single-stranded loop as the target site for RepD nicking activity. DNA supercoiling is also dependent on the environmental conditions such as ionic strength (section 5.2.1), and previous studies showed that RepD has maximal nicking activity at high salt, condition at which the DNA presents a high level of superhelicity [25]. These observations are in agreement with the indication that DNA supercoiling

favours RepD nicking function.

Another important effect of the nicking activity, in addition to the removal of the negative supercoiling, is the opening of a ssDNA stretch on the (−)-strand of the plasmid, which allows the plasmid to be accessible to the replicative enzymes. RepD recruits PcrA at the origin and the formation of the RepD-PcrA complex on the DNA plasmids was visualised by AFM (section 5.5). It was previously shown that RepD increases PcrA binding affinity to the DNA [48]. At this stage, RepD promotes processive unwinding by PcrA, allowing unwinding of plasmids > 6 kb in length (sections 3.3, 5.5). Unwinding by PcrA is unidirectional (3′ > 5′), as also confirmed from AFM imaging of unwound linear DNA plasmids, having the *ori*D at different locations along the DNA (section 5.6) [47]. The covalent attachment of RepD to the 5′-end of the nicked strand is carried around the plasmid with the protein, and so is already in position to take part in the strand exchanges to form the closed, circular parental (+)-strand.

Finally, RepD modulates more chemistry to terminate replication by processes including strand exchange. However, the detailed molecular events of this process still need to be elucidated. After termination, RepD is released as inactive heterodimer with a short oligonucleotide attached (11 nucleotides) to the active site of one subunit, also known as RepD* [31]. This inactivation, upon a complete replication cycle, appears to be common among plasmids of the pT181 family. These plasmids maintain a low, rate-limiting level of the active initiator protein, and any increase in initiator concentration is followed by an increase in plasmid replication [125]. Therefore, the RepD inactivation is likely to represent another level of regulation in order to stably maintain the plasmid copy number. Furthermore, previous studies with the RepD homologue, RepC/RepC*, showed that the inactive heterodimer displays DNA binding at the *ori* [32]. Thus, RepC/RepC* may act as a competitive inhibitor by binding to the free origins and inhibiting initiation by the active RepC *in vivo*.

6.3. Regulation of PcrA helicase activity

PcrA plays a prominent role in plasmid rolling circle replication in Gram-positive bacteria. Part of this investigation was focused on PcrA helicase and the effect of regulatory proteins on its activity during unwinding, such as RepD and PolC protein. Accordingly to previous studies, PcrA is 'inactive' for processive duplex separation in the absence of RepD. As demonstrated here, an interesting feature is that RepD nicking activity is not related to the ability of PcrA to perform unwinding, although the nick is needed to initiate a plasmid and create a DNA site for the helicase recruitment and loading onto origin (section 3.10). In RepD presence, PcrA is able to processively unwind plasmid DNA substrates at a rate of ~ 30 bp s^{-1} (30 ˚C, see the Appendix of this thesis). The coordinated activity of a RepD mutant, N189K, with PcrA leads to complete unwinding of plasmids, albeit at a slightly reduced speed (19 bp s^{-1}, 30 °C, section 3.3.1). These observations suggest that the RepD-mediated activation of PcrA helicase might also regulate its unwinding kinetics. The evidence of complex formation imaged through AFM supports the idea that PcrA and RepD physically interact during unwinding (section 5.5). It is more likely that the interaction with RepD results in a conformational change in PcrA that stimulates the helicase. A potential location of RepD interaction is proposed to be the PcrA 2B domain. It has been previously shown that the 2B domain of the *E.coli* Rep helicase, a PcrA structural homologue, is an important regulatory domain for its unwinding activity [126]. Deletion of the domain increased the helicase unwinding activity in multiple turnover assays. As described in the Introduction, a large conformational change of domain 2B occurs when PcrA binds the DNA duplex. The location of RepD on the duplex would be in the correct orientation to have an interaction with the 2B domain of PcrA. However, this still needs to be examined in detail and is continuing to be investigated.

As shown in this investigation and in previous studies, the PcrA unwinding rate was significantly slower than the translocation rate along ssDNA in the presence of RepD (sections 4.6, 3.3). Furthermore, PolC increased the speed of RepD-PcrA-mediated unwinding (up to 71 bp s^{-1}; section 4.7.2). It is likely that when the polymerase and the helicase move through dsDNA, PcrA

unwinding occurs at a rate closer to the ssDNA translocation. This suggested that the replicative protein might interact during coordinated DNA replication and unwinding. Evidences of formation of a multi-assembly complex were obtained with AFM (section 5.7). Such images showed that the replicative proteins work closely during plasmid replication. Whether and how the helicase and polymerase in this situation physically interact is currently not known, as well as the periodic changes in protein-DNA and protein-protein interactions during movement of the complex. This would be necessary to unreveal the timing of events during normal replication and to predict the consequences when replication stalls.

6.4. Comparison with other replicative systems

Because of the conserved functions of the replicative proteins, it is important to make comparison with other replicative systems. Similar observations of protein-protein interactions and coordinated replication have been made in other replication complexes.

There are examples in the literature of helicase activity regulation by accessory proteins. A PcrA homologue, UvrD helicase has been shown to have an increased activity in the presence of the accessory protein MutL, an important component involved in methyl directed mismatch DNA repair [127]. UvrD becomes a more processive helicase in the presence of MutL unwinding more base pairs of DNA per ATP hydrolysis event than in the absence of MutL. Such a functional coupling is similar to that observed with RepD and PcrA.

In phage T7, the primase and helicase enzymes are fused into the T7 gp4 protein and remain physically associated within the replisome. Such a direct interaction has been shown to enhance the helicase processivity by stabilizing DNA binding. In the pT181 system, RepD resembles the activity of a “primase” as it generates through nicking the DNA substrate for the polymerase. In addition, it is a key partner of PcrA, leading to functional and physical interactions, similarly to the T7 system.

There are several proteins within the replisome that can interact with the helicase. As reported in the Introduction, helicases can also be regulated by

DNA polymerases. In the presence of the T7 DNA polymerase, the T7 helicase moves through the duplex with a speed ~ 10 times faster than the helicase alone [67]. A similar effect was seen in the T4 system, where the unwinding rate of the T4 helicase, gp41 (30 bp s^{-1}), is accelerated ~3 times in the coupled helicase-polymerase system [35]. Similarly, a functional coupling between PcrA and PolC was observed here (section 4.7); the PcrA helicase unwinding rate was increased 2-fold by PolC activation. In turn, PcrA helicase increased PolC synthesis rate (sections 4.7, 4.4).

Another example is given by the *E. coli* replisome. However, compared to the T7 and the Staphylococcus plasmid, that of *E. coli* is more complex as it requires a larger number of replicative proteins (see the Introduction of this thesis). The primary replicative hexameric helicase, DnaB, is able to interact with the primase, the DNA polymerase III and the SSB protein during coordinated synthesis. In particular, the holoenzyme DNA pol III physically associates with DnaB through the τ subunit, and increases the helicase unwinding rate so that the replisome moves at the speed dictated by the polymerase [69].

The SSB protein has an important role in recruiting genome maintenance proteins to the ssDNA through a physical interaction. Although previous and recent studies have elucidated interesting features about the interplay between RepD and PcrA, the potential interactions of SSB with the replicative proteins still need to be investigated.

Despite the differences in replication mechanisms and the number and type of proteins, similarity in protein functions and coordination can be found among the DNA replication machineries suggesting some evolutionary connection between DNA replication systems. Recruitment and stimulation of a DNA helicase by other proteins allows for control and regulation of replication. The presence of an active DNA helicase in the cell might cause undesirable DNA unwinding. Thus, the activator factor, such as RepD, allows for the plasmid replication to be finely regulated.

6.5. Potential targets for antibiotic development

As previously mentioned, antibiotic resistance usually evolves via transfer of resistance genes located on mobile DNA elements like the self-replicating plasmid. Understanding the mechanisms of DNA replication it is of importance in the design and development of new antibiotic compounds to impede the spread of such genetic elements. The recent increase in bacterial strains that are resistant to conventional antibacterial therapies has prompted the development of alternative strategies to treat bacterial diseases.

Currently, a number of antibiotics that interfere with the DNA gyrase and topoisomerase IV activities have been developed. The bacterial DNA gyrase is an attractive target for inhibitors that either regulate or disrupt the DNA binding and cleavage. Novel inhibitors have also been reported for the PolC of gram-positive bacteria [128]. Both the RepD and PcrA proteins, as well as their binary interaction, are essential for the bacterial survival. Thus, these proteins should be legitimate targets for development of new molecules. Specific nucleotide analogues that target the helicase activity have been reported [129].

Our increasing understanding of the molecular interactions and the protein-protein interfaces during replication makes protein complexes feasible targets for the development of novel small molecule inhibitors in the future.

6.6. Future perspectives

Since the discovery of the rolling circle replication plasmids, progress have been made in our understanding of the events and general mechanisms of plasmid replication [28]. However, there are still gaps and opened questions concerning the protein-DNA and protein-protein interactions.

The formation of the initiation complex and the kinetics of the interaction of RepD with DNA as well as information about RepD-PcrA complex were described in this thesis. However, an interesting aspect that needs to be defined is how RepD and PcrA form the unwinding complex on the DNA and which types of protein-protein interactions lead to their functional coupling [52, 99]. We are currently lacking of high-resolution structural data of RepD in complex with

DNA and/or with PcrA. A major step in understanding this function is the determination of the three-dimensional structures by crystallographic methods. This determination would allow the identification of protein-protein interfaces and greatly enhance our understanding of the ternary complex with the DNA.

Further studies are also necessary to elucidate the function of RepD protein during termination. The role of RepD and the sequence of the molecular events, such as the movement and the dissociation of the helicase and polymerase during termination and strand exchange are poorly understood and should be the subject of future investigations.

Another interesting aspect that needs to be investigated is the function of SSB during plasmid unwinding. There might be possible interactions between SSB and PcrA while the helicase moves along the DNA. SSB is not required for duplex separation and PcrA translocation, although it might stimulate the helicase during processive unwinding [48, 52]. Any potential functional and physical interaction between PcrA and SSB should be proved and addressed in the future.

Biochemical and structural studies of PcrA helicase in the past years provided deeper insights into the mechanistic details of its activity [50, 52, 53]. However, such studies need to be extended in order to understand how the helicase interacts with the replicative proteins during replication. RepD and PolC regulate PcrA helicase activity during coordinated replication, and the details of such functional interaction need to be further elucidated.

Evidences of interactions between the replicative proteins and formation of the replisome complex during replication were provided here through AFM experiments. Although, the dynamic nature of such interactions needs to be defined in order to elucidate the periodic changes that might occur as the proteins move along the DNA.

In addition, single molecule studies and the visualisation of labelled proteins on DNA with the combined TIRF-AFM approach could provide further characterisation of the DNA replication system and elucidate crucial macromolecular interactions occurring during replication.

7. References

1. Watson, J.D. and F.H. Crick, *A structure for deoxyribose nucleic acid. 1953.* Nature, 2003. **421**(6921): p. 397-8; discussion 396.
2. Alberts, B., *Molecular Biology of the Cell.* Fourth ed. 2002, New York: Garland Science.
3. Kasamatsu, H. and J. Vinograd, *Replication of circular DNA in eukaryotic cells.* Annu Rev Biochem, 1974. **43**(0): p. 695-719.
4. Bell, S.P. and A. Dutta, *DNA replication in eukaryotic cells.* Annu Rev Biochem, 2002. **71**: p. 333-74.
5. Mitra, S. and A. Kornberg, *Enzymatic mechanisms of DNA replication.* J Gen Physiol, 1966. **49**(6): p. 59-79.
6. Messer, W., *Initiation of DNA replication in Escherichia coli.* J Bacteriol, 1987. **169**(8): p. 3395-9.
7. O'Donnell, M., *Replisome architecture and dynamics in Escherichia coli.* J Biol Chem, 2006. **281**(16): p. 10653-6.
8. Sanders, G.M., H.G. Dallmann, and C.S. McHenry, *Reconstitution of the B. subtilis replisome with 13 proteins including two distinct replicases.* Mol Cell, 2010. **37**(2): p. 273-81.
9. Engelen, S., et al., *Distinct co-evolution patterns of genes associated to DNA polymerase III DnaE and PolC.* BMC Genomics, 2012. **13**: p. 69.
10. Khan, S.A., *Plasmid rolling-circle replication: highlights of two decades of research.* Plasmid, 2005. **53**(2): p. 126-36.
11. Iordanescu, S., et al., *Incompatibility and molecular relationships between small Staphylococcal plasmids carrying the same resistance marker.* Plasmid, 1978. **1**(4): p. 468-79.
12. Actis, L.A., M.E. Tolmasky, and J.H. Crosa, *Bacterial plasmids: replication of extrachromosomal genetic elements encoding resistance to antimicrobial compounds.* Front Biosci, 1999. **4**: p. D43-62.
13. Steitz, T.A., *DNA polymerases: structural diversity and common mechanisms.* J Biol Chem, 1999. **274**(25): p. 17395-8.
14. Gennaro, M.L., et al., *Functional organization of the plasmid pT181 replication origin.* J Mol Biol, 1989. **205**(2): p. 355-62.
15. Noirot, P., J. Bargonetti, and R.P. Novick, *Initiation of rolling-circle replication in pT181 plasmid: initiator protein enhances cruciform extrusion at the origin.* Proc Natl Acad Sci U S A, 1990. **87**(21): p. 8560-4.
16. Jin, R. and R.P. Novick, *Role of the double-strand origin cruciform in pT181 replication.* Plasmid, 2001. **46**(2): p. 95-105.
17. Thomas, C.D., et al., *Determination of sequence specificity between a plasmid replication initiator protein and the origin of replication.* J Mol Biol, 1995. **254**(3): p. 381-91.
18. Rasooly, A., P.Z. Wang, and R.P. Novick, *Replication-specific conversion of the Staphylococcus aureus pT181 initiator protein from an active homodimer to an inactive heterodimer.* EMBO J, 1994. **13**(21): p. 5245-51.
19. Jin, R., M.E. Fernandez-Beros, and R.P. Novick, *Why is the initiation nick site of an AT-rich rolling circle plasmid at the tip of a GC-rich cruciform?* EMBO J, 1997. **16**(14): p. 4456-66.
20. Jin, R., A. Rasooly, and R.P. Novick, *In vitro inhibitory activity of RepC/C*, the inactivated form of the pT181 plasmid initiation protein, RepC.* J Bacteriol, 1997. **179**(1): p. 141-7.
21. Khan, S.A., *Rolling-circle replication of bacterial plasmids.* Microbiol Mol Biol Rev, 1997. **61**(4): p. 442-55.

22. Koepsel, R.R., et al., *The replication initiator protein of plasmid pT181 has sequence-specific endonuclease and topoisomerase-like activities.* Proc Natl Acad Sci U S A, 1985. **82**(20): p. 6845-9.
23. Manch-Citron, J.N., et al., *RepC is rate limiting for pT181 plasmid replication.* Plasmid, 1986. **16**(2): p. 108-15.
24. Projan, S.J. and R. Novick, *Comparative analysis of five related Staphylococcal plasmids.* Plasmid, 1988. **19**(3): p. 203-21.
25. Thomas, C.D., D.F. Balson, and W.V. Shaw, *In vitro studies of the initiation of staphylococcal plasmid replication. Specificity of RepD for its origin (oriD) and characterization of the Rep-ori tyrosyl ester intermediate.* J Biol Chem, 1990. **265**(10): p. 5519-30.
26. Koepsel, R.R., R.W. Murray, and S.A. Khan, *Sequence-specific interaction between the replication initiator protein of plasmid pT181 and its origin of replication.* Proc Natl Acad Sci U S A, 1986. **83**(15): p. 5484-8.
27. Wang, P.Z., et al., *Origin recognition specificity in pT181 plasmids is determined by a functionally asymmetric palindromic DNA element.* EMBO J, 1993. **12**(1): p. 45-52.
28. Khan, S.A., *DNA-protein interactions during the initiation and termination of plasmid pT181 rolling-circle replication.* Prog Nucleic Acid Res Mol Biol, 2003. **75**: p. 113-37.
29. Krogh, B.O. and S. Shuman, *Catalytic mechanism of DNA topoisomerase IB.* Mol Cell, 2000. **5**(6): p. 1035-41.
30. Deweese, J.E., et al., *Metal ion interactions in the DNA cleavage/ligation active site of human topoisomerase IIalpha.* Biochemistry, 2009. **48**(38): p. 8940-7.
31. Thomas, C.D. and L.J. Jennings, *RepD/D*: a protein-DNA adduct arising during plasmid replication.* Biochem Soc Trans, 1995. **23**(3): p. 442S.
32. Jin, R., X. Zhou, and R.P. Novick, *The inactive pT181 initiator heterodimer, RepC/C, binds but fails to induce melting of the plasmid replication origin.* J Biol Chem, 1996. **271**(49): p. 31086-91.
33. Moore, K.J. and T.M. Lohman, *Helicase-catalyzed DNA unwinding: energy coupling by DNA motor proteins.* Biophys J, 1995. **68**(4 Suppl): p. 180S-184S; discussion 184S-185S.
34. Singleton, M.R., M.S. Dillingham, and D.B. Wigley, *Structure and mechanism of helicases and nucleic acid translocases.* Annu Rev Biochem, 2007. **76**: p. 23-50.
35. Patel, S.S., M. Pandey, and D. Nandakumar, *Dynamic coupling between the motors of DNA replication: hexameric helicase, DNA polymerase, and primase.* Curr Opin Chem Biol, 2011. **15**(5): p. 595-605.
36. Gupta, R. and R.M. Brosh, Jr., *Helicases as prospective targets for anti-cancer therapy.* Anticancer Agents Med Chem, 2008. **8**(4): p. 390-401.
37. Ellis, N.A., et al., *The Bloom's syndrome gene product is homologous to RecQ helicases.* Cell, 1995. **83**(4): p. 655-66.
38. Pause, A. and N. Sonenberg, *Mutational analysis of a DEAD box RNA helicase: the mammalian translation initiation factor eIF-4A.* EMBO J, 1992. **11**(7): p. 2643-54.
39. Mahdi, A.A., et al., *A model for dsDNA translocation revealed by a structural motif common to RecG and Mfd proteins.* EMBO J, 2003. **22**(3): p. 724-34.
40. Tanner, N.K., et al., *The Q motif: a newly identified motif in DEAD box helicases may regulate ATP binding and hydrolysis.* Mol Cell, 2003. **11**(1): p. 127-38.
41. Korolev, S., et al., *Comparisons between the structures of HCV and Rep helicases reveal structural similarities between SF1 and SF2 super-families of helicases.* Protein Sci, 1998. **7**(3): p. 605-10.
42. Ye, J., et al., *RecA-like motor ATPases--lessons from structures.* Biochim Biophys Acta, 2004. **1659**(1): p. 1-18.
43. Medagli, B. and S. Onesti, *Structure and mechanism of hexameric helicases.* Adv Exp Med Biol, 2013. **767**: p. 75-95.

44. Iordanescu, S., *Characterization of the Staphylococcus aureus chromosomal gene pcrA, identified by mutations affecting plasmid pT181 replication.* Mol Gen Genet, 1993. **241**(1-2): p. 185-92.
45. Velankar, S.S., et al., *Crystal structures of complexes of PcrA DNA helicase with a DNA substrate indicate an inchworm mechanism.* Cell, 1999. **97**(1): p. 75-84.
46. Soultanas, P., et al., *Uncoupling DNA translocation and helicase activity in PcrA: direct evidence for an active mechanism.* EMBO J, 2000. **19**(14): p. 3799-810.
47. Dillingham, M.S., D.B. Wigley, and M.R. Webb, *Demonstration of unidirectional single-stranded DNA translocation by PcrA helicase: measurement of step size and translocation speed.* Biochemistry, 2000. **39**(1): p. 205-12.
48. Dillingham, M.S., D.B. Wigley, and M.R. Webb, *Direct measurement of single-stranded DNA translocation by PcrA helicase using the fluorescent base analogue 2-aminopurine.* Biochemistry, 2002. **41**(2): p. 643-51.
49. Toseland, C.P., et al., *The ATPase cycle of PcrA helicase and its coupling to translocation on DNA.* J Mol Biol, 2009. **392**(4): p. 1020-32.
50. Petit, M.A., et al., *PcrA is an essential DNA helicase of Bacillus subtilis fulfilling functions both in repair and rolling-circle replication.* Mol Microbiol, 1998. **29**(1): p. 261-73.
51. Zhang, W., et al., *Directional loading and stimulation of PcrA helicase by the replication initiator protein RepD.* J Mol Biol, 2007. **371**(2): p. 336-48.
52. Slatter, A.F., C.D. Thomas, and M.R. Webb, *PcrA helicase tightly couples ATP hydrolysis to unwinding double-stranded DNA, modulated by the initiator protein for plasmid replication, RepD.* Biochemistry, 2009. **48**(27): p. 6326-34.
53. Chisty, L.T., et al., *Monomeric PcrA helicase processively unwinds plasmid lengths of DNA in the presence of the initiator protein RepD.* Nucleic Acids Res, 2013. **41**(9): p. 5010-23.
54. Byrd, A.K., et al., *Dda helicase tightly couples translocation on single-stranded DNA to unwinding of duplex DNA: Dda is an optimally active helicase.* J Mol Biol, 2012. **420**(3): p. 141-54.
55. Park, J., et al., *PcrA helicase dismantles RecA filaments by reeling in DNA in uniform steps.* Cell, 2010. **142**(4): p. 544-55.
56. Fagerburg, M.V., et al., *PcrA-mediated disruption of RecA nucleoprotein filaments--essential role of the ATPase activity of RecA.* Nucleic Acids Res, 2012. **40**(17): p. 8416-24.
57. Veaute, X., et al., *UvrD helicase, unlike Rep helicase, dismantles RecA nucleoprotein filaments in Escherichia coli.* EMBO J, 2005. **24**(1): p. 180-9.
58. Johansson, E. and N. Dixon, *Replicative DNA polymerases.* Cold Spring Harb Perspect Biol, 2013. **5**(6).
59. Zhang, J., et al., *Proofreading genotyping assays mediated by high fidelity exo+ DNA polymerases.* Trends Biotechnol, 2005. **23**(2): p. 92-6.
60. Eom, S.H., J. Wang, and T.A. Steitz, *Structure of Taq polymerase with DNA at the polymerase active site.* Nature, 1996. **382**(6588): p. 278-81.
61. Doublie, S. and T. Ellenberger, *The mechanism of action of T7 DNA polymerase.* Curr Opin Struct Biol, 1998. **8**(6): p. 704-12.
62. Evans, R.J., et al., *Structure of PolC reveals unique DNA binding and fidelity determinants.* Proc Natl Acad Sci U S A, 2008. **105**(52): p. 20695-700.
63. McHenry, C.S., *DNA polymerase III holoenzyme of Escherichia coli: components and function of a true replicative complex.* Mol Cell Biochem, 1985. **66**(1): p. 71-85.
64. Bruck, I., R.E. Georgescu, and M. O'Donnell, *Conserved interactions in the Staphylococcus aureus DNA PolC chromosome replication machine.* J Biol Chem, 2005. **280**(18): p. 18152-62.

65. Johnson, K.A., *The kinetic and chemical mechanism of high-fidelity DNA polymerases.* Biochim Biophys Acta, 2010. **1804**(5): p. 1041-8.
66. Hamdan, S.M. and C.C. Richardson, *Motors, switches, and contacts in the replisome.* Annu Rev Biochem, 2009. **78**: p. 205-43.
67. Stano, N.M., et al., *DNA synthesis provides the driving force to accelerate DNA unwinding by a helicase.* Nature, 2005. **435**(7040): p. 370-3.
68. Pandey, M., et al., *Coordinating DNA replication by means of priming loop and differential synthesis rate.* Nature, 2009. **462**(7275): p. 940-3.
69. Kim, S., et al., *Coupling of a replicative polymerase and helicase: a tau-DnaB interaction mediates rapid replication fork movement.* Cell, 1996. **84**(4): p. 643-50.
70. Lee, S.J. and C.C. Richardson, *Choreography of bacteriophage T7 DNA replication.* Curr Opin Chem Biol, 2011. **15**(5): p. 580-6.
71. Farge, G., et al., *The accessory subunit B of DNA polymerase gamma is required for mitochondrial replisome function.* Nucleic Acids Res, 2007. **35**(3): p. 902-11.
72. Lakowicz, J.R., *Principles of Fluorescence Spectroscopy.* New York: Springer., 2006. **954**.
73. Stokes, G.G., *On the change of refrangibility of light.* Phil. Trans. R Soc, 1852. **142**: p. 463-562.
74. Shanker, N. and S.L. Bane, *Basic aspects of absorption and fluorescence spectroscopy and resonance energy transfer methods.* Methods Cell Biol, 2008. **84**: p. 213-42.
75. LiCata, V.J. and A.J. Wowor, *Applications of fluorescence anisotropy to the study of protein-DNA interactions.* Methods Cell Biol, 2008. **84**: p. 243-62.
76. Heyduk, T., et al., *Fluorescence anisotropy: rapid, quantitative assay for protein-DNA and protein-protein interaction.* Methods Enzymol, 1996. **274**: p. 492-503.
77. Xu, H.Q., et al., *Simultaneously monitoring DNA binding and helicase-catalyzed DNA unwinding by fluorescence polarization.* Nucleic Acids Res, 2003. **31**(14): p. e70.
78. Lidke, D.S., et al., *Imaging molecular interactions in cells by dynamic and static fluorescence anisotropy (rFLIM and emFRET).* Biochem Soc Trans, 2003. **31**(Pt 5): p. 1020-7.
79. Stryer, L., *Fluorescence energy transfer as a spectroscopic ruler.* Annu Rev Biochem, 1978. **47**: p. 819-46.
80. Martinez-Senac, M.M. and M.R. Webb, *Mechanism of translocation and kinetics of DNA unwinding by the helicase RecG.* Biochemistry, 2005. **44**(51): p. 16967-76.
81. Toseland, C.P. and M.R. Webb, *Fluorescence tools to measure helicase activity in real time.* Methods, 2010. **51**(3): p. 259-68.
82. Webb, M.R., *Development of fluorescent biosensors for probing the function of motor proteins.* Mol Biosyst, 2007. **3**(4): p. 249-56.
83. Dillingham, M.S., et al., *Fluorescent single-stranded DNA binding protein as a probe for sensitive, real-time assays of helicase activity.* Biophys J, 2008. **95**(7): p. 3330-9.
84. Kunzelmann, S. and M.R. Webb, *A fluorescent, reagentless biosensor for ADP based on tetramethylrhodamine-labeled ParM.* ACS Chem Biol, 2010. **5**(4): p. 415-25.
85. Brune, M., et al., *Mechanism of inorganic phosphate interaction with phosphate binding protein from Escherichia coli.* Biochemistry, 1998. **37**(29): p. 10370-80.
86. Brune, M., et al., *Direct, real-time measurement of rapid inorganic phosphate release using a novel fluorescent probe and its application to actomyosin subfragment 1 ATPase.* Biochemistry, 1994. **33**(27): p. 8262-71.
87. Lohman, T.M. and L.B. Overman, *Two binding modes in Escherichia coli single strand binding protein-single stranded DNA complexes. Modulation by NaCl concentration.* J Biol Chem, 1985. **260**(6): p. 3594-603.
88. Eccleston, J.F., S.R. Martin, and M.J. Schilstra, *Rapid kinetic techniques.* Methods Cell Biol, 2008. **84**: p. 445-77.
89. Gibson, Q.H., *Apparatus for the study of rapid reactions.* J Physiol, 1952. **117**(4): p. 49P-50P.

90. Goldsbury, C.S., S. Scheuring, and L. Kreplak, *Introduction to atomic force microscopy (AFM) in biology.* Curr Protoc Protein Sci, 2009. **Chapter 17**: p. Unit 17 7 1-19.
91. Binning, G., *Atomic Force Microscope.* Physical Review Letters, 1986. **56**: p. 930-933.
92. Santos, S., D. Billingsley, and N. Thomson, *Atomic force microscopy imaging of macromolecular complexes.* Methods Mol Biol, 2013. **950**: p. 315-41.
93. Kalle, W. and P. Strappe, *Atomic force microscopy on chromosomes, chromatin and DNA: a review.* Micron, 2012. **43**(12): p. 1224-31.
94. Liu, S. and Y. Wang, *Application of AFM in microbiology: a review.* Scanning, 2010. **32**(2): p. 61-73.
95. Liu, S. and Y. Wang, *A review of the application of atomic force microscopy (AFM) in food science and technology.* Adv Food Nutr Res, 2011. **62**: p. 201-40.
96. Yang, J., *AFM as a high-resolution imaging tool and a molecular bond force probe.* Cell Biochem Biophys, 2004. **41**(3): p. 435-50.
97. Kellermayer, M.S., et al., *Spatially and temporally synchronized atomic force and total internal reflection fluorescence microscopy for imaging and manipulating cells and biomolecules.* Biophys J, 2006. **91**(7): p. 2665-77.
98. Bird, L.E., et al., *Characterisation of Bacillus stearothermophilus PcrA helicase: evidence against an active rolling mechanism.* Nucleic Acids Res, 1998. **26**(11): p. 2686-93.
99. Machon, C., et al., *RepD-mediated recruitment of PcrA helicase at the Staphylococcus aureus pC221 plasmid replication origin, oriD.* Nucleic Acids Res, 2010. **38**(6): p. 1874-88.
100. Pourquier, P., et al., *Topoisomerase I and II Activity Assays.* Methods Mol Med, 1999. **28**: p. 95-110.
101. Vosberg, H.P., L.I. Grossman, and J. Vinograd, *Isolation and partial characterisation of the relaxation protein from nuclei of cultured mouse and human cells.* Eur J Biochem, 1975. **55**(1): p. 79-93.
102. Sissi, C. and M. Palumbo, *Effects of magnesium and related divalent metal ions in topoisomerase structure and function.* Nucleic Acids Res, 2009. **37**(3): p. 702-11.
103. Eggleston, A.K., N.A. Rahim, and S.C. Kowalczykowski, *A helicase assay based on the displacement of fluorescent, nucleic acid-binding ligands.* Nucleic Acids Res, 1996. **24**(7): p. 1179-86.
104. Oussatcheva, E.A., et al., *Influence of global DNA topology on cruciform formation in supercoiled DNA.* J Mol Biol, 2004. **338**(4): p. 735-43.
105. Gellert, M., M.H. O'Dea, and K. Mizuuchi, *Slow cruciform transitions in palindromic DNA.* Proc Natl Acad Sci U S A, 1983. **80**(18): p. 5545-9.
106. Toseland, C.P. and M.R. Webb, *Fluorescent nucleoside triphosphates for single-molecule enzymology.* Methods Mol Biol, 2011. **778**: p. 161-74.
107. Hanes, J.W. and K.A. Johnson, *Real-time measurement of pyrophosphate release kinetics.* Anal Biochem, 2008. **372**(1): p. 125-7.
108. Eckert, K.A. and T.A. Kunkel, *DNA polymerase fidelity and the polymerase chain reaction.* PCR Methods Appl, 1991. **1**(1): p. 17-24.
109. Capson, T.L., et al., *Kinetic characterization of the polymerase and exonuclease activities of the gene 43 protein of bacteriophage T4.* Biochemistry, 1992. **31**(45): p. 10984-94.
110. Wong, I., S.S. Patel, and K.A. Johnson, *An induced-fit kinetic mechanism for DNA replication fidelity: direct measurement by single-turnover kinetics.* Biochemistry, 1991. **30**(2): p. 526-37.
111. Arndt, J.W., et al., *Insight into the catalytic mechanism of DNA polymerase beta: structures of intermediate complexes.* Biochemistry, 2001. **40**(18): p. 5368-75.
112. Klemperer, N., et al., *Cross-utilization of the beta sliding clamp by replicative polymerases of evolutionary divergent organisms.* J Biol Chem, 2000. **275**(34): p. 26136-43.

113. Hansma, H.G., et al., *Polymerase activities and RNA structures in the atomic force microscope.* J Struct Biol, 1999. **127**(3): p. 240-7.
114. Lyubchenko, Y.L., L.S. Shlyakhtenko, and T. Ando, *Imaging of nucleic acids with atomic force microscopy.* Methods, 2011. **54**(2): p. 274-83.
115. Crisona, N.J., et al., *The topological mechanism of phage lambda integrase.* J Mol Biol, 1999. **289**(4): p. 747-75.
116. Klenin, K.V., et al., *Computer simulation of DNA supercoiling.* J Mol Biol, 1991. **217**(3): p. 413-9.
117. Dahlgren, P.R. and Y.L. Lyubchenko, *Atomic force microscopy study of the effects of Mg(2+) and other divalent cations on the end-to-end DNA interactions.* Biochemistry, 2002. **41**(38): p. 11372-8.
118. Lyubchenko, Y.L., et al., *Atomic force microscopy of nucleoprotein complexes.* Scanning Microsc, 1995. **9**(3): p. 705-24; discussion 724-7.
119. Kellermayer, M.S., *Combined atomic force microscopy and fluorescence microscopy.* Methods Mol Biol, 2011. **736**: p. 439-56.
120. Brown, A.E., et al., *Cross-correlated TIRF/AFM reveals asymmetric distribution of force-generating heads along self-assembled, "synthetic" myosin filaments.* Biophys J, 2009. **96**(5): p. 1952-60.
121. William Ruyechan, J.G.W., *Cooperative binding of the Escherichia coli DNA unwinding protein to single- stranded DNA.* Biochemistry, 1975. **14**: p. 5529-5534.
122. Hamon, L., et al., *High-resolution AFM imaging of single-stranded DNA-binding (SSB) protein--DNA complexes.* Nucleic Acids Res, 2007. **35**(8): p. e58.
123. Boles, T.C., J.H. White, and N.R. Cozzarelli, *Structure of plectonemically supercoiled DNA.* J Mol Biol, 1990. **213**(4): p. 931-51.
124. Cadman, C.J. and P. McGlynn, *PriA helicase and SSB interact physically and functionally.* Nucleic Acids Res, 2004. **32**(21): p. 6378-87.
125. Swack, J.A., et al., *P1 plasmid replication: measurement of initiator protein concentration in vivo.* J Bacteriol, 1987. **169**(8): p. 3737-42.
126. Brendza, K.M., et al., *Autoinhibition of Escherichia coli Rep monomer helicase activity by its 2B subdomain.* Proc Natl Acad Sci U S A, 2005. **102**(29): p. 10076-81.
127. Matson, S.W. and A.B. Robertson, *The UvrD helicase and its modulation by the mismatch repair protein MutL.* Nucleic Acids Res, 2006. **34**(15): p. 4089-97.
128. Standish, A.J., et al., *Dual inhibition of DNA polymerase PolC and protein tyrosine phosphatase CpsB uncovers a novel antibiotic target.* Biochem Biophys Res Commun, 2013. **430**(1): p. 167-72.
129. Zhang, Y., et al., *Homogenous assays for Escherichia coli DnaB-stimulated DnaG primase and DnaB helicase and their use in screening for chemical inhibitors.* Anal Biochem, 2002. **304**(2): p. 174-9.

8. Appendix

8.1. Anisotropy titrations

Anisotropy (r) was calculated using the equation:

$$\text{Anisotropy (r)} = \frac{I_{\parallel} - I_{\perp}}{I_{\parallel} + 2I_{\perp}}$$

Where $I_{\parallel}$, and $I_{\perp}$ are the fluorescence intensity of the emitted light in the parallel, and perpendicular planes respectively, both with respect to the excitation plane. Raw anisotropy measurements were averaged for each RepD concentration used and fitted to the following equations:

$$\text{Anisotropy (r)} = \frac{A_L \times ([L]-[PL]) + Q \times A_{PL} \times [PL]}{[L]-[PL] + Q \times [PL]}$$

Where A_L and A_{PL} represent the anisotropy of the ligand (DNA) and ligand.protein complexes (DNA.protein) respectively. [L] is the total concentration of ligand, and [PL] is the total concentration of protein.ligand complex, calculated using the equation:

$$[PL] = \frac{([P] + [L] + K_d) - \sqrt{([P] + [L] + K_d)^2 - 4*[P]*[L]}}{2}$$

Where [P] represents the total protein concentration, and K_d represents the equilibrium dissociation constant. To account for the change in total fluorescence intensity between free and bound DNA, the following equation was used to calculate constant Q:

$$Q = \frac{I_{PL}}{I_L}$$

Where I_L and I_{PL} represent the fluorescence intensity of the free ligand (DNA) and bound ligand respectively.

8.2. Michaelis Menten kinetics

The K_m and V_{max} values from steady state measurements performed with PolC on primed DNA junctions were calculated with the equation:

$$v = \frac{V_{max} \times [S]}{K_m + [S]}$$

Where v is the observed rate (i.e. P_i/PolC), V_{max} is the maximum rate, [S] is the variable substrate concentration (i.e. dNTPs), and K_m is the determined Michaelis-Menten constant (expressed as a concentration).

8.3. Single exponential analysis

The rate constant of a particular reaction wasdetermined by fitting the raw data (i.e. fluorescence from a stopped flow trace) to the following single exponential equation:

$$y = -A \times e^{(-k \times T)} + C$$

Where y is the observed signal (i.e. raw fluorescence units), A is the amplitude of the exponential, k is the rate constant, T is time (i.e. seconds), and C is the final value of y.

Where stopped flow fluorescence anisotropy data is used, raw fluorescence data from two collected channels representing the parallel and perpendicular planes to the excitation plane is converted into anisotropy units using the equation above. The anisotropy can then be fitted to the following equation representing a single exponential:

$$\text{Anisotropy (r)} = \frac{e^{(-k \times T)} \times (A_S - A_E)}{\left[e^{(-k \times T)} \times (1-D)\right] + D} + A_E$$

Where k represents the rate constant, T represents the time (i.e. seconds) A_S represents the anisotropy at the start of the exponential, and A_E represents the anisotropy at the end of the exponential. D represents the fluorescence intensity change between A_S and A_E and is calculated using the following equation:

$$D = \frac{I_E}{I_S}$$

Where I_S represents the fluorescence intensity at the start of the exponential, and I_E represents the fluorescence intensity at the end of the exponential.

8.4. Online applications

Swiss Institute of Bioinformatics: ExPASy proteomics server:

http://ca.expasy.org/

For sequence alignment:

http://pbil.univ-lyon1.fr/cgi-bin/acnuc-link-ac2aln?db=Hogenprot&query=Q9WY48

8.5. Supplementary data

Supplementary data for Figure 3.4:
Plasmid nicking by wt RepD. The initial burst (>25 s^{-1}) had amplitudes of ~30% (green data) and 35% (white data); the second slow phase (~ 2 s^{-1}) had amplitues of ~45% (green data) and ~40% (white data).

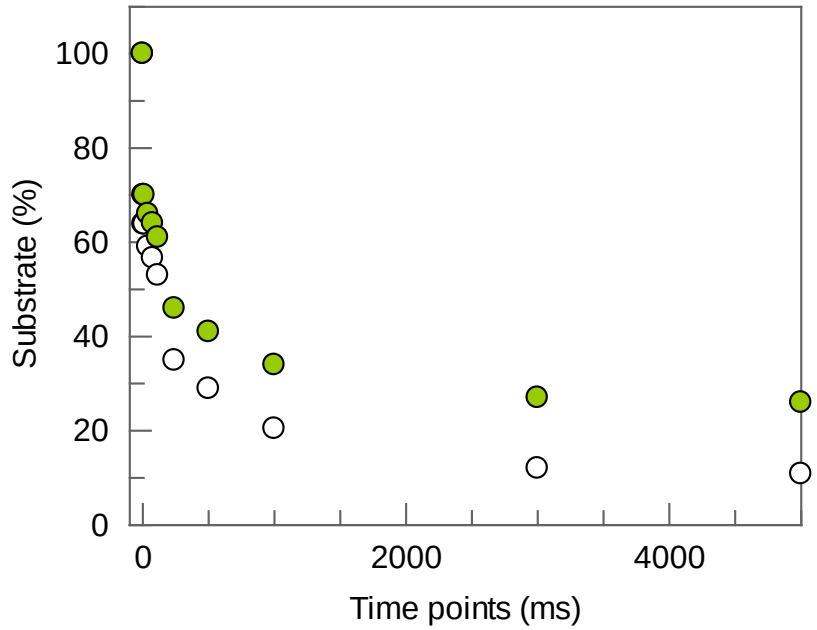

Supplementary data for Figure 3.8:
Plasmid unwinding assay by wt RepD-PcrA complex.
(A-D) Examples of raw data and linear fits. For each plasmid length, indicated in bp, linear fits were made to determine the duration of the observed unwinding phase (shown in the insets). Unwinding rates are collected in Tables for wt and N189K RepD.

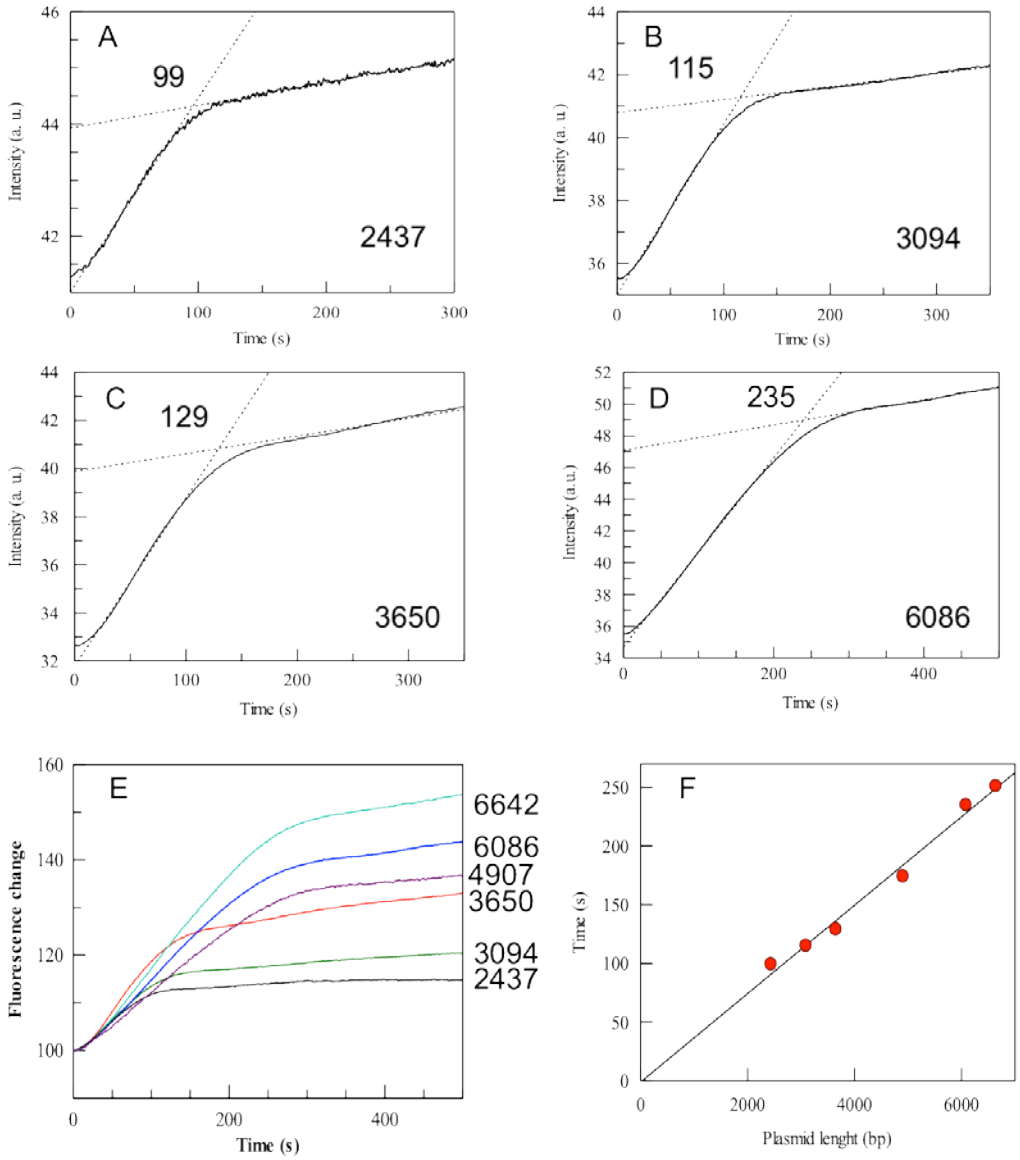

Plasmid length (bp)	N189K RepD Unwinding time (s)		Wt RepD Unwinding time (s)
	Experiment 1	**Experiment 2**	**Experiment 1**
2437	105	103	99
3094	118	117	115
3650	126	127	129
4907	198	198	174
6086	265	267	235
6642	321	320	251
Unwinding rate (bp s^{-1})	19 ± 2	18 ± 3	27 ± 2

Supplementary data for Figure 3.11:
Raw fluorescence intensity data calculated according to:
Fluorescence intensity = $I_{\parallel} + 2I_{\perp}$, where $I_{\parallel}$ is the fluorescence in the parallel plane, and $I_{\perp}$ is the fluorescence in the perpendicular plane.
Example of fluorescence intensity changes during individual titrations:

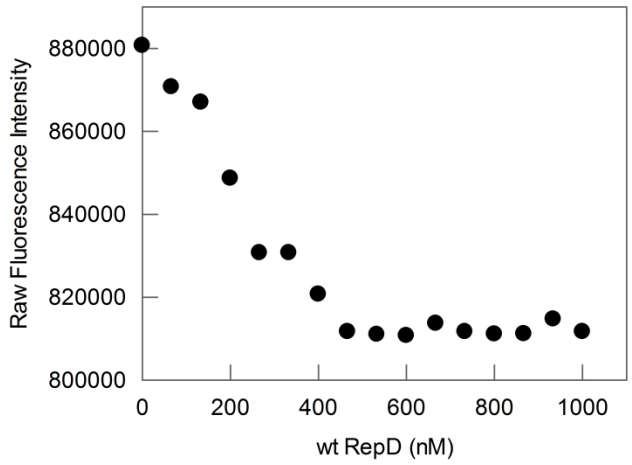

Supplementary data for Figure 3.12:
Each individual trace was fit to a single exponential using Kinetasyst (Hi-tech scientific) software.
Example fits for single traces for each RepD concentration. Rate constants (k_{obs}) and standard errors (S. e.) from each fit are shown with each fit. Y-axis scale is shown in % which represents raw fluorescence units from stopped flow instrument. Data from two separate experiments are collected in Tables for wt and N189K RepD.

250 nM – N189K

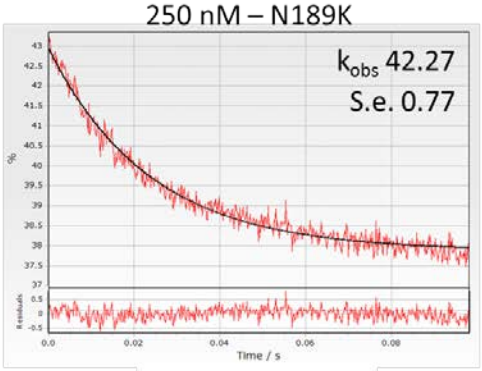

500 nM – N189K

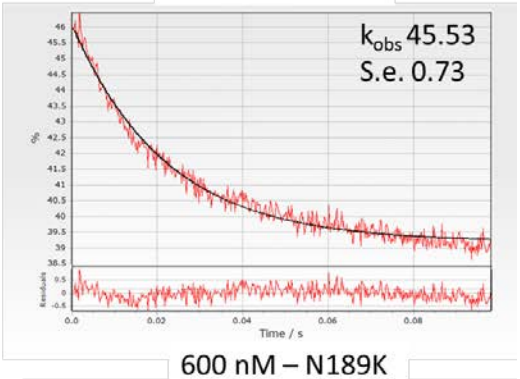

500 nM – N189K

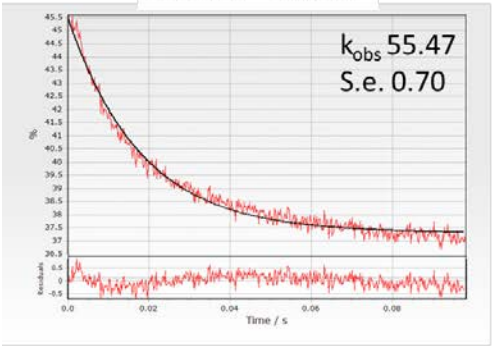

600 nM – N189K

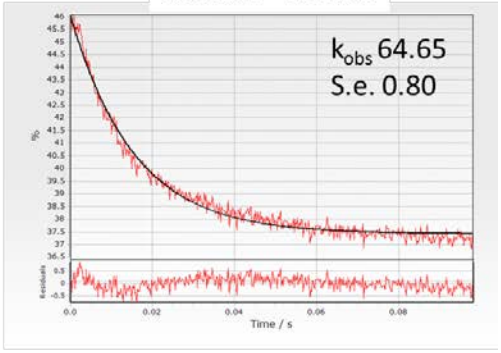

700 nM – N189K

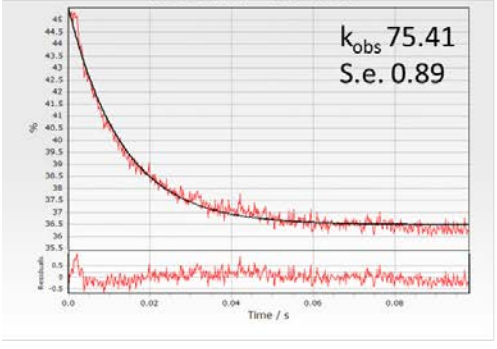

800 nM – N189K

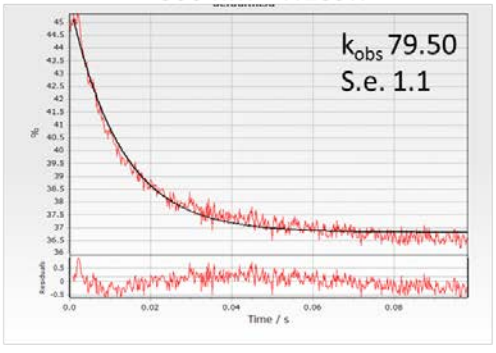

1000 nM – N189K

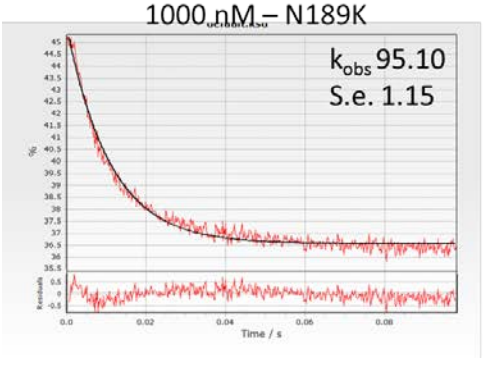

	Experiment 1		Experiment 2	
N189K RepD (nM)	Rate constant (s^{-1})	Std. err.	Rate constant (s^{-1})	Std. err.
250	42.27	0.77	39.33	1.22
400	45.53	0.73	54.24	1.2
500	55.47	0.70	55.7	1.28
600	64.65	0.80	67	1.44
700	75.41	0.89	77.1	1.57
800	79.50	1.1	84.2	1.6
1000	95.10	1.15	94.09	1.83
Binding rate ($\mu M\ s^{-1}$)	77.2	4.9	75.1	4.7
Intercept (s^{-1})	19.47	3.15	21.69	3

	Experiment 1		Experiment 2	
wt RepD (nM)	Rate constant (s^{-1})	Std. err.	Rate constant (s^{-1})	Std. err.
250	37.21	0.53	34.28	0.49
400	45.06	0.49	44.07	0.55
500	52.63	0.53	53.17	0.52
600	59.52	0.59	62.38	0.61
700	67.98	0.66	67.43	0.72
800	81.55	0.79	76.5	0.85
1000	97.96	1.22	95.97	1.03
Binding rate ($\mu M\ s^{-1}$)	85	5	80	2.8
Intercept (s^{-1})	12.48	3.26	12.7	1.8

Supplementary data for Figure 3.13:
Example of fits for fluorescence traces for N189K RepD with and without Mg^{2+}. Each individual trace was fit to a single exponential using Kinetasyst (Hi-tech scientific) software.
Dissociation rate constants and standard errors from each fit are shown. Results from two separate experiments are in Tables.
Y-axis scale is shown in % which represents raw fluorescence units from stopped flow instrument

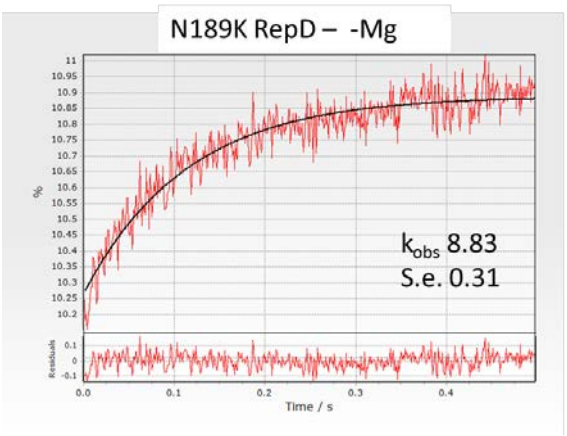

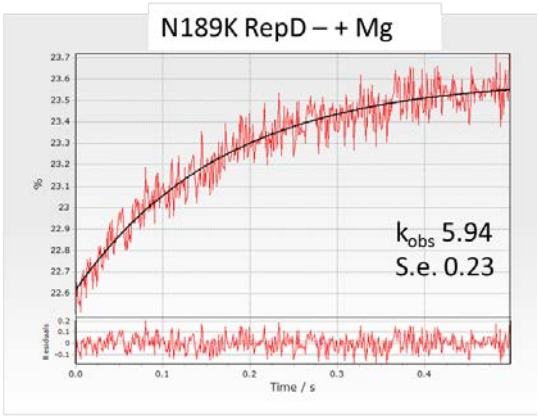

	- Mg		+ Mg	
N189K RepD (nM)	**Rate constant** (s^{-1})	Std. err.	**Rate constant** (s^{-1})	Std. err.
Experiment 1	8.83	0.31	5.94	0.23
Experiment 2	7.87	0.44	5.67	0.32

	- Mg		+ Mg	
wt RepD (nM)	**Rate constant** (s^{-1})	Std. err.	**Rate constant** (s^{-1})	Std. err.
Experiment 1	2.32	0.18	1.3	0.21
Experiment 2	2.1	0.17	1.14	0.08

Supplementary data for Figure 3.15:
Examples of Fluorescence intensity change and anisotropy (800 nM RepD). Fluorescence intensity = $I_{\parallel} + 2I_{\perp}$, where $I_{\parallel}$ is the fluorescence in the parallel plane, and $I_{\perp}$ is the fluorescence in the perpendicular plane, calculated by Kinetasyst software. Y-axis is fluorescence intensity.

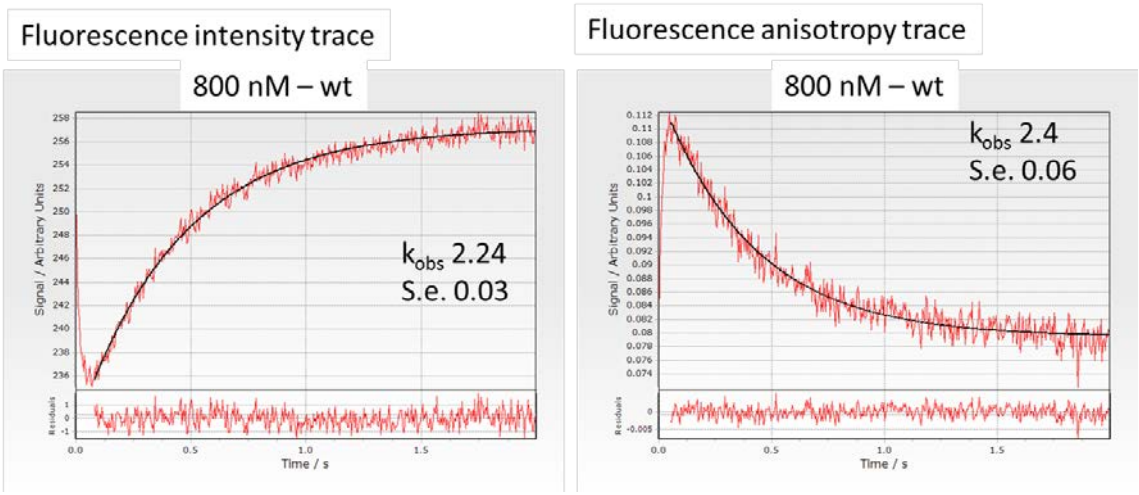

Supplementary data for Figure 3.16:
Individual traces were fit to single exponentials using Kinetasyst (Hi-tech scientific) software. Y-axis is anisotropy, calculated by Kinetasyst software. Rate constants and standard errors from each fit are shown.

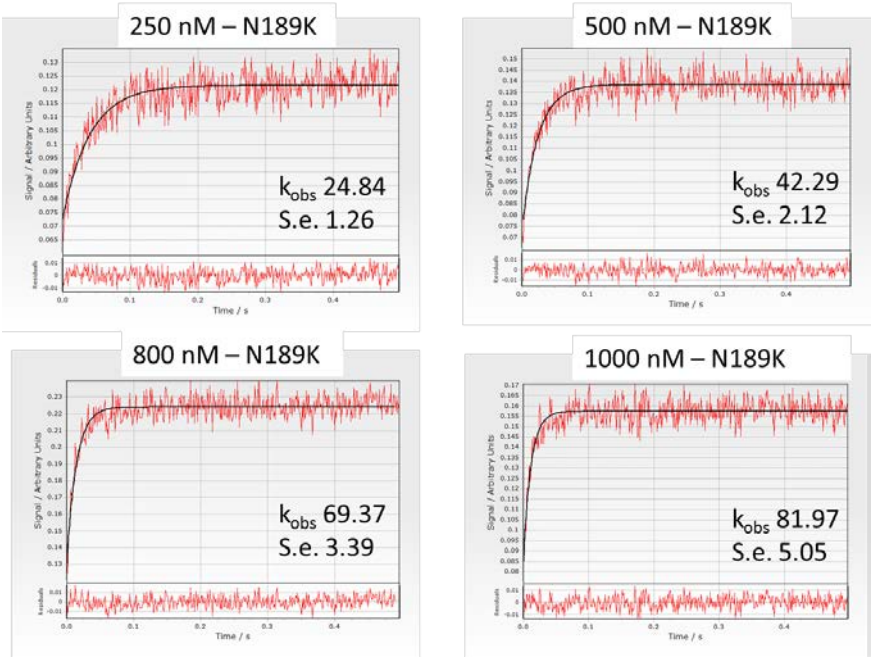

Supplementary data for Figure 3.19:
For each DNA junction, linear fits were made to determine the duration of the observed lag phase as shown. Lag phase duration (inidicated) was calculated from the intercept of the two linear fits. Ata frm two separate experiments are collected in Tables below.

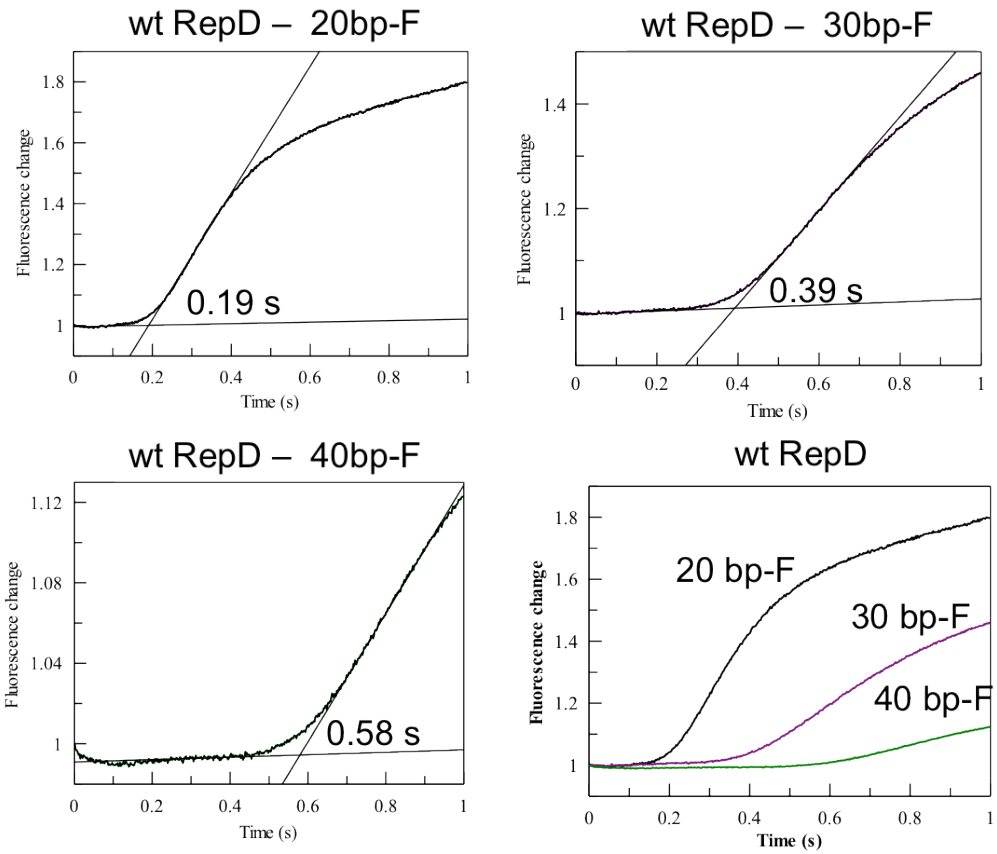

	N189K RepD Lag time (s)		Wt RepD Lag time (s)	
	Experiment 1	**Experiment 2**	**Experiment 1**	**Experiment 2**
20 bp	0.25	0.25	0.19	0.20
30 bp	0.50	0.49	0.39	0.42
40 bp	0.68	0.68	0.58	0.57
Unwinding rate (bp s^{-1})	46.5 ± 4	46.5 ± 3	51.2 ± 2	54 ± 8.6

Supplementary data for Figure 4.2:
Individual traces were fit to single exponentials using Kinetasyst (Hi-tech scientific) software. Y-axis is intensity, calculated by Kinetasyst software. Rate constants and standard errors from each fit are shown. Results from two separate experiments are in listed in the Table.

	Experiment 1		**Experiment 2**	
PolC (nM)	Rate constant (s^{-1})	Std. err.	Rate constant (s^{-1})	Std. err.
100	44.79	6.47	48.44	6.88
250	69.17	5.43	54.67	6.74
350	85.9	6.37	81.87	6.51
750	119.9	15.7	116.39	8.35
1000	157.9	16.39	149.3	15.42
Binding rate ($\mu M\ s^{-1}$)	118.3	8.2	112.7	9.5
Intercept (s^{-1})	37	5.13	34.7	5.4

100 nM PolC

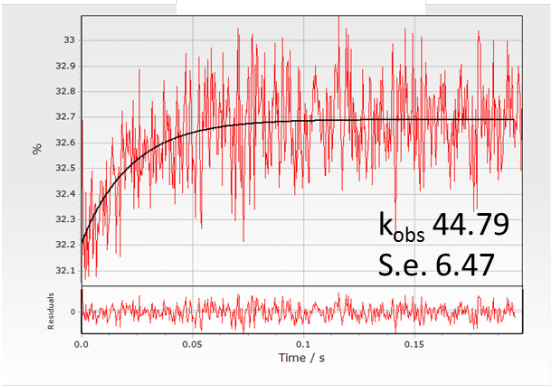

250 nM PolC

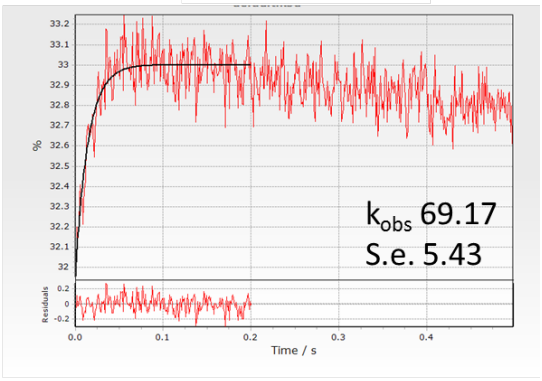

350 nM PolC

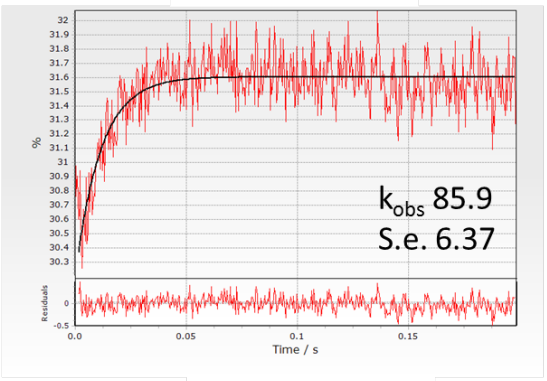

750 nM PolC

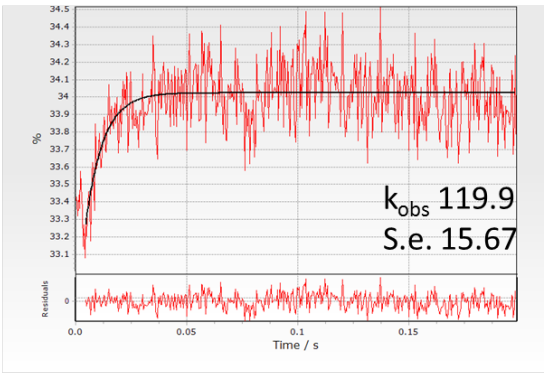

1000 nM PolC

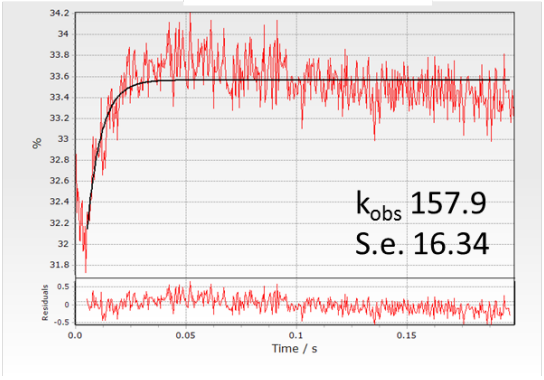

Supplementary data for Figure 4.6:
Individual traces were fit to single exponentials using Kinetasyst (Hi-tech scientific) software. Y-axis is intensity, calculated by Kinetasyst software. Rate constants and standard errors from each fit are shown. The rates and the S. e. are shown. Results from two separate experiments are listed in the Table.

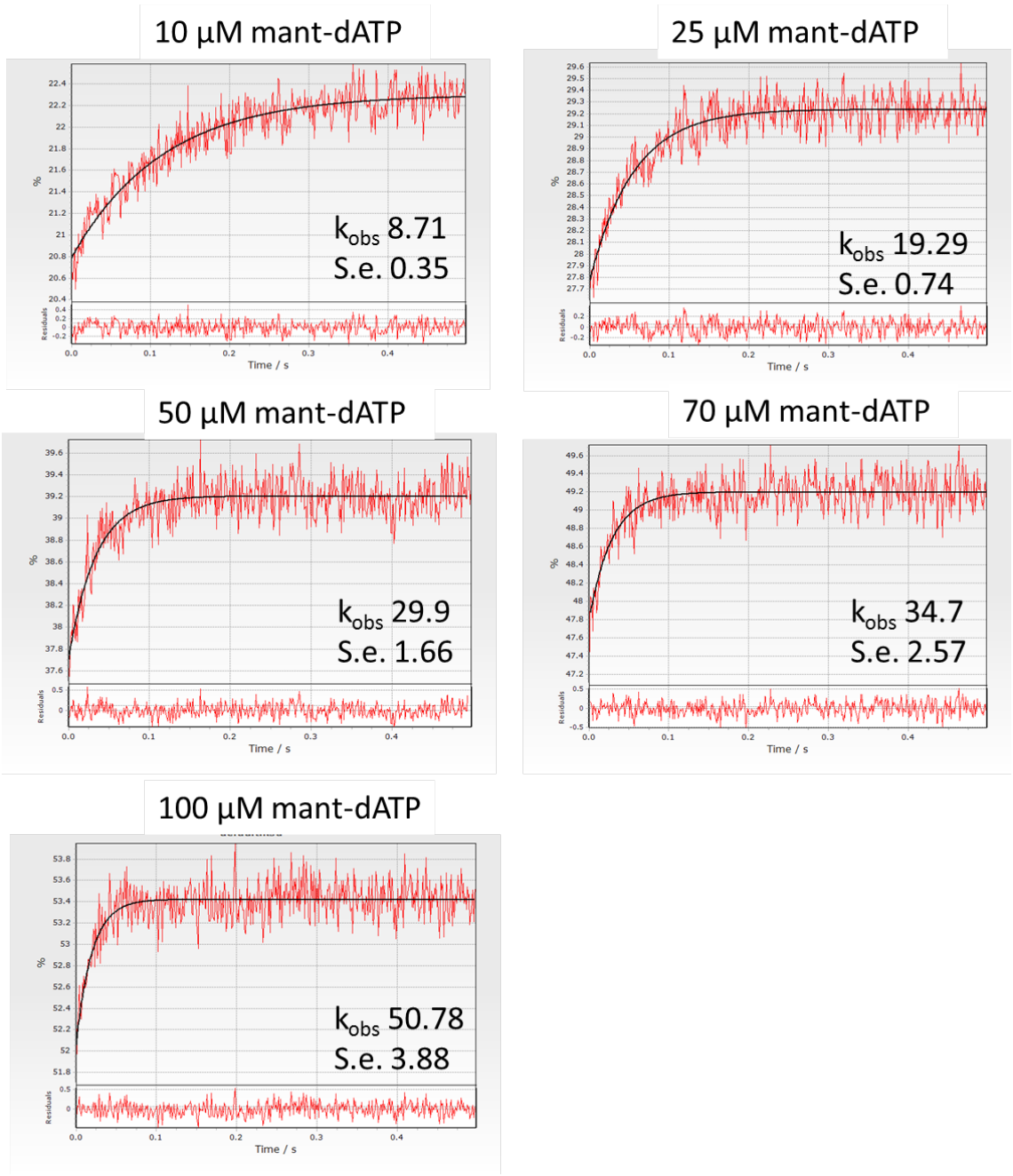

	Experiment 1		Experiment 2	
Mant-dATP (μM)	Rate constant (s^{-1})	Std. err.	Rate constant (s^{-1})	Std. err.
10	8.71	0.35	7.93	0.33
25	19.29	0.74	18.29	0.73
50	29.9	1.66	23.85	1.19
70	34.7	2.57	27.47	1.67
100	50.78	3.88	45.67	3.34
Binding rate ($\mu M\ s^{-1}$)	0.44	0.032	0.38	0.049
Intercept (s^{-1})	6.15	1.94	5.27	2.94

Supplementary data for Figures 4.4 and 4.8:
Dissociation kinetics of PolC from DNA (top panel) and from mant-dATP (bottom panel). Individual traces were fit to single exponentials using Kinetasyst (Hi-tech scientific) software. Y-axis is intensity, calculated by Kinetasyst software. Rate constants and standard errors from each fit are shown. The rates and the S. e. are shown. Results from two separate experiments are in listed in the Table.

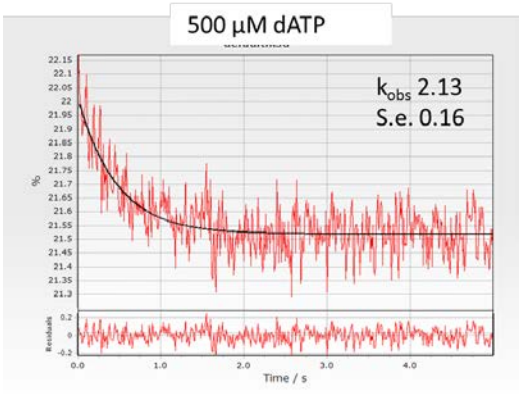

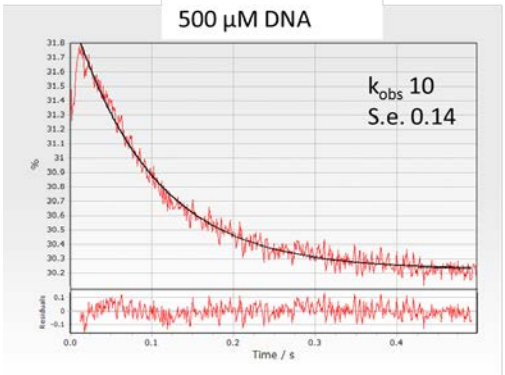

Supplementary data for Figure 4.10:

Steady-state measuremnts with PolC. (A-B) Examples of raw data and linear fits of two concentrations of dATP. Sequential addition of MDCC-PBP, DNA, Pyrophosphatase, dNTPs and PolC. The increase in intensity corresponds to the PolC addition in the complete solution. C and D show an example phosphate calibration. Known concentrations of Pi are added to the reaction mixture. The slope from the Pi calibration gives the fluorescence change per micromolar Pi. This is then used to convert the rate of fluorescence change in to rate of Pi release.

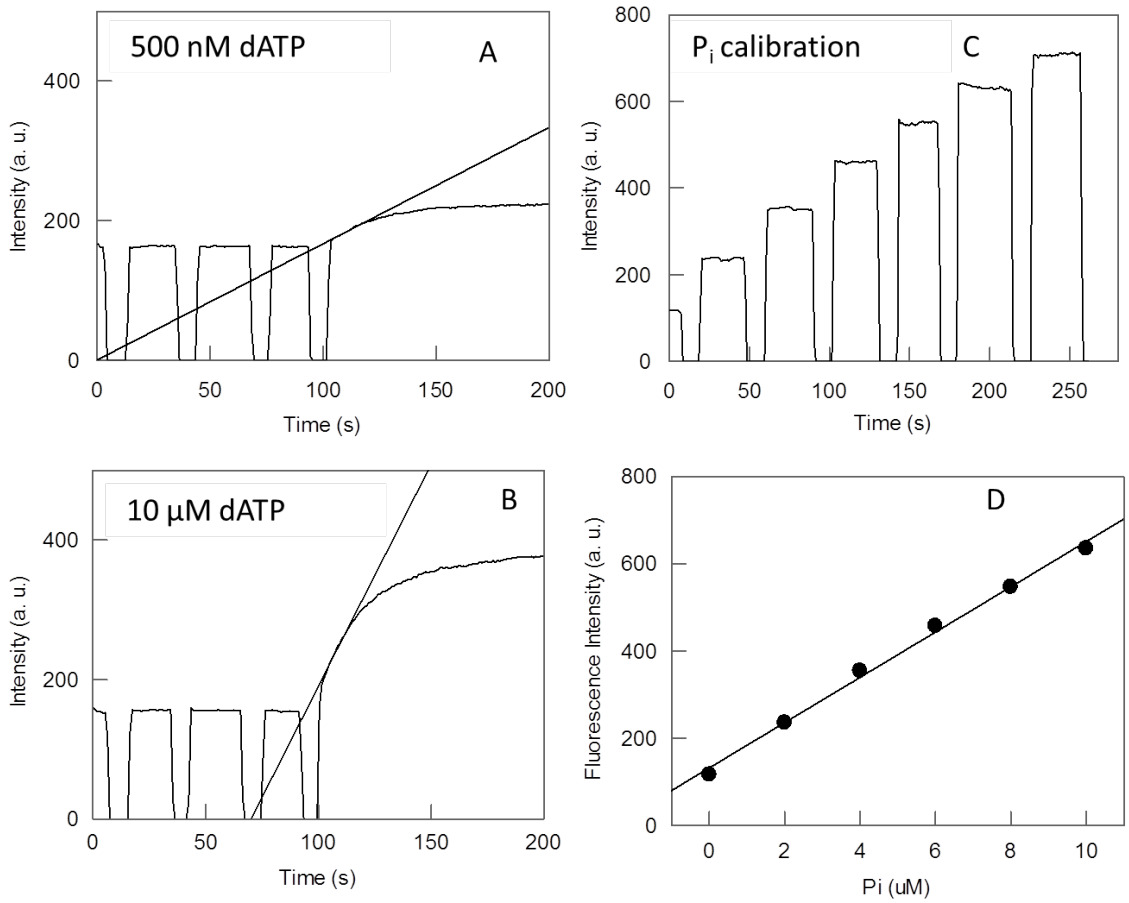

Pyrophospatase activity test

The activity of the PPase was assessed in presence of inorganic pyrophosphate. In this assay, a known concentration of PPi is mixed with the PPase. The Pi production rate was too fast to be measured at a concentration of pyrophosphatase of 0.001U/µL (concentration used for the PolC activity assay, Figure 4.10). A lower concentration of PPase (~ 100-fold) was used in order to allow measurements of the PPi hydrolysis kinetics. Increasing

concentrations of PPi were added to a solution containing 0.00001 U/µL pyrophosphatase and 20 µM MDCC-PBP. Solution conditions were as in Figure 4.10. The Michaelis-Menten equation was used to determine the k_{cat} and K_m values for the reaction. The best fit of the data gave a K_m value of 0.78 µM for PP_i and a k_{cat} of 80 nM s^{-1}.

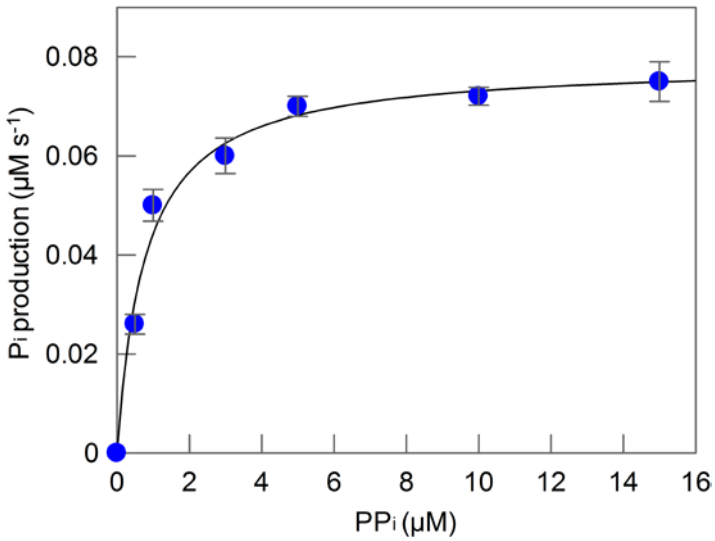

Supplementary data for Figure 4.18:

Examples of raw data and linear fits of two different length of plasmids. Data analysis was performed as described above (Supplementary data for Figure 3.8).

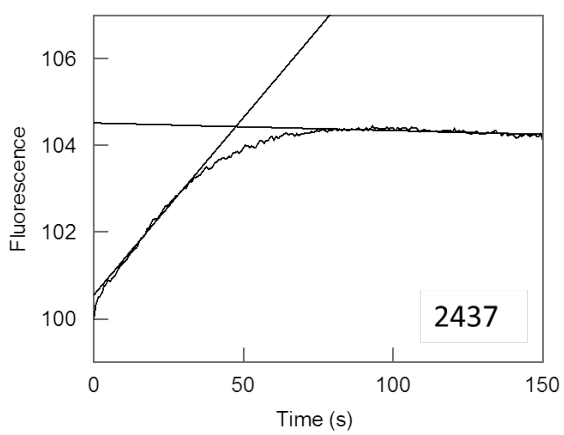

Break point: 48 s

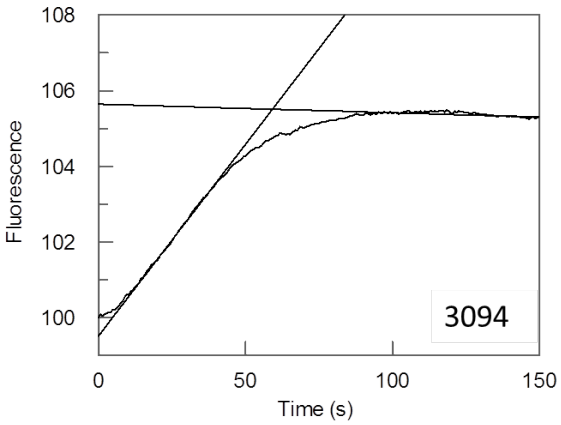

Break point: 57 s

Supplementary data for Figure 5.1:

Typical AFM image of a freshly cleaved mica surface used for sample deposition and imaging. The surface appeared regular and plain.

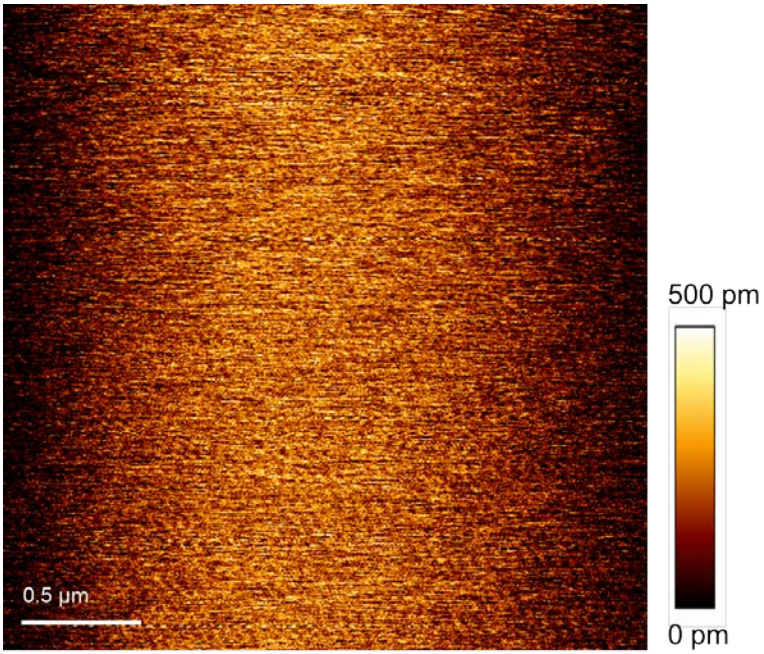

Supplementary data for Figure 5.3

AFM images of supercoiled plasmids upon incubation at different ionic strength.

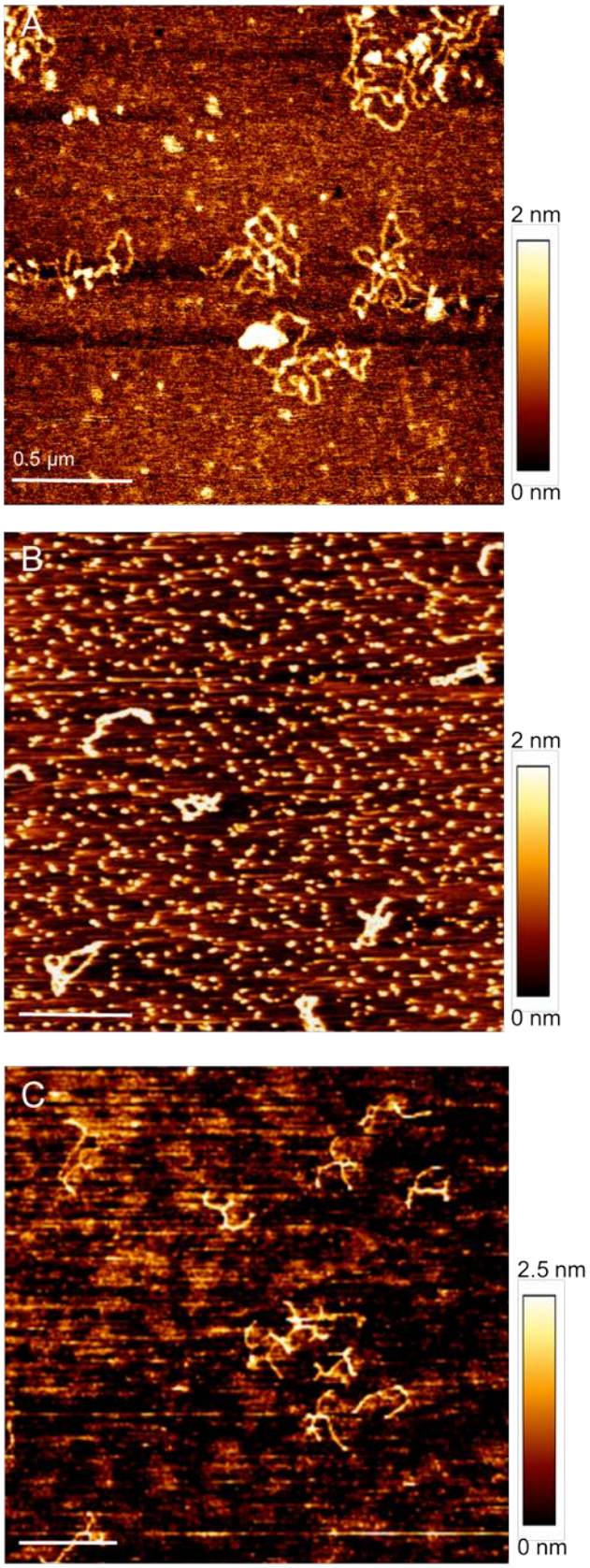

Supplementary data for Figure 5.6

Gel shift assay showing extent of binding of RepD to the OriD, at various concentrations of RepD. RepD, at the concentrations shown (in μM), was incubated with the DNA (10 μl of 1 μM DNA) before loading on a native polyacrylamide gel (see Methods for details). Upon incubation with RepD, a second shifted band was detected as result of interaction with the oriD. At higher RepD concentrations (> 1 μM), a supershift was observed caused by multiple RepD proteins bound on the DNA.

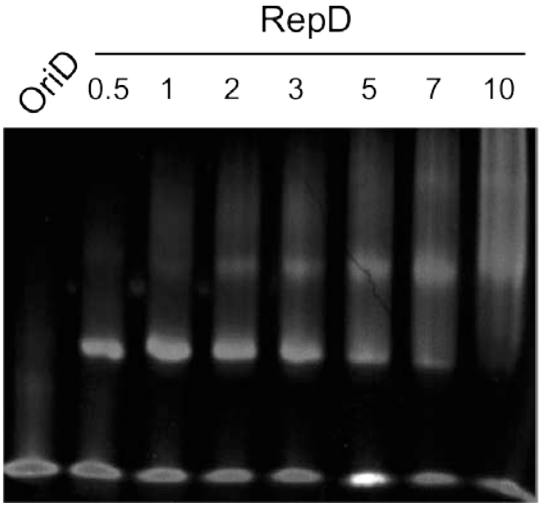

Supplementary data for Figure 5.9.

PcrA helicase bound to a short ssDNA oligonucleotide (oligo dT10). (A) The helicase was incubated with ssDNA for 5 minutes, prior sample deposition and imaging. (B) Height analysis of the helicase showing a single peak of ~ 3.5 nm.

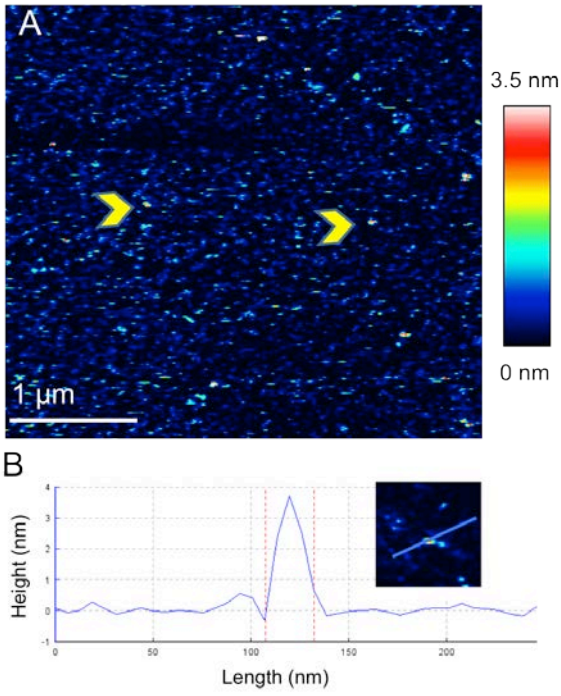

Supplementary data for Figure 5.11.

Fields of view of the “web-like” structures created by RepD-PcrA mediated unwinding in the absence of SSB.

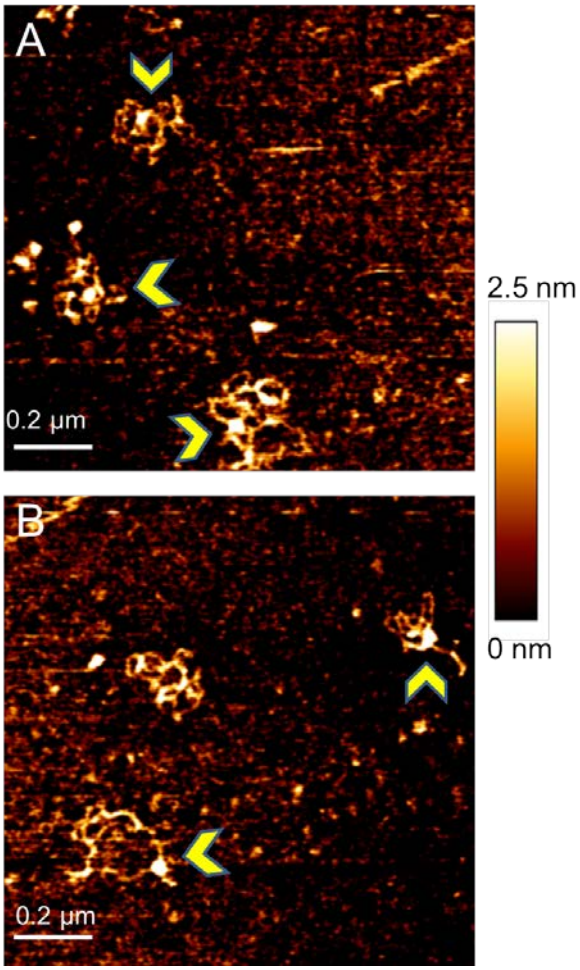

Supplementary data for Figure 5.18.

Heights analysis of the complex showed in Figure 5.18C2 (A) and Figure 5.18C3 (B).